

Copyright Undertaking

This thesis is protected by copyright, with all rights reserved.

By reading and using the thesis, the reader understands and agrees to the following terms:

- 1. The reader will abide by the rules and legal ordinances governing copyright regarding the use of the thesis.
- 2. The reader will use the thesis for the purpose of research or private study only and not for distribution or further reproduction or any other purpose.
- 3. The reader agrees to indemnify and hold the University harmless from and against any loss, damage, cost, liability or expenses arising from copyright infringement or unauthorized usage.

IMPORTANT

If you have reasons to believe that any materials in this thesis are deemed not suitable to be distributed in this form, or a copyright owner having difficulty with the material being included in our database, please contact lbsys@polyu.edu.hk providing details. The Library will look into your claim and consider taking remedial action upon receipt of the written requests.

DEVELOPMENT OF TRANSITION-METAL-BASED ELECTROCATALYSTS FOR EFFICIENT SEAWATER OXIDATION

ZHEN LI

PhD

The Hong Kong Polytechnic University

The Hong Kong Polytechnic University

Department of Applied Biology and Chemical Technology

Development of Transition-Metal-based Electrocatalysts for Efficient Seawater Oxidation

Zhen LI

A thesis submitted in partial fulfilment of the requirements for the degree of Doctor of Philosophy

December 2024

CERTIFICATE OF ORIGINALITY

I hereby declare that this thesis is my own work and that, to the best of my knowledge and

belief, it reproduces no material previously published or written, nor material that has been

accepted for the award of any other degree or diploma, except where due acknowledgement

has been made in the text.

Signature:

Name of student: Zhen Li

Abstract

Green hydrogen produced *via* water electrolysis is pivotal for replacing fossil fuels and achieving carbon neutrality. However, the large-scale deployment of water electrolyzers, which heavily rely on freshwater, raises concerns about water resource sustainability. Given that seawater constitutes 96.5 % of the Earth's water resources, producing green hydrogen through seawater electrolysis is an alternative and viable strategy for achieving dual-carbon goals. Compared to indirect seawater electrolysis, which requires a desalination pre-treatment, direct seawater electrolysis offers a simplified system with easier scalability and economic advantages. However, the efficiency of direct seawater electrolysis is hindered by the high thermodynamic energy barrier of water oxidation (1.23 V vs. reversible hydrogen electrode, RHE) and serious corrosion due to chlorine evolution reaction (CER) in the Cl⁻-rich seawater environment. Although noble-metal-based oxides, such as IrO₂ and RuO₂, exhibit excellent water oxidation performance, their scarcity limits their wide applications. Earth-abundant transition metals, with their d-orbital valence electronic structures, can interact with oxygencontaining intermediates, making them promising candidates for catalyzing the oxygen evolution reaction (OER).

Despite intensive efforts in recent years, the electrocatalytic seawater OER performance of transition-metal-based catalysts remains unsatisfactory, largely due to the competition between OER and CER and severe electrode corrosion. Therefore, designing efficient OER electrocatalysts based on transition metals with strong anti-corrosion properties is essential to advance seawater electrolysis techniques. In this thesis, several important strategies, including element doping, heterojunction construction, and microenvironmental modulation, are adopted to regulate the electronic structure of active sites, optimize OH⁻ adsorption, and increase the overpotential gap between OER and CER. Additionally, the Lewis-acid adsorption principle and electrostatic-repelling effect are applied to reduce the Cl⁻ adsorption, thereby mitigating

CER-induced corrosion. Four types of OER electrocatalysts, *g*-C₃N₄/Li-NiFe layered double hydroxides (LDH), Ni(OH)₂/LiFePO₄, Ni(OH)₂/NiMoO₄, and MoO₃/Fe₂O₃/MoS₂ have been successfully designed, exhibiting excellent OER activity and durability in seawater electrolyte.

Chapter I summarizes the mechanisms of OER and CER, along with a brief review of recent progress in transition-metal-based electrocatalysts. Strategies widely used for improving OER activity and anti-corrosion properties are also introduced. Brief descriptions of characterization techniques and electrochemical methods are summarized in Chapter II.

In **Chapter III**, Li doping and g-C₃N₄ hybridization were employed together to modify the structure of NiFe-LDH and study their effect on electrocatalytic seawater oxidation performance. Li-ion doping increases the Ni³⁺ population, while NiFe-LDH/g-C₃N₄ heterointerface redistributes interfacial charge and constructs a built-in electric field, thereby improving selectivity towards OH⁻. These strategies further decrease the OER Gibbs free energy from 0.72 to 0.53 eV, enabling the g-C₃N₄/Li-NiFe-LDH catalyst to stably operate seawater oxidation at 200 mA cm⁻² for 100 h.

Chapter IV forges a bridge between the recycling of spent Li-ion batteries (LIBs) and seawater electrolysis. By employing pulsed laser ablation and electrodeposition techniques, Ni(OH)₂ interfaced with laser-ablated LiFePO₄ (Ni(OH)₂/L-LFP) was fabricated. The NiOOH/Fe₃(PO₄)₂ active species formed after surface reconstruction are particularly advantageous for promoting OH⁻ while concurrently suppressing Cl⁻ adsorption. Additionally, PO₄³⁻ ions, leached during the reconstruction process, contribute to Cl⁻ ion repelling in seawater, mitigating catalyst corrosion. The Ni(OH)₂/L-LFP demonstrates exceptional OER performance, achieving a current density of 10 mA cm⁻² at a low overpotential of 237 mV in alkaline seawater. It also maintains excellent stability at 100 mA cm⁻² for 600 h.

Chapters V and VI focus on energy-saving seawater electrolysis. In Chapter V, the anionadsorption strategy was used to modulate the local microenvironment on the catalyst surface, improving methanol-assisted seawater electrolysis performance. *In situ* leached MoO₄²⁻ during the reconstruction process of Ni(OH)₂/NiMoO₄ (Ni(OH)₂/NMO) pre-catalyst optimizes the coordination environment on NiOOH surface, simultaneously decreasing the adsorption energy for Cl⁻ and accelerating the proton-coupled electron transfer in the methanol oxidation reaction (MOR). Consequently, the Ni(OH)₂/NMO-based full cell achieves current densities of 0.1 and 0.5 A cm⁻² at considerably lower cell voltages (1.840 and 2.324 V, respectively) in methanol-hybrid seawater compared to seawater electrolyte (1.904 and 2.392 V, respectively). **Chapter VI** discusses ternary heterojunctions of MoO₃/Fe₂O₃/MoS₂ and their effect on light-assisted seawater oxidation. The three-phase heterointerface favors OH⁻ adsorption and increases the overpotential gap between OER and CER, ensuring high OER selectivity. *In situ* leached MoO₄²⁻ and SO₄²⁻ species further reduce Cl⁻ adsorption, enhancing anti-corrosion properties. The catalyst demonstrates excellent stability at 300 mA cm⁻² for 500 h. Built-in electric fields at interfaces lower interfacial resistance and extend the lifetime of photo-generated carriers by 1.47-fold, achieving a 20.4 % increase in seawater OER current density under light irradiation.

Finally, **Chapter VII** presents the conclusions of all research work and perspectives for future research directions.

Acknowledgement

I would like to express sincere gratitude to my supervisor Prof. Lawrence Yoon Suk Lee for his invaluable guidance and comments on my research work. His guidance helped me not only with research improvement but also with personality development. Without his help, I would have never reached this stage.

My grateful thanks also go to Prof. Byungchan Han of Yonsei University and Prof. Liang Dong of Northeastern University at Qinghuangdao for their collaborative support in the theoretical studies.

I would also like to extend my thanks to co-supervisor Prof. Zhongping Yao for his support, Dr. Mengjie Liu, Dr. Yiqun Chen, Dr. Ying Wang, Dr. Daekyu Kim, Dr. Yong Li for sharing their experience in electrocatalysis. Dr. Xiandi Zhang and Dr. Jia Yan for synthesizing precursor materials, Dr. Hui Gao for laser ablation training, Mr. Youbin Zheng of Northeastern University at Qinghuangdao and Miss Wei Tao of Yonsei University for their contributions to the analyses of theoretical calculation results. Acknowledgements also go to all the labmates in Prof. Lawrence Yoon Suk Lee's research team, especially Miss Qixiao Lu, Mr. Xucun Ye, Miss Mengting Li, Miss Wenhan Zu, and Mr. Jianlin Huang.

Finally, I would like to extend my deepest appreciation to my family for their endless love and support.

List of Publications

- 1. Yong Li, Weining Song, Teng Gai, Lipeng Wang, **Zhen Li**, Qi Liu, Peng He,* and Lawrence Yoon Suk Lee,* Self-Activated Oxophilic Surface of porous molybdenum carbide nanosheets promotes hydrogen evolution activity in alkaline environment, *Submitted to Journal of Colloid and Interface Science and under review*.
- 2. Yiqun Chen, Yan Zhang, **Zhen Li**, Biao Feng, Mengting Li, Qiang Wu,* Zheng Hu, Lawrence Yoon Suk Lee,* Harnessing interfacial Cl⁻ ions for concurrent formate production at industrial level *via* CO₂ reduction and methanol oxidation. *Submitted to Advanced Functional Materials and under review*.
- 3. Toan Minh Pham, Kuyngmin Im, Hao Quoc Nguyen, **Zhen Li**, Lawrence Yoon Suk Lee, Jinsoo Kim,* Surface reconstructed hollow Fe-doped CoO_x(OH)_y bifunctional electrocatalysts for rechargeable zinc–air batteries, *Submitted to Journal of Power Sources and under review*.
- 4. **Zhen Li**, Mengting Li, Yiqun Chen, Xucun Ye, Mengjie Liu, Lawrence Yoon Suk Lee,* Upcycling of spent LiFePO₄ cathodes to heterostructured electrocatalysts for stable direct seawater splitting, *Angewandte Chemie International Edition*, **2024**, *63*, e202410396
- 5. **Zhen Li**, Youbin Zheng, Wenhan Zu, Liang Dong,* Lawrence Yoon Suk Lee,* Molybdate-modified NiOOH for efficient methanol-assisted seawater electrolysis, *Advanced Science*, **2024**, 2410911.
- 6. **Zhen Li**, Wei Tao, Ying Wang, Xucun Ye, Yiqun Chen, Byungchan Han,* and Lawrence Yoon Suk Lee*, Corrosion-resistant MoO₃/Fe₂O₃/MoS₂ heterojunctions stabilize OH⁻ for efficient light-assisted seawater electrooxidation, *Submitted to Journal of the American Chemical Society*.
- 7. Yiqun Chen, Yan Zhang, **Zhen Li**, Mengjie Liu, Qiang Wu, Tsz Woon Benedict Lo, Zheng Hu,* Lawrence Yoon Suk Lee,* Amphipathic surfactant on reconstructed bismuth enables industrial-level electroreduction of CO₂ to formate. *ACS Nano*, **2024**, *18*, 19345–19353.
- 8. **Zhen Li**, Mengjie Liu, Jia Yan, Lawrence Yoon Suk Lee,* A "doping-interfacing" strategy enables efficient alkaline freshwater and seawater oxidation by NiFe-layered double hydroxides, *Chemical Engineering Journal*, **2023**, *473*, 145293
- Zhen Li, Ying Wang, and Lawrence Yoon Suk Lee,* Recent advances in synergistic modulation of transition-metal-based electrocatalysts for water oxidation: A mini review, *Catalysts*, 2023, 12, 1230.

List of abbreviations

AIMD *ab initio* molecular dynamics

AEM anion exchange membrane

BET Brunner–Emmet–Teller

CER chlorine evolution reaction

 $C_{\rm dl}$ double-layer capacitance

CV cyclic voltammetry

DOS density of states

DFT density functional theory

EIS electrochemical impedance spectroscopy

ECSA electrochemical surface area

EDS energy-dispersive X-ray spectrometry

 $E_{\rm CB}$ conduction band energy

 $E_{\rm VB}$ valence band energy

 $E_{\rm F}$ Fermi levels

 $E_{\rm a}$ activation energy

FE Faradaic efficiency

GGA generalized gradient approximation

HER hydrogen evolution reaction

ICP-OES inductively coupled plasma optical emission spectroscopy

LSV linear sweep voltammetry

LIBs lithium-ion batteries

MEA membrane electrode assembly

MOR methanol oxidation reaction

OCP open-circuit potential

OER oxygen evolution reaction

PL photoluminescence

PAW projected Augmented-Wave

PBE Perdew-Burke-Enzerhof

PDDA poly(diallyldimethylammonium chloride)

PCET proton-coupled electron transfer

PLAL pulsed laser ablation in liquid

RHE reversible hydrogen electrode

 $R_{\rm ct}$ charge transfer resistance

RF roughness factor

RDS rate-determining step

SEM scanning electron microscopy

STEM scanning transmission electron microscopy

SCE standard calomel electrode

SHE standard hydrogen electrode

TOF turnover frequency

TEM transmission electron microscopy

TRPL time-resolved photoluminescence

UPS ultraviolet photoelectron spectrum

VASP Vienna ab initio simulation package

VBM valence band maximum

XRD X-ray diffraction

XPS X-ray photoelectron spectroscopy

Φ work function

Table of Contents

Abstract	i
Acknowledgement	iv
List of Publications	v
List of abbreviations	vi
Chapter I Introduction	1
1.1. Overview of Freshwater and Seawater Electrolysis	2
1.2. Overview of Oxygen Evolution Reaction	4
1.2.1. Mechanism of Overall Water Electrolysis	4
1.2.2. Mechanism of Oxygen Evolution Reaction	
1.2.3. Evaluation of OER Catalytic Performance	9
1.2.3.3. Overpotentials	
1.2.3.2 Tafel Slope and Exchange Current Density	11
1.2.3.4. Electrochemical Impedance Spectroscopy (EIS)	12
1.2.3.5. Electrochemical Surface Area (ECSA)	12
1.2.3.6. Turnover Frequency (TOF)	13
1.2.3.7. Faradaic Efficiency (FE)	13
1.2.3.8. Stability	14
1.2.4. Strategies for Improving Oxygen Evolution Reaction Activities	14
1.2.4.1. Nanostructuring of Catalysts	16
1.2.4.2. Electronic Structure Optimization	18
1.2.4.3. Synergistic Modulation	20
1.2.4.4. External Fields Assistance	23
1.3. A Brief Review of Seawater Oxidation Electrocatalysts	26
1.3.1. Mechanism of Chlorine Evolution Reaction (CER)	26
1.3.2. Strategies for Enhancing the Selectivity of OER in Seawater	28
1.13.2.1. Design of Anti-corrosion Electrocatalysts	28
1.3.2.2. Anti-corrosion Additives	29
1.3.2.3. Organic-Transformation-Coupled Seawater Electrolysis	30
1.4. Objectives and Novelty of Thesis	31
1.4.1. Objectives of Thesis	31
1.4.2. Novelty of Thesis	32
1.5. References	34
Chapter II Experimental Techniques and Characterization Methods	41
2.1. Introduction	

	2.2.	Characterization Methods	.42
	2.2.1.	X-ray Diffraction (XRD)	.42
	2.2.2.	Scanning Electron Microscopy (SEM)	.43
	2.2.3.	Transmission Electron Microscopy (TEM)	.44
	2.2.4.	X-ray Photoelectron Spectroscopy (XPS)	.46
	2.2.5.	Brunner–Emmet–Teller (BET) Analysis.	.47
	2.2.6.	Inductively Coupled Plasma Optical Emission Spectroscopy (ICP-OES)	.48
	2.2.7.	UV-Vis Absorption Spectroscopy	.49
	2.2.8.	Raman Spectroscopy	.50
	2.2.9.	Photoluminescence (PL) and Time-Resolved PL (TRPL) Spectroscopy	.52
	2.2.10	Ultraviolet Photoelectron Spectroscopy (UPS)	.53
	2.2.11	. Electron Paramagnetic Resonance (EPR) Spectroscopy	.54
	2.3. E	lectrochemical Characterization Methods and Theoretical Calculation	.56
	2.3.1.	Selection of Electrodes and Their Preparation.	.56
	2.3.2.	Electrochemical Measurements	.57
Ch	apter I	II Li-Doped NiFe-LDH/g-C3N4 for Seawater Oxidation	.59
	3.1.	Objective and Motivation	.60
	3.2.	Introduction	.60
	3.3.	Experimental Section	.62
	3.3.1.	Raw Materials	.62
	3.3.2.	Catalysts Synthesis	.63
	3.3.3.	Electrochemical Performance Test	.64
	3.4.	Results and Discussion	.64
	3.4.1.	Structure Characterization	.64
	3.4.2.	Electrochemical Performance	.73
	3.4.3.	Seawater Oxidation Performance	.75
	3.4.4.	OER and Anti-corrosion Mechanisms	.78
	3.4.5.	Theoretical Calculations	.84
	3.6.	References	.92
Ch	apter I	V Upcycling of Spent LiFePO ₄ into Electrocatalysts for Seawater Oxidation	95
	4.1.	Objective and Motivation	.96
	4.2.	Introduction	
	4.3.	Experimental Section	
	4.3.1.	Raw Materials	.98

	4.3.2.	Catalysts Synthesis	98
	4.3.3.	Electrochemical Performance Test.	99
	4.3.4.	Flow Cell Measurements	100
	4.3.5.	Calculation of Electricity Consumed for H ₂ Production	100
	4.4.	Results and Discussion	101
	4.4.1.	Structure Characterization	101
	4.4.2.	Electrochemical OER Performance and Mechanism	108
	4.4.3.	Seawater OER and Overall Seawater Splitting Performance	115
	4.4.4.	OER mechanism and anti-corrosion property of Ni(OH) ₂ /L-LFP	121
	4.5.	Conclusion	134
	4.6.	References	135
Ch	apter V	Molybdate-Modulated NiOOH for MeOH-Assisted Seawater Electrolysis	s 139
	5.1.	Objective and Motivation	140
	5.2.	Introduction	140
	5.3.	Experimental Section	142
	5.3.1.	Raw Materials	142
	5.3.2.	Catalysts Synthesis.	142
	5.3.3.	Electrochemical Performance Test.	143
	5.3.4.	Flow Cell Measurements	144
	5.3.5.	Calculations of Energy Cost and Savings for the H ₂ Production	145
	5.4.	Results and Discussion	145
	5.4.1.	Structure Characterization	145
	5.4.2.	OER Performances of Ni(OH) ₂ /NMO in Alkaline Freshwater and Seawater	149
	5.4.4.	MOR and Methanol-assisted Seawater Electrolysis	155
	5.4.5.	Mechanisms and Anti-corrosion Properties of Ni(OH) ₂ /NMO	159
	5.5.	Conclusions	175
	5.6.	References	176
Ch	apter V	/I Light-Assisted Seawater Electrooxidation by MoO3/Fe2O3/MoS2	179
	6.1.	Objective and Motivation	180
	6.2.	Introduction	180
	6.3.	Experimental Section	182
	6.3.1.	Raw Materials	182
	6.3.2.	Catalysts Synthesis.	183
	633	Electrochemical Performance Test	184

	6.3.4.	Light-assisted Electrocatalysis Measurements	184
	6.4.	Results and Discussion	185
	6.4.1.	Structure Characterization	185
	6.3.2.	Electrocatalytic Performance in Alkaline Freshwater and Seawater	191
	6.4.3.	Exploration of OER and Anti-corrosion Mechanisms	196
	6.3.4.	Light-assisted OER Performance and Mechanism	210
	6.5.	Conclusion	216
	6.6.	References	218
Ch	apter V	II Conclusions and Perspectives	222
	7.1.	Conclusions	223
	7.2.	Perspectives	226
	7.3.	References	228

Chapter I

Introduction

1.1. Overview of Freshwater and Seawater Electrolysis

The rapid increase in population and global industrialization have led to a growing demand for traditional fossil fuels such as natural gas, oil, and coal.^[1-3] The massive consumption of these fossil fuels has resulted in a global energy crisis and excessive greenhouse gas emissions, posing serious threats to the environment and health.^[4] Therefore, it is urgent to shift energy sources to reduce the reliance on fossil fuels.^[5, 6] Developing clean and renewable energy, including wind power, hydropower, solar energy, and tidal energy, has become a significant research focus in recent years.^[7, 8] However, the intermittent nature and geographical restrictions of these energy sources hinder their large-scale application. Therefore, the rational design and development of renewable energy storage and transition techniques are necessary to ensure a continuous supply of clean energy.^[9-11]

Hydrogen is considered one of the most promising clean energy sources due to its high energy density (142.35 kJ g⁻¹) and zero-carbon emission. Currently, most hydrogen gas is produced through methane reforming and coal gasification, which require high-temperature and high-pressure conditions. Unfortunately, these approaches yield hydrogen of unsatisfactory purity due to the inevitable huge emission of CO₂. As an alternative, hydrogen production by water electrolysis has attracted wide attention due to its mild operation conditions and high hydrogen purity. Using electricity generated from renewable energy to drive water electrolysis not only addresses electricity storage issues but also mitigates the intermittent and unstable nature of renewable energy sources (**Figure 1.1**). Currently, hydrogen production from water electrolysis accounts for only 4 % of the global hydrogen market, indicating substantial potential for industrial-scale application. As a production of the solution of the global hydrogen market, indicating substantial potential for industrial-scale application.

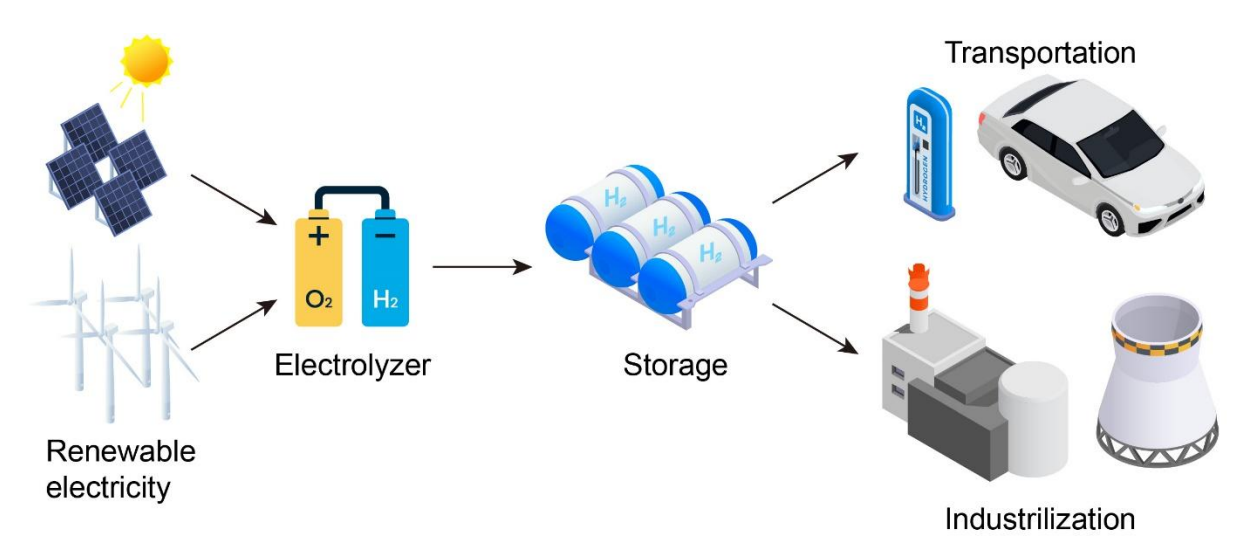


Figure 1.1. Schematic of a sustainable energy landscape based on electrocatalysis. [22]

Electrocatalytic water splitting is an electrochemical process in which water is split into hydrogen and oxygen gases, driven by electric power. Due to the strong chemical stability of water molecules, water electrolysis requires high energy consumption. During water splitting, the hydrogen evolution reaction (HER) occurs at the cathode, where protons gain electrons to form H₂ molecules. Platinum-based catalysts typically exhibit excellent HER activity and are used as benchmarks for evaluating other catalysts. In contrast to HER, the oxygen evolution reaction (OER), occurring at the anode, involves a four-electron transfer process that includes O—H bond breaking and O—O bond formation, resulting in a high reaction energy barrier. As a result, OER is more challenging to initiate compared to HER, making it the limiting factor in the overall reaction efficiency of water electrolysis. Typically, RuO₂ and IrO₂ are used in OER catalysis to reduce the energy barrier and enhance the reaction rate. However, their high cost, rarity, and poor stability greatly hinder the industrial application of water electrolysis. Recently, transition-metal-based materials, such as oxides, hydroxides, sulfides, and phosphates, have shown appealing catalytic OER performance, demonstrating the potential for industrial application of non-noble-metal catalysts. (29, 30)

Given the concern about freshwater shortage with large-scale application of water electrolysis, [31-34] seawater electrolysis is increasingly recognized as an attractive alternative,

as seawater constitutes 96.5 % of the global water supply.^[35] Compared to indirect seawater electrolysis, direct seawater electrolysis, without the need for a desalination step, offers lower costs and economic benefits.^[34, 36] However, the presence of a large amount of chloride anions (approximately 0.5 M) in seawater, which can be adsorbed on the anode and oxidized to Cl₂ (in acidic seawater) or ClO⁻ (in alkaline seawater), results in severe corrosion on electrocatalysts.^[37, 38] Therefore, designing efficient OER electrocatalysts with high selectivity towards OH⁻-reactants is essential to advance seawater splitting techniques.

According to the catalytic reaction mechanism, conductivity, number of catalytic active sites, and reaction energy barrier are the bottlenecks of water electrolysis.^[39] Previous studies demonstrated that designing unique morphologies, exposing more active sites, adopting elemental doping, defect engineering, and interfacial modulation can effectively optimize catalytic performance.^[40-42] Additionally, coating catalysts with a hard protective layer^[43] and modulating the microenvironment around active sites can alleviate corrosion in seawater.^[44-46] Therefore, developing facile and low-cost fabrication methods for the scale-up synthesis of catalysts, in-depth investigation of structure and catalytic mechanisms, and enhancing anticorrosion properties are key to promoting the large-scale application of hydrogen generated from seawater electrolysis.

This chapter discusses the reaction mechanisms of overall water electrolysis and OER. It summarizes evaluation methods of OER performance and strategies for interfacial and structural modulation. The research background, objectives, and novelty are also described.

1.2. Overview of Oxygen Evolution Reaction

1.2.1. Mechanism of Overall Water Electrolysis

Figure 1.2 shows a typical water electrolysis cell consisting of a cathode, an anode, an electrolyte, and a power supply. The cathode and anode are connected through an external circuit to form a complete conductive loop. Water electrolysis involves two half-reactions:

HER at the cathode and OER at the anode. Specifically, when the cell is supplied with direct electricity, electrons are transferred to the cathode, where protons gain electrons and are reduced to hydrogen, while water is oxidized to oxygen at the anode. The overall reaction equation for water electrolysis is:

$$2H_2O \rightarrow 2H_2 + O_2 (E^{\circ}_{cell} = 1.23 \text{ V})$$
 (1.1)

In the actual water electrolysis process, the low ionization of freshwater leads to poor conductivity. Therefore, NaOH, KOH, or H_2SO_4 are usually added to freshwater to increase the conductivity of the electrolyte. In acidic or neutral electrolytes, the electrochemical reactions are as follows:

Cathode:
$$2H^+ + 2e^- \rightarrow H_2$$
 (1.2)

Anode:
$$H_2O \rightarrow \frac{1}{2}O_2 + 2H^+ + 2e^-$$
 (1.3)

In alkaline electrolytes, the electrochemical reactions are:

Cathode:
$$2H_2O + 2e^- \rightarrow H_2 + 2OH^-$$
 (1.4)

Anode:
$$2OH^{-} \rightarrow \frac{1}{2}O_{2} + 2H_{2}O + 2e^{-}$$
 (1.5)

The overall reaction remains the same as in equation (1.1).

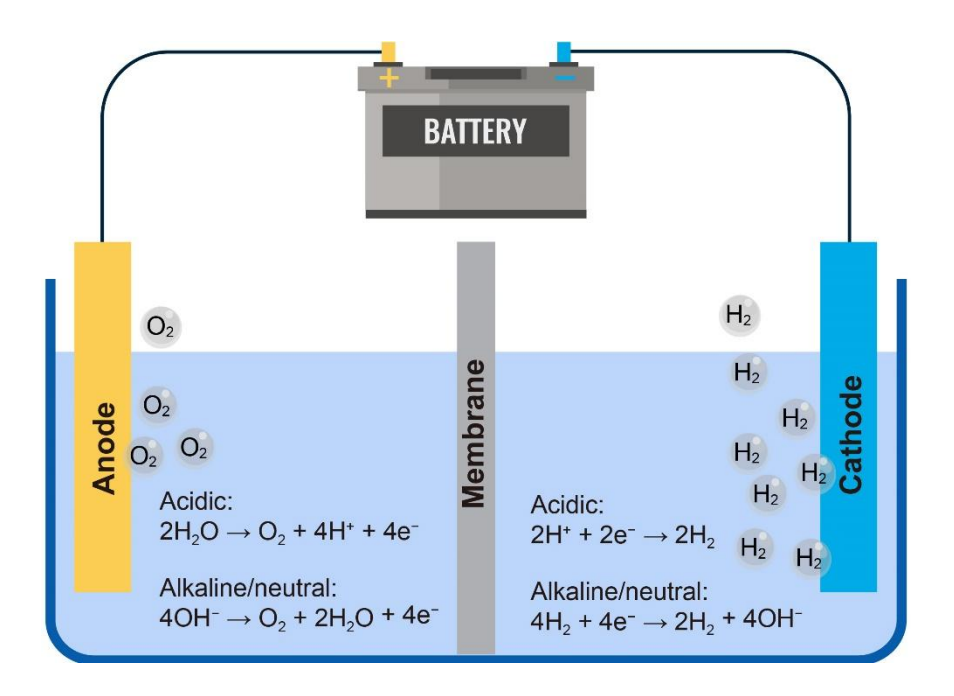


Figure 1.2. A schematic illustration of a typical water electrolyzer. [47]

Under controlled reaction conditions, the theoretical decomposition voltage (E_d) of water electrolysis is determined by thermodynamic parameters. At different temperatures and pressures, E_d is given by:

$$E_{\rm d} \approx 1.23 - \frac{dE}{dT}(T - 25) + 0.0435 \times \log P$$
 (1.6)

where T and P are the temperature and pressure in the electrolysis cell, respectively. According to this equation, E_d can be reduced by increasing the temperature or pressure in the cell. The standard Gibbs free energy (ΔG°) for splitting one mole of water into one mole of hydrogen and 0.5 moles of oxygen is 237.21 kJ mol⁻¹, while the enthalpy change (ΔH°) for the formation of one mole of hydrogen is 285.84 kJ mol⁻¹, making it an energy-increasing reaction. The theoretical decomposition voltage E_d is 1.23 V at room temperature (T = 25 °C) and ambient pressure (P = 1 bar). This voltage is usually called the reversible potential difference or the minimum reversible equilibrium potential that needs to be overcome. The reversible equilibrium potential of 1.23 V consists of 0 V and 1.23 V for HER and OER (versus the reversible hydrogen electrode, RHE), respectively.

In the actual water electrolysis process, the water splitting reaction cannot be triggered by a 1.23-V potential. Higher cell potentials (1.8-2.0 V) are usually required to reach a current density of $0.3-1 \text{ Am}^{-2}$ due to energy consumption resulting from thermodynamic reversibility and energy barriers caused by dynamic obstacles such as bubble formation, mass diffusion, and circuit resistance. An overpotential (η) is typically applied to overcome the activation energy barrier (E_{act}) to drive the water-splitting reaction. Thus, the η value indicates the activation energy barrier, and lower η values mean lower energy barriers, less energy consumption, and higher Faradaic efficiencies (FE). The η in water electrolysis includes overpotentials of HER on the cathode (η_c) and OER on the anode (η_a) and Ohmic potential drop (η_{other}) resulting from

concentration polarization, electrolyte internal resistance, and electrode contact resistance. Therefore, the overall cell voltage (E_{cell}) can be expressed as:^[52]

$$E_{\text{cell}} = E_{\text{d}} + \eta = 1.23 \text{ V} + \eta_{\text{c}} + \eta_{\text{a}} + \eta_{\text{other}}$$
 (1.7)

To obtain the overpotential correctly, iR compensation is used to eliminate the influence of the cell. Additionally, overpotentials resulting from the HER and OER processes should account for the increase in cell potentials. η_c and η_a reveal the extra energy needed to overcome the activation energy barrier of HER and OER, which are intrinsic characteristics of electrochemical reactions on the catalysts' surface. Therefore, highly efficient electrocatalysts are adopted to reduce activation energy barriers, lower cell potentials, and improve the efficiency of water electrolysis.

The largest challenge for hydrogen generation from water electrolysis is the design and fabrication of efficient and stable catalysts. The main functions of electrocatalysts include: 1) maintaining stable charge migration; 2) providing adsorption sites for intermediates; 3) reducing activation energy for water oxidation and reduction. For industrial applications, electrocatalysts are also required to possess the following characteristics: 1) facile fabrication and low cost; 2) excellent catalytic activity and low overpotentials comparable to noble-metal-based catalysts; 3) good catalytic activity across a wide pH range; 4) long-term durability; 5) good conductivity; and 6) bifunctional properties for HER and OER. Currently, Pt-based catalysts are the best HER electrocatalysts, while Ru and Ir oxides are the most active OER electrocatalysts. [53, 54] Although those materials exhibit excellent catalytic activity, their high cost and poor stability limit their large-scale application. Therefore, developing efficient and cost-effective catalysts is key to advancing the water electrolysis technique. Compared to HER, OER is more difficult to trigger due to its thermodynamic uphill characteristics and slow kinetics resulting from the four-electron transfer process. [55] To develop efficient OER electrocatalysts, it is necessary to understand the OER mechanism.

1.2.2. Mechanism of Oxygen Evolution Reaction

The electrocatalytic OER involves four electron-coupled proton transfers, forming multiple intermediates. Consequently, the dynamic process of the OER is more sluggish than HER. There are four isolated electron transfer processes in the OER pathway, which involves three intermediates of oxygen (*O), hydrogen peroxide (*OH), and superoxide (*OOH).^[24, 56] The OER process in acidic and alkaline systems is summarized in **Table 1.1**.

Table 1.1. Overall reaction pathways for OER in acidic and alkaline solutions.

Overall reaction	Reaction pathways
	$* + H2O \rightarrow *OH + H+ + e-$
	$*OH \rightarrow *O + H^+ + e^-$
$2H_2O \rightarrow O_2 + 4H^+ + 4e^-$ (acidic solution)	$*O + H_2O \rightarrow *OOH + H^+ + e^-$
	$*OOH \rightarrow *O_2 + H^+ + e^-$
	$*O_2 \rightarrow * + O_2$
	$* + OH^- \rightarrow *OH + e^-$
	$*OH + OH^- \rightarrow *O + H_2O + e^-$
$4OH^- \rightarrow O_2 + 2H_2O + 4e^-$ (alkaline solution)	$*O + OH^- \rightarrow *OOH + e^-$
	$*OOH + OH^- \rightarrow *O_2 + e^-$
	$*O_2 \rightarrow * + O_2$

In acidic electrolytes, H₂O dissociates into H⁺ and *OH intermediates due to the abundance of H⁺. The *OH species then dissociates into *O and H⁺, and H₂O combines with *O to form *OOH intermediates. Finally, *OOH dissociates into O₂ molecules. In alkaline electrolytes, OH⁻ first adsorbs on active sites to form *OH intermediate due to the presence of abundant OH⁻. The *OH then combines with another OH⁻ to form H₂O and *O intermediate. Consequently, *O reacts with OH⁻ to form *OOH, which dissociates into O₂. According to this analysis, the generation and dissociation of *O, *OOH, and *OH intermediates are key steps in the OER process.^[57]

In both acidic and alkaline electrolytes, the catalytically active sites on the catalyst surface undergo continuous oxidation, where oxygen-containing species, such as *OH and *OOH, undergo adsorption and desorption. The difference lies in the generation process of O₂ molecules (**Figure 1.3a**). In an acidic environment, H₂O is oxidized into O₂ and H⁺ (blue reaction pathway), while in an alkaline environment, OH⁻ is oxidized into O₂ and H₂O (red reaction pathway). Regardless of the environment, the thermodynamic equilibrium potential of OER is 1.23 V (vs. RHE). Additionally, the adsorption and desorption behaviors of intermediates can be analyzed through density functional theory (DFT) calculation. The rate-determining step (RDS) and catalytic activity of OER electrocatalysts can be predicted by DFT calculation. The Gibbs free energy of different OER electrocatalysts is summarized in **Figure 1.3b**, showing that catalysts with optimal Gibbs free energy towards intermediates exhibit excellent OER performance.

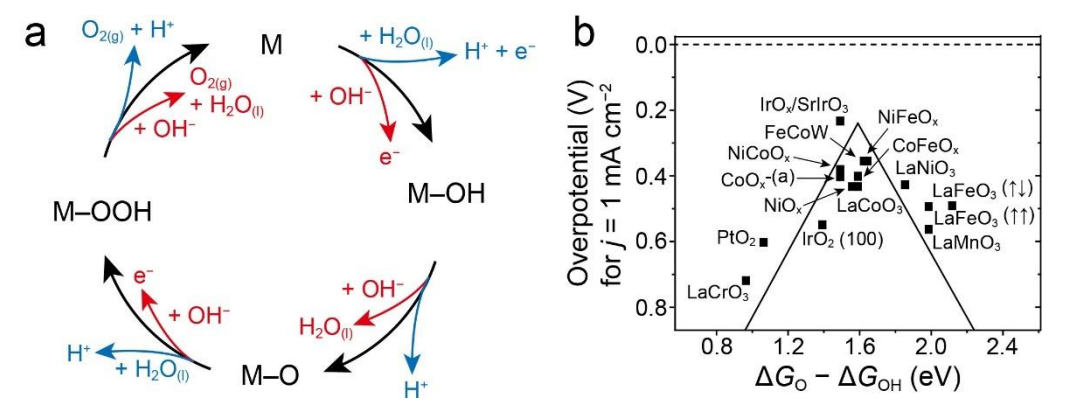


Figure 1.3. (a) Schematic illustration of the OER mechanism under acidic (blue route) and alkaline conditions (red route).^[58] (b) OER volcano plot for metal oxides.^[22]

1.2.3. Evaluation of OER Catalytic Performance

In water electrolysis, several important parameters are used to evaluate the performance of catalysts, including overpotential, Tafel slope, exchange current density, electrochemical stability, Faradaic efficiency, and turnover frequency of gas molecules.

1.2.3.3. Overpotentials

The electrocatalytic water splitting process requires an actual voltage higher than the reversible equilibrium potential of 1.23 V to drive the reaction due to the inevitable reaction kinetic activation energy barrier. The gap between the applied potential and reversible equilibrium potential is known as overpotential, η. Polarization curves are typically used to determine the relationship between overpotential and current (**Figure 1.4**). The η_c equals the actual potential, while the η_a equals the gap between the actual potential and 1.23 V. However, the electrode area significantly affects the response current at the same overpotential. To compare the catalytic activity of different catalysts, the current is normalized to the geometric area of the electrode. The resulting polarization curves reflect the relationship between geometric current density (j) and overpotential. In polarization curves, two parameters, onset overpotential (η_0) and overpotential at specific geometric current density (η_i) , are used to evaluate the catalytic activity of materials. η_0 is the overpotential when the response current becomes noticeable in the OER process. Overpotentials at a current density of 0.5 or 1 mA cm⁻² are used to represent onset overpotential. To compare the catalytic activity of different materials, the overpotential at a current density of 10 mA cm⁻² (corresponding to 12.3 % efficiency of solar-driven water splitting system) is adopted.^[59] Generally, lower overpotentials indicate better catalytic performance. Additionally, overpotentials at large current densities, such as 100, 300, 500, and 1,000 mA cm⁻², are also used to evaluate whether materials can meet industrial application requirements. Catalytic performance is typically assessed by loading catalysts onto conductive substrates to form catalytic electrodes. Nanostructured catalysts and self-supported catalysts exhibit different contact areas when electrodes are immersed into electrolytes compared to their geometric areas. The current response is affected by the particle size of electrocatalysts and the specific areas of electrodes. Therefore, to more accurately characterize the catalytic activity of

materials, the response current should be normalized to the mass of catalysts or electrochemical surface areas to assist performance evaluation. [60]

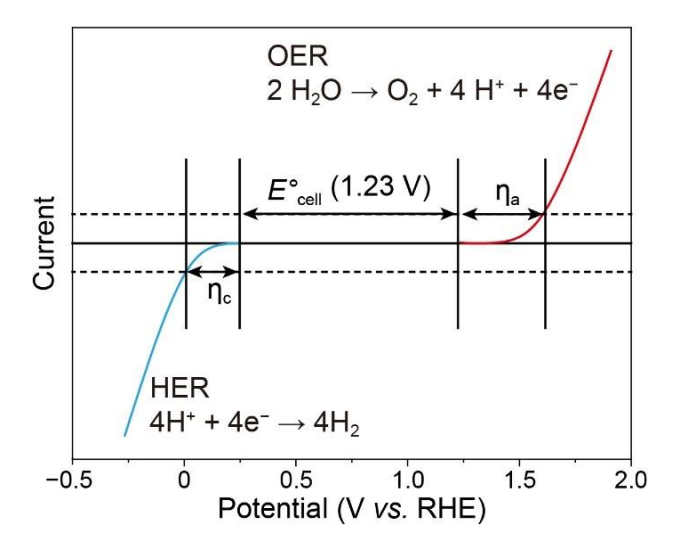


Figure 1.4. Polarization curves for HER (left) and OER (right). The η_c and η_a are the overpotentials for cathode and anode at a certain current, respectively.^[61]

1.2.3.2 Tafel Slope and Exchange Current Density

Tafel slope and exchange current density j_0 serve as dynamic parameters to reflect the intrinsic activity of catalysts. They can be obtained by transforming polarization curves and fitting the linear part of the polarization curve to the Tafel formula:

$$\eta = a + b \log j \tag{1.8}$$

where a = $(2.3\text{RT})/(\alpha\text{F})\log j_0$, b = $(-2.3\text{RT})/(\alpha\text{F})$, j, j_0 , and η are current density, exchange current density, and overpotential, respectively. η changes linearly with $\log j$. F, R, T, α , and b are Faradaic constant, ideal gas constant, reaction temperature, electron transfer coefficient (for single electron reaction process, $0 < \alpha < 1$), and Tafel slope, respectively. A smaller Tafel slope indicates that the same current density can be achieved by lower overpotentials, signifying superior dynamics. The j_0 is the current density when η is zero, revealing the intrinsic activity of catalysts at equilibrium potential. It also quantifies the ease of catalytic reaction and electron transfer ability. A larger j_0 means a smaller driving force for catalytic reactions.

1.2.3.4. Electrochemical Impedance Spectroscopy (EIS)

EIS is a technique used to reflect the impedance characteristics of a catalytic system. By applying a sine wave current signal within a certain angular frequency (ω) range ($\omega = 2\pi f$, 10 mHz $\leq f \leq 100$ kHz) and a small amplitude (generally 10 mV) to perturb the electrode reaction at a fixed potential, the relationship between the numerical ratio of the sinusoidal potential and the current (system impedance Z) of the electrode in the same ω range and the frequency (f), or the relationship between the phase angle (ϕ) and the frequency f are recorded. Z can be expressed as:

$$Z(\omega) = Z'(\omega) + jZ''(\omega) \tag{1.9}$$

where Z' and Z'' are the real and imaginary parts of the impedance, respectively, and $j = \sqrt{-1}$. Nyquist curves can be obtained when |Z'| is represented as a functional relationship of |Z''|. By fitting with a suitable equivalent circuit, various impedance values of the electrode can be obtained. The series resistance (R_s) and charge transfer resistance (R_{ct}) can be obtained in the low-frequency and high-frequency parts of impedance spectra, respectively. The dynamic characteristics of the interfacial reaction between the electrode and electrolyte can be reflected by R_{ct} . Lower R_{ct} indicates faster catalytic dynamics and higher catalytic activity. [63]

1.2.3.5. Electrochemical Surface Area (ECSA)

ECSA, also known as the rough factor (RF), is an important characterization parameter in electrocatalytic reactions, directly revealing the number of activity sites. At a fixed potential, the current response of the electrode is proportional to the specific surface area of the catalyst exposed to the electrolyte. ECSA can be obtained by calculating double-layer capacitance ($C_{\rm dl}$) because $C_{\rm dl}$ is proportional to ECSA. [64] $C_{\rm dl}$ can be acquired by analyzing cyclic voltammograms (CVs) obtained at different scan rates in a non-Faradaic potential range (no charge transfer). By plotting the function of the current difference and scan rates according to

CV curves, the slope, namely $C_{\rm dl}$, can be obtained through linear fitting. There is a linear relationship between $C_{\rm dl}$ and ECSA:

$$ECSA = C_{dl}/C_{s} \tag{1.10}$$

where C_s is the capacitance per unit area of a smooth flat surface of the material. The C_s ranges in acidic and alkaline environments are 0.015 - 0.110 mF cm⁻² and 0.015 - 0.110 mF cm⁻², respectively. To compare ECSA, specific C_s values are used for calculation: 0.035 and 0.040 mF cm⁻² for acidic and alkaline conditions, respectively. Although the ECSA value is not the true contacting surface area between the catalyst and electrolyte, it can approximately reflect the specific surface area of the catalyst exposed to the solution. Therefore, ECSA can also be considered to reflect the electrochemically active surface area of the catalyst. However, not all sites are catalytically active.

1.2.3.6. Turnover Frequency (TOF)

TOF is usually identified as the amount of reactant that a single active site of a catalyst converts into the desired product per unit of time. It reveals the intrinsic catalytic activity of each catalytic site. A larger TOF indicates better catalytic activity. [66] The TOF calculation equation is:

$$TOF = \frac{I}{mFn_c} \tag{1.11}$$

where I, F, m, n_s are current (A), Faradaic constant (96,485 C mol⁻¹), electron transfer number for the formation of one hydrogen or oxygen molecular (m = 2 for HER; 4 for OER), and the number of active sites in catalysts, respectively.

1.2.3.7. Faradaic Efficiency (FE)

FE (coulombic efficiency) describes the charge utilization efficiency, which is the ratio of consumed charges for products to outer charges. FE is an important parameter for water electrolysis and reveals the electron transfer efficiency or energy utilization rate. In the OER process, FE is the ratio of the amount of gas generated in the experiment to the theoretical

amount of gas.^[67] When side reactions occur during the desired reaction, the electron utilization efficiency is lower than 100 %, reducing the Faradic efficiency. Currently, drainage and gas chromatography analysis methods are usually applied to measure the amount of gas produced during electrocatalytic water splitting.

1.2.3.8. Stability

Stability is an indispensable parameter for evaluating catalytic performance and a necessary condition for the industrialization of catalysts. The stability of the catalyst can be evaluated by the CV, chronoamperometry, and chronopotentiometry. In the CV method, continuous cycle testing of the catalyst in a potential range where the electrode reaction occurs is performed, and the polarization curves before and after the cycle are compared. The catalysts with high stability exhibit a post-cycle curve that is similar to the initial one. In chronoamperometric and chronopotentiometric methods, potential and current changes over long periods are recorded at a fixed current and potential, respectively. Catalysts with high stability typically maintain the same level of potential or currents for hundreds of hours, without significant increase in potential or decrease in current. Notably, most OER catalysts undergo surface oxidation during the water oxidation process when the potential is higher than 1.23 V. For example, the surface of transition metals oxides, sulfides, and phosphides would be oxidized to high-valance oxides or hydroxides, but they can maintain catalytic activity. Additionally, the morphological and compositional stability are also evaluated using transmission electron microscopy (TEM) and scanning electron microscopy (SEM).

1.2.4. Strategies for Improving Oxygen Evolution Reaction Activities

Developing highly efficient catalysts is crucial in advancing water electrolysis techniques, as efficient electrocatalysts can effectively reduce the reaction energy barrier, lower fabrication costs, and improve hydrogen production efficiency. The high overpotential of water electrolysis is primarily due to the four-electron OER process. Therefore, water electrolysis

performance largely depends on OER electrocatalysts' catalytic performance. Improving apparent activity (*i.e.*, increasing the number of active sites) and intrinsic activity (*i.e.*, enhancing the activity of each active site) are two approaches to optimize OER catalytic performance (**Figure 1.5**). Increasing active sites in catalysts can be achieved through loading increase, interface control, morphology engineering, and substrate optimization. Intrinsic activity can be improved by tuning crystal structure, optimizing surface and interface, modulating electronic structure, alloying, and building amorphous structure. In summary, the key to developing efficient catalysts is to simultaneously increase the number of active sites per unit area and the intrinsic catalytic activity of each active site.

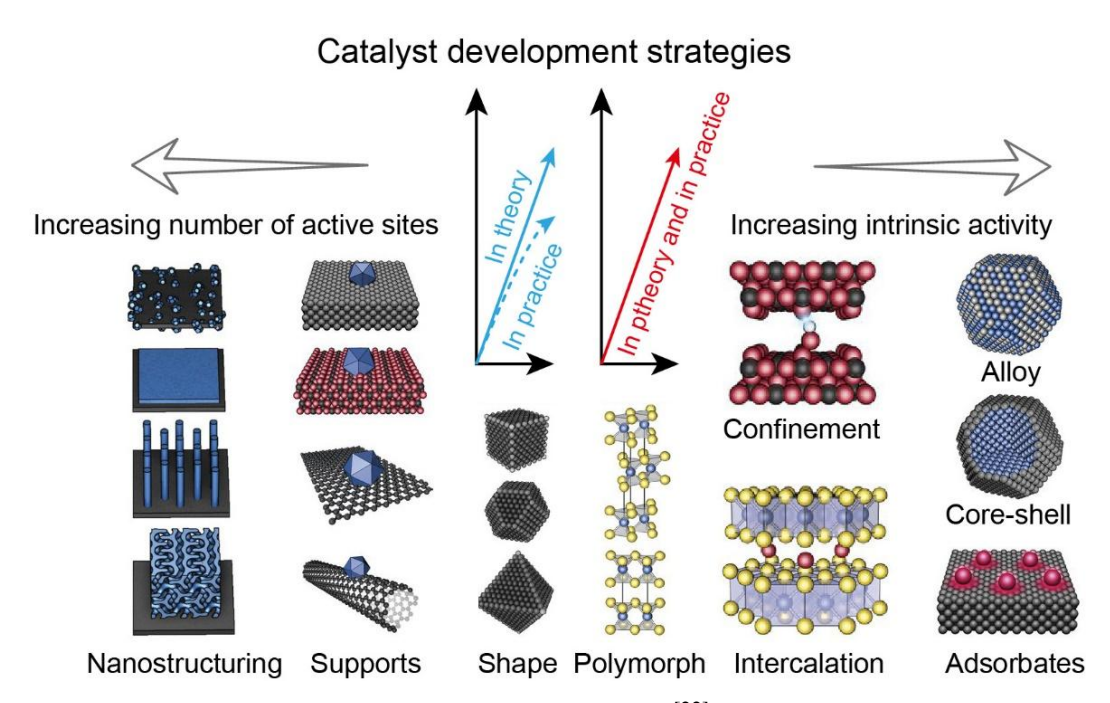


Figure 1.5. Various strategies for catalyst development.^[22]

In the last decade, with the development of nanomaterials fabrication techniques and theoretical calculations, growing research interest has focused on transition-metal-based catalysts, even non-metal-based catalysts.^[33, 68, 69] Currently, non-metal catalysts are mainly based on carbon materials, such as reduced graphene oxide,^[70] carbon nanotubes,^[71] and graphdiyne,^[72] but their catalytic activity is not comparable to metal-based catalysts.

Transition-metal-based catalysts, including borides,^[73] carbides,^[74] nitrides,^[75] phosphides,^[76] oxygen/hydroxides,^[77] chalcogenides,^[78] and metal alloys,^[79] have attracted wide attention due to their low cost, suitable electronic properties, high electronic conductivity, excellent electrochemical activity in theory, and durability. Researchers have found that by adopting appropriate modification strategies to optimize the interface and structure of the catalyst, transition-metal-based catalysts can exhibit excellent catalytic performance, some of which can even be comparable to precious-metal-based catalysts.^[29, 80] These modification strategies, such as nanostructuring, electronic structure optimization, and amorphization, mainly focus on improving conductivity, exposing more catalytic active sites, and enhancing the intrinsic activity of active sites.^[81-85]

1.2.4.1. Nanostructuring of Catalysts

Heterogeneous reactions occur at the surface of the catalyst. The size and morphology of the catalyst influence the exposure of atoms on the catalyst surface, which in turn affects the catalytic activity. Nanostructuring can expose more surface atoms, increase active sites, and enlarge the contact area between active sites and electrolytes, thereby facilitating the catalytic reaction. Nanomaterials can be clarified into zero dimension (0D, nanoparticles, nanospheres, nanoclusters), one dimension (1D, nanorod, nanowire, and nanotubes), two dimensions (2D nanosheets), and three dimensions (3D, hierarchical and self-support structure) according to their morphology and size. Theoretically, as the size of the material gets smaller, the specific surface area becomes larger, more catalytic active sites are exposed on the surface, and thus its catalytic performance improves.

Manjunatha *et al.* synthesized NiS₂ with different morphologies (stone particles, rose type, and tubular bacteria) by adjusting hydrothermal reaction time and studied the influence of morphology on OER performance.^[86] They found that the exposed active sites increased when the morphology changed from aggregated stone particles to tubular bacteria. NiS₂ with a sugar-

cube structure showed the best OER activity, requiring only 360-mV overpotential to achieve 20 mA cm⁻², followed by the rose type and tubular bacteria. Although nanostructuring catalysts made significant progress in enhancing electrocatalytic activity, the catalytic performance of nanomaterials cannot be fully realized due to easy aggregation at room temperature. Therefore, it is usually necessary to hybridize nanomaterials with conductive substrates, such as carbon materials or metal framework, to prevent the aggregation of nanoparticles and improve electron transfer.

Constructing self-supporting 3D interconnected nanostructures can increase the specific surface area and the number of exposed active sites, shorten the transmission path between active sites, reduce the interface connection resistance, and facilitate the rapid release of bubbles, thus improving electrocatalytic activity and durability. For example, Yang's group loaded Ru/Ir-decorated NiV nanosheets on nickel foam and applied them to the water-splitting reaction. This self-supported catalyst exhibited excellent catalytic stability. As a type of heterogeneous electrocatalysts, transition metal nanoparticles have attracted increasing attention in electrocatalytic water splitting. Researchers have committed to further reducing the size of nanomaterials to increase their surface area, thus exposing a higher proportion of catalytic atoms and improving electrocatalytic performance. Wang *et al.* synthesized high-density carbon nanotubes encapsulated with IrCo nanoparticles on carbon cloth through a template-assisted strategy. The diameter of these nanoparticles was less than 10 nm. The catalyst required a low overpotential of 241 mV to reach 10 mA cm⁻² in acidic electrolyte, which is significantly lower than that of the commercial IrO₂ catalyst.

Recently, with the development of nanofabrication technology and characterization methods, transition metal nanoparticles have evolved towards sub-nano clusters and even single-atom scales. In 2011, Zhang's group first loaded Pt single atoms on the surface of FeO_x through the coprecipitation method.^[89] Li *et al.* incorporated Co single atoms onto RuO₂

spheres through a one-pot hydrothermal method (**Figure 1.6**). ^[90] They found that the Co single atom modified the electronic structures of the surrounding Ru atoms and remarkably reduced the energy barriers for HER and OER. The catalyst showed lower overpotentials of 45 mV and 200 mV for HER and OER, respectively, at a current density of 10 mA cm⁻². Lou's group synthesized Ni single atoms embedded in S/N-doped carbon microporous fibers through the pyrolysis method. ^[91] Benefiting from the abundant exposed Ni atoms and hollow microporous structure, the catalyst delivered enhanced activity and stability compared with Ni nanoparticles, demonstrating that atomizing transition metals is also an effective way to obtain appealing catalytic performance.



Figure 1.6. A schematic illustration of the synthesis process of the Co single-atom-incorporated RuO₂ sphere.^[90]

Although nanostructuring benefits macroscopic morphology modulation and active site utilization, developing efficient electrocatalysts suitable for large-scale manufacturing remains a significant challenge. Therefore, further improving the activity and stability of OER catalysts based on nanostructuring continues to be a focus of catalyst development.

1.2.4.2. Electronic Structure Optimization

The essence of the catalytic reaction lies in the electronic interaction between the active sites on the catalyst and the reactants. The electronic structure of transition-metal-based catalysts directly influences the adsorption and activation of the reactants on the catalyst surface. An optimized electronic structure can enhance both the adsorption and desorption of reactants.

Unfortunately, not all materials possess an optimized electronic structure. Therefore, strategies such as ion doping and defect engineering are employed to modulate the electronic structure to obtain ideal catalysts.

Introducing other anions, cations, or multiple elements into catalysts can regulate their electronic structure and catalytic performance, and even create bifunctional catalytic active sites on a single catalyst. Niu *et al.* introduced Se into FeOOH through an FeSe pre-catalyst to reduce the OER reaction energy barrier of the transition from M—OH to M—O, thereby boosting the OER activity of FeOOH.^[92] Retuerto *et al.* doped Na ions into SrRuO₃ to substitute the Sr position, which increased the oxidation state of Ru, displaced O *p*-band and Ru *d*-band centers, and weakened Ru–adsorbate bonds.^[93] Tian *et al.* developed a cation–anion dual doping strategy to modify the electronic structure of CoP *via* Fe and S atoms.^[94] They demonstrated that Fe doping improved the carrier density to produce more ·OH radicals, while S doping further promoted charge transfer, synergistically reducing the energy barrier for the O*–OOH* step (Figure 1.7).

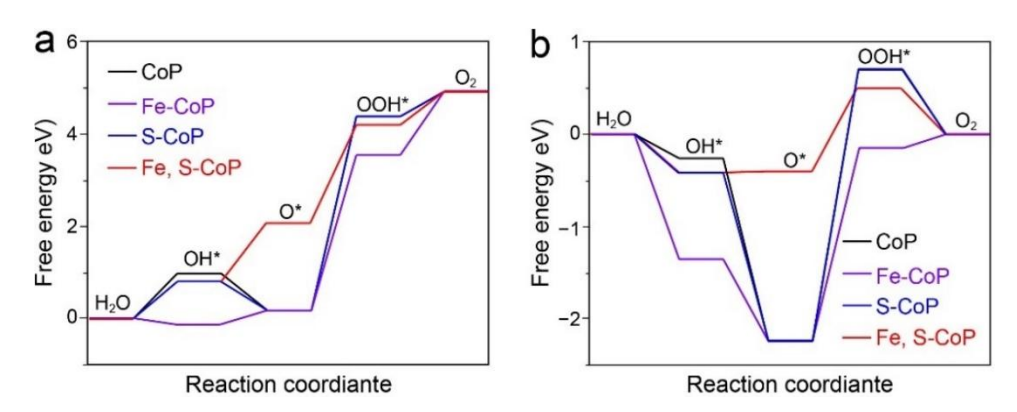


Figure 1.7. Reaction pathways and free energies of CoP, Fe-CoP, S-CoP, and Fe,S-CoP at (a) 0 V and (b) 1.23 V.^[94]

The electronic and surface characteristics can also be modulated by defect engineering. It is well known that point defects, line defects, plane defects, and bulk defects widely exist in materials. Previous works demonstrated that defects (vacancy, edge sites, and interface defects)

can serve as active sites for electrocatalytic reactions. For example, Dai's group created rich O vacancies in Co₃O₄ via an argon plasma-engraving strategy and applied it to OER electrocatalysis.^[95] The generated O vacancies created new defect states in the band gap of Co₃O₄, improving the conductivity and creating more electrochemically active sites, thereby enhancing electrocatalytic OER activity. Cation defects have also been investigated thoroughly in OER catalysis. Zhang et al. fabricated Co-defected Co_{3-x}O₄ and demonstrated that the Co defects led to significant electronic delocalization, facilitating electron transfer during the water-splitting reaction. [96] In recent years, amorphous materials have become one of the research directions due to their unique disordered and loosely bound atoms, which can produce a large number of vacancies and defects with catalytic activity. The unique structure and isotropy of amorphous materials make them highly resistant to corrosion, helping them become efficient and stable catalysts. For example, Huang et al. synthesized amorphous RuTe₂ porous nanorods *via* a simple hydrothermal method.^[97] Theoretical calculations and experimental tests showed that the high degree of amorphization created local short-range disorder in the catalyst structure, providing efficient OER activity across a wide pH range, the catalyst required a low overpotential of 245 mV to reach a current density of 10 mA cm⁻² in 0.5 M H₂SO₄, which is significantly lower than for crystalline counterparts and commercial Ir/C catalysts.

1.2.4.3. Synergistic Modulation

Synergistic catalysis promotes different elementary reaction steps in the reaction process by constructing multiple catalytic structures, achieving an effect of "1 + 1 > 2". Each component in the synergistic catalytic structure can participate in the catalytic reaction as an active site. In recent years, catalysts with heterogeneous structures have received extensive attention because of their multifunctional reaction sites and the synergistic effect formed at the heterogeneous interface, which promotes the reaction rate of OER. [98] Zou's group grew NiFe-LDH nanosheets vertically on the surface of a NiFe-metal-organic-framework, which achieved an

ultralow overpotential of 284.3 mV at 1,000 mA cm^{-2} . [99] The excellent OER performance was attributed to the increased density of states around the Fermi level and cross-junction charge redistribution due to the formation of heterointerfaces, lowering the energy barrier of the ratedetermining *OOH generation step. Meanwhile, the hierarchical heterostructures with abundant exposed active sites, rich channels for mass diffusion, and interconnected conducting networks contributed to the ultrahigh current density. Similarly, Wang et al. used a template method to obtain CoNiFe-LDH/conductive MOF (CoNiFe-LDH/cMOF) heterojunctions. [100] Benefiting from the enhanced conductivity of the MOF shell and abundant active sites on the CoNiFe-LDH core, the synergistic effect between these two components endowed CoNiFe-LDH/MOF with excellent OER performance (**Figure 1.8**). The synergistic effect also occurs between different metal sites. Lou's group investigated the synergistic effect between Fe and Ni sites in Ni–Fe–Se nanocage OER catalysts and found that Ni sites with moderate adsorptions of O-containing intermediates served as the active sites, while Fe sites optimized the electronic structure of active Ni species, thereby promoting the OER catalytic process.^[101] By rationally designing the structure of the catalyst and utilizing the synergistic effect to maximize the catalytic advantages of each active component in each elementary reaction, the performance of catalysts can be greatly improved.

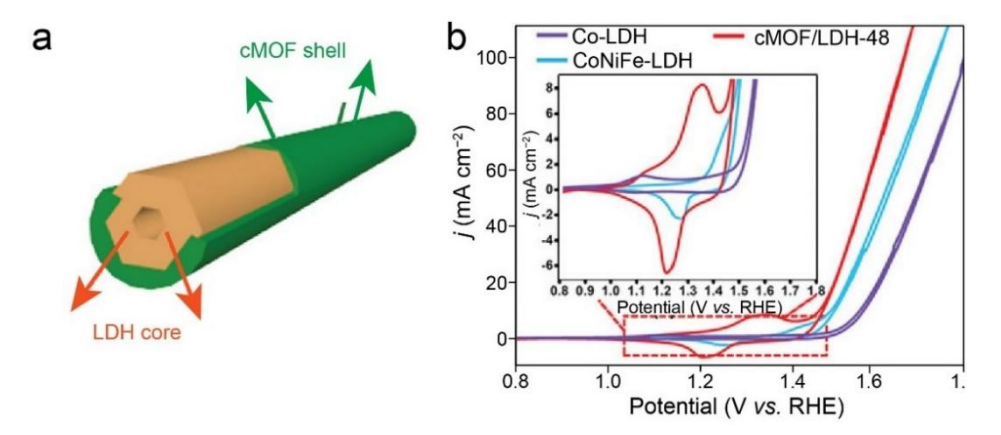


Figure 1.8. (a) An illustration of the core/shell structure of CoNiFe-LDH/cMOF. (b) Polarization curves of Co-LDH, CoNiFe-LDH, and cMOF/LDH-48. [100]

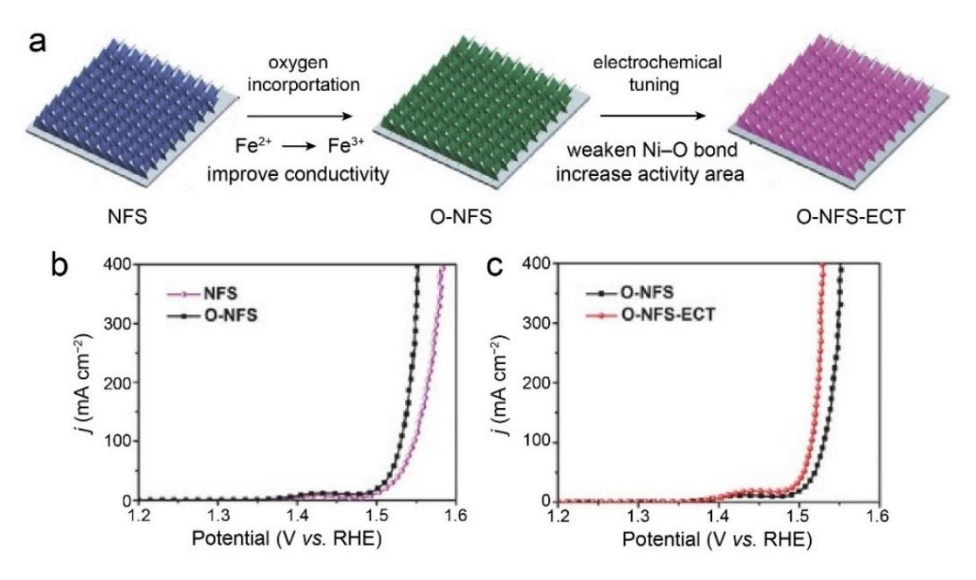


Figure 1.9. (a) Schematic illustration of the preparation of O-NFS ultrathin nanosheets. Polarization curves of (b) NFS and O-NFS and (c) O-NFS and O-NFS-ECT. [102]

In addition, joint-strategy approaches are often adopted to improve OER catalytic performance. For example, Zhang's group started with a material design based on simultaneous regulation of the nanostructure and electronic structure. They used the electrodeposition method to grow amorphous Ni–Fe–S ultra-thin sheets on three-dimensional self-supporting Ti sheets (**Figure 1.9**), and then combined this with O doping to regulate the electronic structure and improve electrocatalytic performance. Through O doping, the valence state of Fe changed from divalent to trivalent. The electronic effect of high-valence Fe extracted electrons from surrounding Ni more easily, thereby accelerating the O₂ production kinetics. At the same time, O doping improved conductivity. The electron binding energy of Ni shifted negatively, contributing to the breaking of Ni–O bonds in Ni–OO intermediates during the oxygen evolution process, thereby promoting the release of oxygen. Along with the increase in the active area of the material resulting from nanostructuring, low overpotentials of 300 and 435 mV were required for the catalyst to reach current densities of 500 and 3,000 mA cm⁻², respectively. The excellent performance was ascribed to the ultrathin and amorphous

nanosheets with more active sites and the multi-strategy synergistic effect between the nanostructure and electronic structure.

1.2.4.4. External Fields Assistance

Field-assisted electrocatalysis has emerged as a promising technique for enhancing electrochemical reactions, particularly in the context of OER. This technique applies external factors, including magnetic fields, strain, and light, to provide additional means of engineering to promote OER processes.

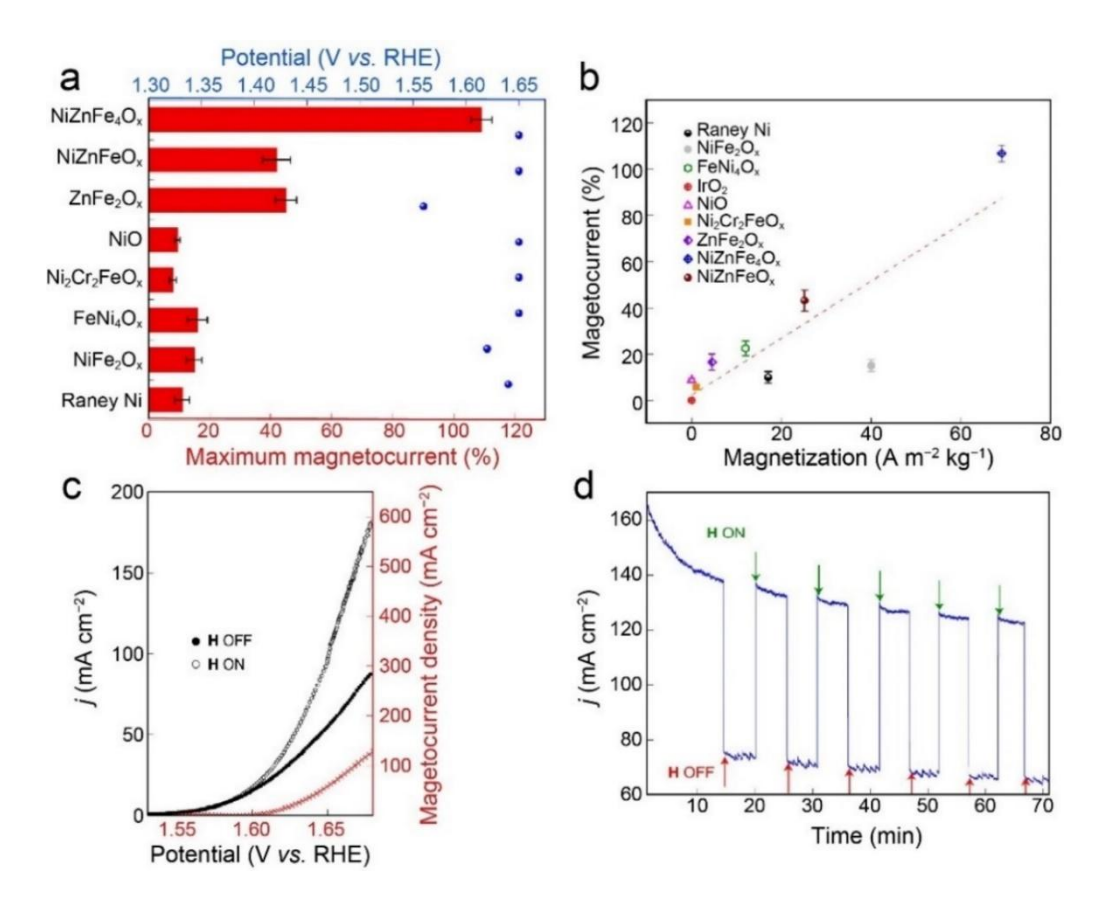


Figure 1.10. (a) Bar diagram with the maximum magneto current observed for the various magnetic OER catalysts expressed as the relative percentage of the based current, and the corresponding applied potential (blue dots). (b) Correlation between the maximum relative magnetocurrent (at 1.67 V vs. RHE) and bulk magnetization. (c) Polarization data for Ni-foam electrodes magnetically decorated with NiZnFe₄O_x particles (OFF, filled circles), and under an applied magnetic field (ON, open circles). (d) A pulsed magneto-chronoamperometry experiment was performed at a constant potential of 1.67V vs. RHE for the NiZn₄O_x electrode. [103]

Three key effects, magnetothermal, spin-polarized, and electron energy state enhancement, are involved in the theoretical explanation of magnetic field-assisted OER. Garcés-Pineda *et al.* performed a comprehensive study on the effect of external static magnetic fields on different transition metal oxides during the electrocatalytic OER process in an alkaline electrolyte. They found that the external magnetic field had negligible influence on non-magnetic catalysts (IrO₂), but significantly enhanced the catalytic performance of materials with strong magnetism (NiZnFe₄O_x, **Figures 1.10a** and **b**). Notably, the increase in the OER current density of NiZnFe₄O_x reached nearly 100 % at a potential of 1.67 V (**Figure 1.10c**). Upon turning off the magnetic field, a clear transition of the anodic current from a high-current state to a low-current state was observed, providing further confirmation of the magnetic field effect (**Figure 1.10d**). They proposed that the magnetic field contributed to the parallel alignment of oxygen radicals during the formation of O–O bond, which dominated the OER mechanistic pathway under alkaline conditions.

Previous works have demonstrated that the electronic structure of the catalyst surfaces is sensitive to mechanical strain, indicating that strain can regulate electrocatalysis. [104-106] Liu *et al.* induced tensile strain into NiFe hydroxide *via* the ball-milling approach and modulated the adsorption energy of reaction intermediates during the OER process. [107] The Ni–O and Fe–O bonds were stretched due to lattice strain, leading to enriched electron density around Ni and Fe sites, enhanced adsorption of oxygenated intermediates, and decreased overpotential. Additionally, coupling lattice strain with oxygen defects can synergistically optimize the OER performance of La_{0.7}Sr_{0.3}CoO_{3- δ}, thin films. [108] However, excessive strain can induce too many oxygen defects, increasing the e_g state occupancy and expanding the energy gap between Co 3*d* and O 2*p* bands, resulting in lower OER activities.

In light-assisted electrocatalytic OER, photocarrier and photothermy are usually used to explain the mechanisms. When photosensitive components are under light irradiation, carriers

are excited to facilitate overcoming potential barriers in charge transfer and redox reactions. [109, 110] Therefore, combining photo-generated carriers with electrocatalytic reactions can promote the catalytic process. Bai's group successfully hybridized CoFe-LDH with WO₃/SnSe₂ *n*–*p* heterojunction and reported that the OER overpotential decreased by 80 mV with the assistance of simulated sunlight (**Figure 1.11a**). [111] During the light-assisted OER process, photo-excited holes on the valence band of SnSe₂ were transferred to CoFe-LDH, oxidizing Co/Fe to higher valence states. Consequently, OH⁻ could rapidly adsorb on metal sites and undergo deprotonation to form *O species. The photoelectric synergy system in the heterojunction led to a reduction in the energy barrier for OER and a remarkable acceleration of the OER kinetics.

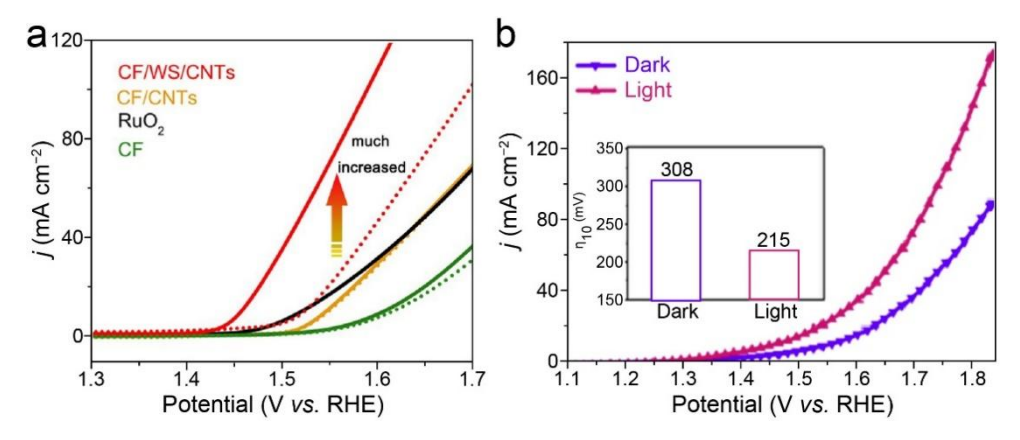


Figure 1.11. (a) Polarization curves of CoFe-LDH with WO₃/SnSe₂ system for OER in alkaline media^[111], where the solid lines are under light, and the dotted lines are under dark conditions. (b) Polarization curves of rGO-decorated carbon cloth in light and dark conditions.^[112]

In the photothermal-enhanced mechanism, thermal energy reduces activation energy to promote electrochemical reaction kinetics.^[113-115] Photo-sensitive materials, including plasmonic metals, semiconductors, and carbon materials, can respond to solar light and increase the temperature on the local surface to promote electron transfer. For example, Liang *et al.* synthesized a self-supported reduced graphene oxide (rGO) film with abundant carbon defects and broad light absorption.^[112] In this system, rGO not only accelerated electron and mass transfers but also served as a substrate to provide active sites and thermal sources. The

surface temperature increased to 70.9 °C in 1 min under simulated sunlight irradiation. As a result, this catalyst exhibited a low OER overpotential of 215 mV (**Figure 1.11b**), which was 93 mV lower than that without irradiation.

1.3. A Brief Review of Seawater Oxidation Electrocatalysts

Although water electrolysis is a promising approach for hydrogen production, the wide deployment of electrolyzers that heavily rely on freshwater raises a concern for water resources. Since seawater accounts for 96.5 % of the Earth's water resources, acquiring green hydrogen *via* seawater electrolysis becomes a promising strategy to achieve dual-carbon goals. Direct seawater electrolysis without desalination step streamlines the process by producing hydrogen directly from seawater. However, there are still challenges for direct seawater electrolysis. Firstly, various anions in seawater trigger different competitive electrochemical reactions, and the electrodes can be eroded due to their corrosive products, thus limiting the water-splitting efficiency. Additionally, seawater microorganisms easily cover the surface of electrodes, leading to sluggish electrocatalytic reactions. Furthermore, insoluble masses in seawater may hinder active sites and obstruct reactions. Since Trasatti proposed direct seawater electrolysis in 1984, [116] reports on seawater electrolysis have been limited due to complex electrochemical reactions, thermodynamics, and difficulties in industrial application.

On the other hand, the carbonate salts in neutral seawater are insufficient to alleviate the strong pH fluctuation around electrodes, resulting in catalyst deterioration. The pH also affects the efficiency of seawater splitting because changes in local pH influence OER and HER. The anodic pH continuously increases during the HER process while the cathodic pH decreases during the OER process. When the current density is fixed, the decreased local pH favors the generation of ClO⁻ over the OER.^[117] To improve the selectivity of OER and avoid CER, maintaining a pH above 7.5 in the electrolyte is necessary.

1.3.1. Mechanism of Chlorine Evolution Reaction (CER)

The chlorine electrochemical reaction favors producing Cl_2 (pH < 3.0), HClO (3.0 < pH < 7.5), and ClO (pH > 7.5). The desired OER is dominant only at current densities below 1 mA cm⁻² or at very high current densities where CER mass-transfer limitations become noticeable which, in turn, favor OER (**Figure 1.12a**). Starting in 1984, Trasatti pioneered the reactivity of different catalyst materials toward the OER and CER activity and demonstrated a parallel activity scaling for both reactions in either alkaline or acidic solutions, independent of the electrode material (**Figure 1.12b**). In alkaline media, the onset potential of the chlorine oxidation reaction is higher than that of OER. The potential gap is positively related to pH value and reaches a maximum of 480 mV under the generation of ClO⁻. According to the Pourbaix diagram (**Figure 1.12c**), in acidic seawater electrolytes, CER has thermodynamic advantages and easily competes with OER. The reaction equations are as follows:

$$2 \text{ Cl}^- \rightarrow \text{Cl}_2 + 2\text{e}^-; E^\circ = +1.36 \text{ V}_{\text{SHE}}$$
 (1.12)

In alkaline electrolyte,

$$Cl^- + 2OH^- \rightarrow ClO^- + H_2O + 2e^-; E^\circ = +0.89 \text{ V}_{SHE, pH14} \text{ or } E^\circ = +1.72 - 0.059 \text{ pH}$$
 (1.13)

However, the formation of ClO⁻ in alkaline electrolytes and the potential gap of ΔE° between OER and chlorine reaction should be considered, as shown in **equation 1.23**. ClO⁻ will not form if the overpotential applied on the electrode is below 0.48 V. Theoretically, seawater alkalization makes OER thermodynamically favorable. By contrast, the potential difference between CER and OER is smaller in acidic conditions, and non-noble-metal-based catalysts can be easily eroded. Therefore, the alkaline environment can be more beneficial to seawater oxidation.

Based on the above analysis, a design standard for seawater oxidation electrocatalysts is $\eta_{OER} < 480 \text{ mV}$ at pH > 7.5. However, it should be noted that CER is a two-electro transfer reaction with one intermediate, leading to faster dynamics than OER. Therefore, designing

non-noble-metal OER electrocatalysts with high efficiency and strong anti-corrosion properties is key to improving hydrogen production efficiency *via* seawater electrolysis.

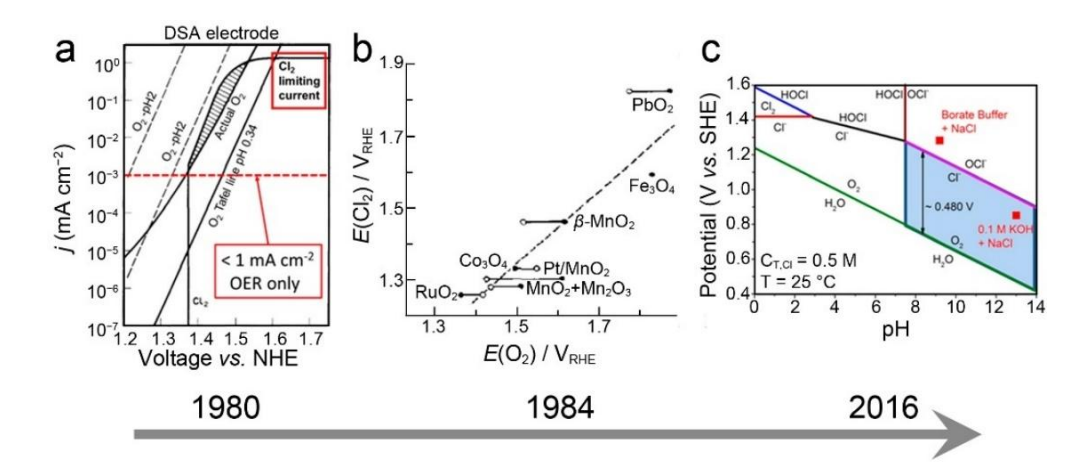


Figure 1.12. Theoretical evolution of seawater anode chemistry knowledge and concepts. (a) Log current *vs.* voltage for chlorine and oxygen in seawater.^[119] (b) The potential of CER vs OER at the same current density for several oxides in alkaline (open circle) and acidic (filled circle) electrolytes.^[116] (c) Pourbaix diagram of OER and chloride chemistry.^[117]

1.3.2. Strategies for Enhancing the Selectivity of OER in Seawater

Strong corrosiveness is one of the main problems that inhibit hydrogen production by direct seawater electrolysis. Achieving high OER selectivity and corrosion resistance is the primary prerequisite for catalyst design.

1.13.2.1. Design of Anti-corrosion Electrocatalysts

Recent studies demonstrated that the reconstruction of catalyst components during the activation process can enhance their intrinsic activity and generate an anti-corrosion protective layer to alleviate the corrosion on the metal substrate. Kuang $et\ al.$ synthesized NiFe/NiS_x-Ni multi-core-shell electrocatalysts. During the anode activation process, the NiS_x layer generated rich sulfate ion intercalations by $in\ situ$ structure reconstruction, which inhibited chloride ions from entering the electrode via the electrostatic repulsion effect, thus improving the catalyst's stability. Similarly, Huang $et\ al.$ designed Se-NiFe-LDH catalysts that generated

selenide anions during OER activation to alleviate Cl⁻ adsorption (**Figure 1.13**).^[121] Yu's group demonstrated that the amorphous NiFe hydroxide formed after the surface reconstruction of NiFeN enhanced the anti-corrosion property.^[122]

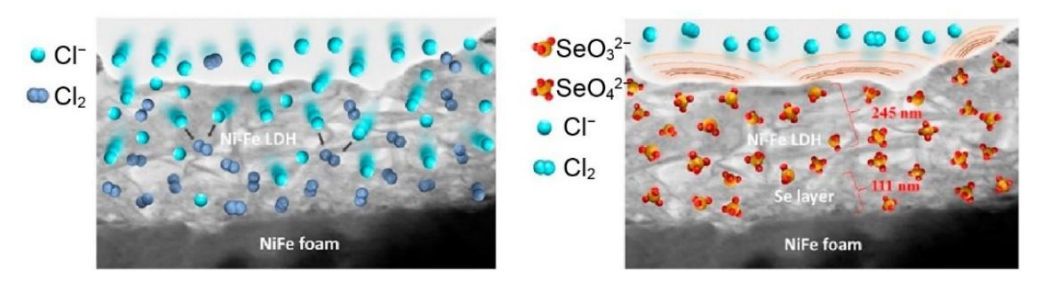


Figure 1.13. Stability improvement mechanism of Se-NiFe-LDH electrode. [121]

Although the design of an anti-corrosion interface layer can effectively shield chloride ions, it may also increase the mass transfer resistance of hydroxide ions, thereby reducing the catalytic activity. Effectively blocking chloride ions without reducing catalytic activity will be the focus of future research.

1.3.2.2. Anti-corrosion Additives

Researchers have focused on improving the electrode's corrosion resistance, while the regulation of the electrolyte has been overlooked. Strong oxidants, such as vanadium pentoxide and potassium dichromate, are typically used in commercial alkaline water electrolyzers to increase the surface activity of the electrode, thereby reducing the reaction overpotential. Inspired by this, adding anti-corrosion agents to the electrolyte may improve the stability of the electrode. Ma *et al.* added Na₂SO₄ to the seawater electrolyte and found that SO₄²⁻ tended to adsorb on the electrode surface even though its concentration was much lower than Cl⁻ in natural seawater.^[123] The lifetime of OER activity was extended from 40 to 120 min after the addition of Na₂SO₄ (**Figures 1.14a** and **b**). Benefiting from the hydrogen bonding force between hydroxide and the surface of nickel foam mesh, the addition of SO₄²⁻ did not affect the diffusion of hydroxide ions on the anode surface (**Figure 1.14c**). As a result, a five-fold

increase in OER stability was observed without sacrificing catalytic activity. However, this work did not evaluate the added amount of SO_4^{2-} and other anions, the relationship between the adsorption behavior of SO_4^{2-} and concentration, the influence of other ions and substrates on hydrogen bonding force, and the application universality to carbonates, nitrates, and phosphates.

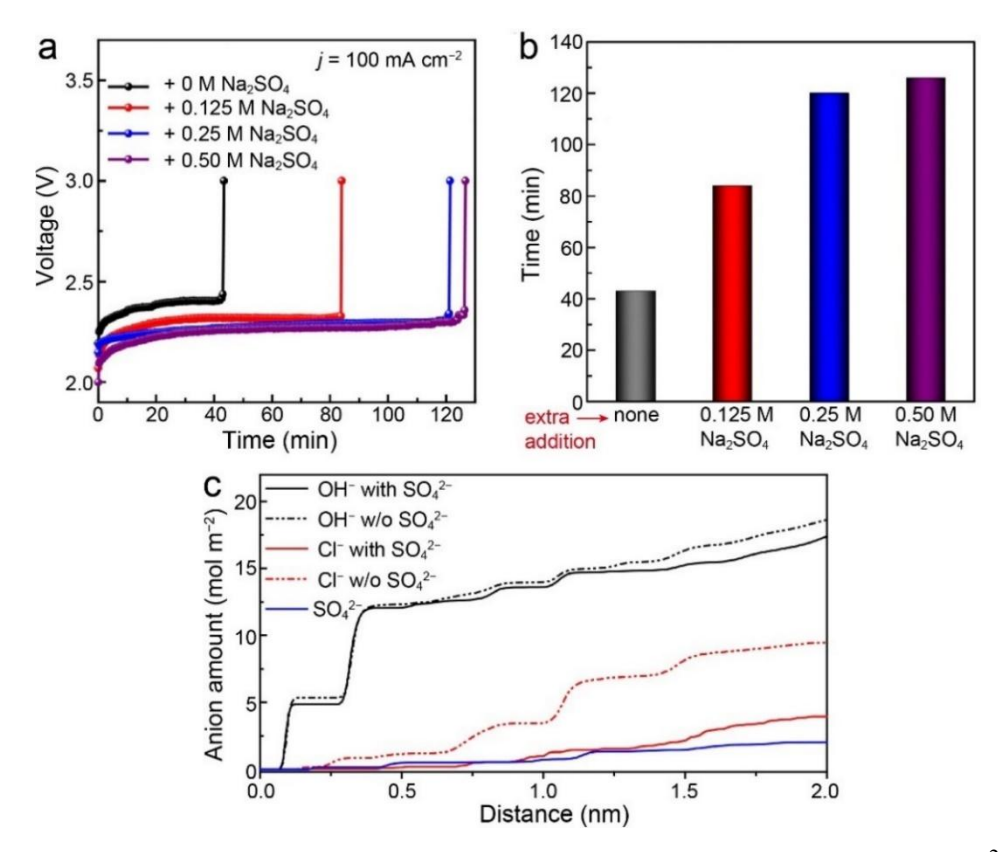


Figure 1.14. (a) Stability tests recorded at a constant current density of 100 mA cm⁻² for pure NF in electrolytes with different proportions of Na₂SO₄. (b) The durability of NF in different electrolytes. (c) The amounts of various anions *vs.* the distance above the electrode surface.^[123]

1.3.2.3. Organic-Transformation-Coupled Seawater Electrolysis

According to the water electrolysis mechanism, the high energy cost is caused by its high thermodynamic potential and sluggish multi-electron dynamics. Although various highly efficient catalysts for seawater electrolysis have been reported, most of their potentials are higher than 1.72 V to reach industrial current densities, leading to extra energy consumption

and chlorine oxidation reaction. Therefore, coupling low-potential anodic reactions, such as oxidation reactions of hydrazine, urea, methanol, sulfide, and furfuraldehyde, with HER in hybrid seawater electrolysis has been proposed. Sun *et al.* used hydrazine oxidation to replace OER, reducing the cell potential and avoiding CER on the anode, thus greatly improving stability.^[124] Du *et al.* coupled methanol oxidation reaction (MOR) on the anode to ensure the electrolyzer could run at low potentials and suppress CER.^[125]

Nonetheless, the efficiency and cost are still far from meeting commercial requirements. Therefore, fabricating novel and low-cost OER electrocatalysts, investigating efficient anti-corrosion mechanisms, and designing energy-saving seawater electrolysis systems are urgently needed for hydrogen production from seawater.

1.4. Objectives and Novelty of Thesis

1.4.1. Objectives of Thesis

Despite tremendous efforts devoted to exploring electrocatalysts for the seawater oxidation reaction, the catalytic performance is still far from meeting practical application requirements. It is urgent to explore and develop potential seawater oxidation electrocatalysts. Transition-metal-based electrocatalysts have been recognized as alternatives to commercial RuO₂ and IrO₂ catalysts due to their *d*-orbital valence electronic structures and low cost. However, severe chlorine corrosion and high thermodynamic energy barriers limit the application of those OER electrocatalysts in seawater electrolytes.

The objective of the research presented in this Thesis is to develop transition-metal-based electrocatalysts for direct seawater oxidation, particularly those based on Ni and Fe. By careful design and modifications, the catalytic and anti-corrosion properties of NiFe-LDH, Ni(OH)₂, NiMoO₄, and Fe₂O₃ are optimized. The impact of these modifications on the electronic configuration and interface environment in Ni- and Fe-based electrocatalytic systems are

investigated to reveal the mechanisms of catalytic activity and stability enhancement. The detailed research contents of this Thesis are as follows:

I. Heteroatom doping and interface engineering: These are simultaneously used to modify the electronic structure of catalysts and tune their intrinsic activity towards seawater OER. In Chapter 3, NiFe-LDH is doped with Li and hybridized with g-C₃N₄ to investigate their influences on the electrocatalytic OER activity and stability in seawater. By understanding the role of Li⁺ atoms and g-C₃N₄ in modulating the electronic structure and energy barrier of OER and CER, the aim is to reveal the possible application of joint strategies of doping and interface engineering for improving the seawater oxidation performance of NiFe-LDH.

II. Upcycling spent lithium-ion batteries into electrocatalysts: This can realize waste management and environmental protection. In Chapter 4, P and Fe are extracted from LiFePO₄ cathodes to repel Cl⁻ by electrostatic effect and optimize the OER activity of Ni species *via* heterointerface engineering. This Chapter presents a design principle combining spent LIBs and seawater electrocatalysts and proposes a double-protective mechanism of heterointerface and anion-repel mechanism for seawater OER.

III. Energy-saving seawater electrolysis: This is important to meet the requirement of low-cost hydrogen production. Chapter 5 induces the incorporation of MOR in seawater oxidation to replace OER. MoO₄²⁻-decorated NiOOH is chosen as the model system to investigate the effect of MoO₄²⁻ adsorption on CER and MOR, aiming to understand the microenvironment modulation on MOR and CER. In Chapter 6, a heterojunction is constructed to be a photo-active and electro-active catalyst for light-assisted seawater OER. The ternary heterointerface and built-in electric fields are formed among MoO₃, Fe₂O₃, and MoS₂, aiming to understand the role of heterointerface in ensuring OH⁻ diffusion and electric fields in promoting charge transfer during the light-assisted seawater OER process.

1.4.2. Novelty of Thesis

- 1) NiFe-LDH is doped with Li ions and hybridized with g-C₃N₄ to form a hybrid nanosheet. Li-doping increases surficial Ni³⁺ sites and oxygen defects, forming a built-in electric field at the interface with g-C₃N₄. The Lewis acid resulting from rich Ni³⁺ and a built-in electric field
- contributes to alleviating Cl⁻ adsorption, thus maintaining stable OER operation in seawater.
- 2) The concept of upcycling spent LIBs is first introduced into seawater electrolysis. Hybrids of Ni(OH)₂/LiFePO₄ are synthesized *via* a simple electrodeposition method. *In situ* formed NiOOH/Fe₃(PO₄)₂ heterointerface reduces the reaction energy barrier of OER and makes the CER more difficult to occur. The heterointerface, together with leached PO₄³⁻, reduces the
- adsorption of Cl⁻, ensuring long-term stability in seawater electrolysis.
- 3) The anion-modulation mechanism is adopted to promote the non-electrochemical process of methanol oxidation, reduce the water oxidation reaction energy barrier, and alleviate the Cl⁻ adsorption. The 3D structure is constructed by the pre-catalyst, Ni(OH)₂/NiMoO₄, while MoO₄²⁻-adsorbed NiOOH is obtained through *in situ* surface reconstruction. Such modifications endow NiOOH with enhanced methanol-assisted seawater electrolysis performance.
- 4) The amorphous MoO₃ and Fe₂O₃ are integrated on MoS₂ *via* one-step laser ablation to form three-phase heterojunctions, which are applied for light-assisted direct seawater electrolysis. The heterojunctions enlarge the overpotential gap between water oxidation and chlorine oxidation reactions while resolving the OH⁻ diffusion issue. The electrostatic influence of *insitu*-leached MoO₄²⁻ and SO₄²⁻ species also alleviates Cl⁻ adsorption. Double built-in electric fields facilitate the transfer of photo-generated charges and increase the water oxidation current density.

1.5. References

- [1] N. S. Lewis, D. G. Nocera, Proc. Natl. Acad. Sci. USA 2006, 103, 15729.
- [2] S. Chu, A. Majumdar, *Nature* **2012**, 488, 294.
- [3] L. Lu, J. S. Guest, C. A. Peters, X. P. Zhu, G. H. Rau, Z. J. Ren, *Nat. Sustain.* **2018**, *1*, 750.
- [4] T. A. Jacobson, J. S. Kler, M. T. Hernke, R. K. Braun, K. C. Meyer, W. E. Funk, *Nat. Sustain.* **2019**, *2*, 691.
- [5] J. A. Turner, Science **2004**, 305, 972.
- [6] S. L. Jiao, X. W. Fu, S. Y. Wang, Y. Zhao, Energy Environ. Sci. 2021, 14, 1722.
- [7] J. Hu, C. X. Zhang, X. Y. Meng, H. Lin, C. Hu, X. Long, S. H. Yang, J. Mater. Chem. A 2017, 5, 5995.
- [8] A. Ursúa, L. M. Gandía, P. Sanchis, *Proc. IEEE* **2012**, *100*, 410.
- [9] C. Liu, F. Li, L. P. Ma, H. M. Cheng, Adv. Mater. 2010, 22, E28.
- [10] L. Xie, P. M. S. Carvalho, L. Ferreira, J. H. Liu, B. H. Krogh, N. Popli, M. D. Ilic, *Proc. IEEE* 2011, 99, 214.
- [11] P. P. Varaiya, F. F. Wu, J. W. Bialek, *Proc. IEEE* **2011**, *99*, 40.
- [12] M. L. Cai, J. X. Liu, Y. S. Wei, Environ. Sci. Technol. 2004, 38, 3195.
- [13] M. S. Dresselhaus, I. L. Thomas, *Nature* **2001**, *414*, 332.
- [14] S. Y. Reece, J. A. Hamel, K. Sung, T. D. Jarvi, A. J. Esswein, J. J. H. Pijpers, D. G. Nocera, *Science* 2011, 334, 645.
- [15] X. X. Zou, Y. Zhang, Chem. Soc. Rev. 2015, 44, 5148.
- [16] P. J. Megía, A. J. Vizcaíno, J. A. Calles, A. Carrero, Energ. Fuel. 2021, 35, 16403.
- [17] Y. Q. Xu, M. N. Wu, X. X. Yang, S. Z. Sun, Q. H. Li, Y. G. Zhang, C. F. Wu, R. E. Przekop, E. Romanczuk-Ruszuk, D. Paku, H. Zhou, *Carbon Capture Sci. Technol.* 2023, 8, 100129.
- [18] A. Vojvodic, J. K. Norskov, Science 2011, 334, 1355.
- [19] J. Y. Jia, L. C. Seitz, J. D. Benck, Y. J. Huo, Y. S. Chen, J. W. D. Ng, T. Bilir, J. S. Harris, T. F. Jaramillo, *Nat. Commun.* 2016, 7, 13237.
- [20] G. R. Lee, J. Kim, D. S. Hong, Y. J. Kim, H. Jang, H. J. Han, C. K. Hwang, D. Kim, J. Y. Kim, Y. S. Jung, *Nat. Commun.* 2023, 14, 5402.
- [21] M. Balat, Int. J. Hydrogen Energ. 2008, 33, 4013.
- [22] Z. W. Seh, J. Kibsgaard, C. F. Dickens, I. B. Chorkendorff, J. K. Norskov, T. F. Jaramillo, *Science* **2017**, *355*, eaad4998.

- [23] F. M. Toma, A. Sartorel, M. Iurlo, M. Carraro, P. Parisse, C. Maccato, S. Rapino, B. R. Gonzalez, H. Amenitsch, T. Da Ros, L. Casalis, A. Goldoni, M. Marcaccio, G. Scorrano, G. Scoles, F. Paolucci, M. Prato, M. Bonchio, *Nat. Chem.* 2010, 2, 826.
- [24] Y. Jiao, Y. Zheng, M. T. Jaroniec, S. Z. Qiao, Chem. Soc. Rev. 2015, 44, 2060.
- [25] N. C. Cheng, S. Stambula, D. Wang, M. N. Banis, J. Liu, A. Riese, B. W. Xiao, R. Y. Li, T. K. Sham, L. M. Liu, G. A. Botton, X. L. Sun, *Nat. Commun.* 2016, 7, 13638.
- [26] Y. M. Shi, B. Zhang, Chem. Soc. Rev. 2016, 45, 1529.
- [27] K. X. Zhang, R. Q. Zou, Small 2021, 17, 2100129.
- [28] H. M. Gao, Z. H. Xiao, S. Q. Du, T. Y. Liu, Y. C. Huang, J. Q. Shi, Y. W. Zhu, G. Huang, B. Zhou, Y. M. He, C. L. Dong, Y. F. Li, R. Chen, S. Y. Wang, *Angew. Chem. Int. Ed.* 2023, 62, e202313954.
- [29] P. R. Chowdhury, H. Medhi, K. G. Bhattacharyya, C. M. Hussain, *Coord. Chem. Rev.* **2023**, *483*, 215083.
- [30] T. Q. Guo, L. D. Li, Z. C. Wang, Adv. Energy Mater. 2022, 12, 2200827.
- [31] Y. N. Guo, T. Park, J. W. Yi, J. Henzie, J. Kim, Z. L. Wang, B. Jiang, Y. Bando, Y. Sugahara, J. Tang, Y. Yamauchi, Adv. Mater. 2019, 31, 1807134.
- [32] F. Lu, M. Zhou, Y. X. Zhou, X. H. Zeng, Small 2017, 13, 1701931.
- [33] L. K. Gao, X. Cui, C. D. Sewell, J. Li, Z. Q. Lin, Chem. Soc. Rev. 2021, 50, 8428.
- [34] W. M. Tong, M. Forster, F. Dionigi, S. Dresp, R. S. Erami, P. Strasser, A. J. Cowan, P. Farràs, *Nat. Energy* **2020**, *5*, 367.
- [35] J. Peng, W. Dong, Z. Wang, Y. Meng, W. Liu, P. Song, Z. Liu, *Mater. Today Adv.* 2020, 8, 100081.
- [36] P. Farràs, P. Strasser, A. J. Cowan, *Joule* **2021**, *5*, 1921.
- [37] X. X. Duan, Q. H. Sha, P. S. Li, T. S. Li, G. T. Yang, W. Liu, E. D. Yu, D. J. Zhou, J. J. Fang, W. X. Chen, Y. Z. Chen, L. R. Zheng, J. W. Liao, Z. Y. Wang, Y. P. Li, H. B. Yang, G. X. Zhang, Z. B. Zhuang, S. F. Hung, C. F. Jing, J. Luo, L. Bai, J. C. Dong, H. Xiao, W. Liu, Y. Kuang, B. Liu, X. M. Sun, *Nat. Commun.* 2024, *15*, 1973.
- [38] X. Kang, F. N. Yang, Z. Y. Zhang, H. M. Liu, S. Y. Ge, S. Q. Hu, S. H. Li, Y. T. Luo, Q. M. Yu, Z. B. Liu, Q. Wang, W. C. Ren, C. H. Sun, H. M. Cheng, B. L. Liu, *Nat. Commun.* 2023, 14, 3607.
- [39] J. D. Benck, T. R. Hellstern, J. Kibsgaard, P. Chakthranont, T. F. Jaramillo, *ACS Catal.* **2014**, *4*, 3957.
- [40] Y. Luo, Y. H. Wu, C. Huang, C. Menon, S. P. Feng, P. K. Chu, *Ecomat* **2022**, *4*, e12197.
- [41] M. Durovic, J. Hnát, K. Bouzek, J. Power Sources 2021, 493, 229708.

- [42] S. Shit, S. Bolar, N. C. Murmu, T. Kuila, J. Energy Chem. 2021, 59, 160.
- [43] J. G. Vos, T. A. Wezendonk, A. W. Jeremiasse, M. T. M. Koper, *J. Am. Chem. Soc.* **2018**, *140*, 10270.
- [44] P. Dobaria, A. Maurya, A. Kaushik, P. Kanani, P. Rajput, S. N. Jha, B. Das, D. N. Srivastava, S. Kushwaha, K. Patel, *ACS Catal.* **2023**, *13*, 4587.
- [45] L. Tan, J. T. Yu, C. Wang, H. F. Wang, X. E. Liu, H. T. Gao, L. T. Xin, D. Z. Liu, W. G. Hou, T. R. Zhan, Adv. Funct. Mater. 2022, 32, 2200951.
- [46] L. B. Wu, L. Yu, B. McElhenny, X. X. Xing, D. Luo, F. H. Zhang, J. M. Bao, S. Chen, Z. F. Ren, Appl. Catal. B-Environ. Energy 2021, 294, 120256.
- [47] A. J. Shih, M. C. O. Monteiro, F. Dattila, D. Pavesi, M. Philips, A. H. M. da Silva, R. E. Vos, K. Ojha, S. Park, O. van der Heijden, G. Marcandalli, A. Goyal, M. Villalba, X. T. Chen, G. Gunasooriya, I. McCrum, R. Mom, N. López, M. T. M. Koper, *Nat. Rev. Methods Primers* 2022, 2, 84.
- [48] B. Y. Xiong, L. S. Chen, J. L. Shi, ACS Catal. 2018, 8, 3688.
- [49] I. Roger, M. A. Shipman, M. D. Symes, Nat. Rev. Chem. 2017, 1, 0003.
- [50] M. Bajdich, M. García-Mota, A. Vojvodic, J. K. Norskov, A. T. Bell, J. Am. Chem. Soc. 2013, 135, 13521.
- [51] M. Zeng, Y. G. Li, J. Mater. Chem. A 2015, 3, 14942.
- [52] T. R. Cook, D. K. Dogutan, S. Y. Reece, Y. Surendranath, T. S. Teets, D. G. Nocera, Chem. Rev. 2010, 110, 6474.
- [53] I. C. Man, H. Y. Su, F. Calle-Vallejo, H. A. Hansen, J. I. Martínez, N. G. Inoglu, J. Kitchin, T. F. Jaramillo, J. K. Norskov, J. Rossmeisl, *Chemcatchem* 2011, 3, 1159.
- [54] T. F. Jaramillo, K. P. Jorgensen, J. Bonde, J. H. Nielsen, S. Horch, I. Chorkendorff, *Science* **2007**, *317*, 100.
- [55] Y. J. Li, Y. J. Sun, Y. N. Qin, W. Y. Zhang, L. Wang, M. C. Luo, H. Yang, S. J. Guo, Adv. Energy Mater. 2020, 10, 1903120.
- [56] T. Reier, H. N. Nong, D. Teschner, R. Schlögl, P. Strasser, *Adv. Energy Mater.* **2017**, *7*, 1601275.
- [57] H. Dau, C. Limberg, T. Reier, M. Risch, S. Roggan, P. Strasser, *Chemcatchem* **2010**, 2, 724.
- [58] N. T. Suen, S. F. Hung, Q. Quan, N. Zhang, Y. J. Xu, H. M. Chen, Chem. Soc. Rev. 2017, 46, 337.
- [59] C. Wei, Z. C. J. Xu, Small Methods 2018, 2, 1800168.
- [60] F. L. Lyu, Q. F. Wang, S. M. Choi, Y. D. Yin, Small 2019, 15, 1804201.

- [61] B. Seo, S. H. Joo, Nano Convergence 2017, 4, 19.
- [62] P. C. Ye, K. Q. Fang, H. Y. Wang, Y. H. Wang, H. Huang, C. B. Mo, J. Q. Ning, Y. Hu, Nat. Commun. 2024, 15, 1012.
- [63] H. Vrubel, T. Moehl, M. Grätzel, X. L. Hu, Chem. Commun. 2013, 49, 8985.
- [64] S. Trasatti, O. A. Petrii, J. Electroanal. Chem. 1992, 327, 353.
- [65] C. C. L. McCrory, S. H. Jung, J. C. Peters, T. F. Jaramillo, J. Am. Chem. Soc. 2013, 135, 16977.
- [66] P. Kumar, K. Kannimuthu, A. S. Zeraati, S. Roy, X. Wang, X. Y. Wang, S. Samanta, K. A. Miller, M. Molina, D. Trivedi, J. Abed, A. C. Mata, H. Al-Mahayni, J. Baltrusaitis, G. Shimizu, Y. A. Wu, A. Seifitokaldani, E. H. Sargent, P. M. Ajayan, J. G. Hu, M. G. Kibria, J. Am. Chem. Soc. 2023, 145, 8052.
- [67] S. Anantharaj, S. R. Ede, K. Sakthikumar, K. Karthick, S. Mishra, S. Kundu, ACS Catal. 2016, 6, 8069.
- [68] Z. Zeb, Y. C. Huang, L. L. Chen, W. B. Zhou, M. H. Liao, Y. Y. Jiang, H. T. Li, L. M. Wang, L. Wang, H. Wang, T. Wei, D. J. Zang, Z. J. Fan, Y. G. Wei, *Coord. Chem. Rev.* 2023, 482, 215058.
- [69] A. H. Al-Naggar, N. M. Shinde, J. S. Kim, R. S. Mane, Coord. Chem. Rev. 2023, 474, 214864.
- [70] V. Thirumal, R. Yuvakkumar, P. S. Kumar, G. Ravi, A. Arun, R. K. Guduru, D. Velauthapillai, *Int. J. Hydrogen Energ.* **2023**, *48*, 6478.
- [71] J. J. Zhang, M. H. Wu, Z. T. Shi, M. Jiang, W. J. Jian, Z. R. Xiao, J. X. Li, C. S. Lee, J. Xu, Small 2016, 12, 4379.
- [72] L. Hui, Y. R. Xue, Y. X. Liu, Y. L. Li, Small 2021, 17, 2006136.
- [73] S. Gupta, M. K. Patel, A. Miotello, N. Patel, Adv. Funct. Mater. 2020, 30, 1906481.
- [74] Y. D. Yu, J. Zhou, Z. M. Sun, Adv. Funct. Mater. 2020, 30, 2000570.
- [75] P. R. Chen, J. S. Ye, H. Wang, L. Z. Ouyang, M. Zhu, J. Alloy. Compd. 2021, 883, 160833.
- [76] A. Ray, S. Sultana, L. Paramanik, K. M. Parida, J. Mater. Chem. A 2020, 8, 19196.
- [77] Y. Y. Wang, D. F. Yan, S. El Hankari, Y. Q. Zou, S. Y. Wang, Adv. Sci. 2018, 5, 1800064.
- [78] J. Yin, J. Jin, H. H. Lin, Z. Y. Yin, J. Y. Li, M. Lu, L. C. Guo, P. X. Xi, Y. Tang, C. H. Yan, *Adv. Sci.* **2020**, *7*, 1903070.
- [79] Z. Y. Jin, J. Lv, H. L. Jia, W. H. Liu, H. L. Li, Z. H. Chen, X. Lin, G. Q. Xie, X. J. Liu, S. H. Sun, H. J. Qiu, Small 2019, 15, 1904180.

- [80] C. X. Wang, W. X. Guo, T. L. Chen, W. Y. Lu, Z. Y. Song, C. C. Yan, Y. Feng, F. M. Gao, X. N. Zhang, Y. P. Rao, L. T. Qian, S. M. Xu, G. Y. Huang, Y. Zheng, W. Yan, J. J. Zhang, *Coord. Chem. Rev.* 2024, 514, 215899.
- [81] Z. Li, X. L. Zhang, C. J. Ou, Y. Z. Zhang, W. J. Wang, S. Y. Dong, X. C. Dong, Coord. Chem. Rev. 2023, 495, 215381.
- [82] X. Wang, J. Wu, Y. W. Zhang, Y. Sun, K. K. Ma, Y. Xie, W. H. Zheng, Z. Tian, Z. Kang, Y. Zhang, *Adv. Mater.* **2023**, *35*, 2206576.
- [83] J. W. Liu, X. Q. Yang, F. Z. Si, B. Zhao, X. A. Xi, L. Wang, J. J. Zhang, X. Z. Fu, J. L. Luo, *Nano Energy* **2022**, *103*, 107753.
- [84] Y. R. Ying, X. Luo, J. L. Qiao, H. T. Huang, Adv. Funct. Mater. 2021, 31, 2007423.
- [85] W. J. Jiang, T. Tang, Y. Zhang, J. S. Hu, Acc. Chem. Res. 2020, 53, 1111.
- [86] C. Manjunatha, N. Srinivasa, S. K. Chaitra, M. Sudeep, R. C. Kumar, S. Ashoka, *Mater. Today Energy* **2020**, *16*, 100414.
- [87] D. W. Wang, Q. Li, C. Han, Q. Q. Lu, Z. C. Xing, X. R. Yang, Nat. Commun. 2019, 10, 3899.
- [88] X. Wang, Z. Qin, J. J. Qian, L. Y. Chen, K. Shen, ACS Catal. 2023, 13, 10672.
- [89] B. T. Qiao, A. Q. Wang, X. F. Yang, L. F. Allard, Z. Jiang, Y. T. Cui, J. Y. Liu, J. Li, T. Zhang, *Nat. Chem.* **2011**, *3*, 634.
- [90] K. Shah, R. Y. Dai, M. Mateen, Z. Hassan, Z. W. Zhuang, C. H. Liu, M. Israr, W. C. Cheong, B. T. Hu, R. Y. Tu, C. Zhang, X. Chen, Q. Peng, C. Chen, Y. D. Li, *Angew. Chem. Int. Ed.* 2022, 61, e202114951.
- [91] Y. F. Zhao, Y. Guo, X. F. Lu, D. Y. Luan, X. J. Gu, X. W. D. Lou, *Adv. Mater.* **2022**, *34*, 2203442.
- [92] S. Niu, W. J. Jiang, Z. X. Wei, T. Tang, J. M. Ma, J. S. Hu, L. J. Wan, J. Am. Chem. Soc. 2019, 141, 7005.
- [93] M. Retuerto, L. Pascual, F. Calle-Vallejo, P. Ferrer, D. Gianolio, A. G. Pereira, A. García, J. Torrero, M. T. Fernández-Díaz, P. Bencok, M. A. Peña, J. L. G. Fierro, S. Rojas, *Nat. Commun.* 2019, 10, 2041.
- [94] L. Tian, X. L. Pang, H. Xu, D. S. Liu, X. H. Lu, J. Li, J. Wang, Z. Li, *Inorg. Chem.* 2022, 61, 16944.
- [95] L. Xu, Q. Q. Jiang, Z. H. Xiao, X. Y. Li, J. Huo, S. Y. Wang, L. M. Dai, Angew. Chem. Int. Ed. 2016, 55, 5277.
- [96] R. R. Zhang, Y. C. Zhang, L. Pan, G. Q. Shen, N. Mahmood, Y. H. Ma, Y. Shi, W. Y. Jia, L. Wang, X. W. Zhang, W. Xu, J. J. Zou, ACS Catal. 2018, 8, 3803.

- [97] J. Wang, L. L. Han, B. L. Huang, Q. Shao, H. L. L. Xin, X. Q. Huang, Nat. Commun. 2019, 10, 5692.
- [98] Z. X. Li, M. L. Hu, P. Wang, J. H. Liu, J. S. Yao, C. Y. Li, Coord. Chem. Rev. 2021, 439, 213953.
- [99] G. M. Mu, G. Z. Wang, Q. P. Huang, Y. J. Miao, D. Wen, D. M. Lin, C. G. Xu, Y. J. Wan, F. Y. Xie, W. H. Guo, R. Q. Zou, Adv. Funct. Mater. 2023, 33, 2211260.
- [100] Y. Wang, L. T. Yan, K. Dastafkan, C. Zhao, X. B. Zhao, Y. Y. Xue, J. M. Huo, S. N. Li, Q. G. Zhai, Adv. Mater. 2021, 33, 2006351.
- [101] Z. P. Wu, H. B. Zhang, S. W. Zuo, Y. Wang, S. L. Zhang, J. Zhang, S. Q. Zang, X. W. Lou, Adv. Mater. 2021, 33, 2103004.
- [102] J. F. Zhang, Y. C. Hu, D. L. Liu, Y. Yu, B. Zhang, Adv. Sci. 2017, 4, 1600343.
- [103] F. A. Garces-Pineda, M. Blasco-Ahicart, D. Nieto-Castro, N. Lopez, J. R. Galan-Mascaros, *Nat. Energy* 2019, 4, 519.
- [104] A. Khorshidi, J. Violet, J. Hashemi, A. A. Peterson, *Nat. Catal.* **2018**, *1*, 263.
- [105] L. Wang, Z. H. Zeng, W. P. Gao, T. Maxson, D. Raciti, M. Giroux, X. Q. Pan, C. Wang, J. Greeley, *Science* 2019, 363, 870.
- [106] H. T. Wang, S. C. Xu, C. Tsai, Y. Z. Li, C. Liu, J. Zhao, Y. Y. Liu, H. Y. Yuan, F. Abild-Pedersen, F. B. Prinz, J. K. Norskov, Y. Cui, *Science* 2016, 354, 1031.
- [107] D. J. Zhou, S. Y. Wang, Y. Jia, X. Y. Xiong, H. B. Yang, S. Liu, J. L. Tang, J. M. Zhang, D. Liu, L. R. Zheng, Y. Kuang, X. M. Sun, B. Liu, *Angew. Chem. Int. Ed.* 2019, 58, 736.
- [108] X. Liu, L. Zhang, Y. Zheng, Z. Guo, Y. M. Zhu, H. J. Chen, F. Li, P. P. Liu, B. Yu, X.
 W. Wang, J. Liu, Y. Chen, M. L. Liu, *Adv. Sci.* 2019, 6, 1801898.
- [109] H. Y. Meng, W. Xi, Z. Y. Ren, S. C. Du, J. Wu, L. Zhao, B. W. Liu, H. G. Fu, Appl. Catal. B-Environ. Energy 2021, 284, 119707.
- [110] L. Tian, H. Y. Chen, X. H. Lu, D. S. Liu, W. J. Cheng, Y. Y. Liu, J. Li, Z. Li, J. Colloid Interface Sci. 2022, 628, 663.
- [111] L. Bai, S. J. Jia, Y. D. Gao, C. Li, X. Chen, S. Zhou, J. W. Han, F. C. Yang, X. Zhang, S. Y. Lu, *Energy Environ. Mater.* 2022, 0, e12456.
- [112] Y. G. Liang, Y. J. Zhang, X. K. Wang, J. Zhou, Z. W. Cao, M. H. Huang, H. Q. Jiang, Mater. Today Energy 2022, 25, 100966.
- [113] Y. J. Zhang, Y. C. Wang, H. Q. Jiang, M. H. Huang, Small 2020, 16, 2002550.
- [114] H. C. Zhai, G. S. Xu, C. H. Zhu, Y. P. Yuan, Int. J. Hydrogen Energ. 2022, 47, 23971.

- [115] B. J. Jin, Y. C. Li, J. N. Wang, F. Y. Meng, S. S. Cao, B. He, S. R. Jia, Y. Wang, Z. Li, X. Q. Liu, Small 2019, 15, 1903847.
- [116] S. Trasatti, *Electrochim. Acta* **1984**, 29, 1503.
- [117] F. Dionigi, T. Reier, Z. Pawolek, M. Gliech, P. Strasser, Chemsuschem 2016, 9, 962.
- [118] R. K. B. Karlsson, A. Cornell, Chem. Rev. 2016, 116, 2982.
- [119] J. E. Bennett, Int. J. Hydrogen Energ. 1980, 5, 401.
- [120] Y. Kuang, M. J. Kenney, Y. T. Meng, W. H. Hung, Y. J. Liu, J. E. Huang, R. Prasanna, P. S. Li, Y. P. Li, L. Wang, M. C. Lin, M. D. McGehee, X. M. Sun, H. J. Dai, *Proc. Natl. Acad. Sci. USA* 2019, *116*, 6624.
- [121] W. H. Hung, B. Y. Xue, T. M. Lin, S. Y. Lu, I. Y. Tsao, *Mater. Today Energy* **2021**, 19, 100575.
- [122] L. Yu, Q. Zhu, S. W. Song, B. McElhenny, D. Z. Wang, C. Z. Wu, Z. J. Qin, J. M. Bao, Y. Yu, S. Chen, Z. F. Ren, *Nat. Commun.* 2019, 10, 5106.
- [123] T. F. Ma, W. W. Xu, B. R. Li, X. Chen, J. J. Zhao, S. S. Wan, K. Jiang, S. X. Zhang, Z.
 F. Wang, Z. Q. Tian, Z. Y. Lu, L. Chen, *Angew. Chem. Int. Ed.* 2021, 60, 22740.
- [124] F. Sun, J. S. Qin, Z. Y. Wang, M. Z. Yu, X. H. Wu, X. M. Sun, J. S. Qiu, *Nat. Commun.* 2021, 12, 4182.
- [125] X. B. W. Du, M. W. Tan, T. Wei, H. Kobayashi, J. J. Song, Z. X. Peng, H. L. Zhu, Z. K. Jin, R. H. Li, W. Liu, *Chem. Eng. J.* 2023, 452, 139404.

Chapter II Experimental Techniques and Characterization Methods

2.1. Introduction

This thesis employs anodic oxidation, electrochemical deposition, hydrothermal reaction, laser ablation in liquid, calcination, and self-assembly methods to prepare a series of catalyst materials. To study the relationship between the physicochemical properties of catalysts and electrocatalytic performance, various characterization techniques are engaged to analyze the structure, morphology, and performance of electrocatalysts.

This Chapter introduces the materials characterization methods, instruments, electrochemical methods, and first-principles calculations.

2.2. Characterization Methods

2.2.1. X-ray Diffraction (XRD)

X-ray diffraction is an indispensable method for material characterization and quality control. It is often used to identify and study the composition and atomic-scale structure of materials. The X-ray diffraction effect can determine the unit cell structure and space group of the material. The irradiation of X-rays causes electron vibration in the material crystal. The electron wavelength is the same as the incident light. Due to the periodic characteristics of the crystal material structure, X-rays will be superimposed and enhanced in certain directions, resulting in a specific diffraction pattern. The basic principle of crystal diffraction can be described by the Bragg formula:

$$2d \sin\theta = n\lambda \tag{2.1}$$

where d is the interplanar spacing in the crystal structure, θ is the incident angle of the X-ray, n is an integer, and λ is the wavelength of the X-ray. Since different samples produce different diffraction spectra, the relationship between the 2θ angles and peak intensity of the measured diffraction peaks is recorded and compared with the standard card to perform qualitative analysis of the material phase.

The applications of XRD characterization include that:

- determining the arrangement of various atoms in the unit cell of a material, and then studying the relationship between different special properties of the material and its atomic arrangement.
- 2) determine the type and content of compounds (phases) in a material, and then study the influence of phase content on performance.
- 3) X-ray diffraction is also often used to determine the unit cell parameters, grain size, microscopic and macroscopic stress, texture, orientation, crystallinity, order of intermetallic compounds, and other properties of materials, and then study the structure-activity relationship of materials. It can be said that X-ray diffraction plays a decisive role in the identification and research of material structure. For example, in the study of mineral composition and content, XRD is usually used to obtain the material spectrum first, and then the mineral composition is obtained through database comparison analysis, and then the content is calculated. This technology provides a strong evidence guarantee for the subsequent experimental analysis of mineral researchers.

The phase and crystal structure of the catalyst materials prepared in this work were analyzed by XRD. The XRD diffractometer used in the experiment uses Cu K α (λ = 1.5418 Å) as the incident light source, a tube voltage of 40 kV, a tube current of 40 mA, wide-angle scanning mode, and a scanning rate of 10° min⁻¹ according to the characteristics of the sample.

2.2.2. Scanning Electron Microscopy (SEM)

The SEM mainly consists of three systems: an electron optical system, a signal detection processing and display system, and a vacuum system. Among them, the main functions of the vacuum system include: reducing the pollution of the electron optical path and increasing the service life of the filament; increasing the mean free path of electrons, so that more electrons can be used for imaging.

The working principle of the energy spectrometer is that the high-energy electron beam emitted by the electron gun bombards the sample, ionizing the inner electrons of the atoms in the sample. Then, the atoms are in a higher excited state, and the high-energy electrons in the outer layer will jump to the inner layer to fill the inner layer vacancy, thereby releasing energy. The part of the electromagnetic radiation photons with specific energy is the characteristic X-ray. The X-ray energy spectrometer determines the corresponding element by detecting the characteristic X-ray energy generated from the sample and conducts qualitative and quantitative analysis on it.

The scanning electron microscope has a wide range of uses in materials science, including nanomaterials, polymer materials, metal materials, ceramic materials, and biomaterials.

The energy-dispersive X-ray spectrometer (EDS) mainly performs micro-area composition analysis on the surface of the sample, including quantitative and qualitative analysis of elements, as well as point, line, and surface scanning distribution analysis of multiple elements. Its acquisition depth is approximately in the range of several hundred nanometers to several microns and can be divided into selected area analysis (point, line, and surface scanning) and element distribution mapping. Both point scanning and line scanning perform micro-area element analysis on a certain position of the sample. The difference between point scanning and line scanning is that the collected data comes from points or lines in a certain area excited by the electron beam. Point scanning can give the relative content of elements with high accuracy, and is often used for component analysis of absorption structure. Surface scanning is a qualitative analysis of the element distribution in a certain area of the sample.

The surface micromorphology and chemical composition of the catalyst material prepared in this Thesis were analyzed using SEM and the corresponding EDS. The SEM instrument used is the field emission scanning electron microscope (Tescan MIRA).

2.2.3. Transmission Electron Microscopy (TEM)

High-resolution electron microscopy is one of the ultimate means to understand and study the structure of materials from a microscopic scale. The advancement of TEM technology allows us to obtain atomic arrangement images with atomic resolution, and then analyze the structure and composition of micro-regions less than 1nm in materials. Therefore, TEM has attracted the attention of workers in the fields of materials science, life science, information science, chemistry, and chemical engineering.

The functions of electron microscopes and optical microscopes are to magnify tiny objects to a level that can be distinguished by the naked eye. The working principle also follows the Abbe imaging principle of rays. The coherent imaging process is completed in two steps. The first step is that the coherent incident light undergoes Fraunhofer diffraction through the object plane, forming a series of diffraction spots on the rear focal plane of the mirror; the second step is that the spherical secondary waves emitted by the diffraction spots are coherently superimposed on the image plane.

Traditional transmission electron microscopes mainly use elastically scattered electrons and transmitted electrons generated when high-energy electron beams interact with thin samples for imaging while scanning transmission electron microscopy (STEM) uses very small beam spots (especially the beam spots formed after spherical aberration correction) for imaging, which can obtain higher spatial resolution and sensitivity.

Usually, transmission electron microscopes can study metals, alloys, glass, semiconductors, polymers, and composites of these materials. Conventional transmission electron microscopes can observe most powders, but due to the size of the microscope rod slot, large samples often require complex cutting and thinning. Even with large block sample rods, the electron beam cannot penetrate the block, causing blurred images.

The microscopic nanostructure, crystal structure, crystal phase composition, and surface defects of the catalyst materials prepared in this Thesis were observed and analyzed using TEM

(JEM-2100F STEM), STEM, and high-resolution TEM. Additionally, the EDS incorporated in the instrument was used to qualitatively analyze the chemical components and elements of the catalyst materials at the microscopic scale.

2.2.4. X-ray Photoelectron Spectroscopy (XPS)

XPS is a conventional surface component analysis instrument. In addition to characterizing the composition of materials, it can also characterize the chemical state of each component and quantitatively characterize the relative content of each component. Therefore, it is widely used in various fields of material research. XPS uses an excitation source, X-rays, to irradiate the surface of the sample. The commonly used X-ray source is an AlKa monochromatic X-ray source with an energy of 1486.6eV. It detects the energy distribution of photoelectrons emitted from the sample surface, which is based on Einstein's photoemission theory. Due to the high energy of X-rays, the main electrons obtained are ionized electrons on the inner shell orbits of atoms. Since photoelectrons possess characteristic information of the sample (element information, chemical state information, etc.), by measuring the kinetic energy of the escaped electrons, the elemental composition and chemical state information in the sample can be obtained.

X-rays incident on the sample surface can excite electrons in the orbital core energy level, called photoelectrons. Based on Einstein's photoemission theory, there is an energy conservation formula: the energy of the incident source is equal to the sum of the kinetic energy and binding energy of the photoelectron. Photoelectrons emitted from different orbits of different elements have different characteristic binding energy information, which means the value of binding energy can be used to characterize different elements and chemical state information. According to Einstein's energy relationship formula:

$$hv = E_{\rm B} + E_{\rm K} \tag{2.2}$$

where v is the frequency of the photon, E_B is the orbital binding energy of the inner electron, and E_K is the kinetic energy of the photoelectron excited by the incident photon.

The analysis depth of XPS is less than 10 nm, and it can qualitatively and semiquantitatively analyze the surface composition information of solid materials (including elemental composition, chemical state, *etc.*). In this Thesis, XPS analysis is used to analyze the chemical element composition, element chemical valence state, relative concentration of elements, and quantitative analysis of different oxidation states of the same element on the surface of materials. The XPS characterization is performed on XPS equipment equipped with monochromatic Al K_{α} radiation (ESCALAB 250 Xi, Thermo Fisher). The C 1s binding energy (284.8 eV) is used as the standard for calibration.

2.2.5. Brunner–Emmet–Teller (BET) Analysis

Gas adsorption analysis technology is currently mainly used to analyze the specific surface area and pore structure of porous materials. It uses the adsorption characteristics of solid materials and applies gas molecules as a 'measuring tool' to describe the surface area and pore structure of materials. It is currently the most mature in application and has good regularity and consistency in testing. The specific surface area and pore size of micropores, mesopores, and some macropores of materials can be analyzed. It has been widely used in many fields such as catalysis, new energy materials, and environmental engineering.

Physical adsorption refers to the process in which adsorbed molecules adhere to the surface of the adsorbent through Van der Waals forces. This type of adsorption can occur in both single- and multi-layer forms. It is non-selective and reversible, which means it can undergo reversible adsorption and desorption processes. In this context, the adsorbent is a solid substance with the capacity to adsorb, while the adsorbate is the gas (commonly nitrogen) used during testing. Adsorption is a dynamic equilibrium process. When the concentration of gas on the surface of the adsorbent increases, it is termed adsorption, conversely when the gas

concentration decreases, this process is known as desorption. Equilibrium is achieved when the amount of gas on the adsorbent surface remains constant. The amount of gas that can be adsorbed is influenced by temperature and pressure. At a constant temperature, there is a specific equilibrium adsorption amount corresponding to a given gas pressure. By varying the pressure of the adsorbed gas, a curve can be generated that illustrates the relationship between adsorption amount and pressure, known as the isothermal adsorption—desorption curve. This curve serves as the foundational experimental basis for analyzing specific surface area and pore size.

The BET instrument used in this Thesis is a MicroActive ASAP 2460 apparatus. Samples are first dehydrated and dried at 200 $^{\circ}$ C and the N_2 adsorption and desorption test is carried out at 77 K. Finally, the specific surface area of the material is calculated using the BET algorithm.

2.2.6. Inductively Coupled Plasma Optical Emission Spectroscopy (ICP-OES)

The term 'plasma' was first proposed by Langmuir in 1929. Currently, it usually refers to ionized gas with an ionization degree exceeding 0.1 %. This gas contains not only neutral atoms and molecules but also a significant number of electrons and ions. In this state, the concentration of positively and negatively charged particles are in balanced, rendering the overall system electrically neutral.

Inductively Coupled Plasma (ICP) is formed through the ionization of a working gas, with argon being the most commonly used gas in commercial instruments. The formation of a stable ICP torch flame requires four essential conditions: a high-frequency, high-intensity electromagnetic field, a suitable working gas, a torch tube that maintains a stable gas discharge, and a source of electrons and ions.

For any spectral line of an element, the intensity is proportional to the concentration of the element, described by the equation:

$$I = ac (2.3)$$

where I is the intensity of the emitted light when an electron transitions from an excited state to a ground state, a is a constant related to plasma temperature and element properties, and c is the element concentration. However, in practical spectral light sources, self-absorption can occur, which diminishes the spectral line intensity. Therefore the formula must be adjusted to account for this effect:

$$I = ac^b (2.4)$$

where b ($b \le 1$) is the self-absorption coefficient. The value of b is related to characteristics of the light source, the concentration of the element in the sample, and the properties of the element itself. In summary, within a certain range, the light intensity I is proportional to the element concentration.

In this Thesis, an Agilent 710 Series spectrometer was used to perform qualitative and quantitative analysis of the types and contents of elements contained in the catalysts. Before the test, samples are fully dissolved using concentrated nitric acid or aqua regia to form a clear liquid with a certain concentration range for detection.

2.2.7. UV-Vis Absorption Spectroscopy

The mechanism of UV-Visible absorption spectroscopy is based on the transition of outer electrons in molecules when they absorb ultraviolet or visible light. When a continuous light beam irradiates organic molecules, the varying compositions and structures at the molecular level lead to different energy level characteristics and energy levels. Each substance can only absorb light radiation that corresponds to the energy level difference within its molecules, making them selective in absorbing light at specific wavelengths. Photons of certain frequencies can excite the valence electrons of the molecules, causing them to transition from lower energy levels to higher ones. The light absorbed during these electron transitions typically falls within the far ultraviolet region $(10 \sim 200 \text{ nm})$, near-ultraviolet region $(200 \sim 400 \text{ nm})$, and visible light part $(360 \sim 760 \text{ nm})$. According to quantum mechanics, the energy

of a photon must precisely match the band gap energy in order to be absorbed. As a result, molecules with different chemical structures exhibit different energy band gaps, leading to distinct absorption spectra.

This Thesis employs diffuse reflectance UV–Vis spectroscopy to characterize the optical properties of semiconductors and metal samples in powder form. The accuracy of UV–Vis DRS was checked against a Jasco V780 spectrophotometer using the standard of BaSO₄ baseline correction and the wavelength ranging from 300 to 780 nm. Liquid UV–Vis absorption spectrum was recorded in the wavelength range from 300 to 550 nm. Quasi-*in-situ* UV–Vis spectra were collected using a spectrophotometer (Jasco V780) and a potentiostat (CHI760E) to identify the presence of anions during the reconstruction of catalysts. Standard absorption spectra were first obtained for solutions containing target anions. To detect anions during the OER process, UV–Vis absorption spectra of the electrolytes were collected at different reaction times. A two-electrode configuration was used, with catalysts as the anode and a Pt wire as the cathode using 3 mL of the reaction reagent as the electrolyte. An applied positive potential was maintained using chronoamperometry for 1 min, and the entire electrolyte was extracted from the cell and analyzed using UV–vis spectroscopy. The electrolyte (3 mL) was added to the cell for subsequent measurements.

2.2.8. Raman Spectroscopy

Raman spectroscopy is a non-destructive, label-free, and non-contact 'fingerprint' analytical technique that provides detailed molecular-level information. It is widely used in research fields such as materials science, life science, and medicine. When light interacts with certain molecules, it engages with molecular vibration, rotation, and various elemental excitations, resulting in inelastic scattering. The spectral lines produced from this interaction are broadly distributed, and recording the relationship between their intensity and energy (or frequency) generates a Raman spectrum.

Chapter II Experimental Techniques and Characterization Methods

Raman spectroscopy is applicable to nearly all types of samples, though sample preparation methods and parameter adjustments can vary significantly. For organic samples that are sensitive to laser radiation, it is often necessary to reduce the laser power to minimize damage, which may require extended sampling times. For small molecules with low concentrations and weak signals, techniques such as injecting precious metal nanosols or using tip-enhanced Raman spectroscopy are often employed to obtain clear Raman spectra. In some cases, modified electrodes may need to be pressurized to collect adequate signals. In this Thesis, Raman spectra were recorded on a confocal micro-Raman spectroscopy system (Renishaw, inVia) with a 785-nm streamline laser excitation.

Raman spectroscopy excels at detecting lower energy vibrations in the low wavenumber region (< 1,000 cm⁻¹), making it valuable for studying the direct interaction between catalysts and reactants. It is particularly effective in monitoring metal—carbon bonds, oxygen species. In the context of electrocatalytic reactions, Raman spectroscopy can provide insights into the microstructure and intermediate products on the electrode surface (interface) under actual reaction conditions. Additionally, its sensitivity to changes in polarizability makes it well-suited for observing electrochemical reactions in aqueous environments. Therefore, the combination of Raman spectroscopy with electrochemical methods represents a powerful approach to studying the processes and mechanisms of electrochemical reactions. The measurement setup for *in situ* electrochemical Raman spectroscopy typically consists of two main components: a Raman spectrometer and *in situ* electrochemical Raman cell. This cell is usually equipped with a working electrode, a counter electrode, a reference electrode, and a ventilation system.

In this thesis, *in situ* Raman spectra were recorded on the Raman spectrometer equipped with a working station (CHI760E). Each spectrum was accumulated twice with 10 s exposure time and 0.5 % laser intensity (the power was decreased to 1.5 mW). Two accumulations were

performed for each spectrum to enhance signal quality. A standard three-electrode configuration was used with a Hg/HgO reference electrode and a Pt wire counter electrode for these measurements. Linear sweep voltammograms (LSVs) were recorded at a scan rate of 0.25 mV s $^{-1}$ to allow sufficient time for Raman signal acquisition.

2.2.9. Photoluminescence (PL) and Time-Resolved PL (TRPL) Spectroscopy

For photoluminescent substances, exposure to light of a specific wavelength induces the substance (molecule) to absorb energy and transition to an excited state. However, excited state molecules are unstable and must release energy. If they return to the ground state or a lowerenergy excited state by emitting radiation, this process is termed a radiative transition. Depending on the properties of the initial and final states involved in the emitted radiation, this can result in fluorescence, phosphorescence, or long afterglow. By fixing the wavelength of the excitation light and detecting the emission intensity at various emission wavelengths, a photoluminescence (PL) spectrum that shows how the emission intensity of the material caries with the emission wavelength can be obtained. In the case of PL excitation spectra, the emission light wavelength is fixed while the luminescence intensity is measured across different excitation light wavelengths. This results in a spectrum that illustrates how the emission intensity (at the fixed emission wavelength) changes with the excitation wavelength. Quantum yield indicates a substance's ability to fluoresce, with values ranging from 0 to 1. It reflects the competition between fluorescence radiation and other radiative or non-radiative transitions. Quantum yield can be further divided into internal quantum yield and external quantum yield. Time-resolved photoluminescence (TRPL) refers to the time required for the fluorescence intensity of a molecule to decrease 1/e of its maximum intensity after excitation ceases. It represents the average duration that the particle remains in the excited state and is commonly referred as the fluorescence lifetime of the excited state.

Engaging an excitation wavelength of 375 nm, PL and TRPL spectra were acquired from the same sample using an Edinburgh FLS 1000 fluorescence spectrometer equipped with the following three standard light sources: steady-state light sources are Xenon lamps with continuous spectrum and energy output, which are mainly used for steady-state spectrum and quantum yield testing; transient light sources are pulse output light sources with adjustable frequency and specific pulse width, mainly including microsecond lamps, nanosecond lamps, and picosecond pulse lasers, which are mainly used for fluorescence lifetime testing.

2.2.10. Ultraviolet Photoelectron Spectroscopy (UPS)

UPS utilizes UV light to excite the sample surface, resulting in the emission of photoelectrons. He lamps (21.21 eV for He I and 40.82 eV for He II) and synchrotron radiation sources can also serve as vacuum UV light sources due to their continuously adjustable energy. Compared with XPS, the energy of UV light is lower, and thus most emitted photoelectrons originate from valence electrons. As a result, UPS is not typically used for quantitative analysis. However, it provides valuable information about the work function and band structure of solid materials. UPS can reveal the electronic states and chemical information within a depth range of approximately 10 Å at the material's surface. This non-destructive surface analysis technique is widely employed in materials science, semiconductor research, and surface chemistry.

The UPS analysis method primarily involves examining the integrated electron kinetic energy distribution curves, often referred to as 'spectral lines', which are obtained by measuring the kinetic energy of the emitted electrons. The overall shape and characteristics of these curves represent the energy distribution of electrons within the material. The peak position in the spectrum corresponds to specific electronic states, indicating where electrons are most likely to be found. For example, in semiconductor materials, certain peaks correlate with electrons in the valence band, conduction band, or surface state. Identifying these peak positions helps determine which electronic energy levels are occupied, thus inferring the band

structure. Additionally, the peak height and area of the spectral lines directly reflect the density of these electronic states, representing the number of electrons present in those energy states. By analyzing the different peaks and their heights, researchers can gain insights into the relative density and distribution of various electronic states in the material, which is crucial for understanding its electronic structure and properties.

By measuring and analyzing the Fermi level and the work function (Φ , the minimum energy required to escape an electron from the surface of the material) of the material surface, researchers can deeply understand the electrical properties of the material. The position of the Fermi level can provide information about the conductivity of the material, and the value of the work function is closely related to the surface chemical properties and electron emission characteristics of the material. The instrument used in this Thesis is an Escalab 250xi X-ray photoelectron spectrometer.

2.2.11. Electron Paramagnetic Resonance (EPR) Spectroscopy

EPR spectroscopy is an electromagnetic spectroscopy method for studying magnetic materials containing one or more unpaired electrons (or unpaired electrons). EPR spectroscopy is one of the means of environmental detection and material performance testing. It is also a spectral method for detecting whether a sample has unpaired electrons. It is an ideal technology to complement other analytical testing methods.

Due to the establishment of new experimental technologies and methods such as electron spin coherence, spin capture, spin labeling, saturation transfer, electron paramagnetic resonance, and paramagnetic imaging, EPR technology has quickly been widely used in physics, chemistry, free radical biology, and materials science, such as direct detection and analysis of free radical intermediates, detection of transient free radicals, EPR spectrum research of paramagnetic ion complexes, lattice defects in solids, etc.

- 1) Direct detection and analysis of free radical intermediates: the detection of free radicals using EPR is a fast, direct, and effective method. In the experiment, the g factor of the corresponding absorption peak in the obtained EPR spectrum is calculated, and by comparing it with the standard value, the type of free radical is estimated, and then the free radical is eliminated by chemical means to verify the above inference.
- 2) Detection of transient free radicals: the method combining free radical capture technology with EPR has the advantages of high detection sensitivity, strong selectivity, and reliable analysis results. It is widely used for the detection of transient free radicals with short life and low steady-state concentration. It is widely used in many studies involving cells and even animal systems and chemical reaction mechanisms. The experimental method of EPR detection of transient free radicals is to first design and synthesize a probe molecule that can capture free radicals. This probe molecule must be able to quickly capture the transient free radicals generated in the reaction process, and then use EPR to analyze the molecular structure of the capture reaction adduct and infer and identify it by identifying the component structure corresponding to each peak on the EPR spectrum line one by one.
- 3) EPR spectrum research of paramagnetic ion complexes: the EPR spectrum study of paramagnetic ion complexes uses paramagnetic metal ions as structural probes to form coordination structures with organic substances such as proteins. By studying the EPR spectrum of paramagnetic ion complexes, important information such as the spin state coordination structure and electronic energy level of the complex molecules can be obtained. The analysis of the paramagnetic ion EPR spectrum depends on the configuration of the complex and the distribution of d electrons and defects. Through the study of theoretical calculation methods, the EPR signal characteristics and catalytic performance of various transition metal ions and their compounds under different coordination fields can be analyzed in depth.

4) Lattice defects in solids: one or more electrons or holes fall into or near the defect, forming a substance with a single electron, such as face-centered, body-centered, *etc.*, or an atomic defect containing a single electron caused by the lack of an atom.

2.3. Electrochemical Characterization Methods and Theoretical Calculation

2.3.1. Selection of Electrodes and Their Preparation

The electrochemical experiments in this Thesis are conducted using the Princeton multichannel electrochemical station in a classic three-electrode configuration consisting of a working electrode, a counter electrode, and a reference electrode, as shown in **Figure 2.1**.^[1] A Hg/HgO (alkaline system) or a standard calomel electrode (SCE, acidic, or neutral system) is used as the reference electrode, and a graphite or platinum sheet/wire is employed as the counter electrode. The working electrode is prepared in two ways depending on whether the catalyst is powder or self-supporting. For the preparation of the powder catalyst electrode, a predetermined amount of catalyst, conductive agent (carbon black), and binder (5 wt.% Nafion solution) are mixed and added to ethanol to form a suspension (5 mg mL^{-1}) after ultrasonication. Then, a certain amount of liquid is pipetted and drop-cast onto the surface of a conductive substrate (carbon paper or nickel foam) and dried for performance testing. For self-supporting catalysts, the electrode sheet loaded with the catalyst is directly immersed in the electrolyte. Before the test, the oxygen gas is bubbled into the electrolyte for 30 min, with a continuous and stable gas blanket maintained during the test. For overall water splitting, two-electrode configuration is used. Pt/C or NiMo alloy catalysts are used for HER (cathode), and together with self-developed catalysts for OER (anode) to form a full-cell water-splitting system. For comparison, commercial RuO2 and Pt/C on Ni foam were used as a benchmark for the anode and cathode, respectively.

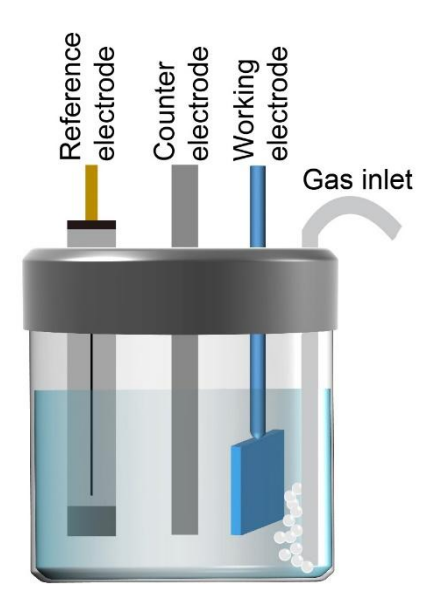


Figure 2.1. A schematic of a three-electrode electrochemical cell showing a working electrode, a reference electrode, a counter electrode, and a gas inlet.^[1]

2.3.2. Electrochemical Measurements

LSV was used to assess the catalytic performance of samples. The current response linearly changes with potential within a certain voltage range. The linear relationship between the reaction potential and the response current is the polarization curve. For convenient comparison and the elimination of any influences from the solution on the potential, it is necessary to convert the measured potential relative to the reversible hydrogen electrode (V vs. RHE). When a Hg/HgO is used as the reference electrode, the measured potential is converted using:

$$E_{\text{RHE}} = E_{\text{Hg/HgO}} + E^{\circ}_{\text{Hg/HgO}} + 0.059 \times \text{pH}$$
 (2.5)

where $E_{\rm Hg/HgO}$ is the actual potential measured against Hg/HgO electrode and $E^{\circ}_{\rm Hg/HgO}$ is the electrode potential of Hg/HgO relative to the standard hydrogen electrode (SHE) at 25 °C (0.098 V). Unless otherwise specified, all the potentials mentioned in this thesis are referenced to the RHE. The OER catalytic activity of electrocatalysts was evaluated by LSV which was conducted with a slow scan rate of 2 mV s⁻¹ or a backward scanning mode to avoid interference from the Ni oxidation current. Before performing LSV measurements, CV was conducted for 100 cycles within a potential window between 1.124 V and 1.624 V at a scanning rate of 0.1

Chapter II Experimental Techniques and Characterization Methods

V s⁻¹ to activate the catalysts. EIS is measured at 1.524 V, in a frequency range of 100 kHz to 0.01 Hz with an amplitude of 10 mV. Based on the Rs values obtained from EIS spectra, all polarization curves in **Chapters 3**, **4**, **5**, and **6** were subjected to 85, 85, 90, and 85 % i*R*-compensation, respectively. Cyclic voltammetry is conducted in the non-Faraday range (1.21 – 1.31 V, 1.254 – 1.354 V, 1.254 – 1.354 V, and 1.175 – 1.275 V for **Chapters 3**, **4**, **5**, and **6**) at various scan rates from 20 to 100 mV⁻¹ (**Chapters 3** and **6**) and 50 to 250 mV⁻¹ (**Chapters 4** and **5**) to calculate the C_{dl} of the catalyst and then the ECSA to evaluate the number of active sites. The chronoamperometry method is used to test the stability of the catalyst. Specifically, the change of the potential over time is tested while the current density remains unchanged. **Table 2.1** summarizes the testing conditions for the chronoamperometry method.

Table 2.1. Summary of testing condition to evaluate the long-term stability of electrocatalysts in this thesis.

Testing sample	Operating conditions (mA cm ⁻²)	Chapter
Li-NiFe-LDH/g-C ₃ N ₄	200	3
Ni(OH) ₂ /L-LFP	100 and 250	4
Ni(OH) ₂ /NiMoO ₄	100, 500, and 1,000	5
$MoO_3/Fe_2O_3/MoS_2$	100 and 300	6

2.4. References

[1] C. Wei, R. R. Rao, J. Y. Peng, B. T. Huang, I. E. L. Stephens, M. Risch, Z. C. J. Xu, Y. Shao-Horn, *Adv. Mater.* **2019**, *31*, 1806296.

Chapter III

Li-Doped NiFe-LDH/g-C₃N₄ for Seawater Oxidation

3.1. Objective and Motivation

As introduced in **Chapter I**, transition-metal-based materials have emerged as promising alternatives to noble metal oxides for electrocatalytic OER. However, the performance of these catalysts remains inadequate for practical applications. Elemental doping and the construction of heterojunctions are potential strategies to enhance catalytic activity. Specifically, elemental doping can modify the crystal structure and tune the surface properties for catalytic reactions, while heterojunction can combine the advantages of each component to facilitate reaction kinetics and improve both catalytic activity and stability. Recently, NiFe-LDH has been widely investigated as an OER electrocatalyst due to its appealing catalytic activity and ease of synthesis. However, challenges such as competitive CER and severe chlorine corrosion limit the effectiveness of NiFe-LDH for OER in seawater environments.

To address these issues, hybrids of *g*-C₃N₄ and Li-doped NiFe-LDH were prepared and systematically studied in this Chapter. The Li-NiFe-LDH/*g*-C₃N₄ heterostructure was synthesized using a facile chemical co-precipitation and sonication-assisted co-assembly method, allowing for precise control of Li doping and *g*-C₃N₄ hybridization levels. The electrocatalytic OER activity of NiFe-LDH in both freshwater and seawater was analyzed with Li doping and *g*-C₃N₄ hybridization, focusing on their effects on electronic structure, electrochemical surface area, and OER selectivity. Theoretical calculations further supported the beneficial effects of Li doping and *g*-C₃N₄ hybridization, revealing the underlying mechanisms that enhance OER selectivity and durability in seawater.

3.2. Introduction

The electrocatalytic water splitting process simultaneously undergoes two half-reactions of HER and OER. Since the OER reaction involves multiple electron transfer processes, it is thermodynamically an uphill reaction (237 kJ mol⁻¹), which increases the kinetic difficulty and energy consumption of overall water splitting.^[1, 2] Precious metal catalysts, such as IrO₂ and

RuO₂, can reduce the OER overpotential, yet their scarcity and high cost hinder the large-scale application. [3, 4] Therefore, there is an urgent need to develop low-cost OER catalysts. Besides, direct seawater electrolysis producing hydrogen directly from seawater can solve the issue of water resources resulting from large-scale practical deployment of water electrolyzers heavily relying on freshwater. However, the efficiency of direct seawater electrolysis is mainly limited by the high thermodynamic energy barrier of water oxidation (1.23 V vs. RHE) and severe corrosion resulting from Cl⁻rich environment in seawater. Transition-metal-based NiFe-LDH catalysts have emerged as promising alternative electrocatalysts due to their earth-abundant composition and relatively low overpotential in alkaline media. Nevertheless, their seawater oxidation performance is still unsatisfactory and restricted by the slow transition of active species (Ni²⁺ to Ni³⁺/Ni⁴⁺), sluggish charge transfer, insufficient catalytic sites, and easy corrosion. [5-7] Modification strategies of element doping and interface engineering are usually adopted to optimize the electronic structure of active sites to modulate the adsorption/desorption behavior of OER intermediates to improve OER catalytic activity. In this chapter, NiFe-LDH catalysts are chosen as the research target. Li⁺ doping and g-C₃N₄/NiFe-LDH interface strategies are used to obtain novel NiFe-LDH-based electrocatalysts for seawater oxidation. The materials fabrication process is shown in **Figure 3.1**. Li-doped NiFe-LDH nanosheets (Li-NFL) were prepared using a chemical coprecipitation method, where LiCl and PDDA solution were used as the Li source and surfactant, respectively. The similar ionic radii of Li and Ni (0.76 Å for Li⁺ and 0.69 Å for Ni²⁺) enable Li ions to be doped into NiFe-LDH by occupying the sites of Ni atoms^[8, 9]. The as-synthesized Li-NFL was dispersed in an ethanol/water mixture and sonicated in the presence of 2D g-C₃N₄ nanosheets at various ratios to form 2D hybrids. The zeta potentials of Li-NFL and g-C₃N₄ are measured to be 19.84 and -3.85 mV, respectively (**Figure 3.2**), which indicates that these two nanosheets of opposite charges can be assembled through electrostatic attraction.

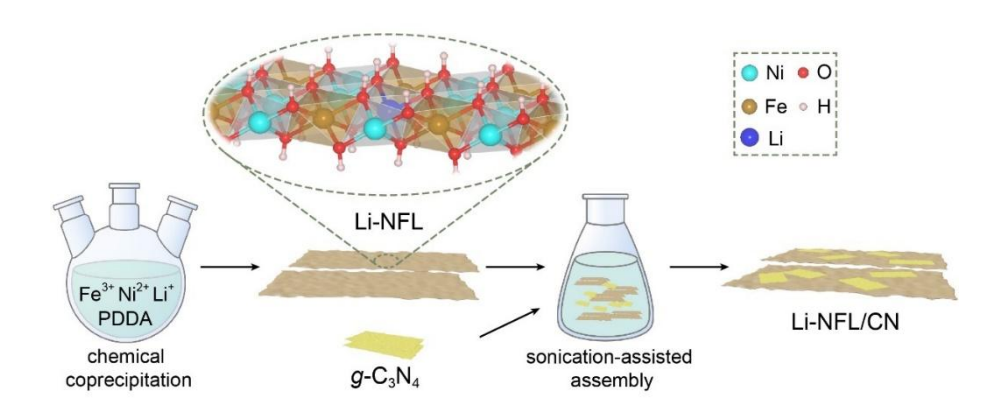


Figure 3.1. A schematic diagram showing the synthetic procedure of Li-NFL/CN. PDDA is poly(diallyldimethylammonium chloride).

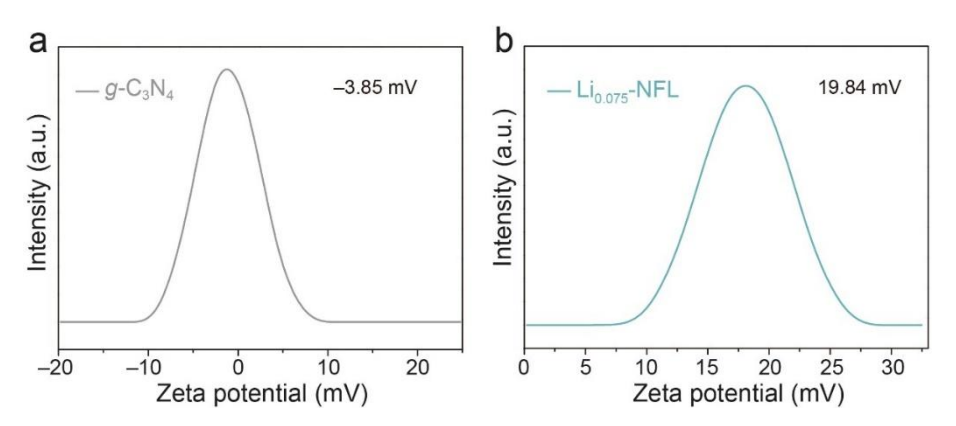


Figure 3.2. Zeta potentials of (a) 2D g-C₃N₄ and (b) Li_{0.075}-NFL.

The Li-NFL/CN achieves a current density of 100 mA cm⁻² at low overpotentials of 276 and 319 mV in 1 M KOH and 1 M KOH seawater, respectively, with high OER selectivity (FE = 96.7 %) and durability (100 h at 200 mA cm⁻²). Such excellent seawater oxidation can be ascribed to the synergistic effect of Li⁺ doping and heterointerface.

3.3. Experimental Section

3.3.1. Raw Materials

Iron nitrate nonahydrate (Fe(NO₃)₃·9H₂O, 99.9 %) nickel nitrate hexahydrate (Ni(NO₃)₂·6H₂O, 99.9 %), ethanol (EtOH, 99.8 %), and potassium hydroxide (KOH, 99.99 %) were purchased from Sigma–Aldrich. Sodium hydroxide (NaOH, AR), sodium chloride (NaCl, AR), lithium

chloride anhydrous (LiCl, 99 %), melamine (99 %), potassium iodide (KI, 99 %), and poly(diallyldimethylammonium chloride) solution (PDDA, 35 %) were provided from Shenzhen Dieckmann Tech. The aqueous solution was prepared using deionized (DI) water produced by MilliQ Water System. Natural seawater (pH ~8) was collected from Tsim Sha Tsui near the Hong Kong Polytechnic University, Kowloon, Hong Kong SAR, China. All chemicals were used as received.

3.3.2. Catalysts Synthesis

Synthesis of Li-doped NiFe-LDH nanosheets: Ni(NO₃)₂·6H₂O (0.75 mmol), Fe(NO₃)₃·9H₂O (0.25 mmol), and a pre-determined amount of LiCl were dissolved in deionized (DI) water (20 mL) and added to 10 vol.% PDDA aqueous solution (20 mL) under magnetic stirring at 80 °C. To this mixed solution, 0.25 M NaOH solution (10 mL) was added dropwise to obtain pH \approx 10. After 10 min of reaction, the product was collected by centrifugation and washed with DI water and ethanol several times. The as-prepared samples were kept in the gel state for subsequent use. Samples were denoted as Li_x-NFL, where *x* is the amount of LiCl used (x = 0, 0.05, 0.075, 0.10, and 0.15 mmol).

Synthesis of g- C_3N_4 nanosheets: Melamine (2 g) was put into a crucible with a cover and heated to 550 °C in a muffle furnace for 4 h at a heating rate of 2 °C min⁻¹. Subsequently, the assynthesized bulk g- C_3N_4 (0.5 g) was further calcined at 550 °C for 1 h with a heating rate of 5 °C min⁻¹. After cooling to room temperature, the product was heated at 550 °C (2 °C min⁻¹) for another 1 h to obtain 2D g- C_3N_4 powder.

Synthesis of Li-doped NiFe-LDH/CN composites: The as-prepared Li_{0.075}-NFL (15 mg) was dispersed in a mixed solvent of ethanol and DI water (1:1 vol. ratio, 3 mL) by sonicating for 30 min. To this suspension, a predetermined amount of *g*-C₃N₄ was added and sonicated for 60 min. A composite Li_{0.075}-NFL/CN was collected by centrifugation and kept in a wet state for

further use. Samples were denoted as $\text{Li}_{0.075}\text{-NFL/CN}_y$, where y indicates the weight ratio of g- C_3N_4 to $\text{Li}_{0.075}\text{-NFL}$ (y = 0.05, 0.1, 0.2, and 0.3 wt.%).

3.3.3. Electrochemical Performance Test

All electrochemical tests were carried out in a standard three-electrode configuration in 1.0 M KOH electrolyte using a graphite rod and a Hg/HgO electrode as the counter and reference electrodes, respectively. All data were collected by an electrochemical station (CHI760E). For OER experiments, homogeneous catalyst ink (5 mg mL⁻¹) was first prepared in an ethanolic solvent (1 mL, 1:1 mixture of EtOH and water) without the addition of binder or carbon conductor. Nickel foam was cleaned by sonication in acetone and washed with 3 M HCl for 10 min to remove the surface oxide layer. Catalyst ink (25 μL) was then pipetted onto a nickel foam (0.25 cm²) and used as the working electrode after the solvent was dried naturally. All potentials in this work were given against the reversible hydrogen electrode Before testing, the working electrode was stabilized by 90 CV cycles in the potential range between 1.124 and 1.624 V. LSV was carried out from 1.2 to 1.8 V (vs. RHE) at a scan rate of 5 mV s⁻¹. All polarization curves were corrected by 85 % iR compensation for ohmic losses.

3.4. Results and Discussion

3.4.1. Structure Characterization

The XRD patterns of pristine NiFe-LDH and 2D g-C₃N₄ exhibit characteristic peaks of hydrotalcite-like LDH (JCPDS: 40-0215) and typical C₃N₄ of a layered graphitic structure (**Figure 3.3a**). No significant peak shift or appearance of new peaks is observed from Li-NFL after introducing Li-ion (**Figure 3.3b**), which is likely due to the relatively low Li contents. Notably, the peak corresponding to g-C₃N₄ can be detected at 28.1° in Li-NFL/CN_{0.2} (**Figure 3.4a**), confirming the existence of g-C₃N₄ in the hybrid. Similarly, the Raman spectrum of Li-NFL exhibits no discernable change from that of pristine NiFe-LDH (**Figure 3.4b**), whereas a new peak at 708 cm⁻¹ attributed to the breathing mode of g-C₃N₄ appears from the Li-NFL/CN

(**Figure 3.5b**)^[10]. This peak intensifies with the amount of g-C₃N₄ used, indicating the successful incorporation of g-C₃N₄ onto the Li-NFL. The modification of Li-NFL by g-C₃N₄ exerts no apparent influence on the XRD and Raman peaks of Li-NFL.

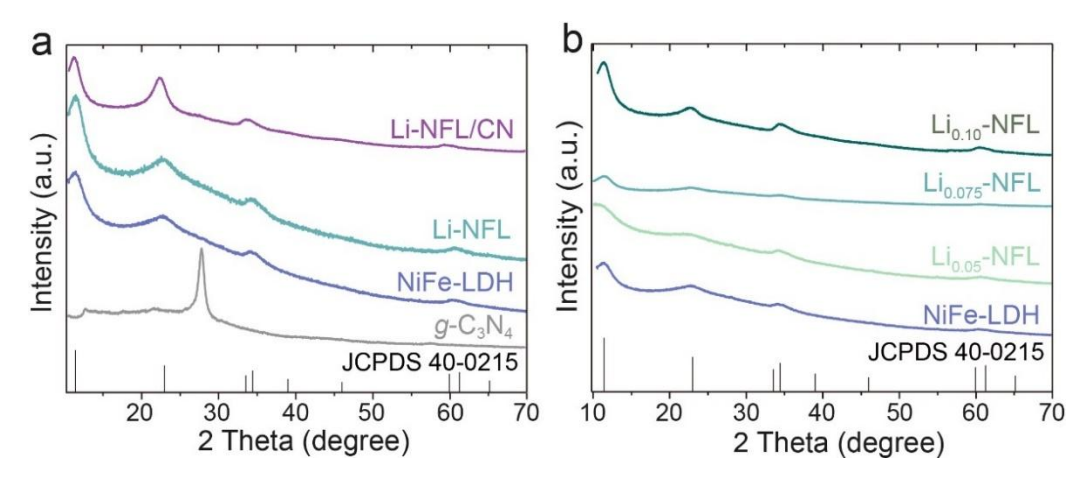


Figure 3.3. (a) XRD patterns of NiFe-LDH, Li-NFL, g-C₃N₄, and Li-NFL/CN. (b) XRD patterns of (a) Li_x-NFL prepared with various Li doses. The x in the sample names indicates the Li dose.

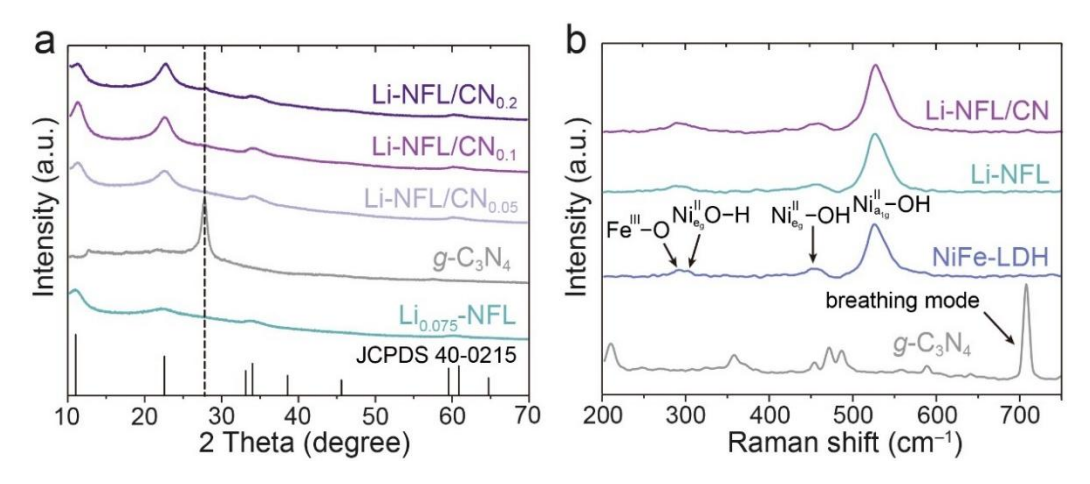


Figure 3.4. (a) XRD patterns of Li-NFL/CN_y samples of various g-C₃N₄-to-Li_{0.075}-NFL ratios. The y in the sample names indicates the weight ratio g-C₃N₄ to Li_{0.075}-NFL. (b) Raman spectra of NiFe-LDH, Li-NFL, g-C₃N₄, and Li-NFL/CN.

A typical TEM image of the as-synthesized NiFe-LDH reveals a thin layer structure (**Figure 3.6a**). An interplanar spacing of 2.3 Å is observed from the high-resolution TEM

image (**Figure 3.6b**) and assigned to the (015) plane of NiFe-LDH. The morphology and lattice fringe of Li-NFL appear similar to those of NiFe-LDH, indicating that incorporating Li ions does not significantly alter the structure (**Figure 3.6c** and **d**). The TEM images of Li-NFL/CN in **Figure 3.6f** display two distinct regions of crystalline NiFe-LDH and amorphous g-C₃N₄, confirming the 2D/2D heterostructure of Li-NFL and g-C₃N₄ composite.

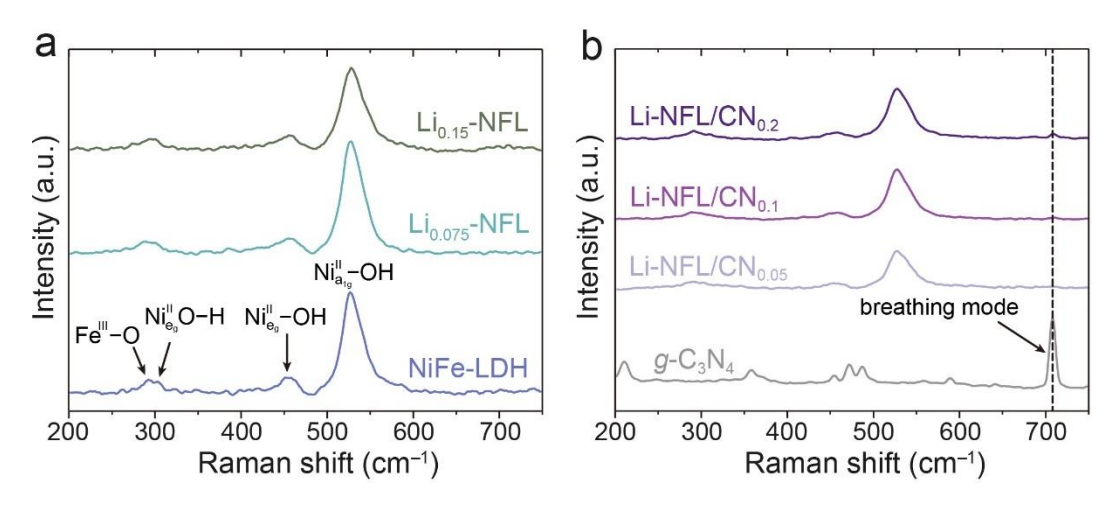


Figure 3.5. Raman spectra of (a) Li_x -NFL prepared with various Li doses and (b) L-NFL/CN_y samples of various g-C₃N₄-to-Li_{0.075}-NFL ratios.

X-ray photoelectron spectroscopy (XPS) was employed to investigate the changes in chemical composition and surface electronic states in the doped and hybrid samples. The survey XPS spectra of pristine NiFe-LDH, Li-NFL, and Li-NFL/CN confirm the presence of Ni, Fe, and O elements in all samples (**Figure 3.7a**). **Figure 3.7b** shows the high-resolution Ni 2*p* spectrum of pristine NiFe-LDH, where two pairs of Ni 2*p*_{3/2} peaks (855.7 and 873.5 eV) and Ni 2*p*_{1/2} peaks (857.1 and 874.9 eV) can be assigned to Ni²⁺ and Ni³⁺ species, respectively. Two satellite peaks at 861.6 and 879.8 eV are ascribed to Ni²⁺ species^[11, 12]. Interestingly, the Ni³⁺/Ni²⁺ peak ratio of the NiFe-LDH (0.59) is increased to 1.10 in Li-NFL, indicating partial electron transfer from Ni²⁺ to Li⁺. The increased Ni³⁺ species could facilitate the formation of NiOOH species, thus accelerating the OER process^[13]. During seawater electrolysis, Cl⁻ ion adsorption onto OER catalysts can compete with OH⁻ ions and cause catalyst corrosion^[14, 15]. According to Pearson's hard and soft acid-base (HSAB) principle, harder acids preferentially

bind to harder bases and *vice versa*^[16, 17]. Because Li⁺ is a harder Lewis acid than Ni²⁺ while OH⁻ is a harder base than Cl^{-[17, 18]}, OH⁻ ions, rather than Cl⁻ ions, would preferentially adsorb onto Li-NFL/CN. This preferential adsorption would contribute to the OER activity and stability of Li-NFL/CN in seawater.

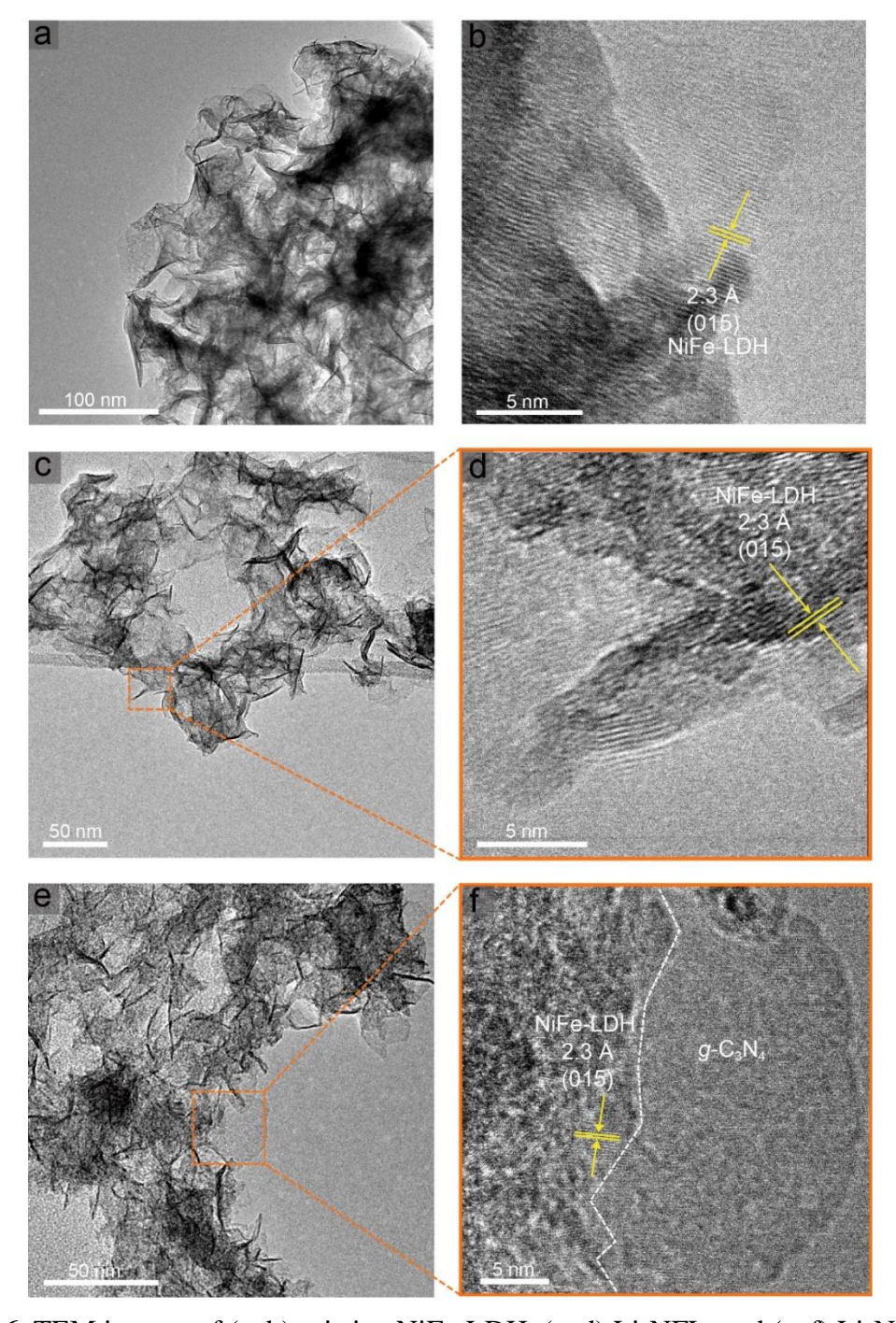


Figure 3.6. TEM images of (a, b) pristine NiFe-LDH, (c, d) Li-NFL, and (e, f) Li-NFL/CN.

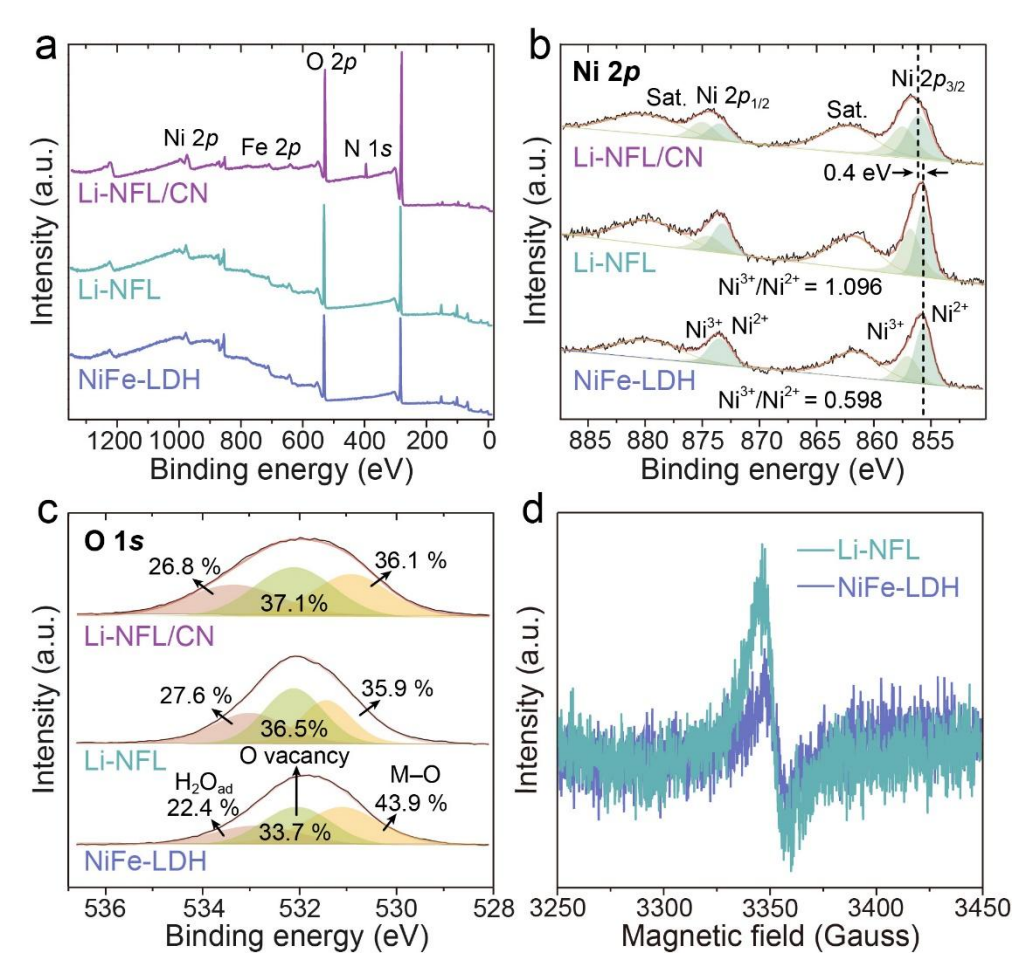


Figure 3.7. (a) XPS survey spectra and (b) High-resolution Ni 2*p* spectra of NiFe-LDH, Li-NFL, and Li-NFL/CN. (c) High-resolution O 1*s* spectra of NiFe-LDH, Li-NFL, and Li-NFL/CN. (d) EPR spectra of pristine NiFe-LDH and Li-NFL.

The high-resolution O 1*s* spectra of three samples are compared in **Figure 3.7c**. The O 1*s* spectrum of NiFe-LDH is deconvoluted into three peaks at 531.1, 532.1, and 532.9 eV, which correspond to the metal—O bond, O defect, and the hydroxyl species of adsorbed water, respectively^[19]. The oxygen defect contents in Li-NFL/CN (37.1 %) and Li-NFL (36.5 %) are higher than in NiFe-LDH (33.7 %). This increase in oxygen defect contents is caused by charge compensation to make the system charge-neutral when Ni²⁺ is replaced by Li⁺ of a lower valence state^[20,21]. The increased oxygen defects may enhance the conductivity [22, 23]. These observations are validated by EPR spectroscopy, which indicates the existence of more oxygen vacancies in Li-NFL than NiFe-LDH as shown by a stronger signal centered at the *g* value of 2.001 (**Figure 3.7d**)^[24]. Moreover, the deconvoluted peaks for the hydroxyl species in Li-NFL

and Li-NFL/CN are much stronger than that in NiFe-LDH, which suggests that more water molecules are adsorbed on the Li-doped sample surfaces. This increased water molecule adsorption can accelerate the mass transfer on the surfaces of Li-NFL and Li-NFL/CN due to more favorable contact between OH⁻ and active sites.

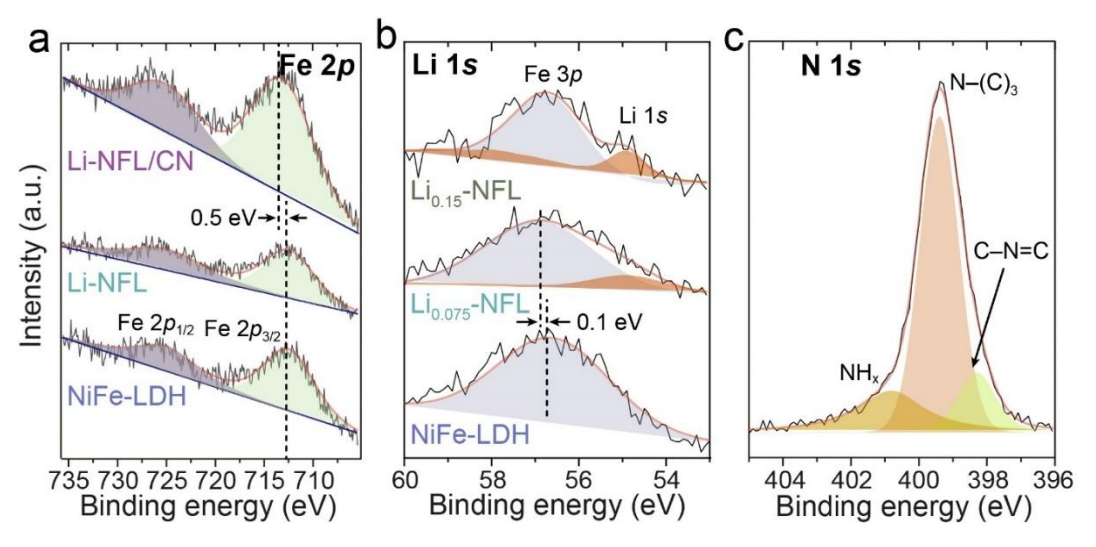


Figure 3.8. (a) High-resolution Fe 2*p* spectra of NiFe-LDH, Li-NFL, and Li-NFL/CN. (b) High-resolution Li 1*s* spectra of NiFe-LDH, Li_{0.075}-NFL, and Li_{0.15}-NFL.

Figure 3.8a compares the Fe 2p XPS spectra of NiFe-LDH, Li-NFL, and Li-NFL/CN. Notably, the Fe $2p_{3/2}$ peak of Li-NFL/CN is positively shifted by 0.5 eV compared with those of NiFe-LDH and Li-NFL. A similar shift (0.4 eV) is observed in the Ni 2p region upon the Li-NFL hybridization with g-C₃N₄ (**Figure 3.7b**). These peak shifts imply reduced electron density around Ni and Fe sites, which is caused by charge migration at the interface between Li-NFL and g-C₃N₄^[25]. The Li-doping also affects the electronic configuration of NiFe-LDH. The pristine NiFe-LDH shows a Fe 3p peak at 56.7 eV (**Figure 3.8b**), which shifts to a higher binding energy (56.8 eV) upon Li-doping. Meanwhile, the Li 1s peak is observed at 54.9 eV^[26]. Inductively coupled plasma optical emission spectroscopy (ICP-OES) confirms successful Li doping into NiFe-LDH, with Li content in Li-NFL increasing from 0.077 to 0.172 at.% when the amount of LiCl is doubled from 0.075 to 0.15 mmol (**Table 3.1**). In the N 1s region (**Figure**

3.8c), three peaks at 398.3, 399.4, and 400.8 eV are identified from g-C₃N₄, which are attributed to C–N=C, N–(C)₃, and NH_x, respectively. [27, 28]

Table 3.1 . ICP-OES an	alysis data	of metals in	the as-prepared	catalysts.
-------------------------------	-------------	--------------	-----------------	------------

Sample	Element o	Element content ($\mu mol\ mL^{-1}$)			
	Li	Fe	Ni	Li/(Li+Ni+Fe)	
NiFe-LDH	/	2.845	9.165	0	
Li _{0.05} -NFL	0.0085	2.861	9.221	0.00070	
Lio.075-NFL	0.0094	2.893	9.316	0.00077	
Li _{0.1} -NFL	0.0128	2.876	9.083	0.00107	
Li _{0.15} -NFL	0.0200	2.764	8.828	0.00172	

The charge concentration can be evaluated using the Mott–Schottky plots obtained by measuring the capacitance at various applied potentials in 0.2 M Na₂SO₄^[29]. As shown in **Figure 3.9**, the carrier density of Li-NFL/CN ($4.22 \times 10^{20} \text{ cm}^{-3}$) is 1.4 and 8 times higher than those of Li-NFL ($3.04 \times 10^{20} \text{ cm}^{-3}$) and NiFe-LDH ($5.25 \times 10^{19} \text{ cm}^{-3}$), respectively. This increase in the electron population originates from the Li dopant and the interface between Li-NFL and g-C₃N₄, as evidenced by XPS peak shifts.

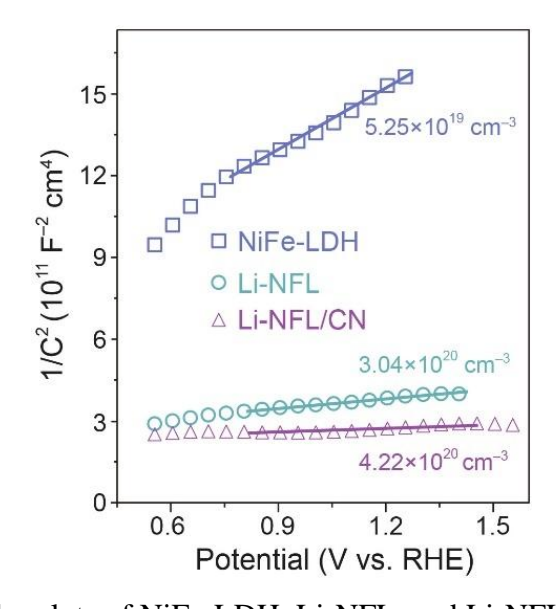


Figure 3.9. Mott–Schottky plots of NiFe-LDH, Li-NFL, and Li-NFL/CN.

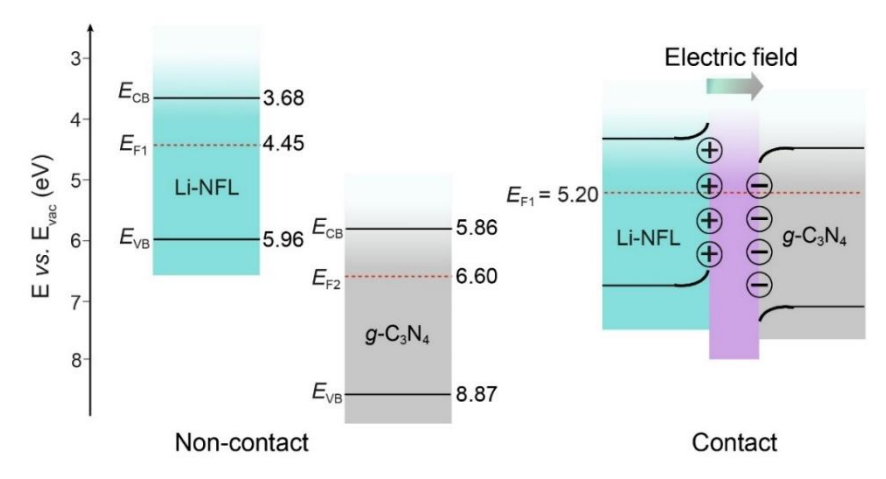


Figure 3.10. Formation of a built-in electric field at the interface of Li-NFL and g-C₃N₄. E_{CB} and E_{VB} are conduction and valence band energies, respectively.

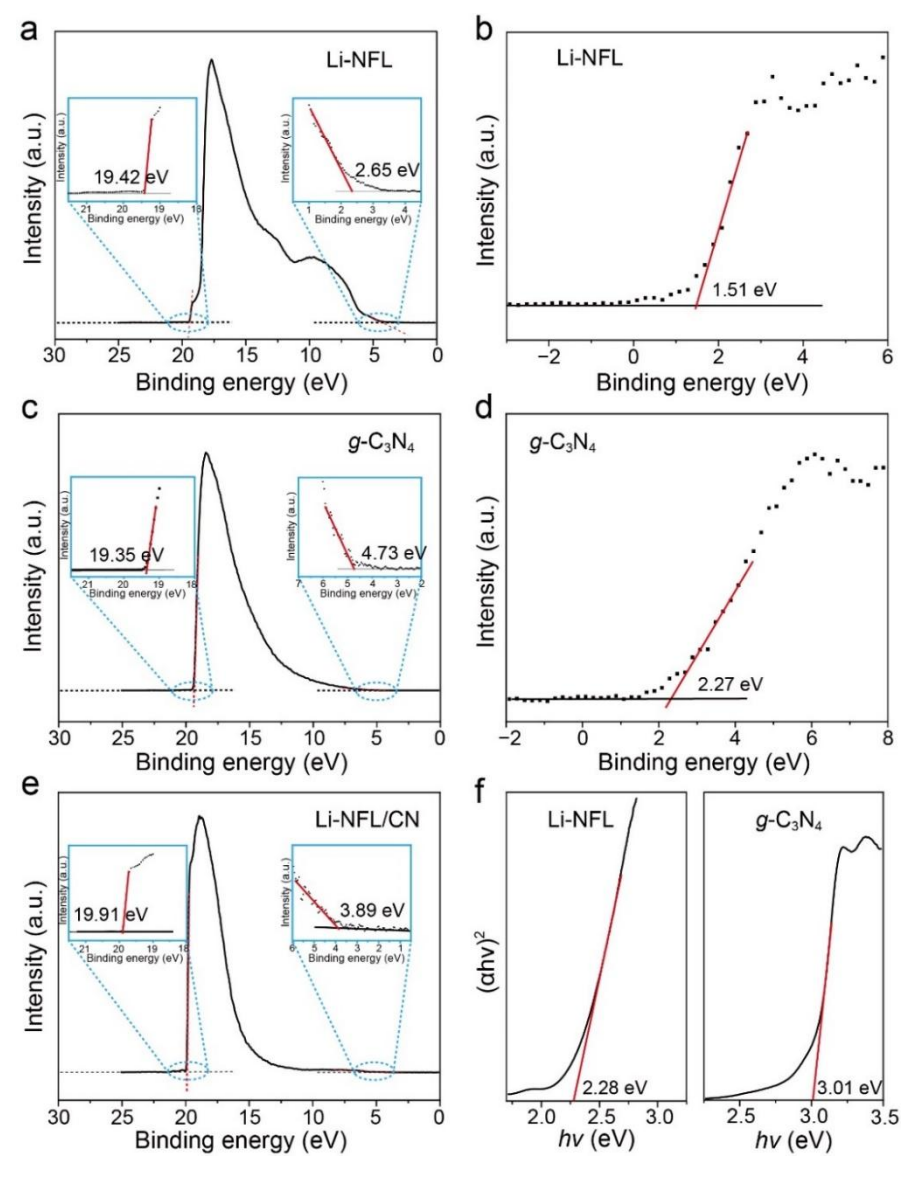


Figure 3.11. UPS spectra of (a) Li-NFL, (c) *g*-C₃N₄, and (e) Li-NFL/CN. VB-XPS spectra of (b) Li-NFL and (d) *g*-C₃N₄. (f) Tauc plots of Li-NFL and *g*-C₃N₄.

The band structure of Li-NFL and g-C₃N₄ before and after contact are illustrated in **Figure 3.10**. Furthermore, the work functions (Φ) of Li-NFL, g-C₃N₄, and Li-NFL/CN were determined by UPS (**Figures 3.11**)^[30]. In detail, Conduction band energy (E_{CB}), valence band energy (E_{VB}), and work function (Φ) can be determined using UPS and XPS-VB spectra. Specifically, UPS spectra of Li-NFL, g-C₃N₄ and Li-NFL/CN were collected using a Helium I α as the ultraviolet source (hv = 21.22 eV)^[31, 32] and used to determine their work functions according to the following equation:

$$\Phi = hv - E_{\text{cutoff}} + E_{\text{F}} \tag{3.1}$$

where E_{cutoff} and E_{F} are the binding energies of secondary electron cutoff edge and Fermi level edge, respectively. **Figures 3.11a**, **3.11c**, and **3.11e** indicate that the E_{cutoff} and E_{F} of Li-NFL are 19.42 and 2.65 eV, respectively, and thus the work function of Li-NFL was determined to be 4.45 eV. The valence band maximum (VBM) of Li-NFL was estimated using XPS-VB spectrum. The energy gap between the Fermi level and VBM is 1.51 eV (**Figure 3.11b**)^[33, 34]. Therefore, the energy level of VBM in Li-NFL is calculated to be 5.96 eV. Similarly, the UPS and XPS-VB spectra of g-C₃N₄ shown in **Figure 3.11c** and **3.11d** were used to determine Φ and VBM relative to the vacuum level as 6.60 and 8.87 eV, respectively. The Φ of Li-NFL/CN relative to the vacuum level was calculated to be 5.20 eV (**Figure 3.11e**). Bandgap energy (E_g) can be calculated according to the Tauc plots. As shown in **Figure 3.11f**, the corresponding E_g values of Li-NFL and g-C₃N₄ were determined to be 2.28 and 3.01 eV, respectively. Subsequently, the E_{CB} values of Li-NFL and g-C₃N₄ were calculated as 3.68 and 5.86 eV according to the following equation:

$$E_{\rm CB} = E_{\rm VB} - E_{\rm g} \tag{3.2}$$

The work function of Li-NFL (4.45 eV) is smaller than that of g-C₃N₄ (6.60 eV), which suggests that electrons spontaneously migrate from Li-NFL to g-C₃N₄ when the interface is formed, narrowing the gap of their Fermi levels (E_F). As a result, a built-in electric field is

formed as the Fermi levels reach an equilibrium and the charge is redistributed at the interface, which is in good agreement with XPS results. The *g*-C₃N₄ accepts electrons and gets negatively charged while the surface of Li-NFL becomes electrophilic. The positively charged Li-NFL can further attract electron-rich OH⁻, which is expected to accelerate the catalytic kinetics.

3.4.2. Electrochemical Performance

The OER activity of the as-prepared samples was accessed in O₂-saturated 1 M KOH using a standard three-electrode cell. **Figure 3.12a** compares the LSVs collected at a scan rate of 5 mV s⁻¹. Li-NFL/CN requires an overpotential of 276 mV to reach 100 mA cm⁻², which is significantly lower than *g*-C₃N₄ (507 mV), NiFe-LDH (340 mV), Li-NFL (299 mV), and commercial RuO₂ (414 mV, **Figure 3.12b**). The Tafel plots obtained from the polarization curves reveal that Li-NFL/CN has the lowest Tafel slope (51.5 mV dec⁻¹) among all samples investigated (**Figure 3.12c**). A series of Li-NFL and Li-NFL/CN samples were prepared to optimize the Li-doping level and the ratio between Li-NFL and *g*-C₃N₄ (**Figure 3.13a** and **3.13b**).

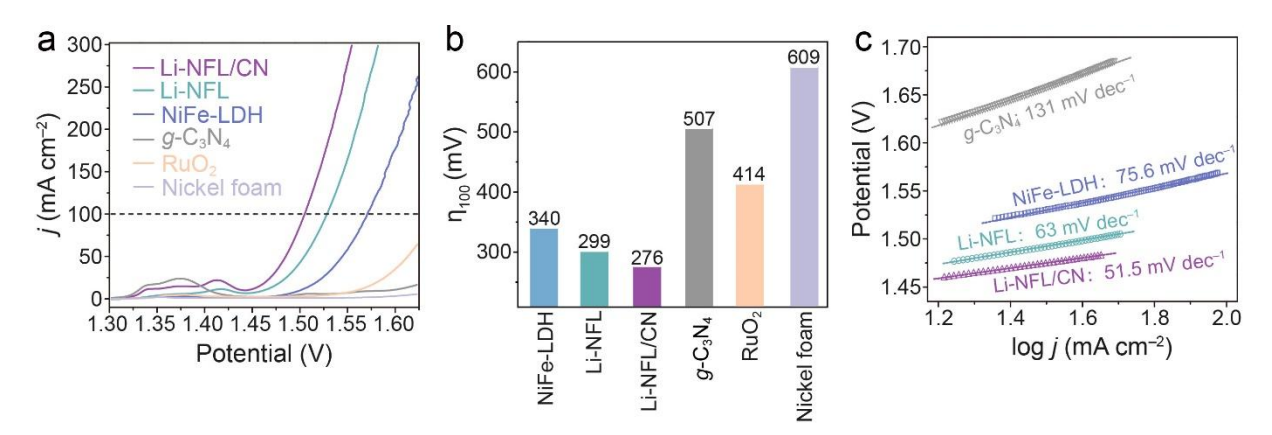


Figure 3.12. (a) LSV curves and (b) the corresponding overpotentials of NiFe-LDH, Li-NFL, Li-NFL/CN, *g*-C₃N₄, RuO₂, and nickel foam. (c) Tafel slopes of NiFe-LDH, Li-NFL, Li-NFL/CN, and *g*-C₃N₄.

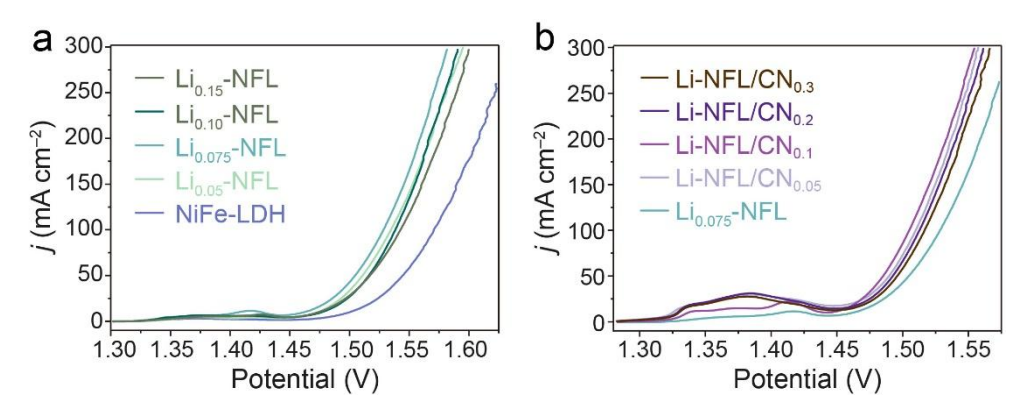


Figure 3.13. LSV curves of (a) Li-NFL prepared with various Li doses and (b) Li-NFL/CN samples of various *g*-C₃N₄-to-Li_{0.075}-NFL ratios.

As shown in **Figure 3.14**, the lowest OER overpotential and Tafel slope are obtained when the Li dopant is ca. 0.077 at.% and the g-C₃N₄-to-Li-NFL weight ratio is ca. 0.001 (0.1 wt.%). It is worth noting that both NiFe-LDH and Li-NFL/CN have almost identical Fe/Ni ratio (**Table 3.2**), which excludes its impact on OER performance. The deteriorated OER activity of the samples with higher amounts of Li dopant and g-C₃N₄ could be ascribed to worse conductivity (**Figure 3.15**).

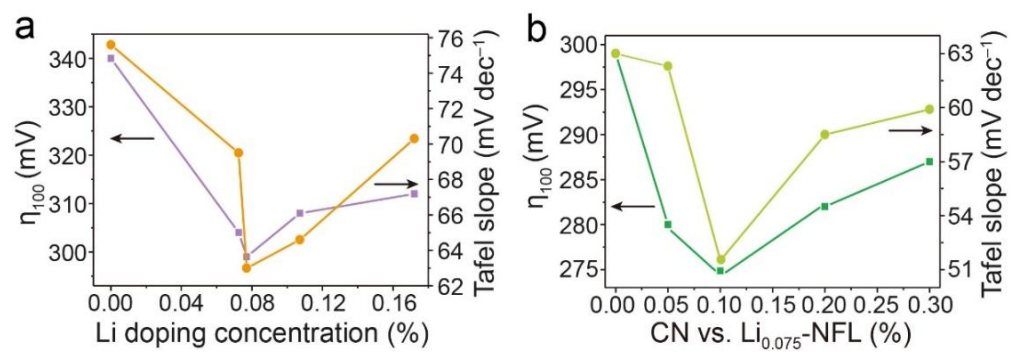


Figure 3.14. Comparisons of overpotentials and Tafel slopes with various doses of (a) Li doping and (b) g-C₃N₄.

Table 3.2. ICP-OES analysis data of metals in NiFe-LDH and Li-NFL/CN.

Sample	Element co	Atomic ratio		
Sumple	Li	Fe	Ni	Fe/Ni
NiFe-LDH	/	2.845	9.165	0.310
Li-NFL/CN	0.00942	2.893	9.316	0.311

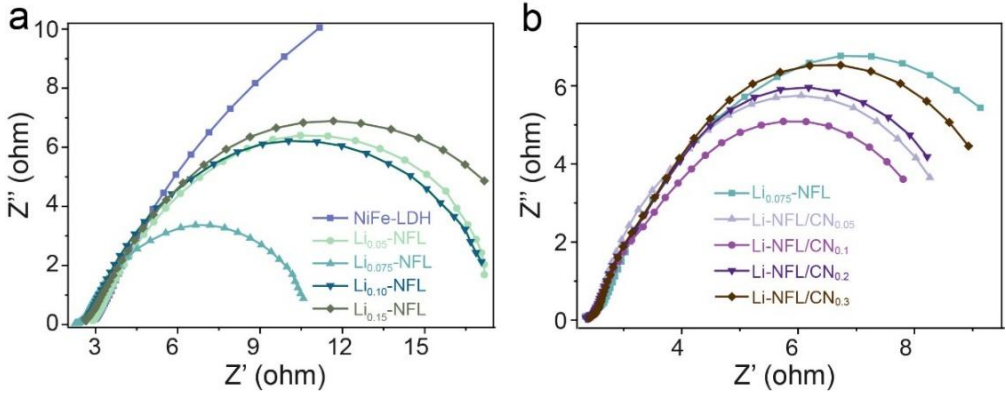


Figure 3.15. Nyquist plots of (a) Li-NFL prepared with various Li doses and (b) Li-NFL/CN samples of various *g*-C₃N₄-to-Li_{0.075}-NFL ratios.

3.4.3. Seawater Oxidation Performance

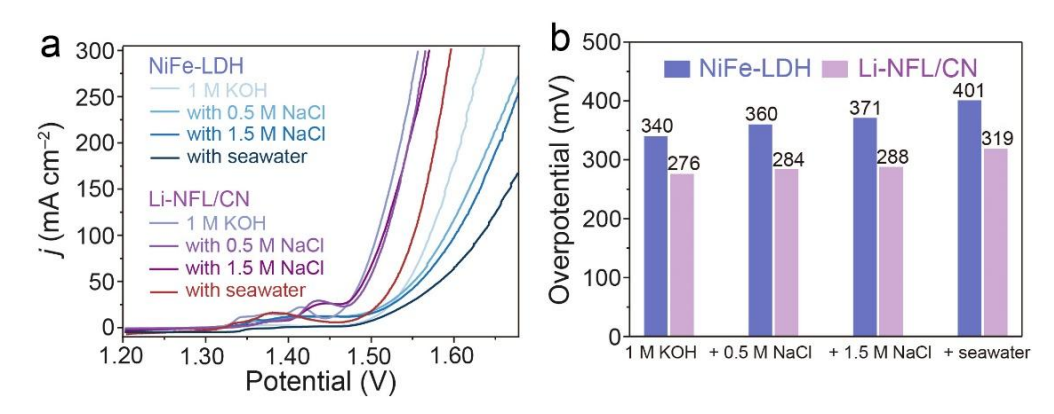


Figure 3.16. (a) LSV curves of NiFe-LDH and Li-NFL/CN in saline water of various NaCl concentrations and seawater. (b) Comparison of overpotentials of NiFe-LDH and Li-NFL/CN at 100 mA cm⁻² in various electrolytes.

The OER activity of NiFe-LDH-based samples was further evaluated in saline and alkaline natural-seawater electrolytes to investigate their potential in seawater electrolysis application. Li-NFL/CN delivers superior OER performance with little activity decline in saline water electrolytes (**Figure 3.16a** and **3.16b**), indicating that the influence of highly concentrated Cl⁻ ions on its catalytic activity is not significant. The deterioration of OER activity is obvious in the alkaline natural-seawater electrolyte (seawater + 1 M KOH), which can be ascribed to the bacteria, microbes, and insoluble precipitates formed during the seawater OER process^[35]. Li-NFL/CN electrode requires only 319 and 401 mV to reach the current densities of 100 and 200

mA cm⁻², respectively, which are far below the theoretical overpotential required to trigger the CER (480 mV)^[36].

More importantly, the Li-NFL/CN electrode exhibits a very high average FE of 96.7 % at a large current density of 200 mA cm⁻² in alkaline seawater electrolyte (**Figure 3.17**). We engaged iodide titration to detect the generation of reactive chlorine species^[14]. As shown in **Figure 3.18**, no typical absorption peak of hypochlorite ions is observed in the electrolyte after the FE test, indicating the catalyst's high selectivity for OER over the hypochlorite reaction.

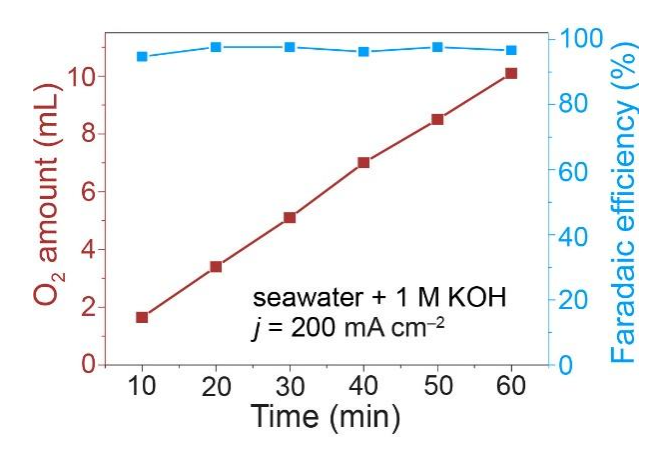


Figure 3.17. FE (blue squares) of Li-NFL/CN measured at 200 mA cm⁻² in seawater + 1 M KOH. Red squares show the amount of O₂ generated during the FE test.

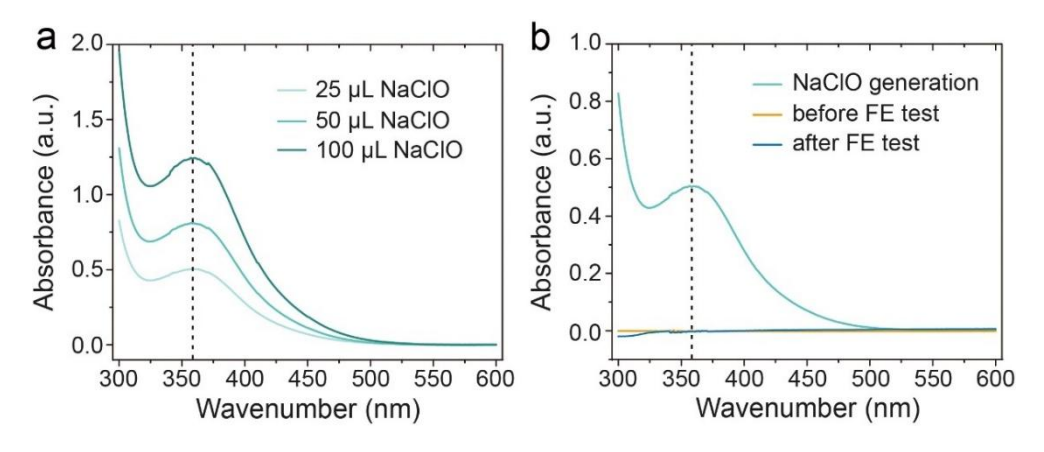


Figure 3.18. UV–vis spectra of (a) iodide titration with various NaClO concentrations and (b) electrolytes before and after the FE test.

The operational stability is another crucial parameter for the electrocatalyst, especially in saline water electrolysis. The accelerated degradation test and long-term chronopotentiometry

were performed to evaluate the electrocatalytic durability of Li-NFL during OER. In a continuous 25-h saline water electrolysis at a constant current density of 200 mA cm⁻², Li-NFL/CN exhibits stable OER activities with a slight increase (26 mV) in overpotential. This is in contrast to the case of NiFe-LDH, where the required overpotential increases by 67 mV (**Figure 3.19**). The OER activity of Li-NFL/CN remains almost the same after 1,000 CV cycles in both alkaline and saline-water electrolytes (**Figure 3.20**). Impressively, Li-NFL/CN shows excellent stability at a current density of 200 mA cm⁻² in natural seawater + 1 M KOH over 100 h (**Figure 3.21**).

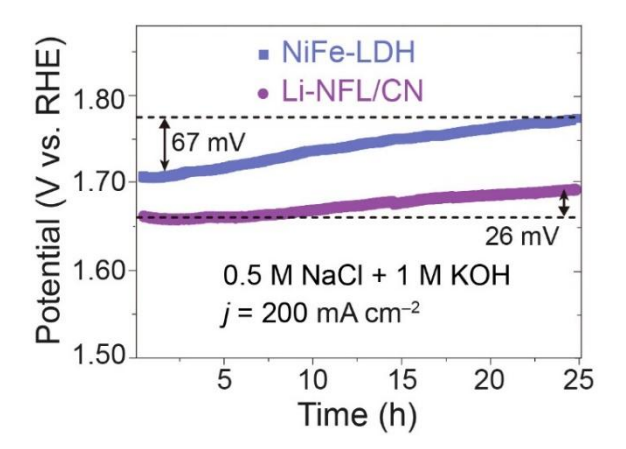


Figure 3.19. Chronopotentiometric curves of NiFe-LDH and Li-NFL/CN in saline water (0.5 M NaCl + 1 M KOH).

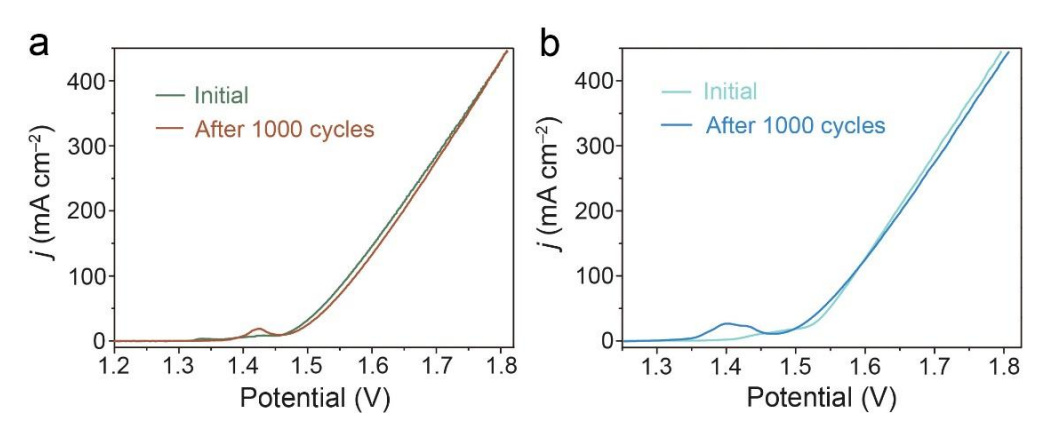


Figure 3.20. LSV curves of Li-NFL/CN before and after 1,000 CV cycles in (a) alkaline and (b) saline-water electrolytes.

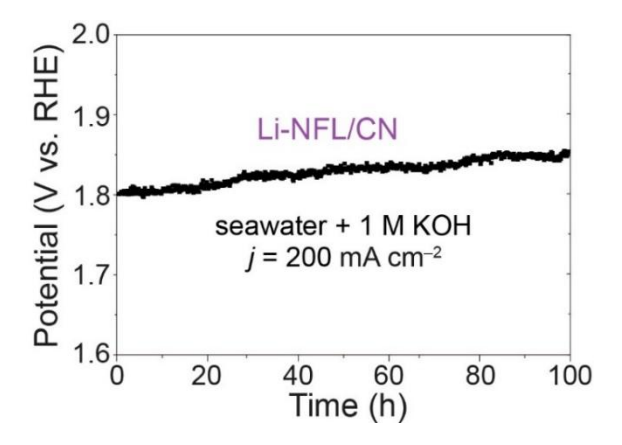


Figure 3.21. The chronopotentiometric curve of Li-NFL/CN in seawater + 1 M KOH.

3.4.4. OER and Anti-corrosion Mechanisms

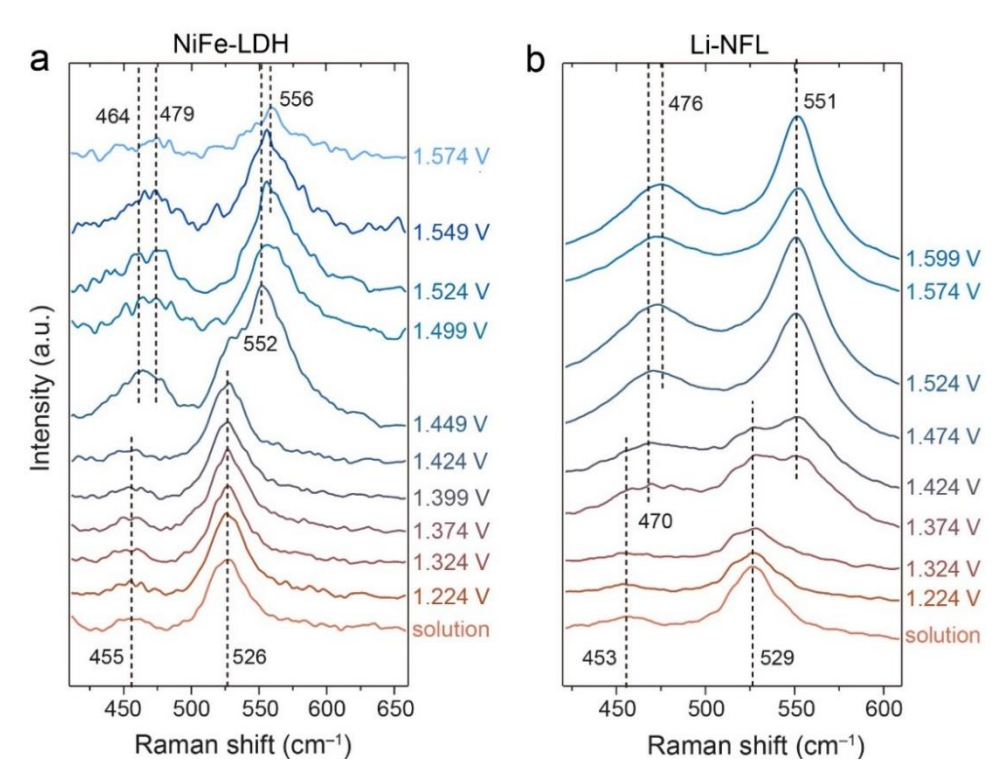


Figure 3.22. In situ Raman spectra of (a) NiFe-LDH and (b) Li-NFL.

To better understand the mechanism of OER catalysis by Li-NFL, *in situ* Raman spectroscopy was employed to monitor the surface species as the applied potential varies in real time. **Figure 3.22a** shows the *in situ* Raman spectra of NiFe-LDH collected between the open-circuit potential and applied potential of 1.574 V (*vs.* RHE). At the open-circuit potential, two characteristic peaks of the Ni^{II}–OH and Ni^{II}–O vibrations are observed at 455 and 526 cm⁻¹, respectively^[37]. As the applied potential approaches 1.449 V, two peaks appear at 464 and 552

cm⁻¹ and intensify with potential, which is assigned to the e_g bending and A_{1g} stretching vibrations of the Ni^{III}–O species in NiOOH, respectively^[38]. A similar LDH-to-NiOOH transition is observed from Li-NFL, but at a lower potential of 1.374 V (**Figure 3.22b**), indicating that the oxidation of Ni²⁺ to Ni³⁺ is accelerated. This is due to the Li doping that induces more surface Ni³⁺ species and oxygen vacancy.

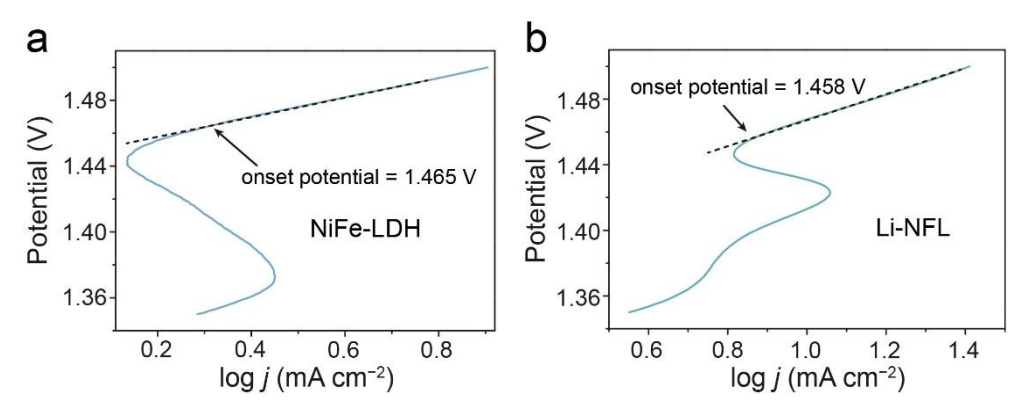


Figure 3.23. Onset potentials of (a) NiFe-LDH and (b) Li-NFL.

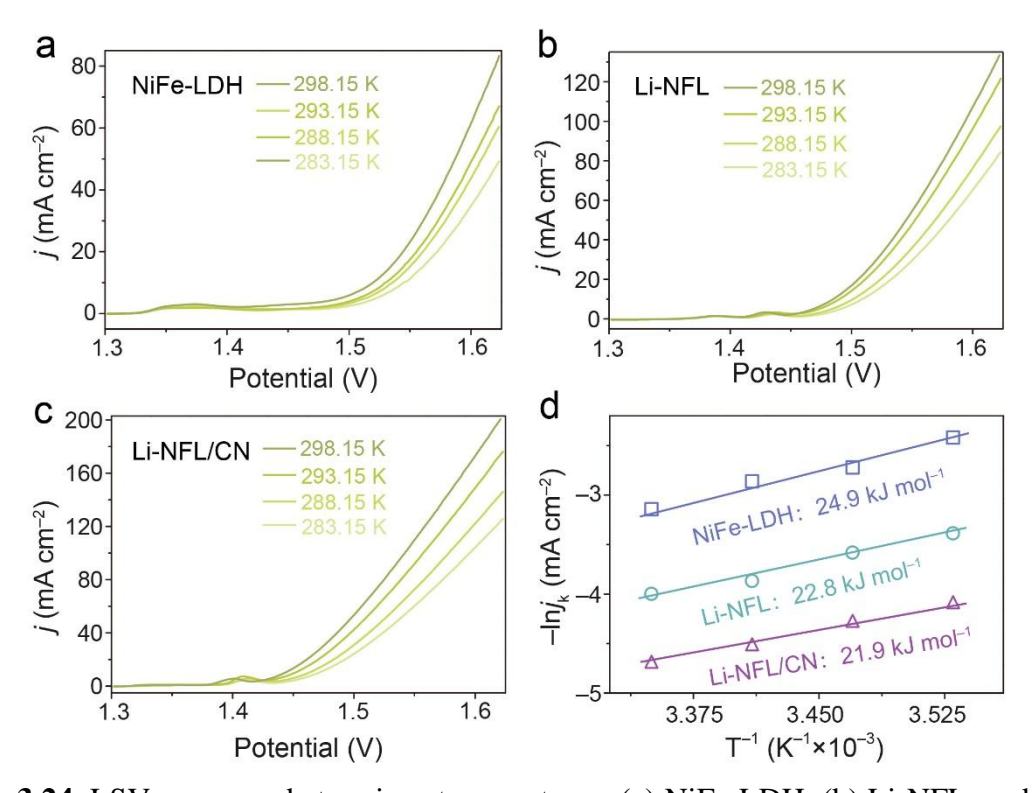


Figure 3.24. LSVs measured at various temperatures: (a) NiFe-LDH, (b) Li-NFL, and (c) Li-NFL/CN. (d) Corresponding Arrhenius plots.

Such facilitated transition to NiOOH is beneficial to the subsequent elementary steps of the OER, as manifested by the lowered onset potential of Li-NFL (1.458 V) compared with pristine NiFe-LDH (1.465 V, **Figure 3.23a** and **3.23b**).

Figure 3.24a compares the Arrhenius plots of NiFe-LDH, Li-NFL, and Li-NFL/CN, which are obtained by measuring LSVs at various temperatures (**Figure 3.24b**– **3.24d**). The activation energy (E_a) extracted from the slope of the Arrhenius plot is the lowest for Li-NFL/CN (21.9 kJ mol⁻¹), followed by Li-NFL (22.8 kJ mol⁻¹) and NiFe-LDH (24.9 kJ mol⁻¹). These results suggest that the Li-NFL/CN has the smallest kinetic barrier for electrocatalytic water oxidation.

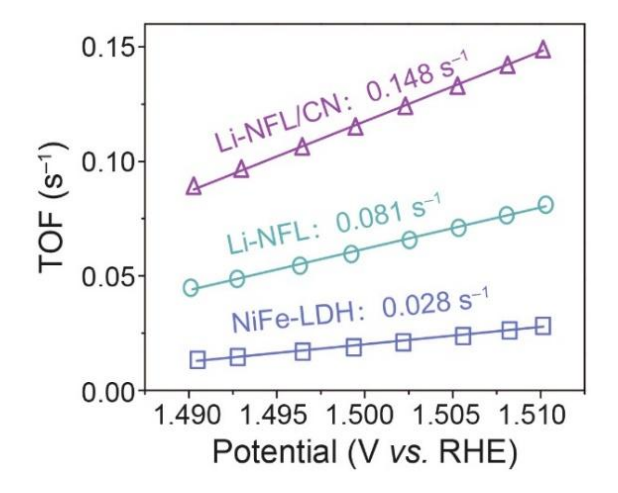


Figure 3.25. TOF plots of NiFe-LDH, Li-NFL, and Li-NFL/CN.

TOF is another important parameter for evaluating the intrinsic activity of electrocatalysts. Li-NFL/CN demonstrates a high TOF value of $0.148 \,\mathrm{s^{-1}}$, which is about 5 times that of NiFe-LDH ($0.028 \,\mathrm{s^{-1}}$), as shown in **Figure 3.25**. Electrochemical surface areas (ECSAs) of the asprepared catalysts were also determined by electrochemical $C_{\rm dl}$ (**Figure 3.26a-c**) and compared in **Figure 3.26d** and **Figure 3.27a**. Li-NFL/CN exhibits the highest $C_{\rm dl}$ value of $2.56 \,\mathrm{mF \, cm^{-2}}$, which is ca. 1.5 times that of NiFe-LDH. These results indicate that Li-doping and the hybridization with g-C₃N₄ not only increase the OER active sites but also enhance the intrinsic catalytic activity by optimizing the electronic configuration. EIS was carried out to understand the charge transfer process, and the corresponding Nyquist plots are given in **Fig. 3.27b**. The

charge transfer resistance (R_{ct}) of NiFe-LDH (29.24 Ω) is considerably reduced to 7.35 Ω by Li-doping (Li-NFL), which is further diminished to 5.93 Ω by the interface formation with g-C₃N₄ (Li-NFL/CN), demonstrating the effective synergistic effects in lowing the charge transfer barrier.

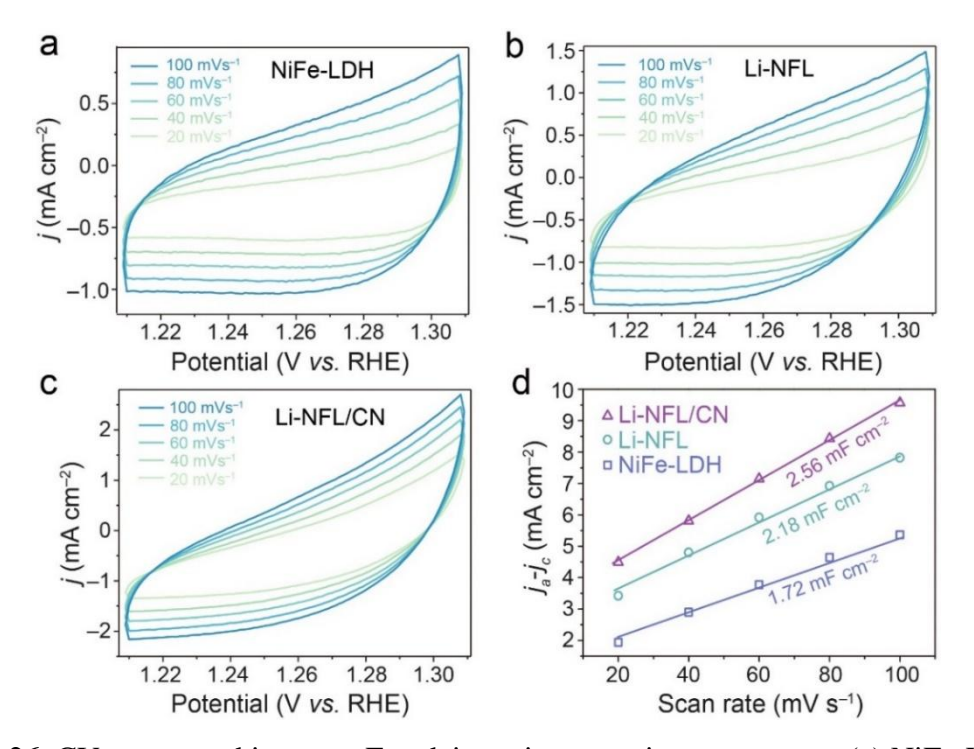


Figure 3.26. CVs measured in a non-Faradaic region at various scan rates. (a) NiFe-LDH, (b) Li-NFL, (c) Li-NFL/CN, and (d) double-layer capacitances.

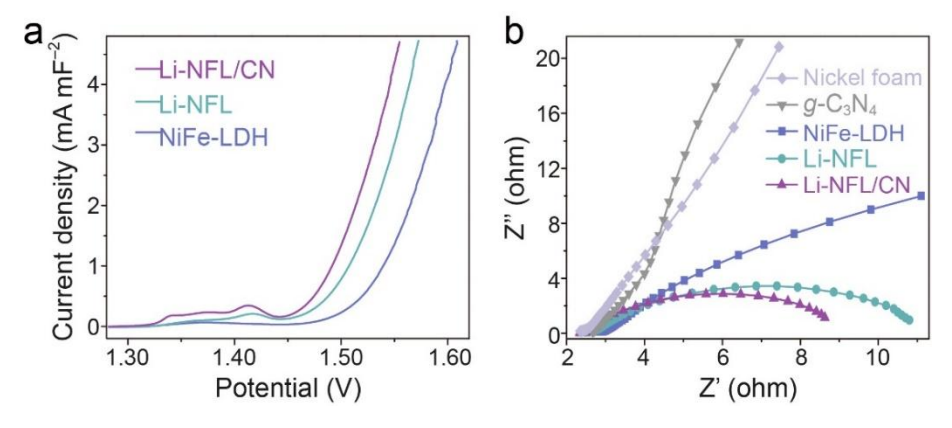


Figure 3.27. (a) Electrochemical surface area (ECSA)-normalized LSV curves of NiFe-LDH, Li-NFL, and Li-NFL/CN. (b) Nyquist plots of NiFe-LDH, Li-NFL, Li-NFL/CN, *g*-C₃N₄, and nickel foam.

From Raman spectroscopic characterization of Li-NFL/CN (**Figure 3.28a**), three new bands at 490, 549, and 565 cm⁻¹, which are attributed to NiOOH, are observed after the stability test in alkaline seawater^[39, 40]. This clearly indicates the surface reconstruction of Li-NFL/CN during the OER process, and the reduced peak intensities suggests poorer crystallinity. Nonetheless, the ultrathin layer structure of Li-NFL/CN is maintained during seawater electrolysis (**Figure 3.28b**). A high-resolution TEM image after the OER test discloses two interplanar spacings of 2.3 and 2.4 Å, assigned to the (015) plane of NiFe-LDH and the (011) plane of NiOOH, respectively, with considerable amorphous domains (dashed circle, **Figure 3.28c**), which is consistent with Raman results. The elemental analyses conducted by EDS show that Fe, Ni, O, C, and N elements are still uniformly distributed in Li-NFL/CN after the OER in seawater (**Figure 3.28d**).

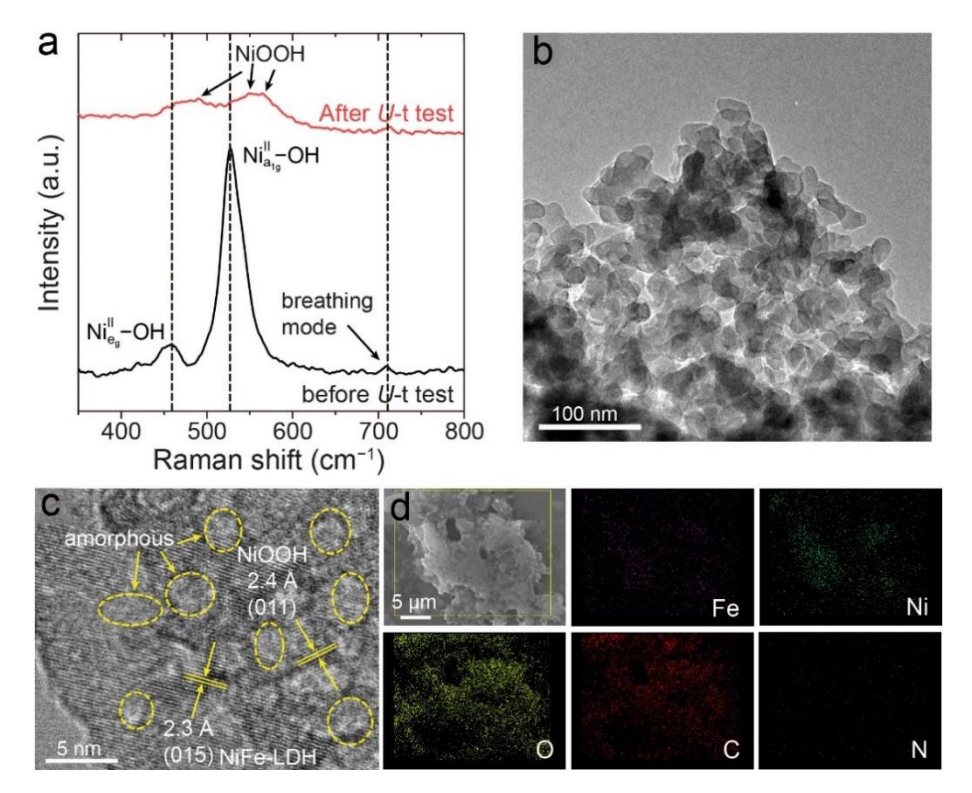


Figure 3.28. (a) Raman spectra of Li-NFL/CN before and after stability test in seawater + 1 M KOH. (b) TEM image of Li-NFL/CN after stability test in seawater + 1 M KOH. (c) TEM image and (d) energy-dispersive spectrometer mapping images of Li-NFL/CN after the OER test.

From the ICP-OES after the OER stability test, slight increases in Li/(Li+Fe+Ni) and Fe/Ni ratios are observed (**Table 3.3**), which can be attributed to the inevitable dissolution of NiFe-LDH during the OER process.

Table 3.3. ICP-OES analysis data of metals in Li-NFL/CN before and after the *U*-t test.

Cample	Element content (µmol/mL)			Atomic ratio	Atomic ratio
Sample	Li	Fe	Ni	Li/(Li+Ni+Fe)	Fe/Ni
Before <i>U</i> -t test	0.00942	2.893	9.316	0.00077	0.311
After U-t test	0.00403	1.184	3.457	0.00086	0.342

The zeta potentials of NiFe-LDH and Li-NFL/CN are shown in **Figure 3.29**. Li-NFL/CN presents a weaker surface charge after Li⁺ doping and g-C₃N₄ hybridization, which can mitigate the adsorption of Cl⁻. To further explore such remarkable stability in seawater, corrosion polarization curves of pristine NiFe-LDH and Li-NFL/CN were obtained in natural seawater (**Figure 3.30a** and **b**). As shown in **Figure 3.30c**, Li-NFL/CN has a lower corrosion current density (5.14 μ A cm⁻²) and a higher corrosion potential (0.384 V) compared with NiFe-LDH (6.07 μ A cm⁻² and 0.273 V), suggesting its stronger corrosion resistance ability in seawater.

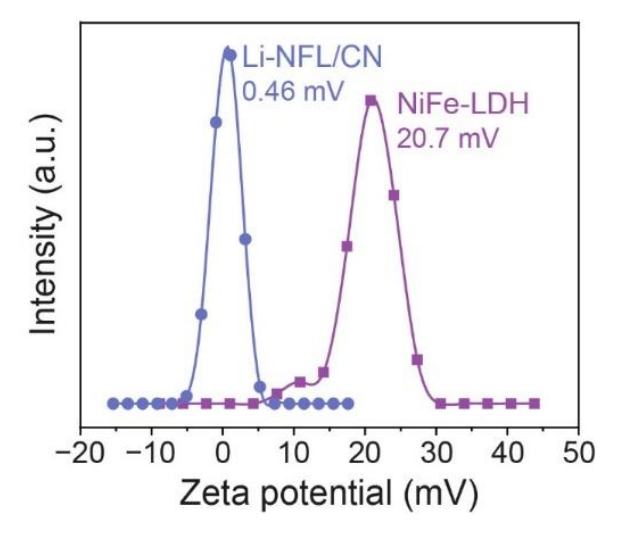


Figure 3.29. Zeta potentials of (a) NiFe-LDH and (b) Li-NFL/CN.

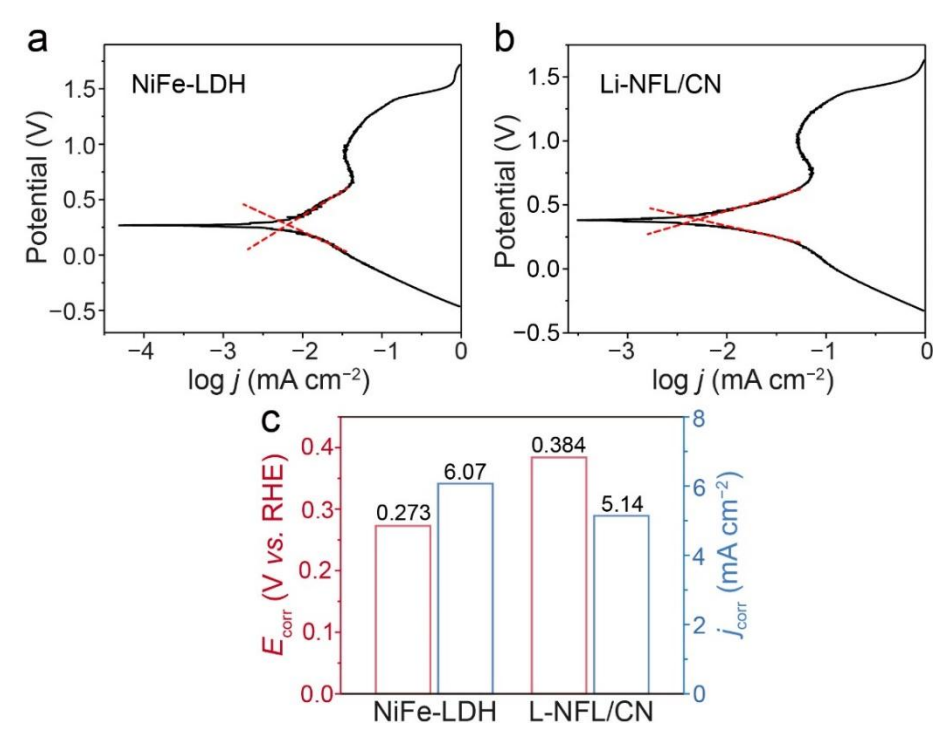


Figure 3.30. Corrosion polarization curves of (a) NiFe-LDH and (b) Li-NFL/CN. (c) Corrosion current densities and potentials of Li-NFL/CN in natural seawater.

3.4.5. Theoretical Calculations

To unveil the mechanism of how Li-ion doping and hybridization enhance the anticorrosion and water oxidation properties of NiFe-LDH, we conducted theoretical calculations based on DFT adopting the crystal structures of pristine NiFe-LDH, NiFe-LDH incorporating Li atoms, and Li-NFL hybridizing with g-C₃N₄ as calculation models (**Figure 3.31**). A two-step Volmer–Heyrovsky mechanism involving Cl⁻ adsorption and the subsequent release of molecular Cl₂ was employed to study the CER. To examine the effect of Li⁺ and g-C₃N₄ incorporation on anticorrosion, our focus was on Cl⁻ adsorption on the Ni site since it served as the active site (**Figure 3.32**). The free energy diagrams presented in **Figure 3.33** reveal that both Li⁺ doping and g-C₃N₄ hybridization can elevate the adsorption free energy for Cl⁻ compared with pristine NiFe-LDH. This suggests that Cl⁻ adsorption on the NiFe-LDH surface becomes more challenging after the modification with Li⁺ and g-C₃N₄, effectively preventing the catalyst from Cl⁻ erosion and enhancing the anticorrosion property. Compared with the pristine NiFe-LDH

catalyst, the CER processes on both Li-NFL and Li-NFL/CN are significantly inhibited due to sluggish Cl⁻ adsorption. Specifically, the theoretical overpotentials for CER are calculated to be 0.7 and 1.09 V for Li-NFL and Li-NFL/CN, respectively, which are notably higher than their overpotentials for OER observed in polarization curves. This explains why OER is more favorable than the competitive CER on Li-NFL and Li-NFL/CN catalysts, leading to high OER selectivity.

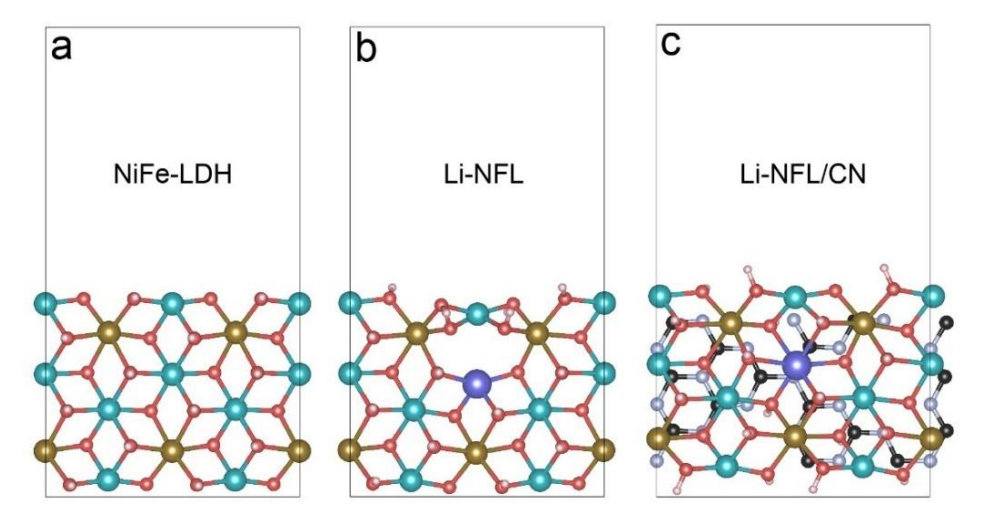


Figure 3.31. Optimized atomic structures of (a) pristine NiFe-LDH, (b) Li-NFL, and (c) Li-NFL/CN used for DFT calculations. Ni, Fe, Li, O, and H atoms are shown in blue, brown, purple, red, and pink, respectively.

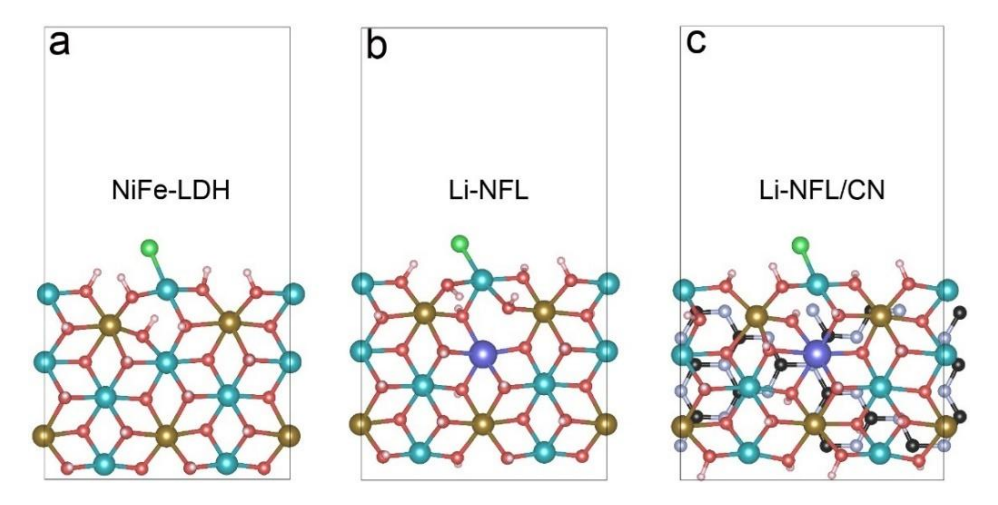


Figure 3.32. Cl⁻ adsorption on Ni site of the optimized atomic structure of (a) NiFe-LDH, (b) Li-NFL, and (c) Li-NFL/CN.

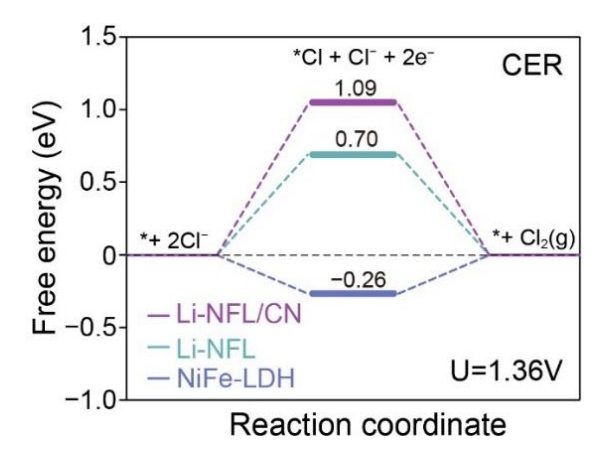


Figure 3.33. Free energy diagrams of CER on Ni site of NiFe-LDH, Li-NFL, and Li-NFL/CN, where * represents an active site on the catalyst surface.

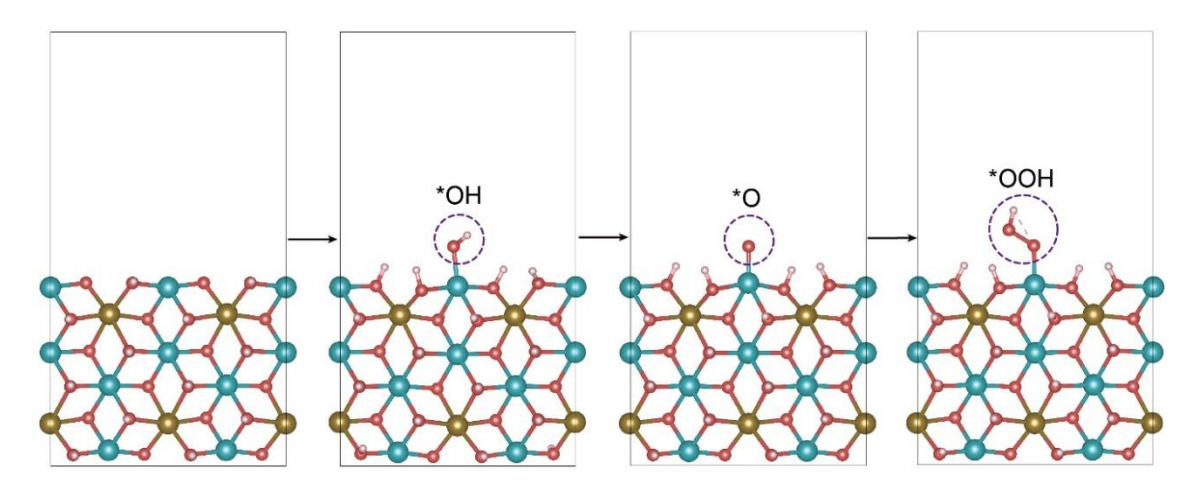


Figure 3.34. Structures of *OH, *O, and *OOH intermediates adsorbed on the Ni site of NiFe-LDH. Ni, Fe, O, and H atoms are shown in blue, brown, red, and pink, respectively.

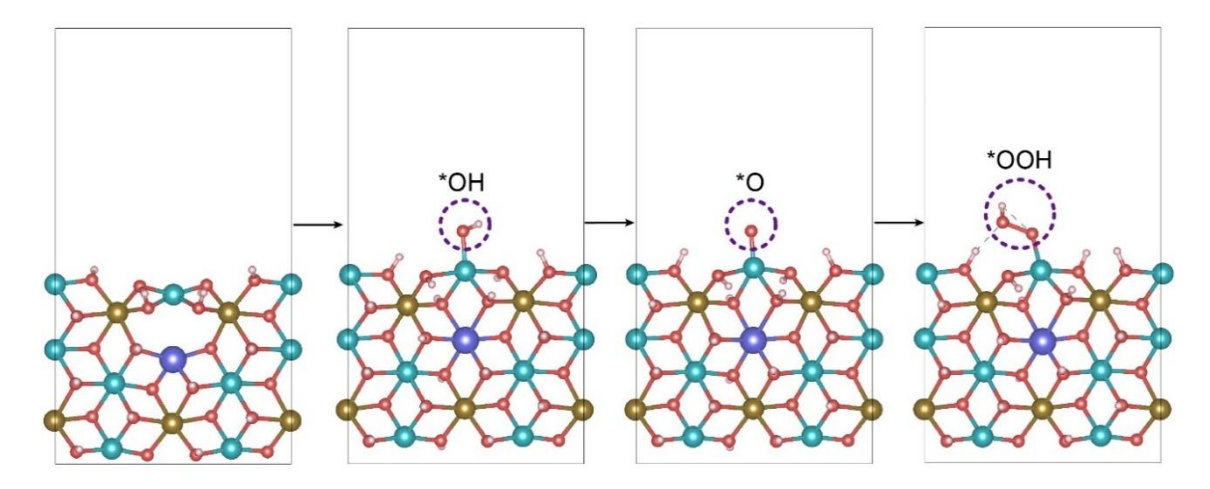


Figure 3.35. Structures of *OH, *O, and *OOH intermediates adsorbed on the Ni site of Li-NFL. Ni, Fe, Li, O, and H atoms are shown in blue, brown, purple, red, and pink, respectively.

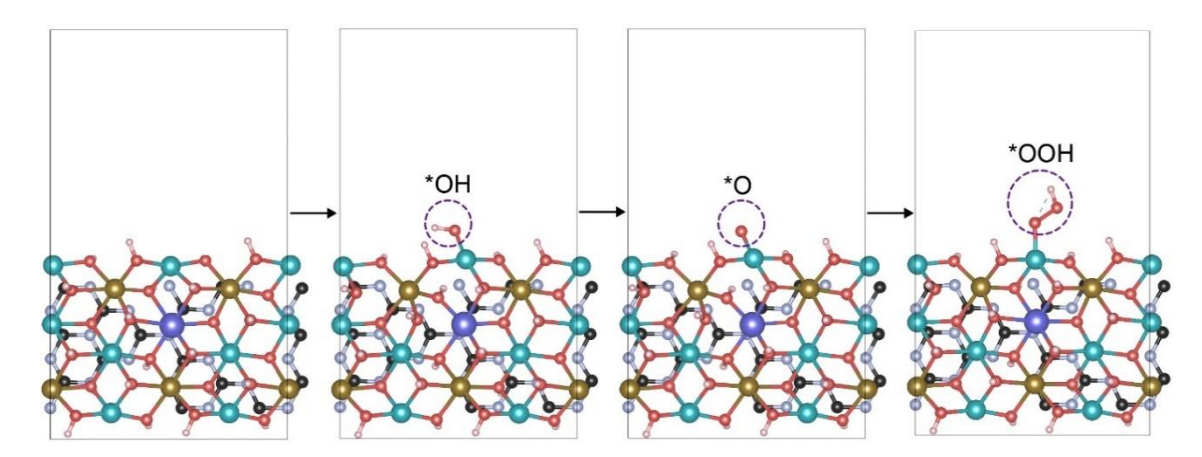


Figure 3.36. Structures of *OH, *O, and *OOH intermediates adsorbed on the Ni site of Li-NFL/CN. Ni, Fe, Li, O, C, N, and H atoms are shown in blue, brown, purple, red, black, gray, and pink, respectively.

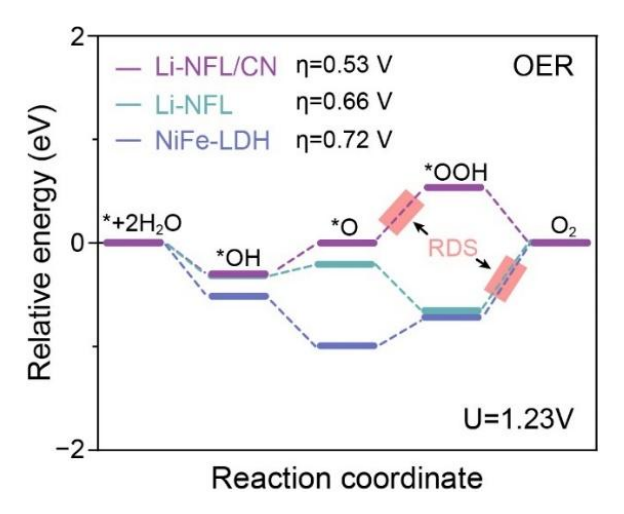


Figure 3.37. Free energy diagrams of OER on Ni site of NiFe-LDH, Li-NFL, and Li-NFL/CN, where * represents an active site on the catalyst surface.

We also investigated the free energy diagrams for each step in OER using DFT calculations (**Figures 3.34–3.36**). The proposed OER process of NiFe-LDH, Li-NFL, and Li-NFL/CN involves three intermediates: *OH, *O, and *OOH. The calculated free energy of each elementary step is shown in **Figure 3.37**. Inducing Li⁺ and *g*-C₃N₄ accelerates each step compared with those of pristine NiFe-LDH. Specifically, Li⁺ doping greatly benefits the M–*OH step, while *g*-C₃N₄ hybridization is more conducive to the M–*O process and alters the RDS from M–*OOH to M–*O. Moreover, the theoretical OER overpotential for Li-

NFL/CN is determined to be 0.53 V, much lower than that for NiFe-LDH (0.72 V), demonstrating the better OER performance of Li-NFL/CN. NiOOH is observed after surface reconstruction of Li-NFL/CN. To investigate the influence of Li doping and CN hybridization on the OER and CER of NiOOH, DFT calculation is applied to NiOOH and Li-NiOOH/CN. CN/Li-NiOOH shows a lower overpotential of 0.52 V than NiOOH (0.75 V, **Figure 3.40**), which means OER occurs easily on NiOOH after the modification of Li and CN. We compared the adsorption energies of the two Cl⁻ adsorption sites of CN/Li-NiOOH and found that the adsorption at the Ni site is spontaneous (energy release), while the adsorption at the Li site is non-spontaneous (energy adsorption, **Figure 3.43**), indicating that the Ni site is the adsorption site of Cl⁻. Compared to NiOOH, CN/Li-NiOOH needs to overcome a higher energy barrier to trigger CER (**Figure 3.44**), which means CER is more difficult to occur on CN/Li-NiOOH.

These theoretical calculations align with the experimental results, fully confirming that the co-effect of Li⁺ doping and interface formation endows Li-NFL/CN with higher selectivity and activity for OER in seawater electrolysis.

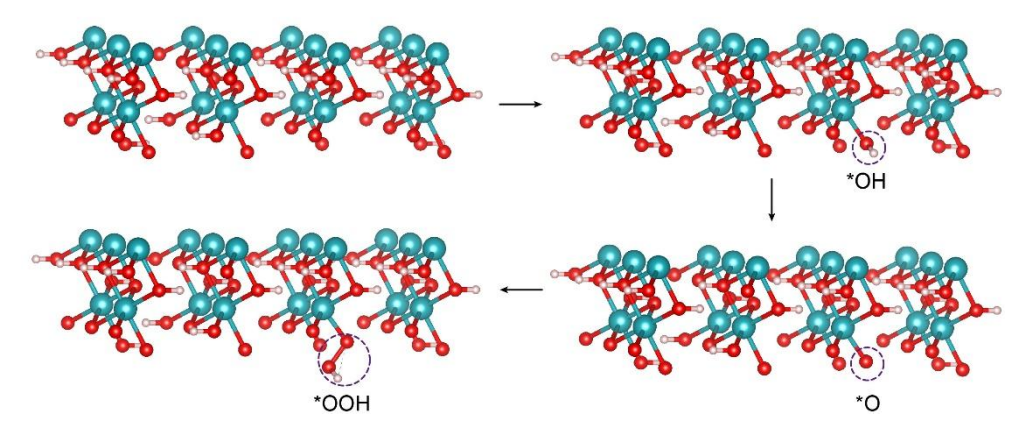


Figure 3.38. Structures of *OH, *O, and *OOH intermediates adsorbed on the Ni site of NiOOH. Ni, O, and H atoms are shown in blue, red, and pink, respectively.

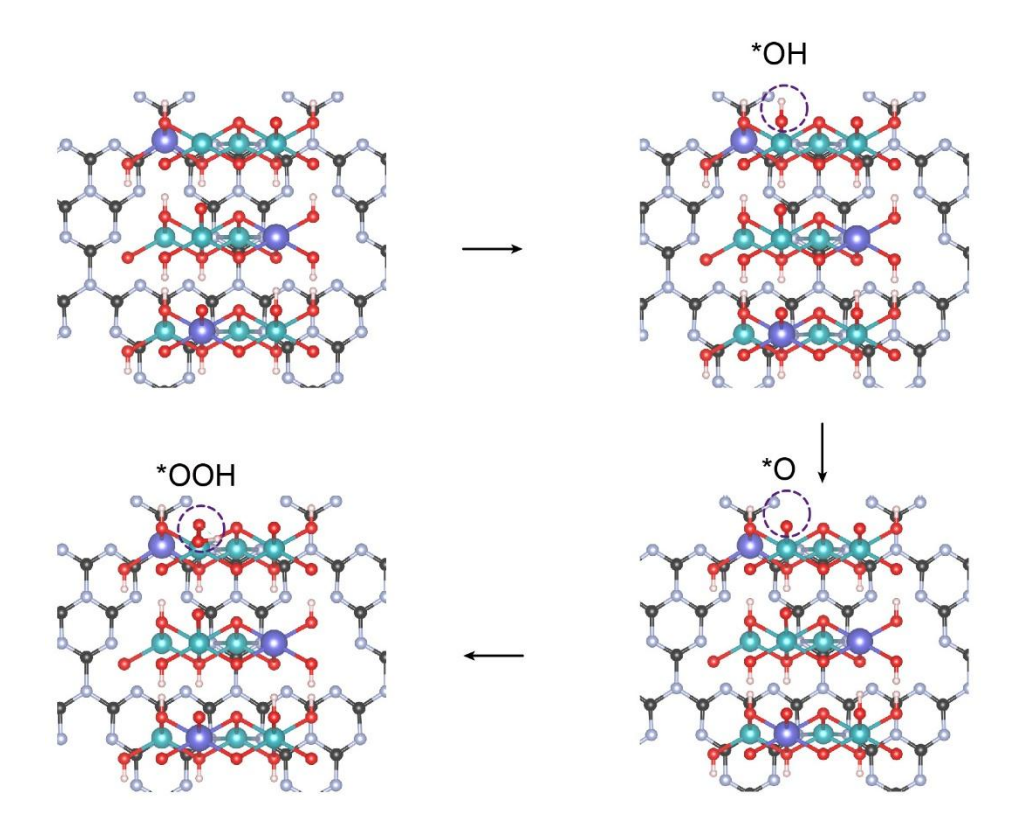


Figure 3.39. Structures of *OH, *O, and *OOH intermediates adsorbed on the Ni site of Li-NiOOH/CN. Ni, Li, O, C, N, and H atoms are shown in blue, purple, red, black, gray, and pink, respectively.

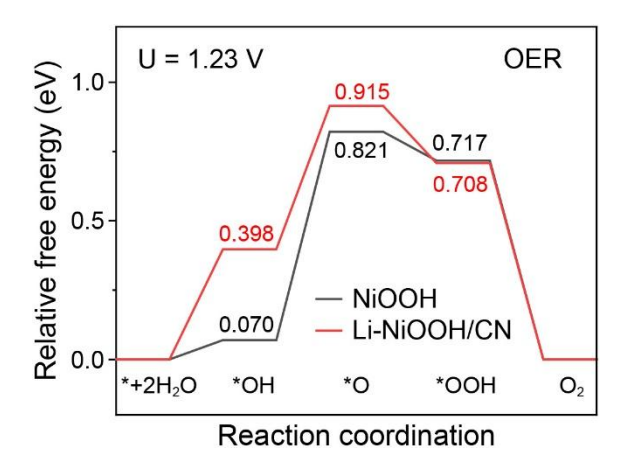


Figure 3.40. Free energy diagrams of OER on Ni site of NiOOH and Li-NiOOH/CN, where * represents an active site on the catalyst surface.

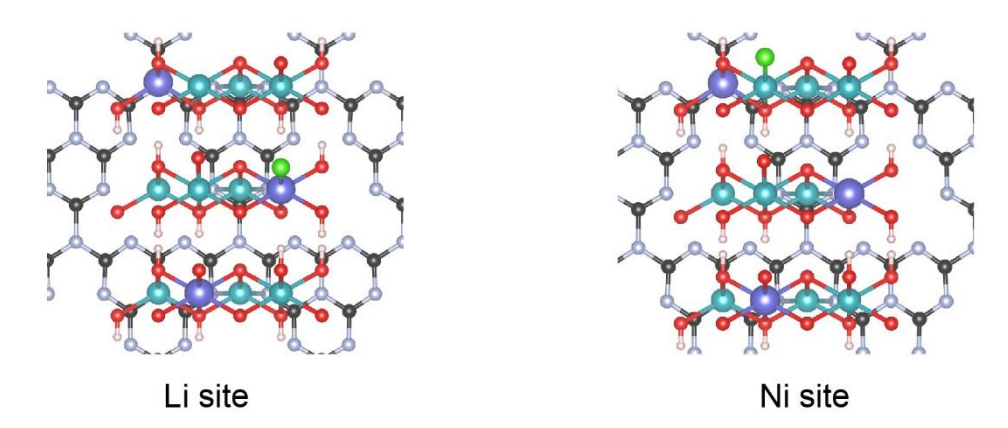


Figure 3.41. Cl⁻ adsorption on Ni and Li sites of the optimized atomic structure of Li-NiOOH/CN.

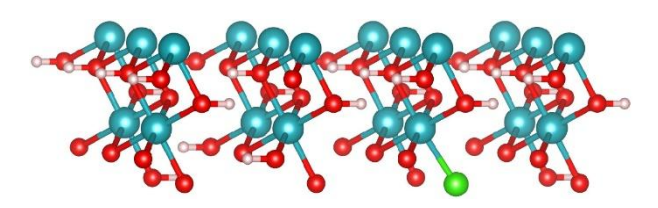


Figure 3.42. Cl⁻ adsorption on Ni site of the optimized atomic structure of NiOOH.

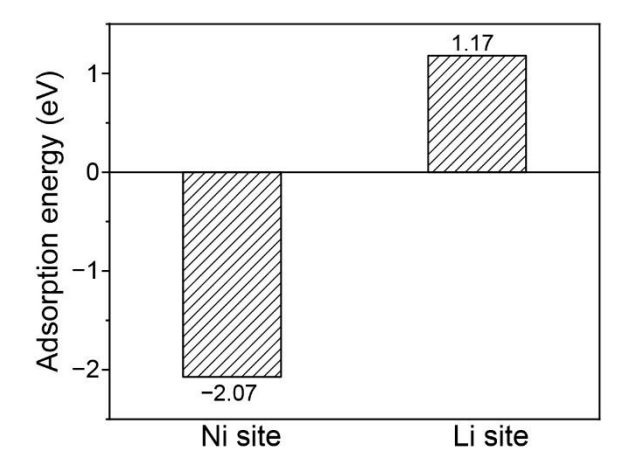


Figure 3.43. The adsorption energy of Cl⁻ on Ni and Li sites of Li-NiOOH/CN.

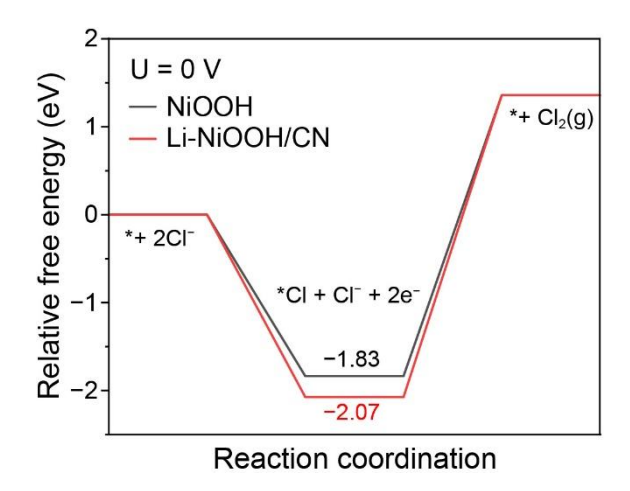


Figure 3.44. Free energy diagrams of CER on Ni site of NiOOH and Li-NiOOH/CN, where * represents an active site on the catalyst surface.

3.5. Conclusion

In summary, we have successfully synthesized Li-doped NiFe-LDH/*g*-C₃N₄ hybrid nanosheets through a facile chemical co-precipitation and sonication-assisted co-assembly method. DFT calculation results prove that integrating Li⁺ doping and *g*-C₃N₄ hybridization can effectively modulate the adsorption free energy of OER and CER active intermediates, resulting in lower and higher Gibbs free energy change, respectively. The resulting Li-NFL/CN exhibits highly enhanced OER activity and durability in both alkaline-freshwater and alkaline-seawater electrolytes, delivering a current density of 100 mA cm⁻² at low overpotentials of 276 and 319 mV, respectively. Li doping triggers the formation of more Ni³⁺ sites and oxygen defects in NiFe-LDH, which, upon interfacing with *g*-C₃N₄, leads to charge density redistribution, charge transfer acceleration, and a lower activation barrier. The built-in electric field formed at the interface between Li-NFL and *g*-C₃N₄, together with the doped Li⁺ sites, promotes the OH⁻ adsorption, thereby improving the selectivity towards OER performance.

3.6. References

- H. Ren, X. L. Sun, C. F. Du, J. Zhao, D. B. Liu, W. Fang, S. Kumar, R. Chua, S. Z. Meng,
 P. Kidkhunthod, L. Song, S. Q. Li, S. Madhavi, Q. Y. Yan, *ACS Nano* 2019, *13*, 12969.
- [2] H. Han, H. Choi, S. Mhin, Y. R. Hong, K. M. Kim, J. Kwon, G. Ali, K. Y. Chung, M. Je, H. N. Umh, D. H. Lim, K. Davey, S. Z. Qiao, U. Paik, T. Song, *Energy Environ. Sci.* 2019, 12, 2443.
- [3] A. Majeed, X. Li, P. X. Hou, H. Tabassum, L. L. Zhang, C. Liu, H. M. Cheng, *Appl. Catal. B-Environ. Energy* **2020**, *269*, 118823.
- [4] H. Tabassum, A. Mahmood, B. J. Zhu, Z. B. Liang, R. Q. Zhong, S. J. Guo, R. Q. Zou, *Energy Environ. Sci.* **2019**, *12*, 2924.
- [5] C. G. Kuai, Z. R. Xu, C. Xi, A. Y. Hu, Z. J. Yang, Y. Zhang, C. J. Sun, L. X. Li, D. Sokaras, C. K. Dong, S. Z. Qiao, X. W. Du, F. Lin, *Nat. Catal.* 2020, 3, 743.
- [6] Y. Du, D. P. Liu, T. Z. Li, Y. D. Yan, Y. Liang, S. C. Yan, Z. G. Zou, Appl. Catal. B-Environ. Energy 2022, 306, 121146.
- [7] Y. Kuang, M. J. Kenney, Y. T. Meng, W. H. Hung, Y. J. Liu, J. E. Huang, R. Prasanna, P. S. Li, Y. P. Li, L. Wang, M. C. Lin, M. D. McGehee, X. M. Sun, H. J. Dai, *Proc. Natl. Acad. Sci. USA* 2019, 116, 6624.
- [8] Z. Y. Xiao, W. Zhou, N. Zhang, C. A. Liao, S. C. Huang, G. X. Chen, G. Chen, M. Liu, X. H. Liu, R. Z. Ma, *Chem. Commun.* 2021, 57, 6070.
- [9] Z. M. Sun, M. W. Yuan, K. F. Shi, Y. H. Liu, D. Wang, C. Y. Nan, H. F. Li, G. B. Sun, X. J. Yang, *Chem-Eur. J.* 2020, 26, 7244.
- [10] X. D. Zhang, D. Kim, J. Yan, L. Y. S. Lee, ACS Appl. Mater. Inter. 2021, 13, 9762.
- [11] Y. N. Zhou, W. L. Yu, Y. N. Cao, J. Zhao, B. Dong, Y. Ma, F. L. Wang, R. Y. Fan, Y. L. Zhou, Y. M. Chai, Appl. Catal. B-Environ. Energy 2021, 292, 120150.
- [12] Z. Y. Zhao, Q. Shao, J. Y. Xue, B. L. Huang, Z. Niu, H. W. Gu, X. Q. Huang, J. P. Lang, Nano Res. 2022, 15, 310.
- [13] Y. Y. Wang, M. Qiao, Y. F. Li, S. Y. Wang, Small 2018, 14, 1800136.
- [14] H. J. Song, H. Yoon, B. Ju, D. Y. Lee, D. W. Kim, ACS Catal. 2020, 10, 702.
- [15] B. H. Cui, Z. Hu, C. Liu, S. L. Liu, F. S. Chen, S. Hu, J. F. Zhang, W. Zhou, Y. D. Deng,
 Z. B. Qin, Z. Wu, Y. A. Chen, L. F. Cui, W. B. Hu, Nano Res. 2021, 14, 1149.
- [16] R. G. Pearson, J. Chem. Educ. 1968, 45, 581.
- [17] Q. Q. Tu, W. W. Liu, M. Jiang, W. J. Wang, Q. Kang, P. C. Wang, W. J. Zhou, F. M. Zhou, *ACS Appl. Energy Mater.* **2021**, *4*, 4630.

- [18] B. M. Hunter, W. Hieringer, J. R. Winkler, H. B. Gray, A. M. Muller, *Energy Environ. Sci.* **2016**, *9*, 1734.
- [19] H. C. A. Sun, W. Zhang, J. G. Li, Z. S. Li, X. Ao, K. H. Xue, K. K. Ostrikov, J. Tang, C.
 D. Wang, *Appl. Catal. B-Environ. Energy* 2021, 284, 119740.
- [20] Z. Cheng, D. S. Baser, S. G. Nadgouda, L. Qin, J. A. Fan, L. S. Fan, *ACS Energy Lett.* **2018**, *3*.
- [21] K. S. Ranjith, C. L. Dong, Y. R. Lu, Y. C. Huang, C. L. Chen, P. Saravanan, K. Asokan, R. T. R. Kumar, *ACS Sustainable Chem. Eng.* **2018**, *6*, 8536.
- [22] S. X. Liu, H. W. Zhang, E. L. Hu, T. Y. Zhu, C. Y. Zhou, Y. C. Huang, M. Ling, X. H. Gao, Z. Lin, J. Mater. Chem. A 2021, 9, 23697.
- [23] J. W. Li, R. Q. Lian, J. Y. Wang, S. He, S. Jiang, Z. B. Rui, *Electrochim. Acta* **2020**, *331*, 135395.
- [24] M. Asnavandi, Y. C. Yin, Y. B. Li, C. H. Sun, C. Zhao, ACS Energy Lett. 2018, 3, 1515.
- [25] J. R. Ran, W. W. Guo, H. L. Wang, B. C. Zhu, J. G. Yu, S. Z. Qiao, *Adv. Mater.* **2018**, *30*, 1800128.
- [26] W. B. Zhang, Z. J. Zhang, S. H. Choi, W. Yang, Catal. Today 2019, 321, 67.
- [27] Y. Wang, X. Q. Cui, J. X. Zhao, G. R. Jia, L. Gu, Q. H. Zhang, L. K. Meng, Z. Shi, L. R. Zheng, C. Y. Wang, Z. W. Zhang, W. T. Zheng, ACS Catal. 2019, 9, 336.
- [28] J. Yan, X. D. Zhang, W. R. Zheng, L. Y. S. Lee, ACS Appl. Mater. Inter. 2021, 13, 24723.
- [29] M. Q. Guan, C. Wang, S. Li, H. W. Du, Y. P. Yuan, ACS Sustainable Chem. Eng. 2020, 8, 10313.
- [30] Z. Li, F. Huang, Y. F. Xu, A. H. Yan, H. M. Dong, X. Xiong, X. H. Zhao, Chem. Eng. J. 2022, 429, 132476.
- [31] C. Gao, Q. Q. Meng, K. Zhao, H. J. Yin, D. W. Wang, J. Guo, S. L. Zhao, L. Chang, M. He, Q. X. Li, H. J. Zhao, X. J. Huang, Y. Gao, Z. Y. Tang, *Adv. Mater.* 2016, 28, 6485.
- [32] M. T. Greiner, M. G. Helander, W. M. Tang, Z. B. Wang, J. Qiu, Z. H. Lu, *Nat. Mater.* 2012, 11, 76.
- [33] X. B. Chen, L. Liu, P. Y. Yu, S. S. Mao, Science 2011, 331, 746.
- [34] Y. Hermans, A. Klein, H. P. Sarker, M. N. Huda, H. Junge, T. Toupance, W. Jaegermann, *Adv. Funct. Mater.* **2020**, *30*, 1910432.
- [35] J. Y. Liu, X. Liu, H. Shi, J. H. Luo, L. Wang, J. S. Liang, S. Z. Li, L. M. Yang, T. Y. Wang, Y. H. Huang, Q. Li, *Appl. Catal. B-Environ. Energy* **2022**, *302*, 120862.
- [36] X. Luo, P. X. Ji, P. Y. Wang, X. Tan, L. Chen, S. C. Mu, Adv. Sci. 2022, 9, 2104846.
- [37] M. W. Louie, A. T. Bell, J. Am. Chem. Soc. 2013, 135, 12329.

Chapter III Li-Doped NiFe-LDH/g-C₃N₄ for Seawater Oxidation

- [38] J. Jiang, F. F. Sun, S. Zhou, W. Hu, H. Zhang, J. C. Dong, Z. Jiang, J. J. Zhao, J. F. Li, W. S. Yan, M. Wang, *Nat. Commun.* 2018, 9, 2885.
- [39] B. Konkena, J. Masa, A. J. R. Botz, I. Sinev, W. Xia, J. Kossmann, R. Drautz, M. Muhler, W. Schuhmann, ACS Catal. 2017, 7, 229.
- [40] J. Huang, Y. Li, Y. Zhang, G. Rao, C. Wu, Y. Hu, X. Wang, R. Lu, Y. Li, J. Xiong, *Angew. Chem. Int. Ed.* **2019**, *58*, 17458.

Chapter IV Upcycling of Spent LiFePO₄ into Electrocatalysts for Seawater Oxidation

4.1. Objective and Motivation

In Chapter 3, the NiFe-LDH electrocatalyst was successfully modified using a joint strategy of doping and heterointerface construction, resulting in enhanced seawater oxidation activity and stability. However, these catalysts, like most materials mentioned in Chapter 1, are typically synthesized from purified chemicals, which leads to high costs and challenges in large-scale production. Recently, the upcycling of waste materials into electrocatalysts has emerged as a significant research trend focused on resource restructuring. Given the presence of transition metal elements in LIBs, numerous studies have suggested extracting these metal species from end-of-life cathodes. However, there have been no reports to date on seawater OER electrocatalysts directed upcycled from spent LIB cathodes.

In this Chapter, the spent LiFePO₄ (LFP) cathode was upcycled to serve as seawater OER electrocatalysts through hybridization with Ni(OH)₂. The reconstruction process of the hybrid was closely monitored to elucidate the role of Fe species in promoting the formation of OER-active species. Comprehensive materials characterization and DFT calculations were employed to reveal the synergistic effect of heterojunction and anion-repelling mechanism on improving OER selectivity in seawater oxidation reactions. This Chapter aims to bridge the fields of waste electrode management and sustainable green hydrogen production.

4.2. Introduction

Although harnessing green hydrogen *via* direct seawater electrolysis becomes a crucial strategy to achieve dual-carbon goals, [1, 2] a significant challenge arises at the anode: the oxidation of high concentrations (approximately 0.5 M) of chloride ions (Cl⁻) to hypochlorite (ClO⁻) or chlorine (Cl₂). [3, 4] These corrosive byproducts threaten electrode durability, potentially compromising the system's overall efficiency. [5, 6] Alkalizing seawater makes the OER (E°_{anode} = 1.23 V) thermodynamically favorable over the CER (E°_{anode} = 1.72 V). [7] In an alkaline environment, OER predominates in the anodic oxidation process, rather than CER, within a

potential range of 490 mV. However, Cl⁻ ions in seawater can still attack electron-deficient sites on transition metals, leading to catalyst deactivation.^[8] For instance, Ni-based OER electrocatalysts demonstrate promising activity in alkaline media due to the formation of NiOOH with Ni³⁺ under anodic oxidation.^[9-11] Yet, in chlorine-rich environments, NiOOH degrades rapidly, resulting in a loss of activity.^[12] Recent studies suggest that introducing anions, such as sulfate and phosphate ions, onto OER catalyst surfaces can electrostatically repel Cl⁻ ions, effectively mitigating corrosion from chlorine derivatives and ensuring the stability of seawater oxidation operations.^[13, 14] However, this anion-enriched layer may also impede the diffusion of OH⁻ ions, creating a higher energy barrier for OER.^[15]

Constructing heterointerfaces has been shown to modulate the electronic structure and enhance the adsorption of intermediates on active sites, thereby reducing the thermodynamic reaction energy barrier of the OER. [10, 16-18] For example, heterojunctions composed of Ni- and Fe-based species, such as Ni(OH)₂/Fe₂O₃ and Ni(OH)₂/FeOOH, exhibit superior OER performance compared to their single-component counterparts. This improvement is largely due to the optimized adsorption behavior of oxygen-containing intermediates, which stems from the strong synergistic effects between the Ni and Fe sites. [19, 20] Given the presence of P and Fe elements in LiFePO₄ (LFP)-based LIBs, it is conceivable that converting end-of-life LFP cathodes into Ni-based catalysts is a promising strategy for upcycling and repurposing spent LIBs. Different from existing strategies that are proposed to advance the LIBs-upcycling techniques in the electrocatalytic field, [21-24] rational design of heterojunction and phosphate-repelling mechanism can offer effective and stable electrocatalysts for direct seawater oxidation, contributing to waste management and environmental protection.

This chapter presents a three-step strategy to convert waste LFP cathodes into a highly effective seawater OER electrocatalyst. By employing pulsed laser ablation in liquid (PLAL) and electrodeposition, Ni(OH)₂ interfaced with laser-ablated LFP (Ni(OH)₂/L-LFP) is

fabricated. Our characterizations indicate that the formation of Ni(OH)₂/L-LFP heterojunctions significantly increases the electrochemical surface areas, enhancing mass transfer capabilities. During OER, *in situ* generated NiOOH and Fe₃(PO₄)₂ serve as the primary active species and electron transfer mediator, respectively. The NiOOH/Fe₃(PO₄)₂ heterointerface is particularly advantageous for maintaining OH⁻ adsorption while increasing the energy barrier of CER concurrently. Additionally, PO₄³⁻ ions, which are leached during the reconstruction process, contribute to repelling Cl⁻ ions in seawater, thus mitigating catalyst corrosion.

4.3. Experimental Section

4.3.1. Raw Materials

LFP scraps were collected from waste batteries received from GRST company. Nickel nitrate hexahydrate (Ni(NO₃)₂·6H₂O, 99.9 %), ethanol (EtOH, 99.8 %), Nafion perfluorinated resin solution (5 wt.%), sodium hypophosphite (NaH₂PO₂, 99.0 %), potassium persulfate ($K_2S_2O_8$, 99.0 %), ascorbic acid ($C_6H_8O_6$, 99.0 %), ammonium molybdate tetrahydrate ((NH₄)₆Mo₇O₂₄·4H₂O, 83.0 %), sodium thiosulfate (Na₂S₂O₃, 99.0 %), sodium sulfate (Na₂SO₄, 99.0 %), and potassium hydroxide (KOH, 99.9 %) were purchased from Sigma–Aldrich. Sulfuric acid (H₂SO₄, 98.0 %) was purchased from Duksan Chemicals. Sodium chloride (NaCl, 99.5 %) and potassium iodide (KI, 99.0 %) were obtained from Shenzhen Dieckmann Tech. Aqueous solutions were prepared using deionized (DI) water produced by MilliQ Water System. Natural seawater (pH = ~8) was collected from Hung Hom Bay near the Hong Kong Polytechnic University, Kowloon, Hong Kong SAR, China. All chemicals were used as received.

4.3.2. Catalysts Synthesis

Laser ablation of LiFePO₄ (L-LFP): LFP scraps were calcined at 500 °C for 2 h under Ar flow and manually ground into powder using a mortar. The LFP powder (50 mg) was uniformly dispersed in DI water (5 mL) by sonication for 30 min. A Nd:YAG Q-switched pulsed laser (λ

= 1,064 nm, Nimma-600 Laser system, Beamtech Optronics Co. Ltd., China) with an energy output of 320 mJ (650 V) and energy stability (root mean square) \leq 1% was used for laser ablation. The LFP suspension was ablated with the laser (beam diameter = 8 mm) under continuous stirring at 20 °C for various durations (15, 60, and 120 min). The ablated product was collected by centrifugation, washed with DI water and ethanol several times, and dried at 60 °C under vacuum for 12 hours.

Synthesis of Ni(OH)₂/L-LFP: A homogeneous L-LFP ink (5 mg mL⁻¹) was prepared by mixing the L-LFP powder with a 5 wt.% Nafion solution (40 μ L) in ethanol (960 μ L). The L-LFP ink (50 μ L) was then dropped onto carbon paper (0.25 cm²) and dried naturally in the air. This L-LFP on carbon paper served as the working electrode in a three-electrode configuration. A standard calomel electrode and a carbon rod were employed as the reference and counter electrodes, respectively, in an aqueous electrolyte. To remove residual Li in L-LFP, 1 V was applied for a predetermined duration (60, 90, 120, and 180 min). Subsequently, Ni(OH)₂ was electrodeposited onto the L-LFP by applying –1 V in an electrolyte containing 0.1 M Ni(NO₃)₂ for various duration. The Ni(OH)₂/L-LFP composite was rinsed with DI water and dried at 60 °C under vacuum for 12 hours. To prepare a Ni(OH)₂ electrode as the control sample, a pristine carbon paper (0.25 cm²) was employed without L-LFP, following the same procedure. Pt/C (or RuO₂) ink was prepared by mixing 20 wt.% Pt/C (or RuO₂, 5 mg) with a 5 wt.% Nafion solution (40 μ L) in ethanol (960 μ L) and sonicated for 60 min. The catalyst ink (100 μ L) was drop-cast on a nickel foam (1 cm × 1 cm) and dried naturally in the air.

4.3.3. Electrochemical Performance Test

Electrocatalytic properties of samples toward OER were investigated using a standard threeelectrode configuration in 1.0 M KOH electrolyte. The high-purity O₂ is bubbled through the electrolyte during testing to fix the reversible oxygen potential. A graphite rod and a Hg/HgO electrode were used as the counter and reference electrodes, respectively. All data were acquired using a Princeton multichannel electrochemical station. All potentials in this work were calibrated against the reversible hydrogen electrode (RHE, $E_{RHE} = E_{Hg/HgO} + 0.059 \times pH + 0.098$). Before the OER catalysis, the working electrodes were cycled between 1.124 and 1.624 V for 100 cycles to achieve a stable CV curve. LSV was then conducted from 1.2 to 1.9 V at a scan rate of 2 mV s⁻¹. All polarization curves were corrected for ohmic losses by applying 85 % iR compensation to obtain accurate overpotentials. all measurements were repeated at least three times.

4.3.4. Flow Cell Measurements

For the HER, the Pt/C on nickel foam (cathode) was coupled with the Ni(OH)₂/L-LFP anode that was scaled up to 1 cm² (1 cm × 1 cm). As a comparison, a commercial RuO₂ on carbon paper was used as the anode. The full-cell water splitting reaction was carried out on a Princeton multichannel electrochemical station equipped with a membrane electrode assembly (MEA) electrolyzer and peristaltic pump. The MEA electrolyzer consisted of anode and cathode flow fields with active surface areas of 1 cm². These flow fields were responsible for delivering aqueous anolyte over the surface of the anode and cathode. In the MEA, the cathode and anode were placed on their respective flow-field plates and physically separated by an anion exchange membrane (AEM, Fumasep, Fuel Cell Store). The MEA was then subjected to uniform pressure to ensure good contact and sealing between the electrodes and the AEM. Following the MEA assembly, an alkaline seawater electrolyte was supplied through the anode and cathode compartments at a constant flow rate of 5 mL min⁻¹. For chronopotentiometric tests, a constant current density of 250 mA cm⁻² was applied to the anode, and the corresponding voltage was continuously recorded throughout the measurement.

4.3.5. Calculation of Electricity Consumed for H₂ Production

The electricity consumption for H₂ production was calculated according to the equation:

$$W = I \times \int U \, \mathrm{d}t \tag{4.1}$$

where W is the total electricity consumption, I is current, and U is potential. The amount of H_2 generated is calculated according to the equation:

$$V = \frac{22.4 \times I \times t}{7. \times F} \tag{4.2}$$

where V is the volume of H_2 produced, Z is the electron transfer number for the HER, and F is the Faraday constant. The electricity consumption Q (kWh Nm⁻³) is determined by the equation:

$$Q = \frac{W}{V} \tag{4.3}$$

4.4. Results and Discussion

4.4.1. Structure Characterization

LiFePO₄ powder was obtained from waste LFP batteries, and the detailed procedure is provided in the Supporting Information. **Figure 4.1** illustrates a three-step approach to synthesizing a hybrid consisting of Ni(OH)₂ and Ni(OH)₂/L-LFP on carbon paper. Briefly, the bulk LFP powder was transformed into nanoparticles through pulsed laser ablation in water, destroying the initial structure of LFP (**Figures 4.2a** and **4.2b**). The size of nanoparticles was modulated by laser ablation time, and uniform-sized (270 nm) nanoparticles were obtained with 180 min of laser ablation (**Figures 4.2c-1f**). BET analysis using adsorption–desorption isotherms indicates that the surface area of laser-ablated LFP (L-LFP; 11.43 m² g⁻¹) has increased compared to pristine LFP (7.67 m² g⁻¹, **Figure 4.3**).



Figure 4.1. A schematic diagram showing the synthetic procedure of Ni(OH)₂/L-LFP.

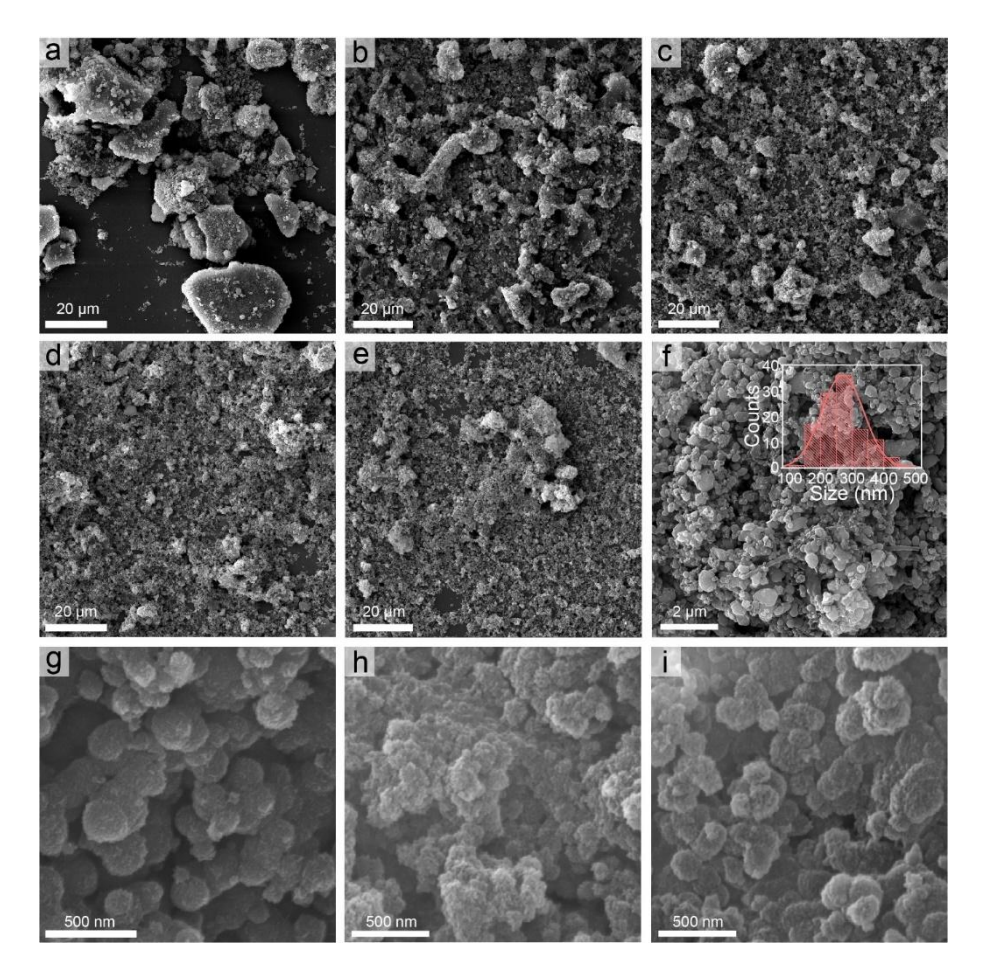


Figure 4.2. SEM images of (a) LFP, (b) L-LFP-60 min, (c) L-LFP-90 min, (d) L-LFP-120 min, (e-f) L-LFP-180 min, (g) Ni(OH) $_2$ /L-LFP-5 min, (h) Ni(OH) $_2$ /L-LFP-10 min, and (i) Ni(OH) $_2$ /L-LFP-20 min.

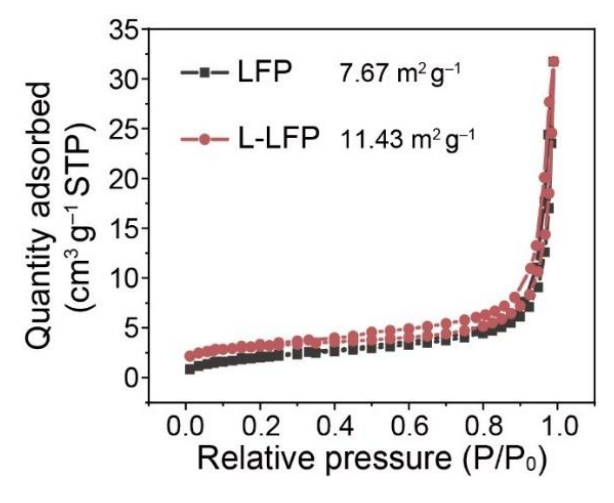


Figure 4.3. Adsorption/desorption isotherms of LFP and L-LFP.

Table 4.1. ICP-OES analysis data of metals at various stages of Ni(OH)₂/L-LFP preparation.

Campla	Element content (ppm)			Atomic ratio	
Sample	Fe	Ni	Li	Ni/(Ni+Fe+Li)	Li/(Fe+Li)
LFP	12.60	/	1.00	/	0.39
L-LFP	12.67	/	0.92	/	0.37
L-LFP-charging 60 min	7.07	/	0.37	/	0.30
L-LFP-charging 90 min	7.65	/	0.21	/	0.18
L-LFP-charging 120 min	5.58	/	0.10	/	0.13
L-LFP-charging 180 min	5.29	/	0.04	/	0.06
Ni(OH) ₂ /L-LFP-5 min	6.04	8.09	0.12	0.52	0.14
Ni(OH) ₂ /L-LFP-10 min	5.92	21.61	0.11	0.75	0.13
Ni(OH) ₂ /L-LFP-20 min	6.27	55.19	0.12	0.88	0.13
Ni(OH) ₂	0	24.37	0	1	/

To remove residual Li in L-LFP, the L-LFP ink was coated on carbon paper and charged by applying 1 V (vs. standard calomel electrode, SCE) for 120 min. The elemental analysis by ICP-OES (**Table 4.1**) indicates that the concentration of Li decreases dramatically from 0.92 to 0.04 ppm by charging for 180 min. Electroreduction of Ni(NO₃)₂ at -1 V (vs. SCE) forms a Ni(OH)₂ layer on the L-LFP electrode with precise control of Ni(OH)₂/L-LFP ratio and morphology (**Table 4.1** and **Figures 4.2g – 4.2i**). The morphology of Ni(OH)₂/L-LFP mainly consists of irregular particles with diameters in the range of 200 – 400 nm while some nanoparticles aggregate together to become thicker particles (**Figure 4.4a**). The Ni(OH)₂ layer deposition reduces the contact angle to 83° from 149° of bare L-LFP (**Figure 4.4b**), indicating its enhanced hydrophilicity desirable for the solid–liquid interface during catalysis.

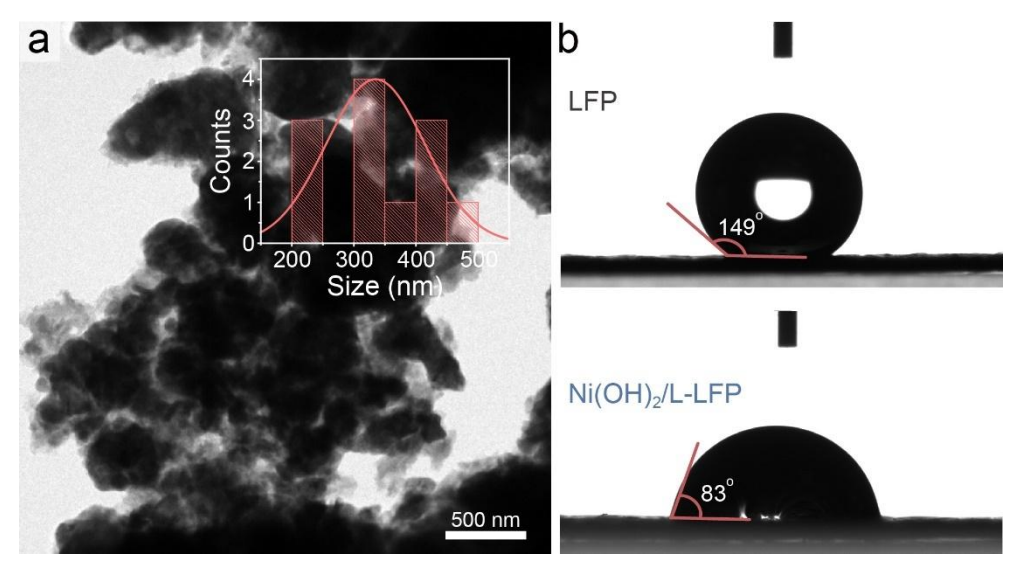


Figure 4.4. (a) The TEM image of Ni(OH)₂/L-LFP. (b) Contact angle images of LFP and Ni(OH)₂/L-LFP

The XRD pattern of L-LFP suggests that the crystal structure of LFP is maintained during laser ablation (**Figure 4.5a**). However, the XRD pattern of Ni(OH)₂/L-LFP reveals the presence of a new phase of LiFeP₃O₉, which is formed as a result of Li loss during the charging process. From Raman spectroscopic analysis of Ni(OH)₂/L-LFP, two typical Ni(OH)₂ peaks are detected at 460 and 1,045 cm⁻¹, which confirms the successful deposition of Ni(OH)₂ on L-LFP (**Figure 4.5b**). The graphite peaks of D (1350 cm⁻¹) and G (1580 cm⁻¹) bands can be found in Raman spectra of L-LFP and Ni(OH)₂/L-LFP, which suggests the carbon species in those samples. The D peak with much higher intensity than the G band reveals a high degree of disorder in carbon.^[25] The high-resolution TEM image of Ni(OH)₂/L-LFP reveals three lattice spacings of 2.55, 4.27, and 3.45 Å (**Figure 4.5c**) that can be ascribed to the (111), (101), and (211) planes of Ni(OH)₂, LiFePO₄, and LiFeP₃O₉, respectively. The interface boundary of Ni(OH)₂ and LiFeP₃O₉ is depicted by the dotted lines. **Figure 4.6** shows a scanning TEM image of Ni(OH)₂/L-LFP and the corresponding EDS images, where Ni, Fe, O, and P elements are uniformly distributed over the entire area.

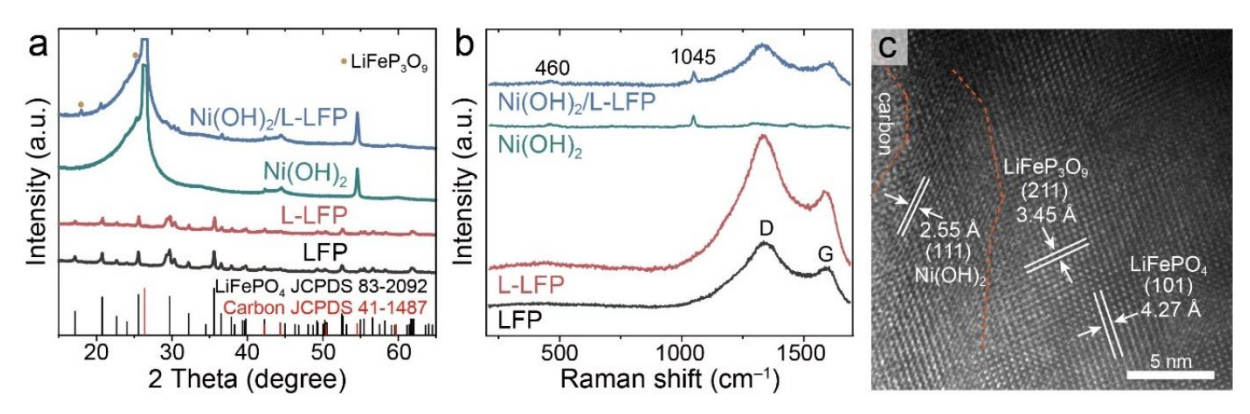


Figure 4.5. (a) XRD patterns and (b) Raman spectra of LFP, L-LFP, Ni(OH)₂, and Ni(OH)₂/L-LFP. (c) High-resolution TEM image of Ni(OH)₂/L-LFP.

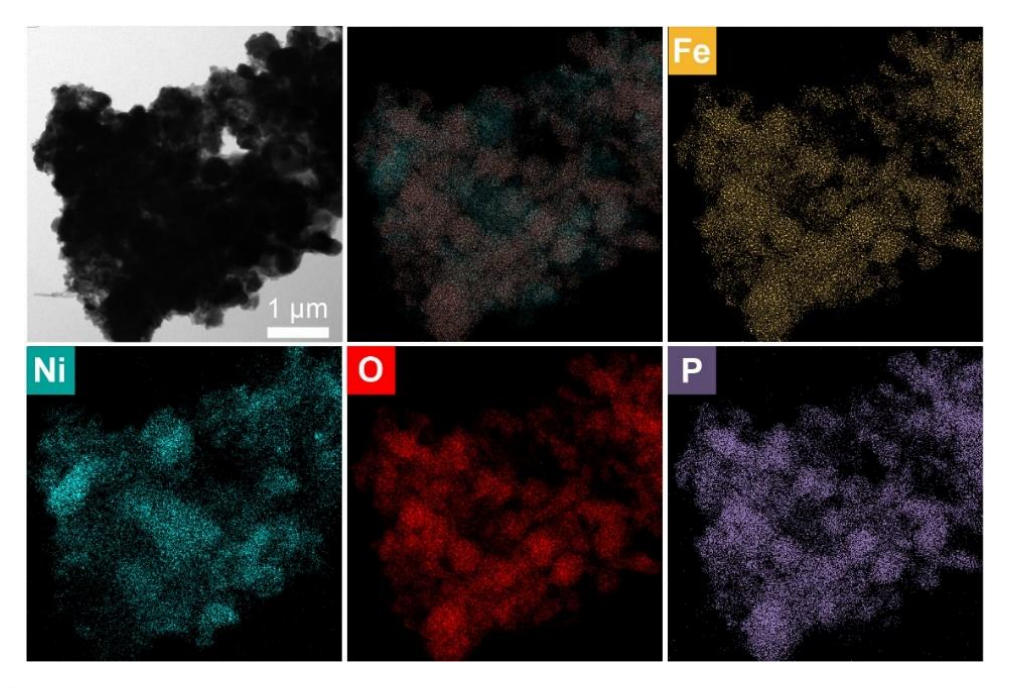


Figure 4.6. STEM, and the corresponding EDS mapping images of Ni(OH)₂/L-LFP.

XPS was employed to investigate the changes in chemical composition and surface electronic states. The high-resolution Ni 2p spectra of both Ni(OH)₂ and Ni(OH)₂/L-LFP display two pairs of Ni $2p_{3/2}$ and Ni $2p_{1/2}$ peaks corresponding to Ni²⁺ and Ni³⁺ (**Figure 4.7a**). The formation of Ni³⁺ in Ni(OH)₂ can be explained by the NO₃⁻ intercalation during the electrodeposition process. [26, 27] Additionally, two satellite peaks associated with Ni²⁺ species are observed. [28, 29] The XPS Ni 2p peaks of Ni(OH)₂/L-LFP exhibit a positive shift by 0.9 eV from Ni(OH)₂ peaks, indicating a reduced electron density around the Ni sites. This can be

ascribed to charge migration at the interface between Ni(OH)₂ and L-LFP.^[30] Furthermore, the Ni³⁺/Ni²⁺ peak intensity ratio escalates from 0.62 in Ni(OH)₂ to 1.22 in Ni(OH)₂/L-LFP (**Figure 4.7b**), denoting a higher proportion of Ni³⁺ species within the composite, which is known to promote the formation of NiOOH, the catalytically active species for OER.^[31] A similar shift of 2.2 eV is observed in the Fe 2*p* region of Ni(OH)₂/L-LFP (**Figure 4.7c**), indicating that Fe atoms in Ni(OH)₂/L-LFP are in a higher valence state, which is caused by Li leaching and electronic interplay with Ni(OH)₂. The O 1*s* spectrum of Ni(OH)₂/L-LFP is deconvoluted into three distinct peaks at 529.6, 530.35, 531.5, and 533.6 eV, which are ascribed to Fe–O bond, Ni–O bond, hydroxyl group, and adsorbed water molecules, respectively (**Figure 4.8a**).^[32-34] The negative shift of the Ni–O bond suggests the increased electron density around O. In the P 2*p* region, the P–O peak in Ni(OH)₂/L-LFP is shifted to a higher binding energy relative to L-LFP (**Figure 4.8b**), which suggests electron transfers from P to O.^[35] The Li 1*s* peak observed at 54.7 eV in L-LPF shifts to a lower binding energy (54.5 eV) with a notably diminished intensity upon integration with Ni(OH)₂ (**Figure 4.8c**) due to the Li⁺ leaching process.^[36]

The formation of an interface between Ni(OH)₂ and L-LFP is conducive to a redistribution of charge within the space charge layer that exists at the juncture of the electrode and solution. To assess the charge concentration, Mott–Schottky analysis was performed, which involved measuring the capacitance across a range of applied potentials.^[37] The Mott–Schottky plot for the Ni(OH)₂/L-LFP shows a carrier density $(1.25 \times 10^{23} \text{ cm}^{-3})$ ca. 1.6 times greater than that of pristine Ni(OH)₂ $(7.90 \times 10^{22} \text{ cm}^{-3})$, as shown in **Figure 4.9**. This enhancement in charrier density indicates that the Ni(OH)₂/L-LFP interface provides an increased number of charges that can be mobilized for participation in the catalytic reactions, potentially leading to improved catalytic performance.

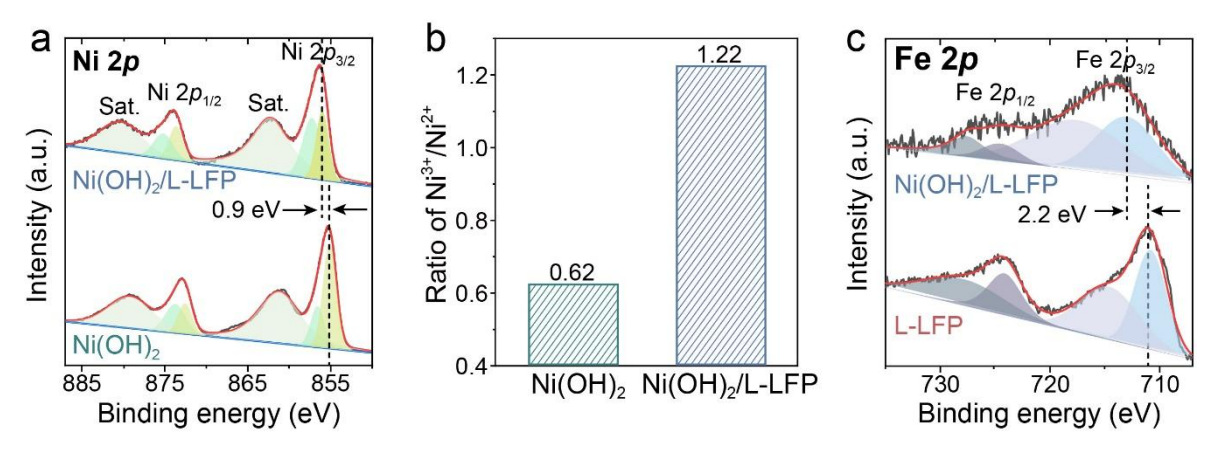


Figure 4.7. (a) XPS Ni 2p spectra of Ni(OH)₂ and Ni(OH)₂/L-LFP. (b) Comparison of the Ni³⁺/Ni²⁺ ratios in Ni(OH)₂ and Ni(OH)₂/L-LFP. (c) XPS Fe 2p spectra of LFP and Ni(OH)₂/L-LFP.

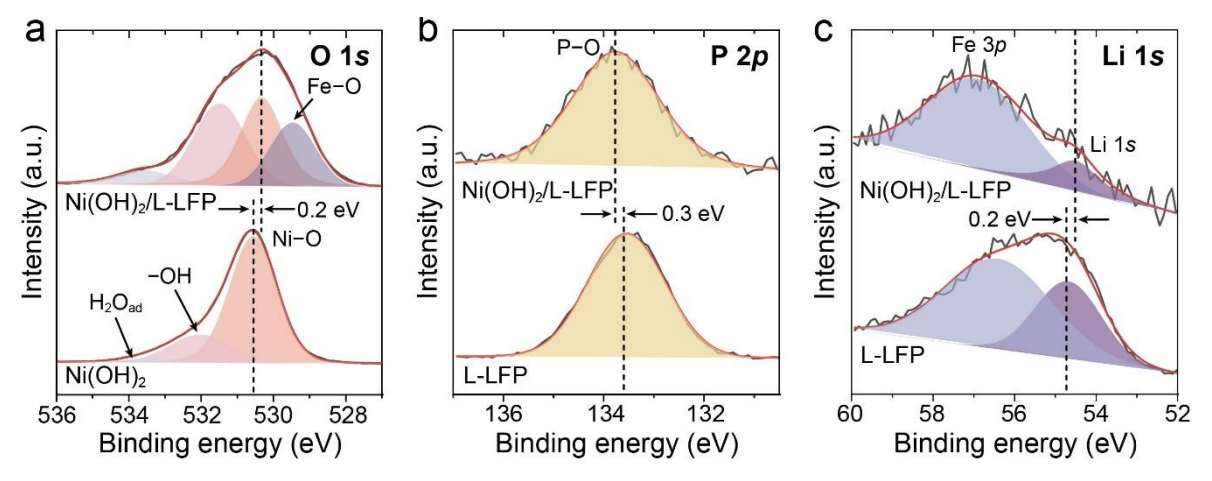


Figure 4.8. XPS (a) O 1s spectra of Ni(OH)₂ and Ni(OH)₂/L-LFP. XPS (b) P 2p and (c) Li 1s spectra of LFP and Ni(OH)₂/L-LFP.

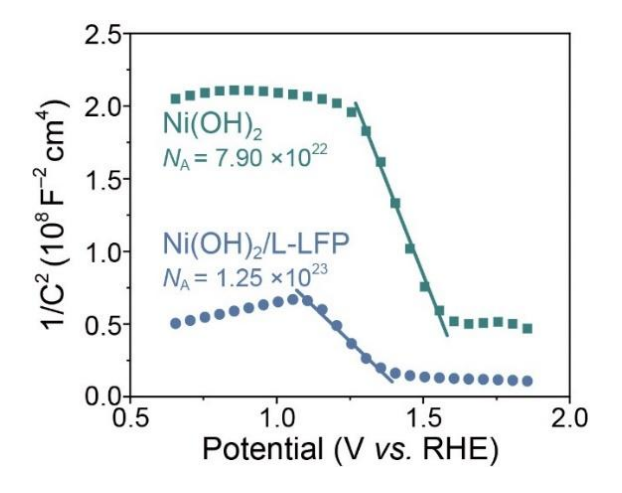


Figure 4.9. Mott Schottky plots of Ni(OH)₂ and Ni(OH)₂/L-LFP.

4.4.2. Electrochemical OER Performance and Mechanism

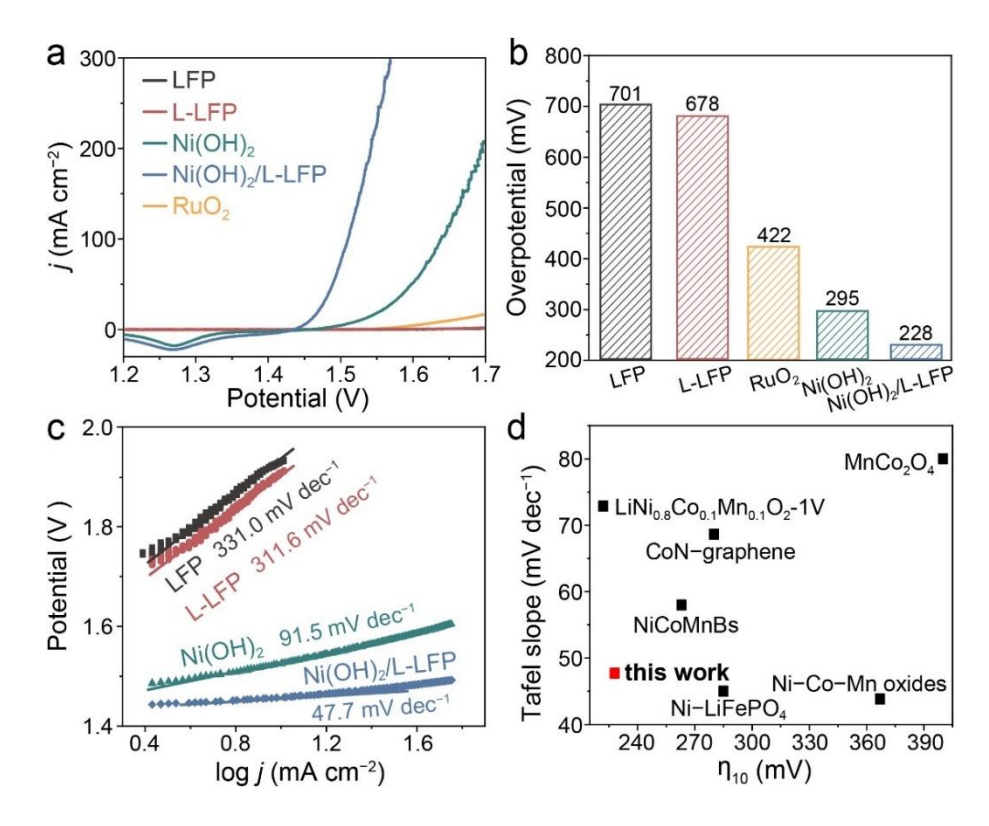


Figure 4.10. (a) LSV curves of LFP, L-LFP, Ni(OH)₂, Ni(OH)₂/L-LFP, and commercial RuO₂. (b) The corresponding comparison of the OER overpotentials of samples required to achieve a current density of 10 mA cm⁻². (c) Tafel slopes of LFP, L-LFP, Ni(OH)₂, and Ni(OH)₂/L-LFP. (d) Comparison of overpotential at 10 mA cm⁻² and Tafel slope of Ni(OH)₂/L-LFP with other electrocatalysts based on recycled LIBs.

The OER activity of the as-prepared samples was evaluated in an O₂-saturated 1 M KOH using a standard three-electrode setup. The LSV with *i*R correction, recorded at a scan rate of 2 mV s⁻¹, are compared in **Figure 4.10a**. Notably, the Ni(OH)₂/L-LFP achieves a current density of 10 mA cm⁻² at a significantly reduced overpotential (η₁₀) of 228 mV, which is markedly lower than that of Ni(OH)₂ (295 mV), L-LFP (678 mV), LFP (701 mV), and commercial RuO₂ (422 mV, **Figure 4.10b**). Tafel analysis derived from the polarization curves reveals that Ni(OH)₂/L-LFP possesses the most favorable Tafel slope of 47.7 mV dec⁻¹ among all the samples investigated (**Figure 4.10c**), indicating its rapid reaction kinetics. This OER performance of

Ni(OH)₂/L-LFP is superior to or compatible with other state-of-the-art catalysts, including those recycled from LIBs, as evidenced by the comparative data in **Figure 4.10d** and **Table 4.2**.

Table 4.2. Comparison of electrocatalytic performance of Ni(OH)₂/L-LFP in 1 M KOH with previously reported materials based on recycled lithium-ion batteries.

Samples	Overpotential (mV, at 10 mA cm ⁻²)	Tafel Slope (mV dec ⁻¹)	Ref.
Ni(OH) ₂ /L-LFP	228	47.7	this work
NiCoMnBs	263	57.98	[38]
Recovered MnCo ₂ O ₄	400	80	[39]
Ni-Co-Mn oxides	367	43.84	[40]
CoN-graphene	280	68.83	[41]
Ni-LiFePO ₄	285	68.83	[42]
$LiNi_{0.8}Co_{0.1}Mn_{0.1}O_{2}1V$	222	72.9	[43]

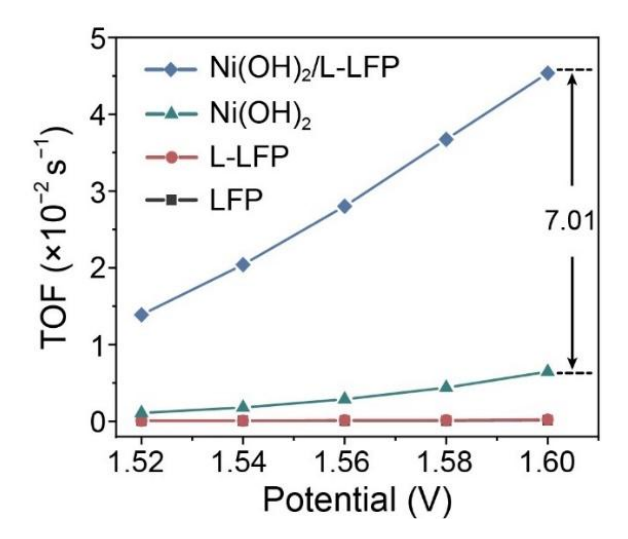


Figure 4.11. TOF values of LFP, L-LFP, Ni(OH)₂, and Ni(OH)₂/L-LFP in a range of applied potentials.

The TOF, an important parameter for assessing the intrinsic activity of electrocatalysts, is given in **Figure 4.11**. The Ni(OH)₂/L-LFP demonstrates a high TOF value of 0.0454 s⁻¹, which

is approximately sevenfold greater than that of Ni(OH)₂ (0.0065 s⁻¹). This indicates an enhancement in the intrinsic activity afforded by the construction of heterojunctions in Ni(OH)₂/L-LFP. The OER performance of Ni(OH)₂/L-LFP is highly influenced by the conditions of the sample preparation process, as detailed in **Figures 4.12 and 4.13** and **Table 4.3**. Specifically, three samples were synthesized using only two steps among laser ablation, charging, and electrodeposition to investigate how the synthetic steps affect the catalyst's properties. Notably, the sample prepared without electrodeposition shows the lowest OER performance, as evidenced by a high overpotential of 544 mV at 10 mA cm⁻² (**Table 4.3**), which suggests that the loading of Ni(OH)₂ is crucial for OER activity (**Figure 4.12c**). The Ni(OH)₂/L-LFP of Ni/(Li + Fe + Ni) ratio ca. 0.75 exhibits the best OER performance (**Figures 4.13**).

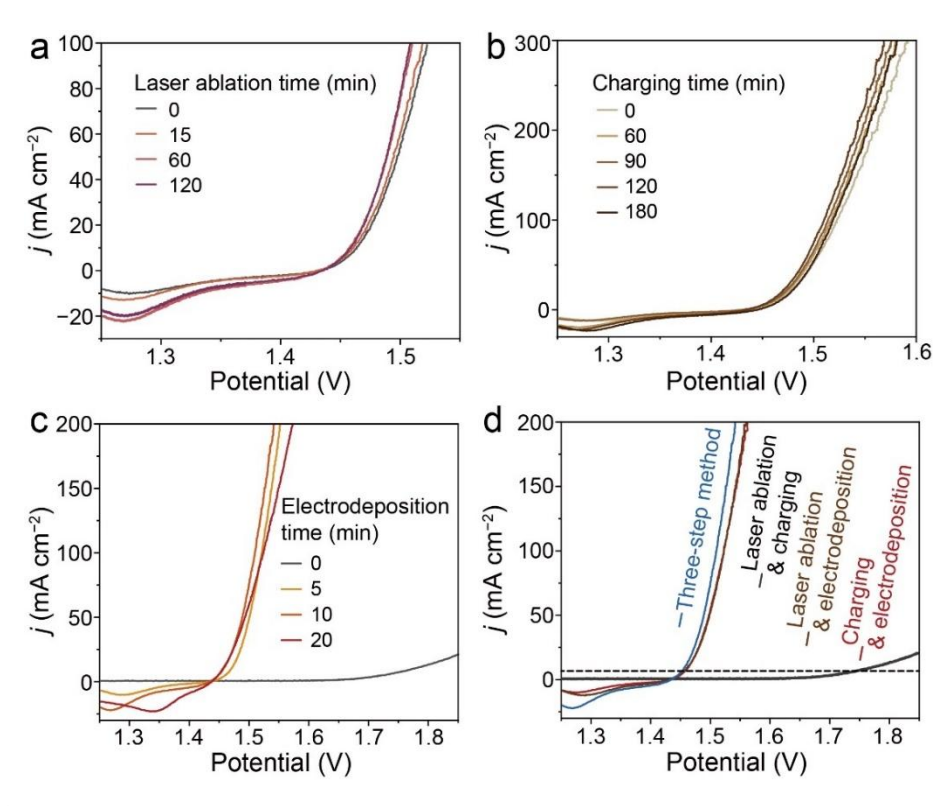


Figure 4.12. LSV curves of samples prepared with various (a) laser ablation times, (b) charging time, and (c) electrodeposition time. (d) LSV curves of samples synthesized through two-step methods (laser ablation & electrodeposition, charging & electrodeposition, and laser ablation & charging).

Table S3. Overpotentials of samples synthesized through two-step methods (laser ablation & electrodeposition, charging & electrodeposition, and laser ablation & charging) to reach 10 mA cm⁻².

Sample preparation	Overpotential (mV, at 10 mA cm ⁻²)
Charging & electrodeposition	234
Laser ablation & electrodeposition	232
Laser ablation & charging	544
Three steps	228

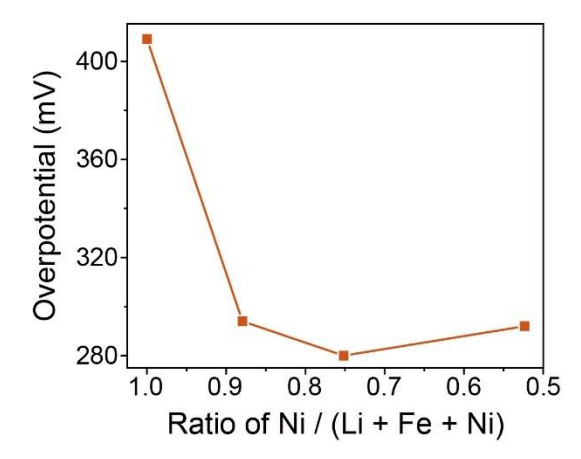


Figure 4.13. Relation between overpotential at 100 mA cm⁻² and Ni/(Ni + Fe + Li) ratio.

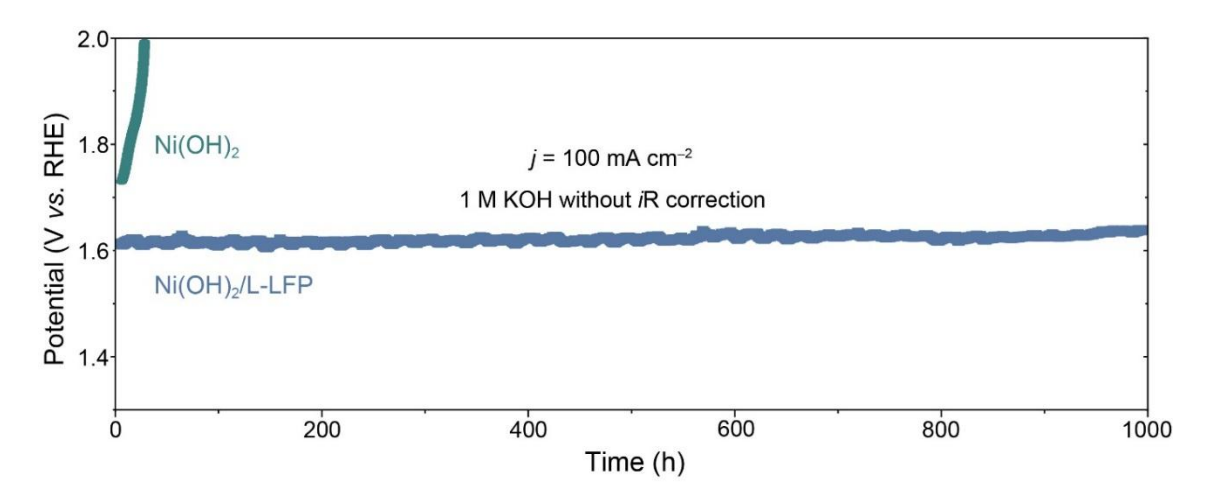


Figure 4.14. Chronopotentiometric curves of Ni(OH)₂ and Ni(OH)₂/L-LFP in 1 M KOH.

Operational stability is another crucial metric for evaluating electrocatalysts. To this end, long-term chronopotentiometry was conducted to ascertain the electrocatalytic durability of

Ni(OH)₂/L-LFP during OER in 1 M KOH. Impressively, Ni(OH)₂/L-LFP demonstrates exceptional stability, maintaining a current density of 100 mA cm⁻² in alkaline freshwater over 1,000 h (**Figure 4.14**). In contrast, Ni(OH)₂ exhibits a gradual decline in activity, ceasing within 26 h.

To elucidate the mechanism responsible for the enhanced OER performance, EIS was conducted to probe the charge transfer dynamics, with the corresponding Nyquist plots presented in **Figure 4.15**. The impedance at the solid–liquid interface (R_{ct}) for Ni(OH)₂ (117.1 Ω) is significantly reduced to 1.34 Ω when hybridized with LFP, indicating the interfacial effects in lowering the charge transfer barrier. Additionally, the ECSA of the as-prepared catalysts was estimated by measuring the electrochemical C_{dl} in a non-Faradaic potential region at varying scan rates (**Figures 4.16** and **4.17a**). The Ni(OH)₂/L-LFP exhibits the largest ECSA, which is 3.4 and 28.3 times larger than that of Ni(OH)₂ and LFP, respectively (**Figure 4.17b**). This suggests that the construction of the heterointerface provides a larger surface area with more accessible active sites for the OER. When the polarization curves are normalized by ECSA, it is evident that the intrinsic OER activity of Ni(OH)₂/L-LFP surpasses that of Ni(OH)₂ and LFP (**Figure 4.17c**).

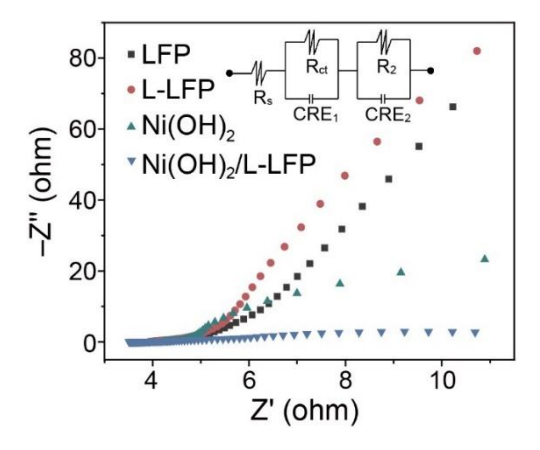


Figure 4.15. EIS curves of LFP, L-LFP, Ni(OH)₂, and Ni(OH)₂/L-LFP. The inserted image is an equivalent circuit, in which R_s stands for the electrolyte resistance, CPE₁ represents double-layer capacitance, R_{ct} is related to the interfacial charge transfer reaction, and CPE₂ and R_2 are associated with the dielectric properties and the resistance of the electrode itself.

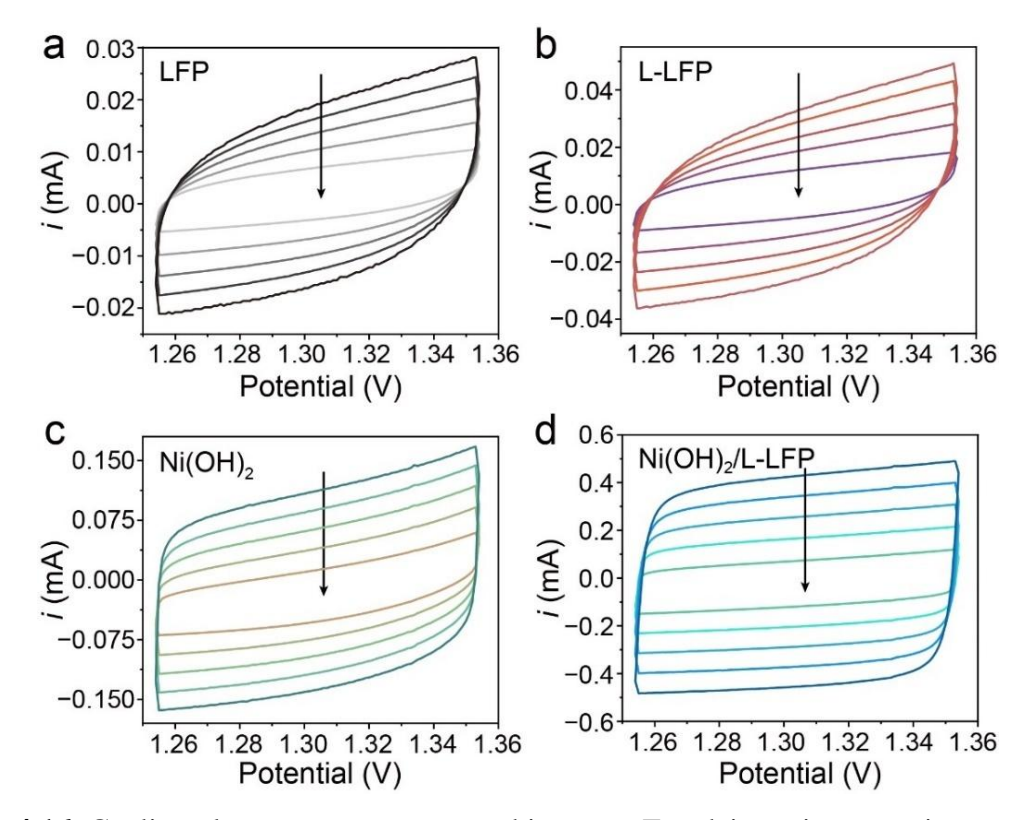


Figure 4.16. Cyclic voltammograms measured in a non-Faradaic region at various scan rates. (a) LFP, (b) L-LFP, (c) Ni(OH)₂, and (d) Ni(OH)₂/L-LFP. The scan rate decreased from 250 to 50 mV s^{-1} .

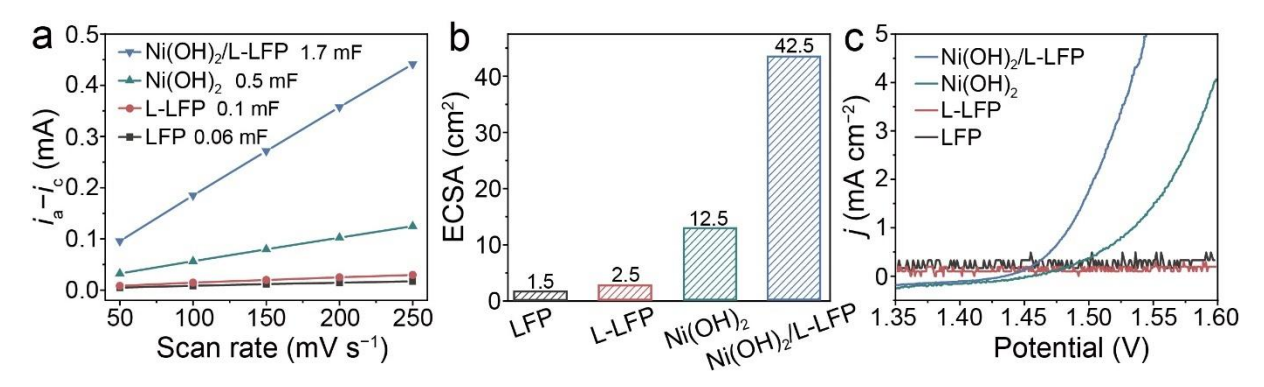


Figure 4.17. (a) Linear fitting of double-layer capacitance (C_{dl}) *vs.* CV scan rate for the estimation of electrochemically active surface area of different catalysts of LFP, L-LFP, Ni(OH)₂, and Ni(OH)₂/L-LFP. (b) ECSA and (c) ECSA-normalized LSV curves of LFP, L-LFP, Ni(OH)₂, and Ni(OH)₂/L-LFP.

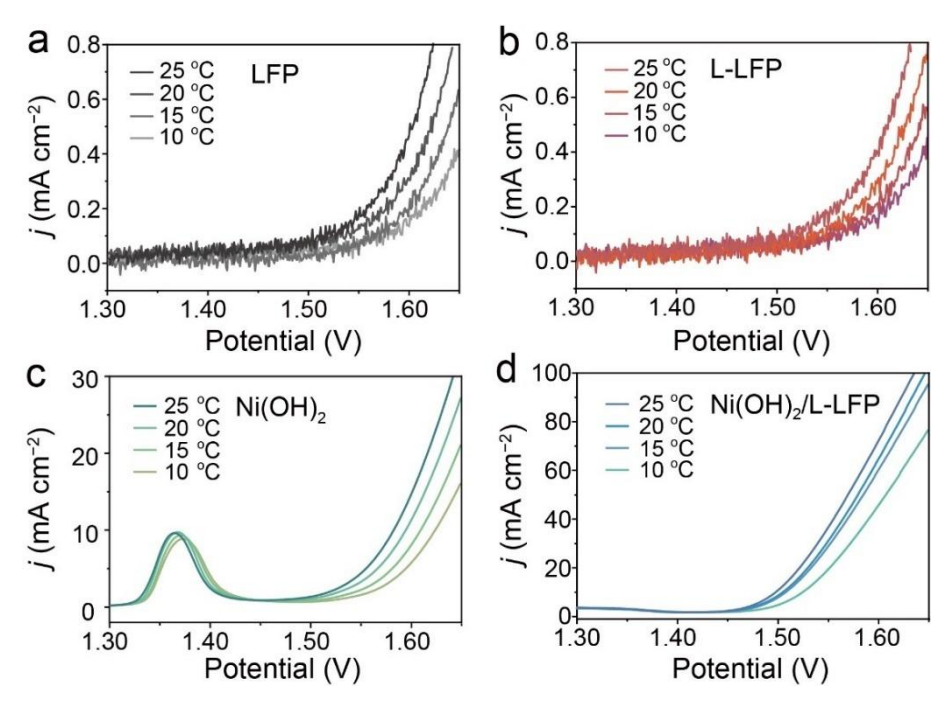


Figure 4.18. LSVs measured at various temperatures: (a) LFP, (b) L-LFP, (c) Ni(OH)₂, and (d) Ni(OH)₂/L-LFP.

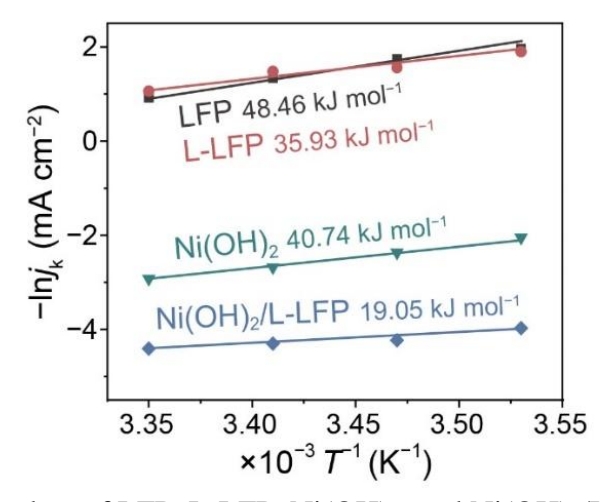


Figure 4.19. Arrhenius plots of LFP, L-LFP, Ni(OH)₂, and Ni(OH)₂/L-LFP.

Furthermore, the Arrhenius plots for LFP, L-LFP, Ni(OH)₂, and Ni(OH)₂/L-LFP (**Figure 4.19**), derived from LSVs at various temperatures (**Figure 4.18**) provide additional insights. The E_a , deduced from the slope of the Arrhenius plot, is the lowest for Ni(OH)₂/L-LFP (19.05 kJ mol⁻¹), followed by L-LFP (35.93 kJ mol⁻¹), Ni(OH)₂ (40.74 kJ mol⁻¹), and LFP (48.46 kJ

mol⁻¹). The formation of heterojunction between Ni(OH)₂ and L-LFP significantly reduces the kinetic barrier for electrocatalytic water.

4.4.3. Seawater OER and Overall Seawater Splitting Performance

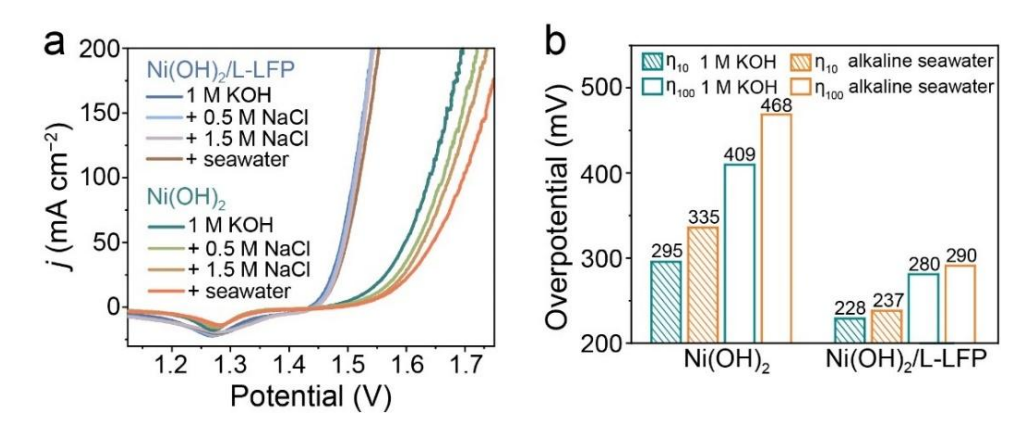


Figure 4.20. (a) LSV curves and (b) the corresponding overpotentials of Ni(OH)₂/L-LFP and Ni(OH)₂ in saline water and alkaline seawater oxidation.

The OER activity of Ni(OH)₂/L-LFP was further assessed in saline and alkaline natural seawater electrolytes to evaluate its potential for seawater electrolysis application. As shown in **Figure 4.20a**, Ni(OH)₂/L-LFP demonstrates superior OER performance with minimal activity decline in saline water electrolytes, indicating that the presence of highly concentrated Cl⁻ ions exerts a negligible influence on its catalytic activity. Importantly, its overpotentials at 10 and 100 mA cm⁻² in seawater only show a slight increase of 10 mV, which is a much smaller rise compared to that of Ni(OH)₂ (**Figure 4.20b**). This suggests that Ni(OH)₂/L-LFP possesses enhanced selectivity for the OER process. Additionally, Ni(OH)₂/L-LFP achieves a high average FE of 95.8 % at a high current density of 100 mA cm⁻² in alkaline seawater (**Figure 4.21a**). To confirm the high selectivity of Ni(OH)₂/L-LFP for OER against the hypochlorite reaction, iodide titration was conducted to detect the generation of reactive chlorine species. [46] The absence of a characteristic absorption peak for hypochlorite ions in the post-FE test electrolyte (**Figure 4.21c**) further corroborates the high OER selectivity of Ni(OH)₂/L-LFP.

To explore the practical application of seawater splitting, a solar cell was employed to power a Ni(OH)₂/L-LFP||Pt/C electrolysis system. An H-type electrolytic configuration with an anion exchange membrane for overall seawater splitting is schematically shown in **Figure 4.22**, which can be used to collect the produced H₂ and O₂ gases through a water drainage strategy. A solar cell was used for power supply. The Pt/C on nickel foam (cathode) was coupled with the Ni(OH)₂/L-LFP anode in this electrolytic configuration. Impressively, 10.2 mL H₂ and 5.1 mL O₂ could be achieved with 30 min examination. This matches well with the theoretical volume ratio of 2:1, suggesting an FE of approximately 100 % toward overall water splitting. This confirms its feasibility in practical application.

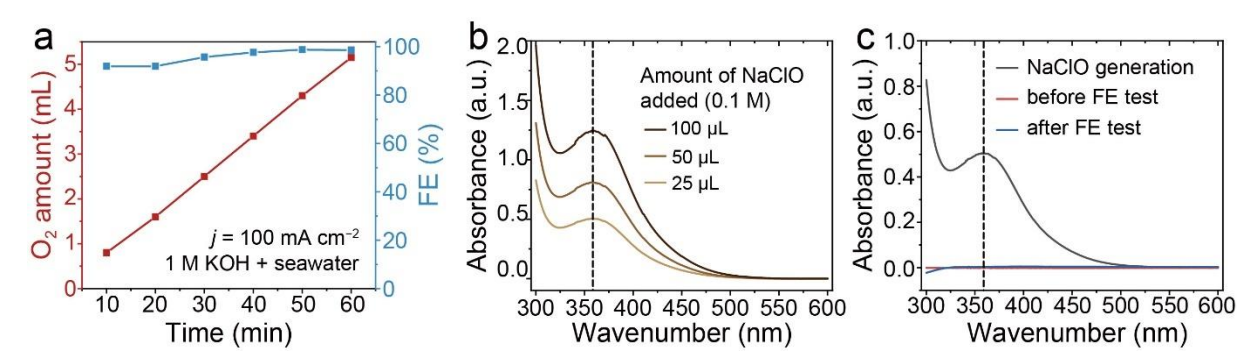


Figure 4.21. (a) FE (blue squares) of Ni(OH)₂/L-LFP measured at 100 mA cm⁻² in seawater + 1 M KOH. Red squares show the amount of O₂ generated during the FE test. UV–Vis spectra of (b) iodide titration with various NaClO concentrations and (c) electrolytes before and after the FE test.

The long-term electrocatalytic durability of Ni(OH)₂ and Ni(OH)₂/L-LFP during the OER in seawater was evaluated by chronopotentiometry. Remarkably, Ni(OH)₂/L-LFP maintains excellent stability at a current density of 100 mA cm⁻² in natural seawater + 1 M KOH over 600 h (**Figure 4.23**). Although there is a slight increase (3.3 %) in the potential required to sustain 100 mA cm⁻² for seawater OER, this is significantly less than the 6.3 % increase observed for Ni(OH)₂ within just 2 h. This further demonstrates the superior long-term durability of Ni(OH)₂/L-LFP in seawater oxidation. Ni element in the saline-water electrolyte

(0.5 M NaCl + 1 M KOH) leaching from electrodes was monitored. When Ni(OH)₂ was used as the electrode, the concentration of Ni element in the electrolyte increased continuously from 0 to 0.28 ppm during the 2-h operation (**Figure 4.30**), suggesting the loss of Ni active species. For Ni(OH)₂, however, the concentration of Ni in the electrolyte only increased to 0.02 ppm at 1.5 h and was maintained at the same level when the time was extended to 2 h, indicating the enhanced anti-corrosion characteristics.



Figure 4.22. The image of seawater splitting of Ni(OH)₂/L-LFP||Pt/C in an H-type cell driven by a solar cell in nature.

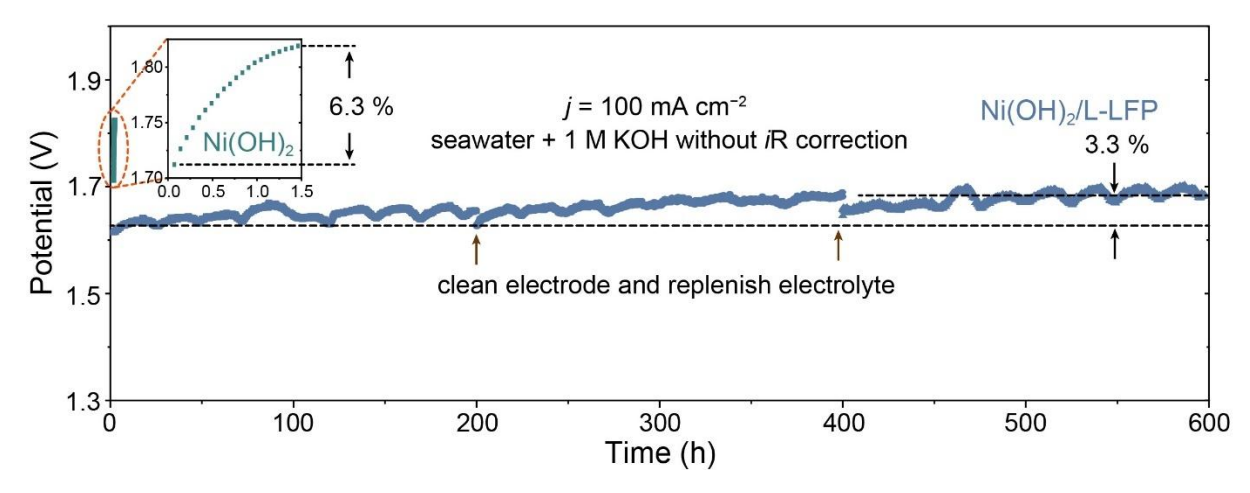


Figure 4.23. Chronopotentiograms of Ni(OH)₂ and Ni(OH)₂/L-LFP in alkaline seawater.

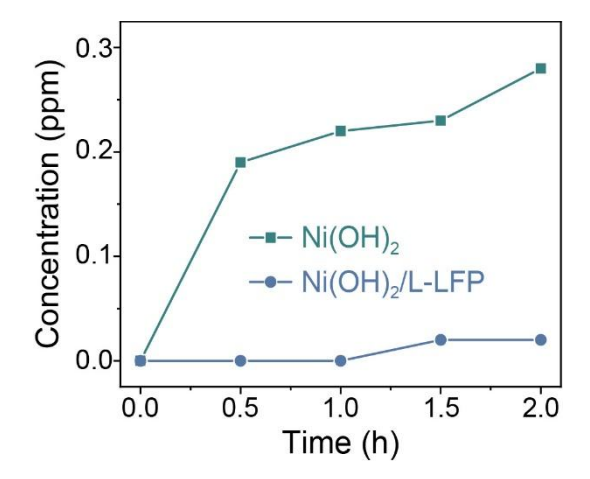


Figure 4.24. The change in concentration of Ni in electrolytes was observed during the stability test using Ni(OH)₂ and Ni(OH)₂/L-LFP, respectively.

Post-electrolysis SEM image of Ni(OH)₂/L-LFP reveals that its morphology remains unchanged (**Figure 4.25**), supporting its high corrosion resistance in seawater. However, EDS mapping images detect the deposition of additional Ca and Mg atoms, likely due to the formation of insoluble Ca(OH)₂ and Mg(OH)₂ on the catalyst surface during OER. These deposits can obscure active sites, potentially contributing to the increased potential required for sustained long-term alkaline seawater oxidation.

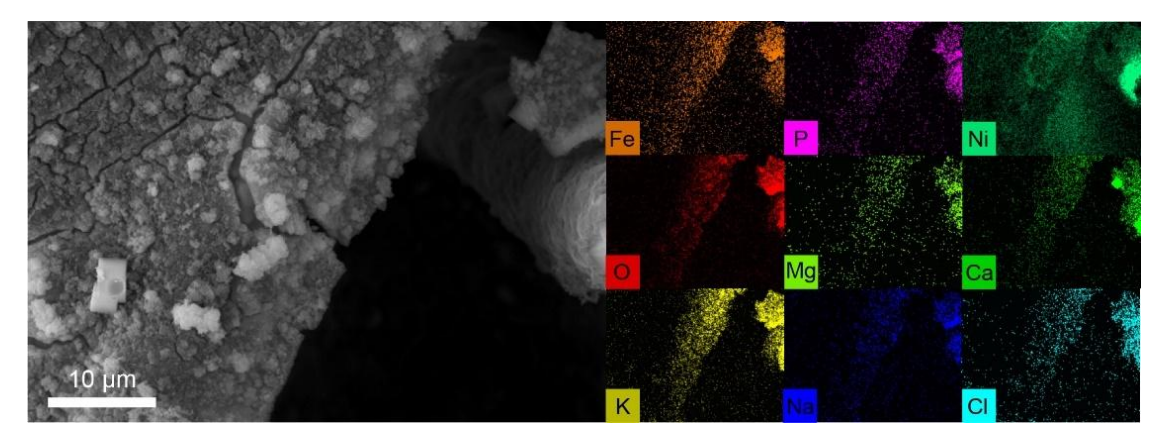


Figure 4.25. SEM and the corresponding EDS mapping images of Ni(OH)₂/L-LFP after the long-term seawater OER in a three-electrode configuration.

To assess the scalability of the Ni(OH)₂/L-LFP catalysts for potential industrial applications, the electrode size was expanded from 0.25 to 25 cm² (**Figure 4.26a**). Subsequently, a 1 cm²-piece of Ni(OH)₂/L-LFP (catalyst loading = 1 mg cm⁻²) was paired with Pt/C (1 mg cm⁻²) to serve as the anode and cathode, respectively, in an MEA, as depicted in **Figure 4.26b**. The setup of the electrolysis system is shown in **Figure 4.26c**. In a 1 M KOH seawater at 23 °C, the Ni(OH)₂/L-LFP||Pt/C system delivers 100 mA cm⁻² at a cell voltage of only 1.799 V (**Figure 4.26d**), which is significantly lower than the commercial RuO₂||Pt/C system (2.165 V). The overall seawater splitting performance is further enhanced in a mixture of 6 M KOH and seawater at 60 °C, where the system operates at an even lower voltage of 1.668 V to reach the same current density. Importantly, the Ni(OH)₂/L-LFP||Pt/C flow cell demonstrates stable operation for 100 h at 250 mA cm⁻² with minimal performance degradation (**Figure 4.27**).

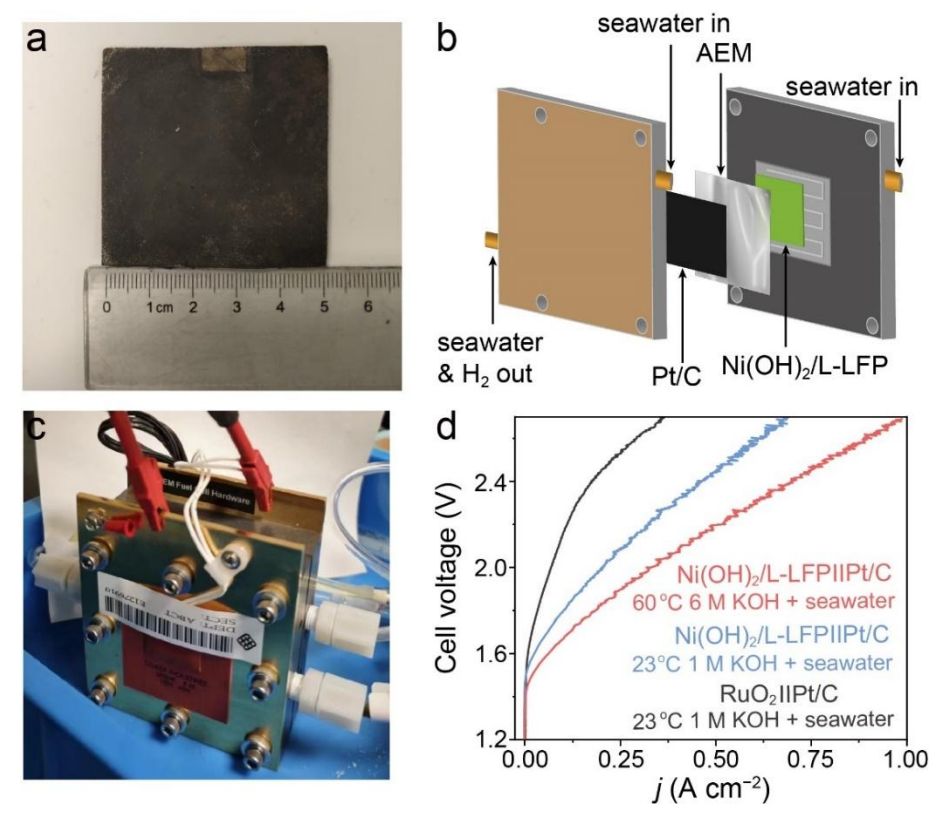


Figure 4.26. (a) A photo of Ni(OH)₂/L-LFP on nickel foam scaled up to 25 cm². (b) A photo of the flow cell water splitting system. (c) A photo of the flow cell water splitting system. (d) The polarization curve of MEA was measured in alkaline seawater.

The energy costs associated with H₂ production using the Ni(OH)₂/L-LFP system are calculated to be 4.76 and 5.85 kWh Nm⁻³ H₂ at current densities of 0.2 and 0.5 A cm⁻², respectively (**Figure 4.28**). These figures are substantially lower than those for the RuO₂||Pt/C system (5.87 and 6.77 kWh Nm⁻³ H₂), which highlights the potential of the Ni(OH)₂/L-LFP system for practical H₂ production from seawater, offering a more energy-efficient alternative to current commercial systems.

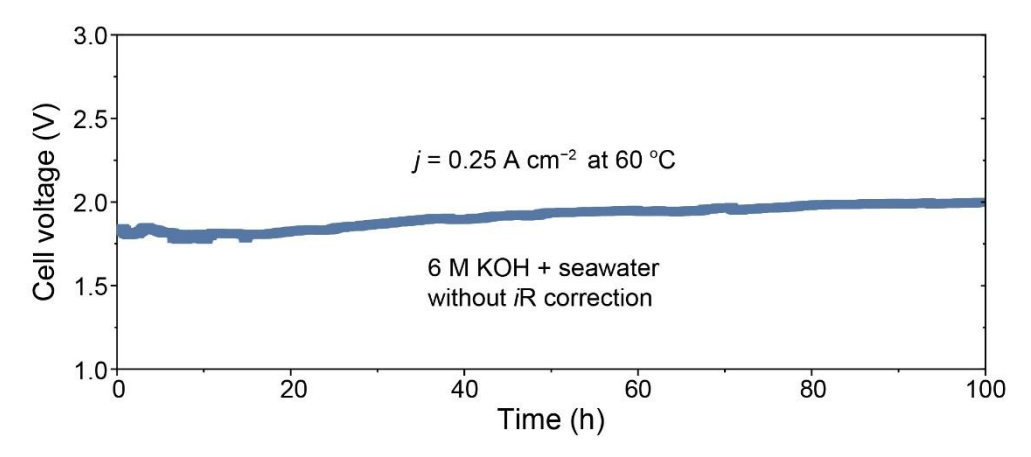


Figure 4.27. Chronopotentiograms of Ni(OH)₂/L-LFP||Pt/C measured at 250 mA cm⁻² in alkaline seawater.

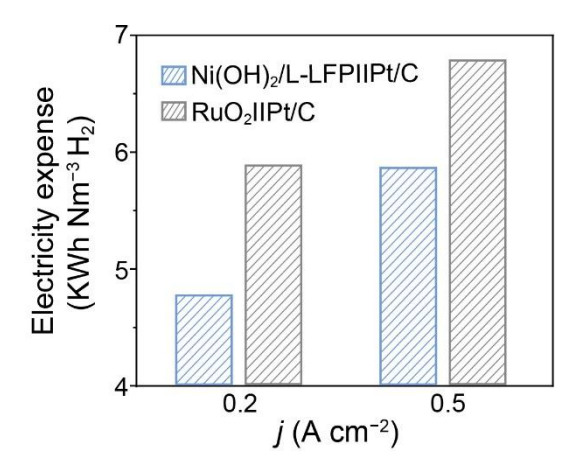


Figure 4.28. Electricity expense of different catalysts systems.

4.4.4. OER mechanism and anti-corrosion property of Ni(OH)₂/L-LFP

In situ Raman spectroscopy was employed to track the real-time evolution of surface species as the applied potential was varied. **Figure 4.29a** shows the Raman spectra of Ni(OH)₂, captured from the open-circuit potential (OCP) to an applied potential of 1.511 V (vs. RHE). At 1.411 V, the emergence of characteristic NiOOH peaks, associated with the Ni³⁺(e_g)–O and Ni³⁺(a_{1g})–O vibration modes, are observed at 476 (peak **i**) and 558 cm⁻¹ (peak **ii**), respectively. These peaks signify the transformation to NiOOH during the OER process. The intensity ratio of these peaks (I₅₅₈/I₄₇₆) increases from 1.2 at 1.411 V to 2.0 at 1.461 V (**Figure 4.29b**). The pronounced increase in the intensity of peak **ii** relative to peak **i** suggests

a phase transition from the initial γ-NiOOH to the more active β-NiOOH phase at elevated anodic potentials. ^[48, 49] A similar trend is evident in the Raman spectra of Ni(OH)₂/L-LFP (**Figure 4.29c**); however, the transition to the β-NiOOH phase occurs at a lower potential, as reflected by a higher I_{558}/I_{476} ratio of 1.71 at 1.411 V. This earlier onset of the β-NiOOH phase formation is corroborated by the lower OER onset potential observed for Ni(OH)₂/L-LFP (1.428 V) compared to that of Ni(OH)₂ (1.443 V, **Figure 4.30**). Additionally, the appearance of a new peak at 974 cm⁻¹, which can be attributed to the PO₃⁴⁻ vibration, is likely due to the release from the LPF during the reconstruction process.

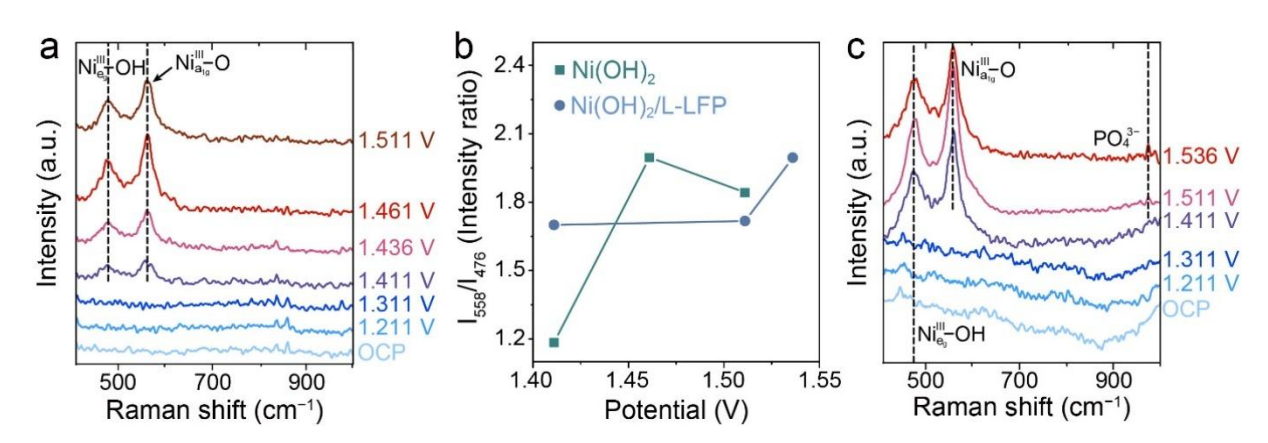


Figure 4.29. *In situ* Raman spectra of Ni(OH)₂. (b) Intensity ratio of peak **ii** to peak © at various applied potentials. (c) *In situ* Raman spectra of Ni(OH)₂/L-LFP.

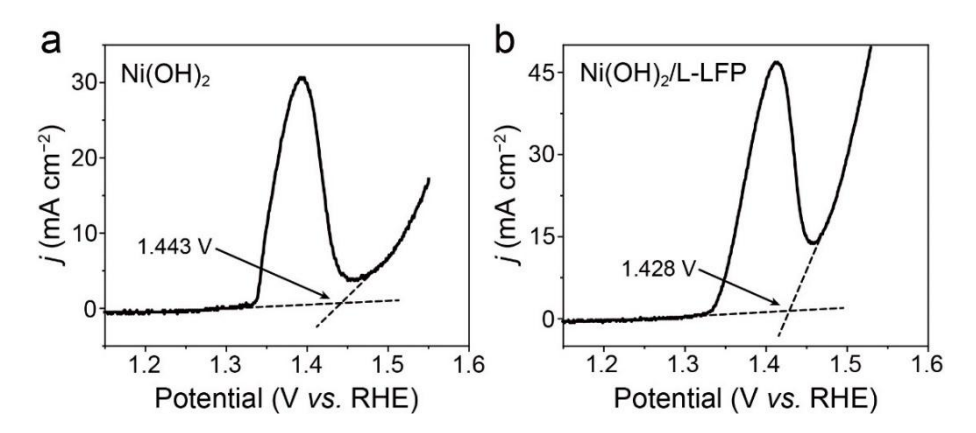


Figure 4.30. Onset potentials of (a) Ni(OH)₂ and (b) Ni(OH)₂/L-LFP.

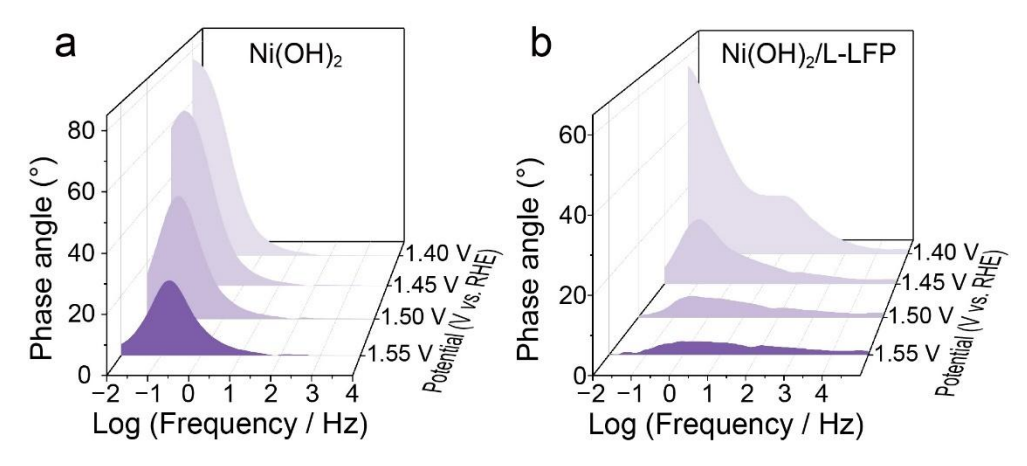


Figure 4.31. Bode phase plots of (a) Ni(OH)₂ and (b) Ni(OH)₂/L-LFP obtained from *operando* EIS.

Operando EIS serves as a powerful technique for probing interfacial dynamics and electron transfer mechanisms during electrochemical reactions. **Figures 4.31a** and **4.31b** present the Bode plots for Ni(OH)₂ and Ni(OH)₂/L-LFP, respectively. The low-frequency domain (0.01 – 10 Hz) is indicative of the OER interfaces, while the high-frequency region (10 – 10⁵ Hz) is related to surface oxidation processes. ^[50, 51] As the applied potential increases, a notable reduction in the phase angles at low frequencies is observed for both samples. At 1.55 V, the phase angle for Ni(OH)₂ is approximately 24°, whereas, for Ni(OH)₂/L-LFP, it approaches zero, indicating a more expedited OER rate at the interface for the latter. The presence of a second peak in the high-frequency region, exclusive to Ni(OH)₂/L-LFP, is attributed to the oxidation of LFP, which vanishes at higher potentials. This electrooxidation process, transforming LiFePO₄ to Fe₃(PO₄)₂, is supported by the post-OER XRD pattern of Ni(OH)₂/L-LFP (**Figure 4.32a**). The identification of two lattice spacings of 2.39 and 3.51 Å (**Figure 4.32b**), corresponding to the (011) and (210) planes of NiOOH and Fe₃(PO₄)₂, respectively, suggests the formation of a new NiOOH/Fe₃(PO₄)₂ (NiOOH/FP) interface following OER activation.

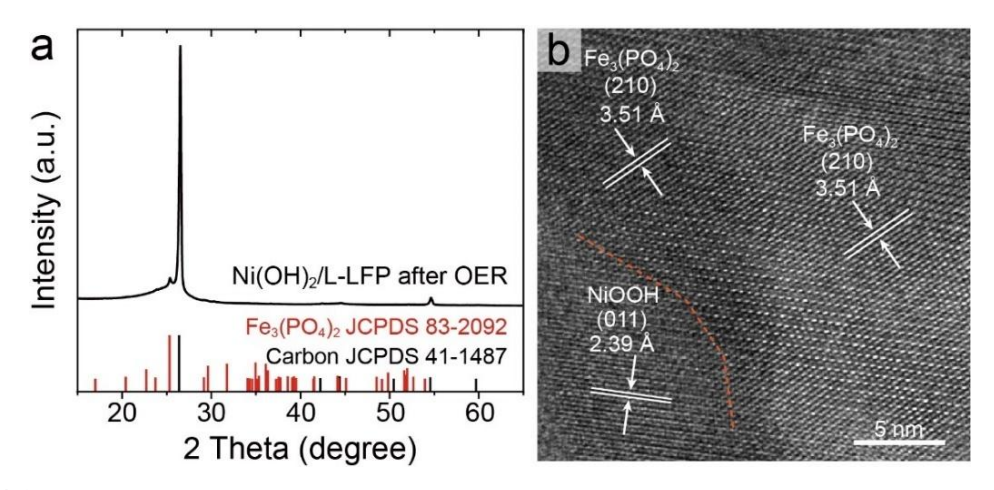


Figure 4.32. (a) XRD pattern of Ni(OH)₂/L-LFP after OER. (b) The TEM image of Ni(OH)₂/L-LFP after OER.

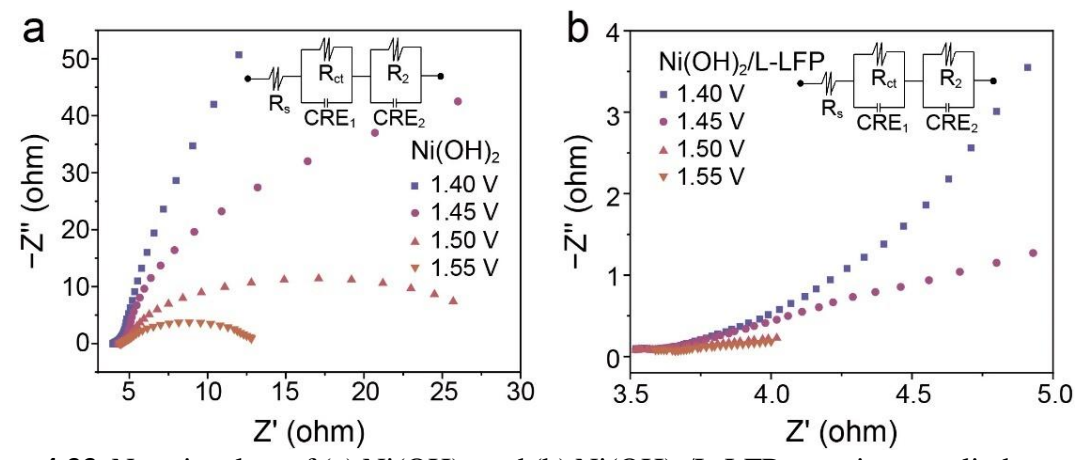


Figure 4.33. Nyquist plots of (a) Ni(OH)₂ and (b) Ni(OH)₂/L-LFP at various applied potentials.

Furthermore, Nyquist plots provide insights into the internal and interfacial resistances of the samples under varying potentials (**Figure 4.33** and **Tables 4.4** and **4.5**). As depicted in **Figure 4.34a**, Ni(OH)₂/L-LFP consistently demonstrates lower resistances, both within the electrode and at the electrode/electrolyte interface, compared to Ni(OH)₂, indicating enhanced conductivity and charge transfer efficiency.

Table 4.4. Inside resistances of catalysts at various applied potentials

Potential (V) —	Resistance (Ω)		
	Ni(OH)2	Ni(OH)2/L-LFP	
1.40	1.14	0.16	
1.45	0.91	0.13	
1.50	0.96	0.22	
1.55	0.74	0.13	

Table 4.5. Resistances of catalyst/electrolyte interfaces at various applied potentials.

D-44'-1 (T/)	Resistance (Ω)		
Potential (V) —	Ni(OH) ₂	Ni(OH) ₂ /L-LFP	
1.40	33810	10.730	
1.45	117.1	1.336	
1.50	24.450	0.954	
1.55	8.466	1.051	

To understand the charge transition dynamics within Ni(OH)₂/L-LFP, the valence states of Fe and Ni after OER activation were examined using XPS (**Figures 4.34b** and **4.34c**). The Fe 2*p* peaks shift by 0.32 eV toward lower binding energies, indicating an electron density increase around Fe atoms. Conversely, the Ni 2*p* spectra reveal a shift of 0.46 eV toward higher binding energies, accompanied by a 2.8-fold increase in the Ni³⁺/Ni²⁺ ratio after OER activation (**Figure 4.34d**), suggesting a decrease in electron density around Ni atoms. These observations imply that electrons are transferred from Ni to Fe, mediated by the Fe–O–Ni bond, which then facilitates their subsequent transfer to the external circuit, thereby enhancing charge migration during the OER process.^[52] Following a 100-h stability test in seawater, the XPS spectra for Fe and Ni show no significant changes, and the Ni³⁺/Ni²⁺ ratio remains at 2.58, affirming the robust anti-corrosion characteristics of Ni(OH)₂/L-LFP.

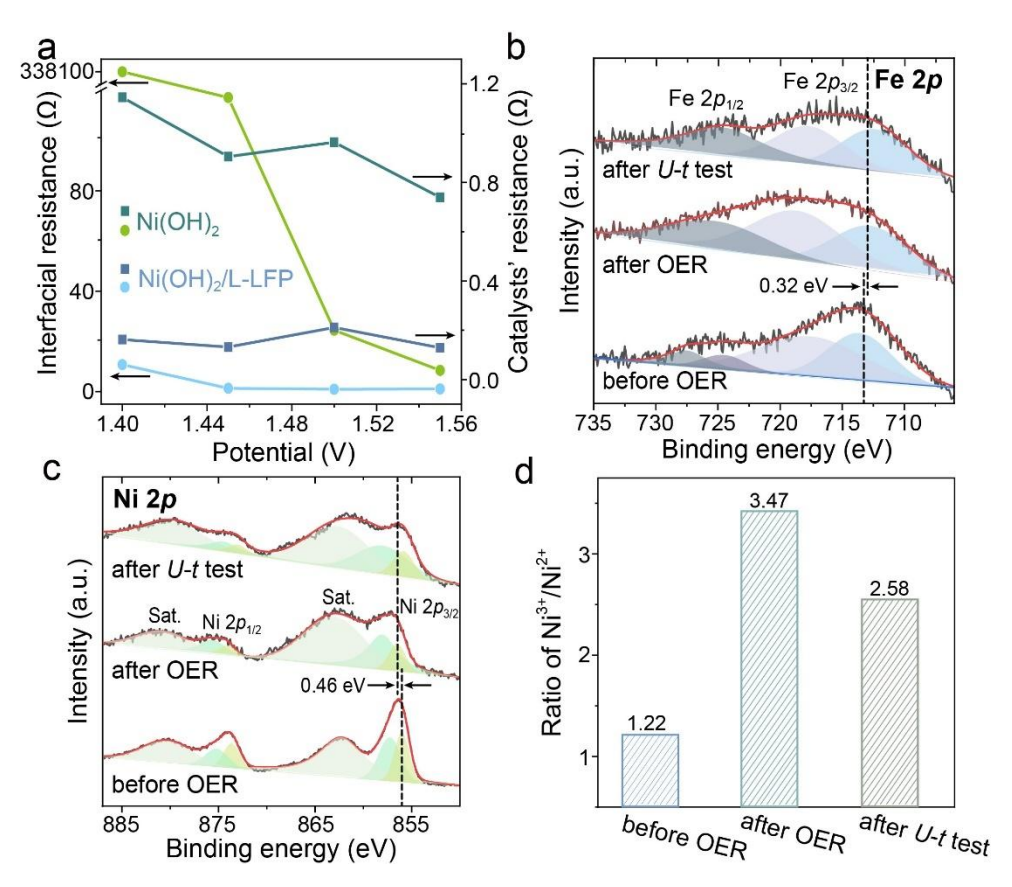


Figure 4.34. (a) The interfacial and catalysts' resistance at various potentials. XPS (b) Fe 2p and (c) Ni 2p spectra of Ni(OH)₂/L-LFP before OER, after OER, and after the 100-h stability (*U*-t) test. (d) The corresponding intensity ratio of Ni³⁺ to Ni²⁺ peaks.

Quasi-in-situ UV-Vis spectroscopy, utilizing the ammonium molybdate spectrophotometry method, was employed to verify the release of PO₄³⁻ anion (**Figure 4.35a**). When a potential of 3.5 V is applied to Ni(OH)₂/L-LFP in a two-electrode system, an absorption peak for PO₄³⁻ appears at around 850 nm after 4 min (**Figure 4.35b**). This peak gradually intensifies with prolonged oxidation time, further substantiating the release of PO₄³⁻ from LFP during the OER process. Notably, the PO₄³⁻ anions, which form around NiOOH/FP under the influence of the positive potential, can repel and obstruct Cl⁻ through electrostatic repulsion, thereby mitigating corrosion during seawater oxidation (Figure 4.36a).^[53] Concurrently, the robust hydrogen bonding between OH⁻ and NiOOH can prevent electrostatic repulsion from hindering OH⁻ diffusion, ensuring rapid OER kinetics^[54, 55]. This is supported by the OCP measurements, which reflect the extent of Cl⁻ adsorption on the Helmholtz layer;

the greater the influence of the catalyst surface on Cl⁻, the more profound the shift in OCP upon introducing an equivalent concentration of Cl⁻.^[56, 57] A significant decrease in OCP of 21 mV is observed for Ni(OH)₂ compared to Ni(OH)₂/L-LFP upon adding 1.5 M NaCl to the electrolyte (**Figure 4.36b**), indicating a reduced impact of Cl⁻ on Ni(OH)₂/L-LFP.

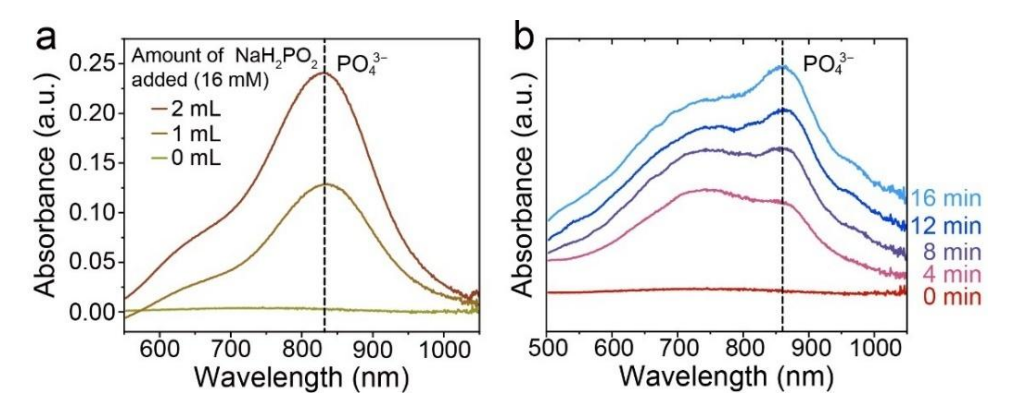


Figure 4.35. (a) UV–Vis spectra of ammonium molybdate spectrophotometry with various NaH₂PO₂ concentrations. (b) Quasi-*in-situ* UV–Vis spectra for PO₄^{3–} detection.

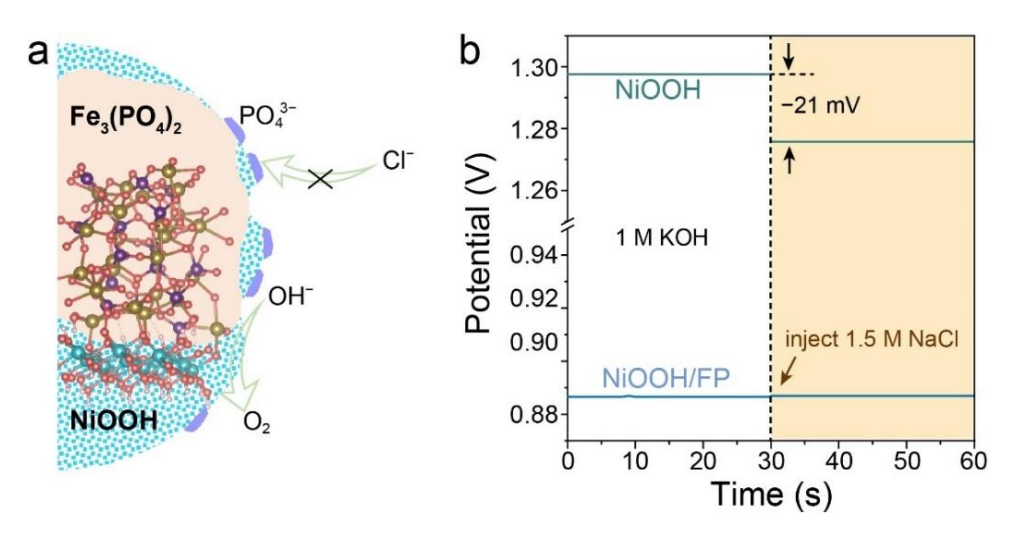


Figure 4.36. (a) Cl⁻-repelling mechanism of Ni(OH)₂/L-LFP during seawater oxidation. (b) OCP curves of NiOOH and NiOOH/FP.

Furthermore, corrosion polarization curves for Ni(OH)₂ and Ni(OH)₂/L-LFP were obtained in natural seawater (**Figure 4.37**). As depicted in **Figure 4.38a**, Ni(OH)₂/L-LFP demonstrates enhanced corrosion resistance in seawater, evidenced by a lower corrosion current density (0.501 mA cm⁻²) and a higher corrosion potential (1.65 V) than Ni(OH)₂ (0.549 mA cm⁻² and

1.53 V).^[58] Notably, after a 600-h stability test in alkaline seawater, Raman spectroscopy confirms the persistence of NiOOH and PO₄³⁻ species (**Figure 4.38b**),^[59, 60] further attesting to the durability and corrosion resistance of the Ni(OH)₂/L-LFP catalyst under challenging electrolysis conditions.

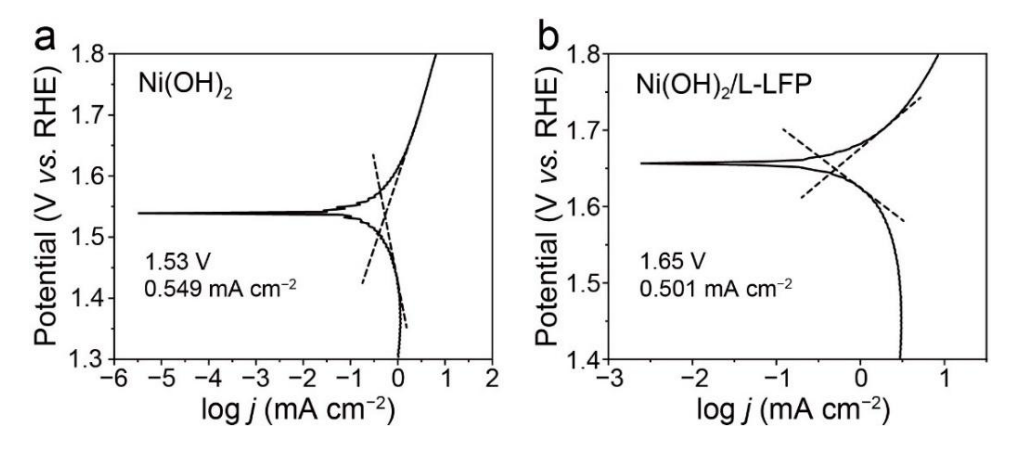


Figure 4.37. Corrosion polarization curves of (a) Ni(OH)₂ and (b) Ni(OH)₂/L-LFP.

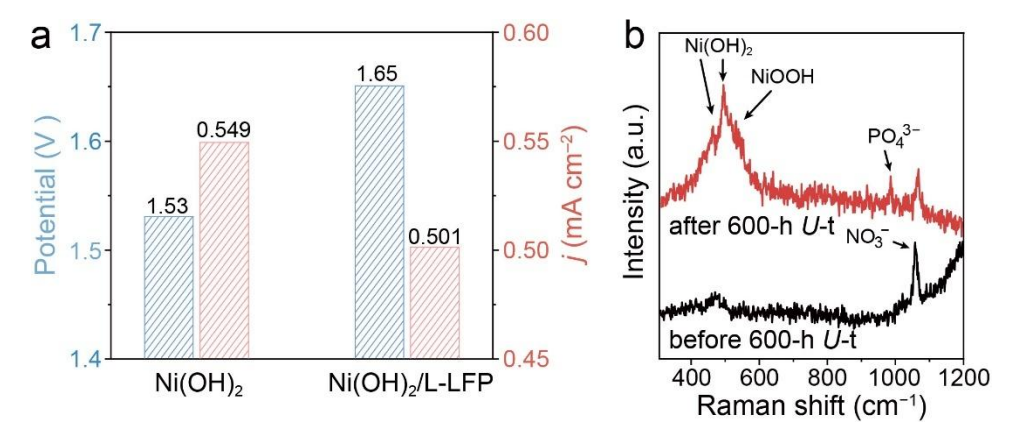


Figure 4.38. (a) Corrosion current densities and potentials of Ni(OH)₂ and Ni(OH)₂/L-LFP in natural seawater. (b) Raman spectra of Ni(OH)₂/L-LFP before and after 600-h *U*-t OER in seawater.

To understand how hybridization enhances the anti-corrosion and water oxidation properties of Ni(OH)₂/L-LFP, theoretical calculations using density functional theory (DFT) were conducted. The activated states of Ni(OH)₂ and Ni(OH)₂/L-LFP were modeled using the crystal structures of NiOOH and NiOOH/FP, respectively (**Figure 4.39**).

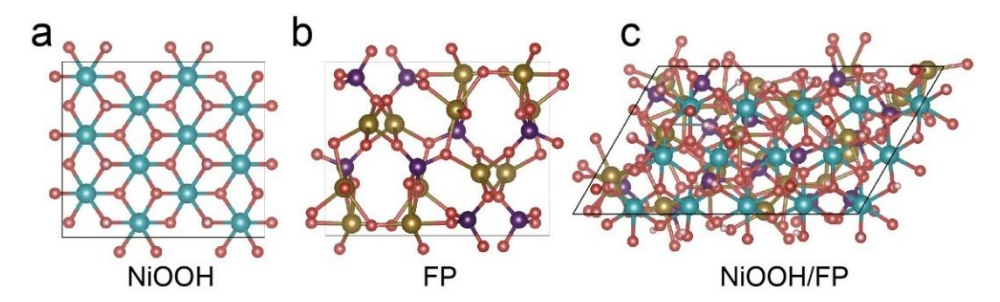


Figure 4.39. Optimized atomic structures of (a) NiOOH, (b) Fe₃(PO₄)₂ (denoted as FP), and (c) NiOOH/Fe₃(PO₄)₂ (denoted NiOOH/FP) used for DFT calculations. Ni, Fe, P, O, and H atoms are shown in blue, brown, violet, red, and pink, respectively.

Electrostatic potential distributions of NiOOH and NiOOH/FP are shown in Figures 4.40a and **4.40b**. Qualitative Bader charge analysis was further applied to clarify the role of PO₄³⁻. The charge is redistributed after the construction of heterointerfaces (Figure 4.40c and 4.40d). Compared to NiOOH, the charges on Ni sites tend to be more positive (from 1.10 to 1.21), which can be ascribed to the polarization of P to O in P-O-Ni. The theoretical simulation presents the formation of the hydrogen bond between OH⁻ and the surface of NiOOH/FP (**Figure 4.41**), which is well consistent with previous reports. [54, 55, 61] Such higher charge states can strengthen the polarization to O in Ni-O-H, and make H a better hydrogen bond donor. As a result, the hydrogen bond between OH⁻ and NiOOH/FP becomes stronger, thus promoting the adsorption of OH on electrodes. To confirm the enhanced adsorption of OH, we conducted EIS at low potentials to monitor the OH- adsorption behaviors on NiOOH and NiOOH/FP. Capacitive reactance brought by the ion adsorption and OH⁻ migration in the double layer takes the main place at low potentials. [62] The peak at the frequency range of 1-100 Hz refers to the resistance resulting from $C_{\rm dl}$ caused by OH⁻ adsorption and migration. [63] The phase angle of the peak in NiOOH at 1.25 V is approximately 28°, which is lower than that of NiOOH/FP (Figure 4.60), suggesting that the resistance brought by OH⁻ adsorption and migration on the NiOOH is higher than that of NiOOH/FP. In other words, the OER basic steps evolving OH will be more beneficial for NiOOH/FP. Moreover, the NiOOH/FP heterointerface has an abundant density of states (DOS) at adsorption sites near the Fermi level (**Figure 4.43**), implying enhanced electronic conductivity.

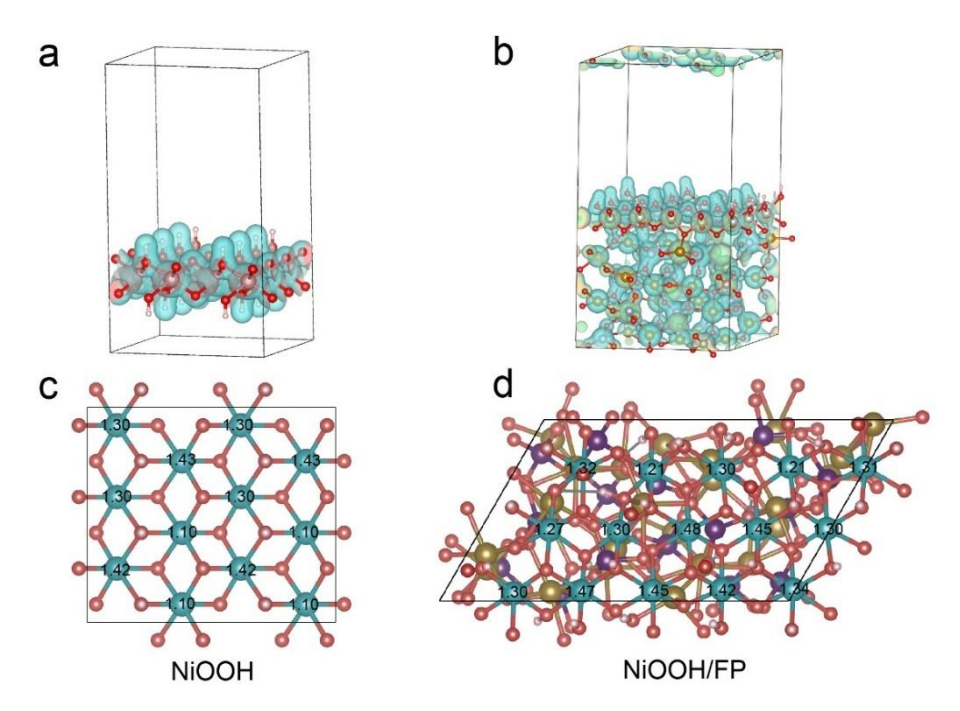


Figure 4.40. DFT simulations of electrostatic potential mappings of (a, c) NiOOH and (b, d) NiOOH/FP. Ni, Fe, P, O, and H atoms are shown in blue, brown, violet, red, and pink, respectively.

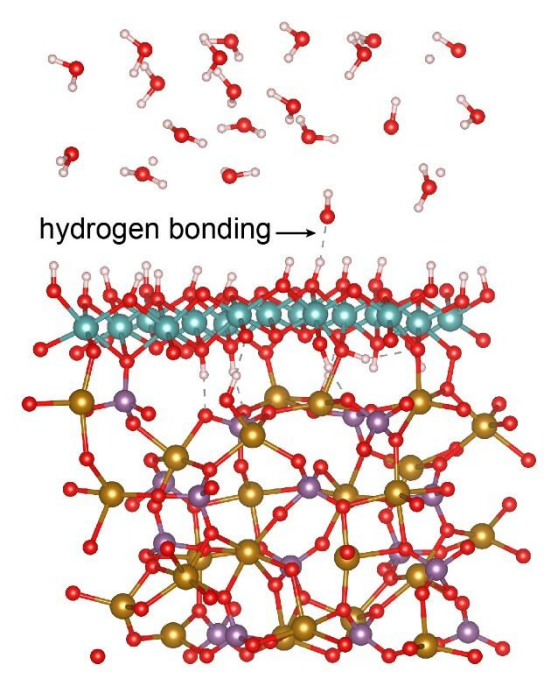


Figure 4.41. Snapshots of classical molecular dynamics simulations of electrolyte systems above the NiOOH/FP surface.

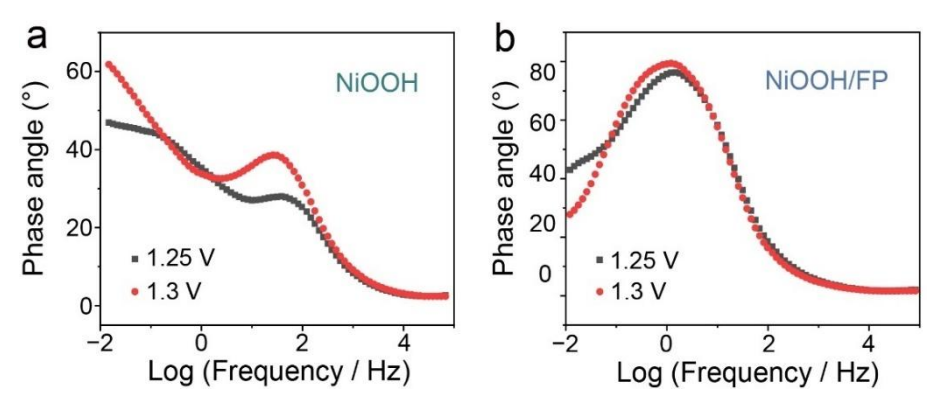


Figure 4.42. Bode phase plots of (a) NiOOH and (b) NiOOH/FP obtained from EIS.

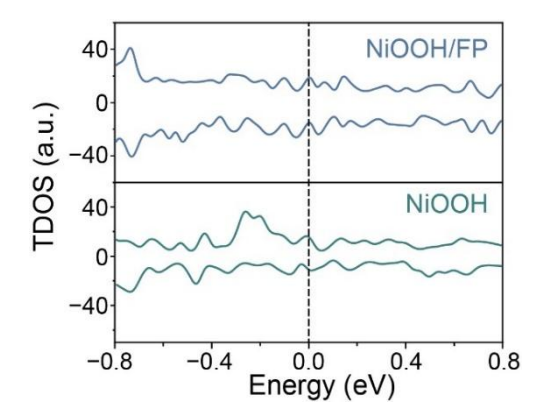


Figure 4.43. The density of states (DOS) for NiOOH and NiOOH/FP heterointerface. The zero energy indicates the Fermi level.

We applied a two-step Volmer–Heyrovsky mechanism that includes Cl⁻ adsorption and subsequent molecular Cl₂ release to investigate the CER (**Figures 4.44** and **4.45**); and the adsorption energy of each step in the OER pathway is also investigated (**Figures 4.46** and **4.47**).

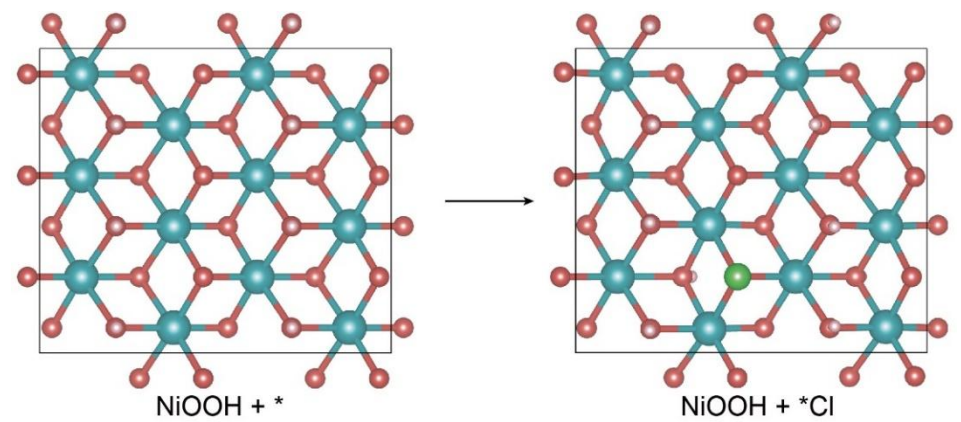


Figure 4.44. Structures of *Cl intermediate adsorbed on the O site of NiOOH. Ni, Fe, P, O, Cl, and H atoms are shown in blue, brown, violet, red, green, and pink, respectively.

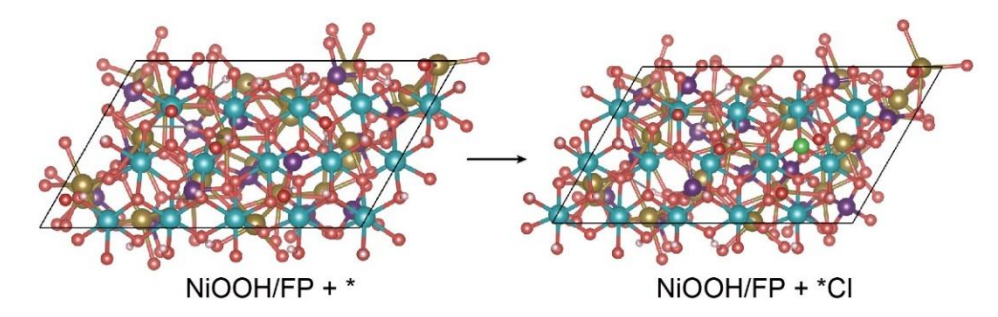


Figure 4.45. Structures of *Cl intermediate adsorbed on the O site of NiOOH/FP. Ni, Fe, P, O, Cl, and H atoms are shown in blue, brown, violet, red, green, and pink, respectively.

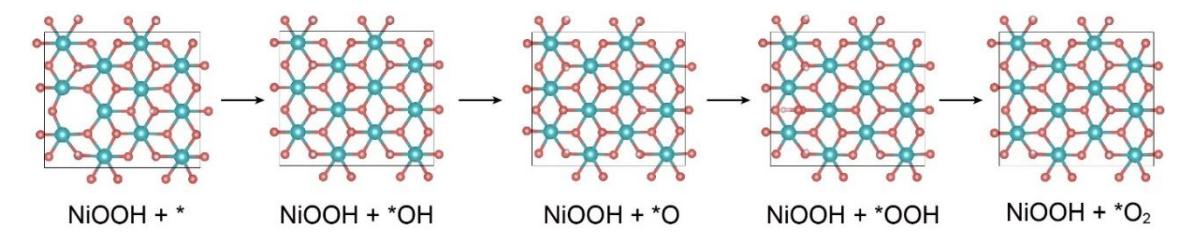


Figure 4.46. Structures of *OH, *O, and *OOH intermediates adsorbed on the O site of NiOOH. Ni, Fe, P, O, and H atoms are shown in blue, brown, violet, red, and pink, respectively.

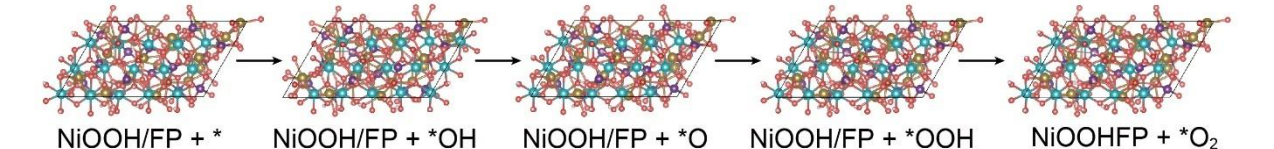


Figure 4.47. Structures of *OH, *O, and *OOH intermediates adsorbed on the O site of NiOOH/FP. Ni, Fe, P, O, and H atoms are shown in blue, brown, violet, red, and pink, respectively.

The Gibbs free energy changes for each elementary step of the CER are calculated and presented in **Figure 4.48a**. The theoretical findings reveal that Cl⁻ adsorption on NiOOH is energetically more favorable (0.49 eV) compared to NiOOH/FP (3.63 eV), suggesting that Cl⁻ is less likely to adsorb on the hybridized NiOOH/FP surface. Moreover, NiOOH/FP exhibits a smaller energy gap between E_{*OH} and E_{slab} (**Figure 4.48b**), which indicates a more challenging Cl⁻ adsorption process on NiOOH/FP. The free energy diagram for CER shows that NiOOH/FP requires a substantially higher overpotential (2.27 V) for CER compared to NiOOH (0.87 V), implying that CER is effectively suppressed on the NiOOH/FP, thus enhancing the electrode's

resistance to corrosion. DFT calculations were also extended to the free energy diagrams for The OER free energy diagram (**Figure 4.49**) identifies the second step, involving the deprotonation and electron transfer from *OH to form *O, as the most energetically demanding step for both NiOOH and NiOOH/FP. For NiOOH, the free energy of this step is 1.51 eV, with an associated overpotential of 0.28 V. In contrast, on NiOOH/FP, these values are significantly reduced to 1.27 eV and 0.04 V, respectively. This reduction in free energy and overpotential lead to superior OER activity of NiOOH/FP compared to NiOOH, highlighting the beneficial effects of hybridization on OER catalysis.

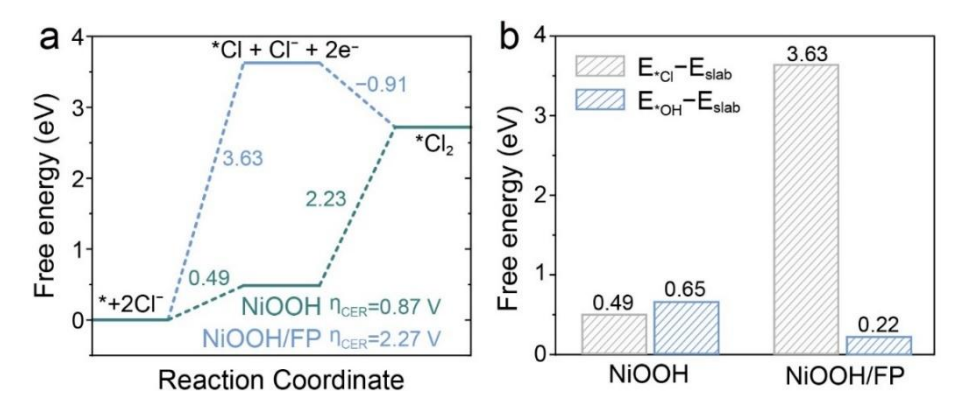


Figure 4.48. (a) The Gibbs free energy diagrams for CER pathways for NiOOH and NiOOH/FP. (b) Free energy change of $E_{\text{CI}}-E_{\text{slab}}$ and on $E_{\text{*OH}}-E_{\text{slab}}$ in NiOOH and NiOOH/FP.

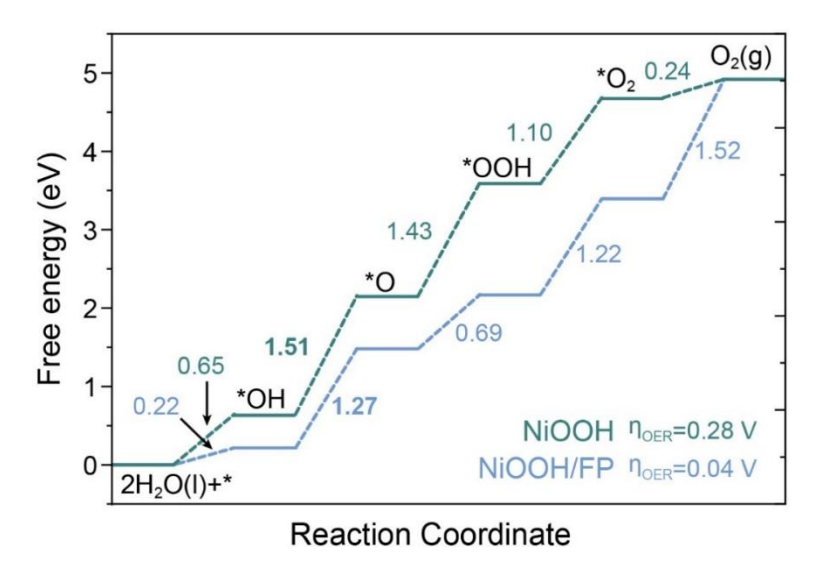


Figure 4.49. The Gibbs free energy diagrams for OER pathways for NiOOH and NiOOH/FP.

4.5. Conclusion

In this chapter, our study demonstrates that the strategic combination of a heterointerface and PO₄³⁻ species can effectively protect OER-active NiOOH from chlorine-induced corrosion during seawater oxidation. The PO₄³⁻ species, leached from upcycled LFP, serve to electrostatically repel Cl⁻ ions. The *in-situ* formation of a NiOOH/FP interface further promotes the adsorption of OH⁻ ions while simultaneously increasing the energy barrier for CER. Additionally, electron transfer is facilitated both within the electrode and at the electrode/electrolyte interface, assisted by the synergistic effect of NiOOH and FP. Consequently, Ni(OH)₂/L-LFP catalyst exhibits significantly enhanced OER activity and durability in alkaline seawater, achieving a current density of 10 mA cm⁻² at a low overpotential of 237 mV and demonstrating remarkable long-term stability for 600 h at 100 mA cm⁻², with only a 3.3 % loss in reaction activity. Furthermore, Ni(OH)₂/L-LFP maintains stable performance over 100 hours at 250 mA cm⁻² in a seawater-splitting electrolyzer when scaled up. This study introduces a novel design concept for creating an effective catalytic surface shielding Ni-based catalysts during alkaline seawater electrolysis, shedding light on a new avenue for upcycling waste LIBs.

4.6. References

- J. Peng, W. Dong, Z. Wang, Y. Meng, W. Liu, P. Song, Z. Liu, *Mater. Today Adv.* 2020, 8, 100081.
- [2] J. F. Chang, G. Z. Wang, Z. Z. Yang, B. Y. Li, Q. Wang, R. Kuliiev, N. Orlovskaya, M. Gu, Y. G. Du, G. F. Wang, Y. Yang, Adv. Mater. 2021, 33, 2101425.
- [3] F. S. Hegner, F. A. Garces-Pineda, J. Gonzalez-Cobos, B. Rodriguez-Garcia, M. Torrens, E. Palomares, N. Lopez, J. R. Galan-Mascaros, *ACS Catal.* **2021**, *11*, 13140.
- [4] X. Luo, P. X. Ji, P. Y. Wang, X. Tan, L. Chen, S. C. Mu, Adv. Sci. 2022, 9, 2104846.
- [5] N. Wang, P. F. Ou, S. F. Hung, J. E. Huang, A. Ozden, J. Abed, I. Grigioni, C. R. Chen, R. K. Miao, Y. Yan, J. Q. Zhang, Z. Y. Wang, R. Dorakhan, A. Badreldin, A. Abdel-Wahab, D. Sinton, Y. C. Liu, H. Y. Liang, E. H. Sargent, *Adv. Mater.* 2023, 35, 2210057.
- [6] L. Z. Zhuang, J. K. Li, K. Y. Wang, Z. H. Li, M. H. Zhu, Z. Xu, Adv. Funct. Mater. 2022, 32, 2201127.
- [7] W. M. Tong, M. Forster, F. Dionigi, S. Dresp, R. S. Erami, P. Strasser, A. J. Cowan, P. Farràs, *Nat. Energy* **2020**, *5*, 367.
- [8] P. F. Guo, D. Liu, R. B. Wu, Small Struct. 2023, 4, 2300192.
- [9] L. Lei, D. L. Huang, C. Y. Zhou, S. Chen, X. L. Yan, Z. H. Li, W. J. Wang, Coord. Chem. Rev. 2020, 408, 213177.
- [10] Z. D. He, R. Tesch, M. J. Eslamibidgoli, M. H. Eikerling, P. M. Kowalski, *Nat. Commun.* **2023**, *14*, 3498.
- [11] M. M. Cai, Q. Zhu, X. Y. Wang, Z. Y. Shao, L. Yao, H. Zeng, X. F. Wu, J. Chen, K. K. Huang, S. H. Feng, Adv. Mater. 2023, 35, 2209338.
- [12] H. H. You, D. S. Wu, D. H. Si, M. N. Cao, F. F. Sun, H. Zhang, H. M. Wang, T. F. Liu, R. Cao, J. Am. Chem. Soc. 2022, 144, 9254.
- [13] L. Yu, L. B. Wu, B. McElhenny, S. W. Song, D. Luo, F. H. Zhang, Y. Yu, S. Chen, Z. F. Ren, *Energy Environ. Sci.* 2020, 13, 3439.
- [14] B. S. Zhang, S. Liu, S. J. Zhang, Y. Cao, H. L. Wang, C. Y. Han, J. Sun, Small 2022, 18, 2203852.
- [15] T. ul Haq, M. Arooj, A. Tahir, Y. Haik, *Small* **2023**, *20*, 2305694.
- [16] G. M. Mu, G. Z. Wang, Q. P. Huang, Y. J. Miao, D. Wen, D. M. Lin, C. G. Xu, Y. J. Wan, F. Y. Xie, W. H. Guo, R. Q. Zou, Adv. Funct. Mater. 2023, 33, 2211260.
- [17] Q. L. Wen, K. Yang, D. J. Huang, G. Cheng, X. M. Ai, Y. W. Liu, J. K. Fang, H. Q. Li, L. Yu, T. Y. Zhai, Adv. Energy Mater. 2021, 11, 2102353.

- [18] R. Liu, M. Z. Sun, X. J. Liu, Z. H. Lv, X. Y. Yu, J. M. Wang, Y. R. Liu, L. H. Li, X. Feng, W. X. Yang, B. L. Huang, B. Wang, *Angew. Chem. Int. Ed.* 2023, 62, e202312644.
- [19] D. S. Yu, Y. X. Hao, S. L. Han, S. Zhao, Q. C. Zhou, C. H. Kuo, F. Hu, L. L. Li, H. Y. Chen, J. W. Ren, S. J. Peng, ACS Nano 2023, 17, 1701.
- [20] S. Q. Niu, Y. C. Sun, G. J. Sun, D. Rakov, Y. Z. Li, Y. Ma, J. Y. Chu, P. Xu, ACS Appl. Energy Mater. 2019, 2, 3927.
- [21] J. Ma, J. X. Wang, K. Jia, Z. Liang, G. J. Ji, H. C. Ji, Y. F. Zhu, W. Chen, H. M. Cheng, G. M. Zhou, *Nat. Commun.* 2024, 15, 1046.
- [22] M. L. Jiao, Q. Zhang, C. L. Ye, Z. B. Liu, X. W. Zhong, J. X. Wang, C. Li, L. X. Dai, G.
 M. Zhou, H. M. Cheng, *Proc. Natl. Acad. Sci. USA* 2022, 119, e2202202119.
- [23] G. J. Ji, D. Tang, J. X. Wang, Z. Liang, H. C. Ji, J. Ma, Z. F. Zhuang, S. Liu, G. M. Zhou, H. M. Cheng, *Nat. Commun.* 2024, 15, 4086.
- [24] M. L. Jiao, Q. Zhang, C. L. Ye, R. H. Gao, L. X. Dai, G. M. Zhou, H. M. Cheng, ACS Nano 2022, 16, 13223.
- [25] F. Withers, M. Dubois, A. K. Savchenko, *Phys. Rev. B* **2010**, 82, 073403.
- [26] M. Aghazadeh, M. Ghaemi, B. Sabour, S. Dalvand, *J. Solid State Electrochem.* **2014**, *18*, 1569.
- [27] X. P. Liu, R. Wang, M. Y. Wei, X. H. Wang, J. Y. Qiu, J. R. Zhang, S. L. Li, Y. Chen, *J. Colloid Interface Sci.* **2024**, 657, 438.
- [28] Y. N. Zhou, W. L. Yu, Y. N. Cao, J. Zhao, B. Dong, Y. Ma, F. L. Wang, R. Y. Fan, Y. L. Zhou, Y. M. Chai, Appl. Catal. B-Environ. Energy 2021, 292, 120150.
- [29] Z. Y. Zhao, Q. Shao, J. Y. Xue, B. L. Huang, Z. Niu, H. W. Gu, X. Q. Huang, J. P. Lang, Nano Res. 2022, 15, 310.
- [30] J. R. Ran, W. W. Guo, H. L. Wang, B. C. Zhu, J. G. Yu, S. Z. Qiao, Adv. Mater. 2018, 30, 1800128.
- [31] Z. Li, M. J. Liu, J. Yan, L. Y. S. Lee, Chem. Eng. J. 2023, 473, 145293.
- [32] K. Dastafkan, X. J. Shen, R. K. Hocking, Q. Meyer, C. Zhao, *Nat. Commun.* **2023**, *14*, 547.
- [33] L. N. Sha, K. Ye, J. L. Yin, K. Zhu, K. Cheng, J. Yan, G. L. Wang, D. X. Cao, Chem. Eng. J. 2020, 381, 122603.
- [34] J. Hu, S. W. Li, J. Y. Chu, S. Q. Niu, J. Wang, Y. C. Du, Z. H. Li, X. J. Han, P. Xu, ACS Catal. 2019, 9, 10705.
- [35] R. Kumar, H. R. Inta, H. Koppisetti, S. Ganguli, S. Ghosh, V. Mahalingam, *ACS Appl. Energy Mater.* **2020**, *3*, 12088.

- [36] W. B. Zhang, Z. J. Zhang, S. H. Choi, W. Yang, Catal. Today 2019, 321, 67.
- [37] M. Q. Guan, C. Wang, S. Li, H. W. Du, Y. P. Yuan, ACS Sustainable Chem. Eng. 2020, 8, 10313.
- [38] Z. J. Chen, W. S. Zou, R. J. Zheng, W. F. Wei, W. Wei, B. J. Ni, H. Chen, *Green Chem.* **2021**, *23*, 6538.
- [39] S. Natarajan, S. Anantharaj, R. J. Tayade, H. C. Bajaj, S. Kundu, *Dalton Trans.* **2017**, *46*, 14382.
- [40] F. Balqis, Y. Irmawati, D. S. Geng, F. A. A. Nugroho, A. Sumboja, ACS Appl. Nano Mater. 2023, 10.1021/acsanm.3c02092.
- [41] T. T. Liu, S. Cai, G. F. Zhao, Z. H. Gao, S. M. Liu, H. N. Li, L. J. Chen, M. A. Li, X. F. Yang, H. Guo, *J. Energy Chem.* **2021**, *62*, 440.
- [42] B. H. Cui, C. Liu, J. F. Zhang, J. J. Lu, S. L. Liu, F. S. Chen, W. Zhou, G. Y. Qian, Z. Wang, Y. D. Deng, Y. N. Chen, W. B. Hu, Sci. China Mater. 2021, 64, 2710.
- [43] L. Jia, G. Du, D. Han, Y. Wang, W. Zhao, S. Chen, Q. Su, B. Xu, *J. Colloid Interface Sci.* **2024**, *653*, 246.
- [44] L. Yan, B. B. Xie, C. Yang, Y. H. Wang, J. Q. Ning, Y. J. Zhong, Y. Hu, *Adv. Energy Mater.* **2023**, *13*, 202204245.
- [45] P. C. Ye, K. Q. Fang, H. Y. Wang, Y. H. Wang, H. Huang, C. B. Mo, J. Q. Ning, Y. Hu, Nat. Commun. 2024, 15, 1012.
- [46] H. J. Song, H. Yoon, B. Ju, D. Y. Lee, D. W. Kim, ACS Catal. 2020, 10, 702.
- [47] M. X. Chen, Y. Y. Zhang, R. Wang, B. Zhang, B. Song, Y. C. Guan, S. W. Li, P. Xu, J. Energy Chem. 2023, 84, 173.
- [48] B. J. Trzesniewski, O. Diaz-Morales, D. A. Vermaas, A. Longo, W. Bras, M. T. M. Koper, W. A. Smith, J. Am. Chem. Soc. 2015, 137, 15112.
- [49] M. J. Liu, K. A. Min, B. Han, L. Y. S. Lee, Adv. Energy Mater. 2021, 11, 2101281.
- [50] S. Q. Li, S. B. Wang, Y. H. Wang, J. H. He, K. Li, Y. J. Xu, M. X. Wang, S. Y. Zhao, X. N. Li, X. Zhong, J. G. Wang, Adv. Funct. Mater. 2023, 33, 2214488.
- [51] Y. X. Lu, T. Y. Liu, C. L. Dong, C. M. Yang, L. Zhou, Y. C. Huang, Y. F. Li, B. Zhou, Y. Q. Zou, S. Y. Wang, Adv. Mater. 2022, 34, 2107185.
- [52] J. Jiang, F. F. Sun, S. Zhou, W. Hu, H. Zhang, J. C. Dong, Z. Jiang, J. J. Zhao, J. F. Li, W. S. Yan, M. Wang, *Nat. Commun.* 2018, 9, 2885.
- [53] T. F. Ma, W. W. Xu, B. R. Li, X. Chen, J. J. Zhao, S. S. Wan, K. Jiang, S. X. Zhang, Z. F. Wang, Z. Q. Tian, Z. Y. Lu, L. Chen, *Angew. Chem. Int. Ed.* 2021, 60, 22740.

- [54] P. Li, S. E. Zhao, Y. Q. Huang, Q. H. Huang, Y. T. Yang, H. Yang, ACS Catal. 2023, 13, 15360.
- [55] M. J. Eslamibidgoli, A. Gross, M. Eikerling, Phys. Chem. Chem. Phys. 2017, 19, 22659.
- [56] Z. H. Yang, S. Wang, C. Y. Wei, L. Chen, Z. M. Xue, T. C. Mu, Energy Environ. Sci. 2024, 17, 1603.
- [57] Y. X. Lu, T. Y. Liu, C. L. Dong, Y. C. Huang, Y. F. Li, J. Chen, Y. Q. Zou, S. Y. Wang, Adv. Mater. 2021, 33, 2007056.
- [58] F. H. Zhang, Y. F. Liu, L. B. Wu, M. H. Ning, S. W. Song, X. Xiao, V. G. Hadjiev, D. E. Fan, D. Z. Wang, L. Yu, S. Chen, Z. F. Ren, *Mater. Today Phys.* 2022, 27, 100841.
- [59] B. Konkena, J. Masa, A. J. R. Botz, I. Sinev, W. Xia, J. Kossmann, R. Drautz, M. Muhler, W. Schuhmann, ACS Catal. 2017, 7, 229.
- [60] J. Huang, Y. Li, Y. Zhang, G. Rao, C. Wu, Y. Hu, X. Wang, R. Lu, Y. Li, J. Xiong, *Angew. Chem. Int. Ed.* **2019**, *58*, 17458.
- [61] J. M. P. Martirez, E. A. Carter, Chem. Mater. 2018, 30, 5205.
- [62] J. X. Feng, M. P. Chen, P. F. Zhou, D. Liu, Y. Y. Chen, B. C. He, H. Y. Bai, D. Liu, W. F. Ip, S. Chen, D. T. Liu, W. L. Feng, J. Ni, H. Pan, *Mater. Today Energy* 2022, 27, 101005.
- [63] R. L. Doyle, M. E. G. Lyons, J. Electrochem. Soc. 2013, 160, H142.

Chapter V Molybdate-Modulated NiOOH for MeOH-Assisted Seawater Electrolysis

5.1. Objective and Motivation

In **Chapters 3** and **4**, the focus has been on the generation of OER-active NiOOH and its anticorrosion properties. However, another issue of high energy consumption associated with the
theoretical 1.23 V required for the OER has not yet been adequately addressed. It is well
established that utilizing organic molecule oxidation reactions, such as MOR, as a substitute
for OER in water electrolysis presents a promising approach for energy-saving hydrogen
production due to the lower oxidation potential of organic transformation reactions.

Nonetheless, challenges such as chlorine corrosion and limited catalytic efficiency of MOR
must be considered when applying NiOOH to methanol-assisted seawater electrolysis. As
discussed in **Chapter 4**, *in-situ-*leached PO₄³⁻ ions alter the microenvironment, affecting the
adsorption behavior of Cl⁻. This raises the question of whether anion-modulated local
microenvironments can enhance MOR activity.

To investigate the effectiveness of the anion-modulation strategy in simultaneously improving MOR catalytic activity and anti-corrosion properties of NiOOH, MoO₄²⁻-adsorbed NiOOH was synthesized through the reconstruction of the Ni(OH)₂/NiMoO₄ pre-catalyst in **Chapter 5**. Systematic studies on MoO₄²⁻ adsorption revealed its impact on methanol molecule adsorption, Cl⁻ repelling, and overall enhancement of MOR catalytic activity. Moreover, *in situ* characterizations, combined with electrochemical analysis and DFT calculations, were employed to understand the role of MoO₄²⁻ in promoting PCET during the MOR process. This work presents the first application of an anion-modulation strategy in methanol-assisted seawater electrolysis.

5.2. Introduction

Seawater, constituting 96.5 % of the Earth's water, presents a compelling alternative for green hydrogen generation *via* direct electrolysis and the realization of dual-carbon goals.^[1, 2] This approach eliminates desalination steps, simplifying the process and reducing production costs.

Nevertheless, direct seawater electrolysis faces challenges due to the high thermodynamic energy barrier for water oxidation (1.23 V vs. RHE) and severe corrosion of electrocatalysts by Cl⁻-rich environment.^[3, 4]

In recent years, exploring alternative anodic reactions to the OER has emerged as a strategy to reduce the required potential of electrolysis cells.^[5-8] Methanol, with its low cost and thermodynamic oxidation potential (0.016 V vs. RHE), is a promising candidate for smallmolecule-assisted seawater splitting.^[9] NiOOH species, in situ formed during the surface reconstruction of Ni-based electrocatalysts, is considered the critical active species for the MOR.[10-12] The high-valence Ni³⁺ facilitates PCET by capturing protons from methanol molecules. [10, 13] Thus, efficient Ni3+ utilization and MOR activity hinge on this nonelectrochemical Ni³⁺-methanol interaction. Recently, it was suggested that residual or adsorbed anionic species could modulate the electronic structure of active sites in NiOOH, thereby optimizing anodic oxidation activities including organic molecular oxidation. [14-17] However, the influence of these anionic species on MOR, especially, the non-electrochemical process, remains largely unexplored. On the other hand, Cl⁻ ions in seawater readily attack electron-deficient sites on transition metals, such as Ni³⁺, triggering the CER and generating corrosive Cl₂ or ClO⁻, which often leads to catalyst deactivation. While limiting the anodic potential below 1.72 V in an alkaline media can suppress CER, this strategy usually results in current densities significantly lower than industrial standards.^[18, 19] Recent studies suggest that manipulating the catalyst surface microenvironment through anions adsorption can reduce Cl⁻ adsorption, thus effectively mitigating corrosion from chlorine derivatives and ensuring the stability of seawater oxidation.^[20-23] The key challenge lies in simultaneously accelerating the non-electrochemical process in MOR and alleviating chlorine corrosion during methanol oxidation-assisted seawater electrolysis.

Herein, we present a MoO₄²⁻-adsorption strategy to modulate the surface microenvironment of NiOOH. This approach simultaneously adjusts Cl⁻ adsorption behavior and promotes the non-electrochemical process in MOR. The pre-catalyst, Ni(OH)₂/NiMoO₄ (Ni(OH)₂/NMO), possesses a three-dimensional (3D) hierarchical structure that effectively enlarges the electrochemical surface area for efficient mass diffusion. The heterojunction between Ni(OH)₂ and NiMoO₄ facilitates the reconstruction process of Ni(OH)₂ to generate NiOOH, which serves as the active site for both MOR and OER. *In situ* leached MoO₄²⁻ optimizes the coordination environment on the NiOOH surface to promote proton capture from methanol, thus facilitating PCET during MOR. Furthermore, the surface-coordinated MoO₄²⁻ decreases the adsorption energy of Cl⁻ ions, thereby mitigating catalyst corrosion.

5.3. Experimental Section

5.3.1. Raw Materials

Nickel nitrate hexahydrate (Ni(NO₃)₂·6H₂O, 99.9 %), Nafion perfluorinated resin solution (5 wt.%), sodium molybdate dihydrate (NaMoO₄·2H₂O, 99.0 %), potassium nitrate (KNO₃, 99.0 %), and potassium hydroxide (KOH, 99.9 %) were purchased from Sigma–Aldrich. Sulfuric acid (H₂SO₄, 98.0 %), methanol (99.8 %), and acetone (99.8 %) were purchased from Duksan Chemicals. Ammonium molybdate tetrahydrate ((NH₄)₆Mo₇O₂₄·4H₂O, 83.0 %), sodium chloride (NaCl, 99.5 %), and potassium iodide (KI, 99.0 %) were obtained from Shenzhen Dieckmann Tech. Aqueous solutions were prepared using deionized (DI) water produced by MilliQ Water System. Natural seawater (pH = ~8) was collected from Hung Hom Bay near the Hong Kong Polytechnic University, Kowloon, Hong Kong SAR, China. All chemicals were used as received.

5.3.2. Catalysts Synthesis

Synthesis of NiMoO₄: NiMoO₄ nanorods were directly grown on Ni foam through a hydrothermal method. A Ni foam $(1.0 \times 3.5 \text{ cm}^2)$ was cleaned by sonication in acetone and

washed with 3 M HCl for 10 min to remove surface oxides. A solution was then prepared by dissolving Ni(NO₃)₂·6H₂O (0.175 g) and Na₂MoO₄·2H₂O (0.145 g) in DI water (10 mL) under magnetic stirring for 30 min. This solution was transferred to a 15 mL Teflon-lined autoclave containing the Ni foam. The autoclave was sealed and heated at 150 °C for 4 h. After cooling to room temperature, the sample was washed with DI water several times and dried at 60 °C under vacuum for 12 hours.

Synthesis of Ni(OH)₂/NMO: An electrodeposition method was engaged to prepare Ni(OH)₂/NMO. As-prepared NiMoO₄ on Ni foam (0.25 cm²) served as the working electrode in a three-electrode configuration. A standard calomel electrode and a carbon rod were employed as the reference and counter electrodes, respectively, in an aqueous electrolyte. Ni(OH)₂ was electrodeposited onto the NiMoO₄ nanorods by applying -1 V for various durations in an electrolyte containing Ni(NO₃)₂ (1 M) and KNO₃ (0.2 M). The resulting Ni(OH)₂/NMO composite was rinsed with DI water and dried at 60 °C under vacuum for 12 h. For comparison, a control Ni(OH)₂ electrode was prepared using the same procedure but on pristine Ni foam (0.25 cm²) without NMO nanorods. Separately, Pt/C (or RuO₂) catalyst ink was prepared by mixing 20 wt.% Pt/C (or RuO₂, 5 mg) with a solution of 5 wt.% Nafion (40 μL) in ethanol (960 μL). The mixture was sonicated for 60 min. The catalyst ink (100 μL) was drop-cast on a Ni foam (1 × 1 cm²) and allowed to dry naturally in the air.

Synthesis of NiMo: NiMo electrode was synthesized according to a previously reported method. ^[24] Briefly, as-prepared NMO nanorods on Ni foam were placed in a tube furnace and heated under an Ar/H₂ (50 sccm) environment. The temperature was ramped to 550 °C at a rate of 5 °C min⁻¹ and held for 1 h. The NiMo on Ni foam was then allowed to cool down to room temperature.

5.3.3. Electrochemical Performance Test

Electrocatalytic properties of the samples for OER and MOR were evaluated using a standard three-electrode configuration in 1.0 M KOH electrolyte. A graphite rod and a Hg/HgO electrode were used as the counter and reference electrodes, respectively. All data were acquired using a Princeton multichannel electrochemical station. All potentials in this work were calibrated against the RHE ($E_{\rm RHE} = E_{\rm Hg/HgO} + 0.059 \times \rm pH + 0.098$). Prior to OER testing, the working electrodes were cycled between 1.124 and 1.624 V for 100 cycles to achieve a stable CV. LSV was then conducted from 1.2 to 1.9 V at a scan rate of 2 mV s⁻¹. The MOR activity of the samples was evaluated using the same method in 0.1 M methanol + 1 M KOH. All polarization curves were corrected for ohmic losses with 90 % iR compensation.

5.3.4. Flow Cell Measurements

For HER evaluation, the NiMo cathode was coupled with a scaled-up Ni(OH)₂/NMO anode (1 cm × 1 cm) to form a full-cell water-splitting system. For comparison, commercial RuO₂ and Pt/C on Ni foam were used as a benchmark for the anode and cathode, respectively. The water-splitting reaction was conducted using a Princeton multichannel electrochemical station equipped with an MEA electrolyzer and a peristaltic pump. The MEA electrolyzer consisted of separate flow fields for the anode and cathode, each with an active surface area of 1 cm². These flow fields were responsible for the continuous delivery of aqueous electrolytes over the electrode surfaces. Inside the MEA, the cathode and anode were positioned on their respective flow-field plates and physically separated by an AEM (Fumasep, Fuel Cell Store). The MEA was then uniformly compressed to ensure proper contact and sealing between the electrodes and the AEM. Following the MEA assembly, alkaline seawater electrolyte was continuously pumped through the anode and cathode compartments at a constant flow rate of 5 mL min⁻¹. For performance evaluation, chronopotentiometric tests were conducted by applying constant current densities of 0.1, 0.5, and 1.0 A cm⁻² to the anode. The corresponding cell voltage was continuously monitored and recorded throughout each test.

5.3.5. Calculations of Energy Cost and Savings for the H₂ Production

The electrical energy required to produce a specific amount of H₂ in the electrochemical cells of NiMo||Ni(OH)₂/NMO and Pt/C||RuO₂ was calculated using Equation (1):

$$E = U \times n \times F \tag{5.1}$$

where U is the cell voltage, n is the amount of produced H_2 in mol, and F is the Faraday constant (96,485 C mol⁻¹). The percentage of energy saved during H_2 generation using the NiMo||Ni(OH)₂/NMO cell compared to the Pt/C||RuO₂ cell was calculated using Equation (2):

$$P_{energy \ saving} = \frac{U_{\text{Pt/C}||\text{RuO2}} - U_{\text{NiMo}||\text{Ni(OH)2/NMO}}}{U_{\text{Pt/C}||\text{RuO2}}} \times 100\%$$
 (5.2)

where $U_{Pt/C||RuO2}$ and $U_{NiMo||Ni(OH)2/NMO}$ are the cell voltage of $Pt/C||RuO_2$ cell and $NiMo||Ni(OH)_2/NMO$ cell at a specific current density, respectively.

5.4. Results and Discussion

5.4.1. Structure Characterization



Figure 5.1. A schematic diagram of the synthetic procedure for Ni(OH)₂/NMO.

Figure 5.1 depicts a two-step route for synthesizing hierarchical Ni(OH)₂/NMO on Ni foam. Firstly, NiMoO₄ nanorods (d = 110 nm) were hydrothermally grown on Ni foam (**Figure 5.2a**). Subsequent electroreduction of Ni(NO₃)₂ at -1 V (vs. saturated calomel electrode, SCE) forms Ni(OH)₂ nanosheets on the NiMoO₄ nanorods (**Figure 5.3a**). This approach enables precise control over the Ni(OH)₂-to-NMO ratio and Ni(OH)₂ morphology (**Figures 5.2b** and **5.2c** and **Table 5.1**).

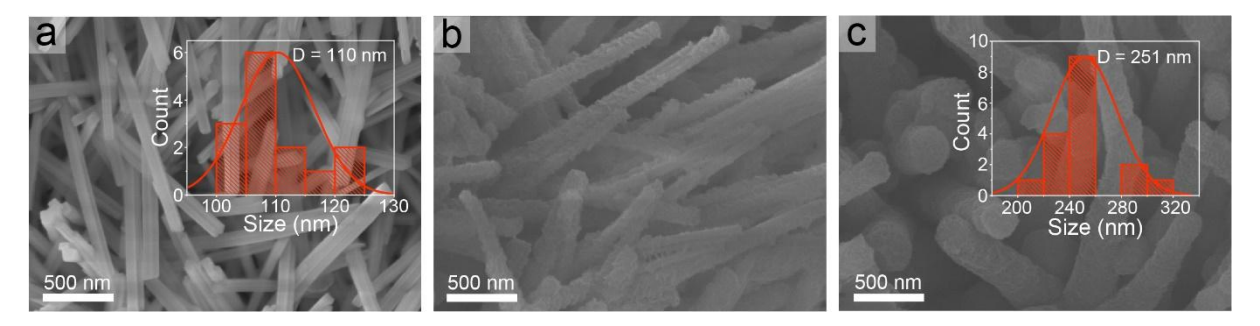


Figure 5.2. SEM images of (a) NiMoO₄ and (b,c) Ni(OH)₂/NMO prepared using different electrodeposition durations: (a) 0 min, (b) 5 min, and (c) 15 min.

Table 5.1. ICP-OES analysis data of Ni(OH)₂/NMO at various deposition stages.

Comple	Element co	Atomic ratio	
Sample	Mo	Ni	Ni/(Ni+Mo)
NiMoO ₄	97.33	65.80	0.52
Ni(OH) ₂ /NMO-5 min	98.64	82.46	0.58
Ni(OH) ₂ /NMO-10 min	94.47	101.62	0.64
Ni(OH) ₂ /NMO-15 min	96.40	124.80	0.68
Ni(OH) ₂	0	33.29	1

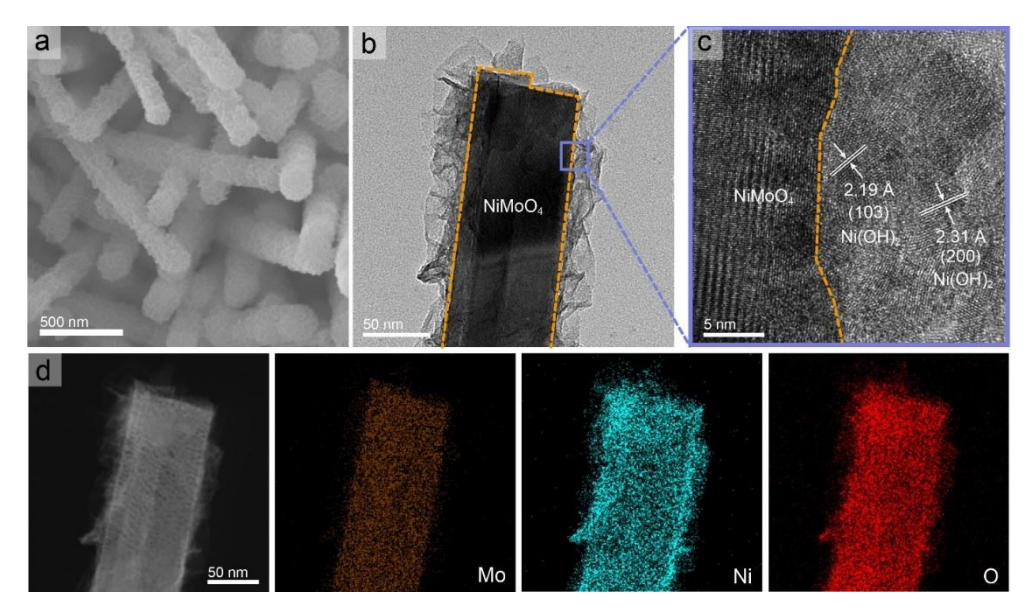


Figure 5.3. (a) SEM image, (b) TEM, and (c) high-resolution TEM images of Ni(OH)₂/NMO. (d) STEM and the corresponding EDS mapping images of Ni(OH)₂/NMO.

TEM image displays the hierarchical morphology of Ni(OH)₂/NMO (**Figure 5.3b**), confirming the nanorod structure of NiMoO₄ remaining intact after Ni(OH)₂ nanosheet decoration. The high-resolution TEM image, presented in **Figure 5.3c**, reveals two lattice spacings of 2.19 and 2.31 Å, corresponding to the (103) and (200) planes of Ni(OH)₂, respectively. STEM analysis of Ni(OH)₂/NMO along with the corresponding EDS mappings reveal Mo enrichment within the inner nanorod region, while Ni and O are uniformly distributed throughout the entire structure (**Figure 5.3d**).

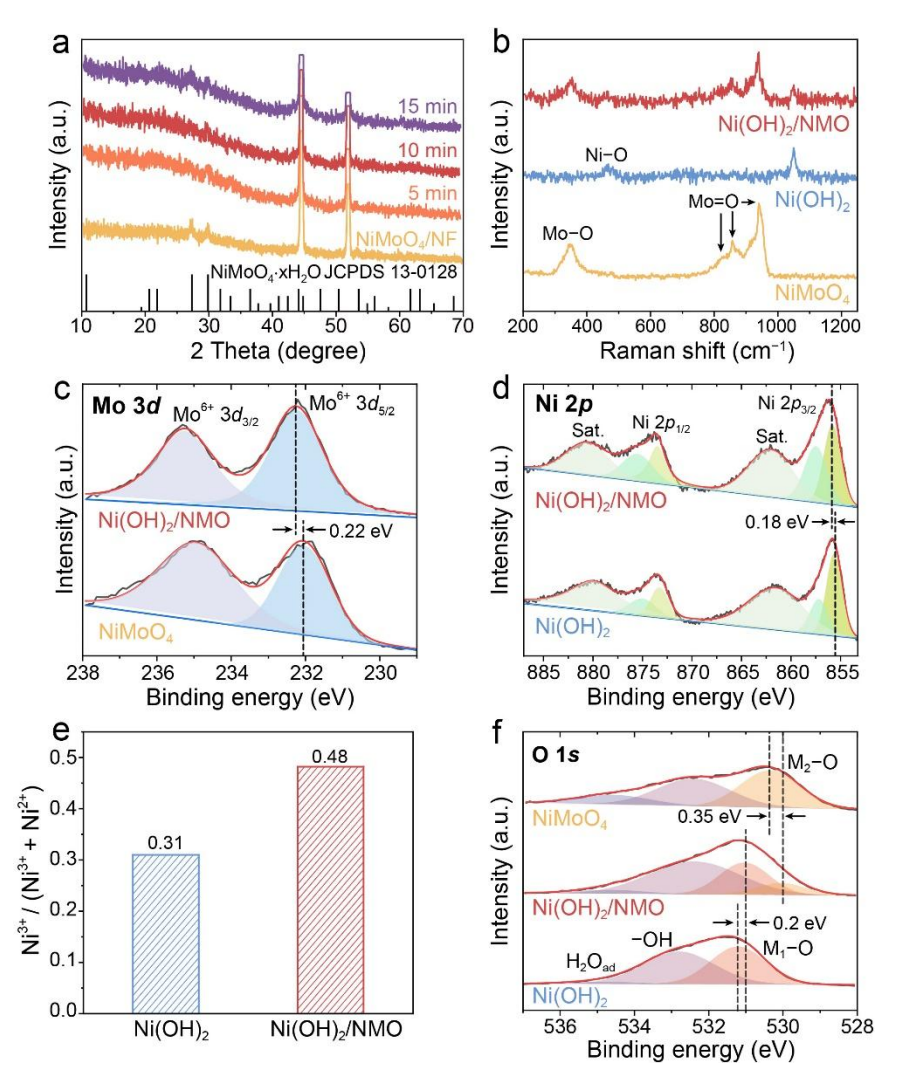


Figure 5.4. (a) XRD patterns and (b) Raman spectra of NiMoO₄, Ni(OH)₂, and Ni(OH)₂/NMO. (c) XPS Mo 3*d* spectra of Ni(OH)₂/NMO and NiMoO₄. (d) XPS Ni 2*p* spectra of Ni(OH)₂/NMO and Ni(OH)₂. I Ni³⁺/(Ni³⁺+Ni²⁺) peak area ratio of Ni(OH)₂ and Ni(OH)₂/NMO. (f) XPS O 1*s* spectra of NiMoO₄, Ni(OH)₂, and Ni(OH)₂/NMO.

The XRD analysis of the pristine NiMoO₄ nanorods confirms its structure matches the reference pattern for hydrated NiMoO₄ (JCPDS 13-0128) and is well maintained after the electrodeposition process (Figure 5.4a). Raman spectroscopic analysis further supports the successful deposition of Ni(OH)₂ on NiMoO₄ nanorods (**Figure 5.4b**). Characteristic Raman peaks for NiMoO₄ at 347 cm⁻¹ (Mo–O bending), 825 and 857 cm⁻¹ (asymmetric Mo–O stretching), and 941 cm⁻¹ (symmetric Mo=O stretching)^[25] are observed alongside peaks corresponding to Ni(OH)₂ at 460 and 1,045 cm⁻¹. [26] XPS was employed to investigate the changes in chemical composition and surface electronic states. The high-resolution Mo 3d spectrum of pristine NiMoO₄ nanorod displays two peaks at 232.05 and 235.15 eV, which can be ascribed to Mo $3d_{5/2}$ and Mo $3d_{3/2}$, respectively (**Figure 5.4c**). These peaks are separated by 3.10 eV, indicating the Mo⁶⁺ oxidation state. [27] In Ni(OH)₂/NMO, the Mo 3d peaks shift positively by 0.22 eV compared to pristine NiMoO₄, suggesting a reduction in electron density around the Mo sites. This can be attributed to charge migration at the interface between Ni(OH)₂ and NiMoO₄. [28] The Ni 2p spectra of both Ni(OH)₂ and Ni(OH)₂/NMO exhibit two pairs of Ni $2p_{3/2}$ and Ni $2p_{1/2}$ peaks corresponding to Ni²⁺ and Ni³⁺ species (**Figure 5.4d**). Additionally, satellite peaks associated with Ni²⁺ species are observed.^[29, 30] Similar to the Mo 3d peaks, a positive shift of 0.18 eV is observed in the Ni 2p region of Ni(OH)₂/NMO. This indicates that Ni atoms in Ni(OH)₂/NMO are in a higher valence state due to electronic interplay with NiMoO₄. This is further supported by an increase in the Ni³⁺/(Ni³⁺+Ni²⁺) peak area ratio from 0.31 in Ni(OH)₂ to 0.48 in Ni(OH)₂/NMO (**Figure 5.4e**). These observations signify a higher proportion of Ni³⁺ species within the composite, which is known to promote the formation of NiOOH, the catalytically active species for OER. [22] The O 1s spectra of Ni(OH)₂, NiMoO₄, and Ni(OH)₂/NMO can be deconvoluted into three peaks of metal-oxygen (M–O) bond, hydroxyl group, and adsorbed water molecules (Figure 5.4f). [31-33] The M₁–O and M₂–O peaks in Ni(OH)₂ and NiMoO₄ are observed at 531.2 and 530.35 eV, respectively.

In Ni(OH)₂/NMO, those two peaks show negative shifts of 0.2 and 0.35 eV, suggesting the increased electron density around O sites.

The M–O peaks in Ni(OH)₂ and NiMoO₄ are observed at 531.35 and 530.30 eV, respectively. In Ni(OH)₂/NMO, this peak shifts to an intermediate binding energy of 530.9 eV, again suggesting a strong interaction between Ni(OH)₂ and NiMoO₄.

5.4.2. OER Performances of Ni(OH)2/NMO in Alkaline Freshwater and Seawater

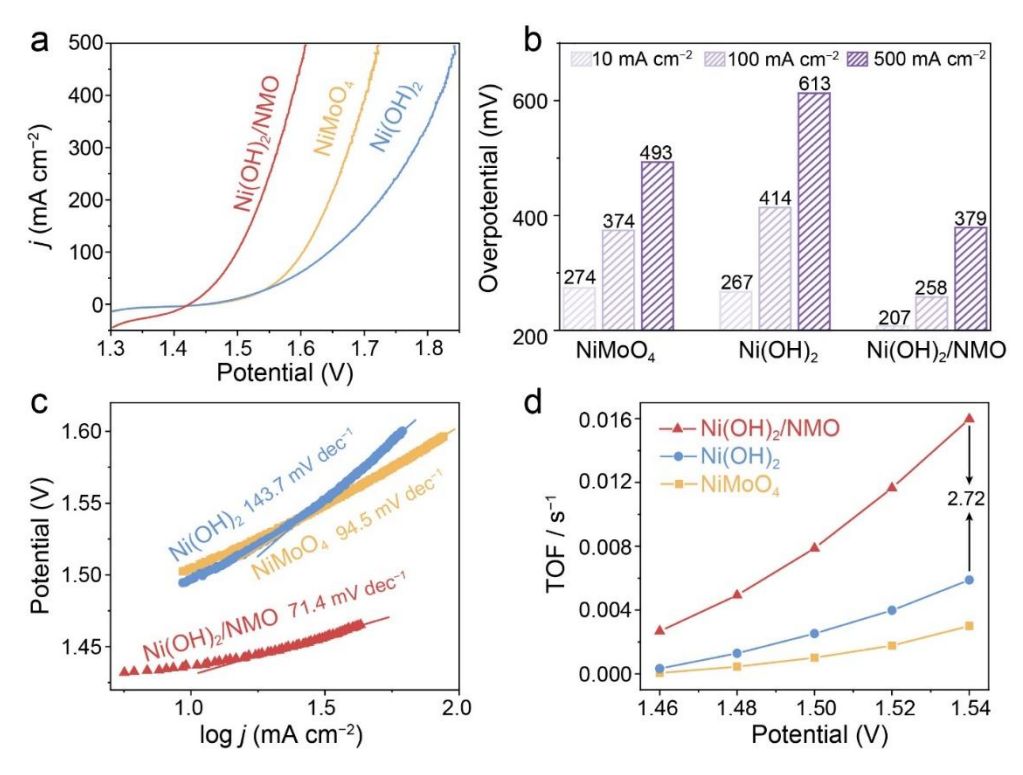


Figure 5.5. (a) LSV curves (with *i*R correction), (b) overpotentials to reach 10, 100, and 500 mA cm⁻², corresponding Tafel slopes, and (d) TOF of NiMoO₄, Ni(OH)₂, and Ni(OH)₂/NMO.

The OER activity of the as-prepared samples was evaluated in an O₂-saturated 1 M KOH using a standard three-electrode setup. **Figure 5.5a** compares the LSVs recorded at a scan rate of 2 mV s⁻¹. Notably, Ni(OH)₂/NMO achieves a current density of 10 mA cm⁻² at a significantly lower overpotential (η₁₀) of 207 mV compared to Ni(OH)₂ (267 mV) and NiMoO₄ (274 mV, **Figure 5.5b**). Moreover, Ni(OH)₂/NMO only requires 258 and 379 mV to reach current densities of 100 and 500 mA cm⁻², respectively. Tafel analysis conducted on the polarization

curves reveals a superior Tafel slope of 71.4 mV dec^{-1} for Ni(OH)₂/NMO compared to the two counterparts (**Figure 5.5c**), indicating its faster reaction kinetics. TOF is an important parameter for evaluating the intrinsic activity of electrocatalysts. The high TOF value of 0.016 s^{-1} , approximately $2.72 \text{ times greater than Ni(OH)}_2 (0.006 \text{ s}^{-1}, \text{$ **Figure 5.5d** $}), further highlights the enhanced intrinsic activity due to the heterojunctions in Ni(OH)₂/NMO.$

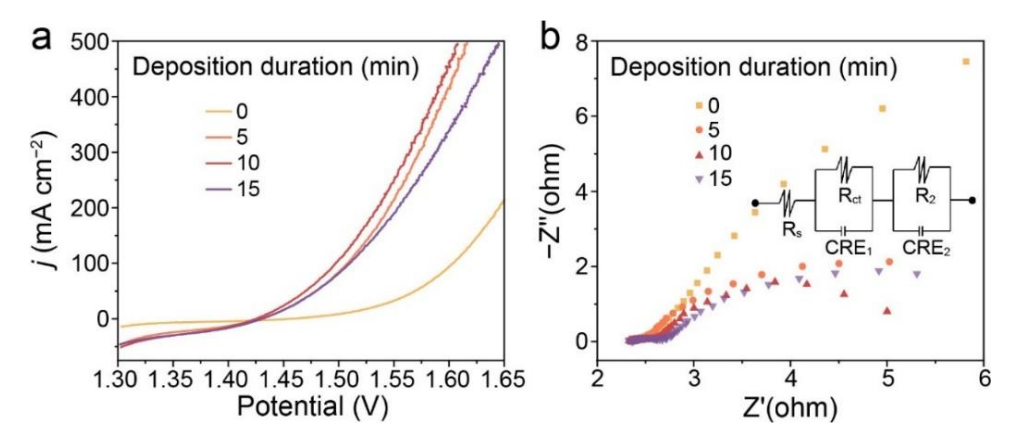


Figure 5.6. (a) LSVs of Ni(OH)₂/NMO samples synthesized using various electrodeposition durations. (b) Nyquist plots of Ni(OH)₂/NMO composites prepared using various electrodeposition durations. The inserted image is an equivalent circuit, in which R_s stands for the electrolyte resistance, CPE_1 represents double-layer capacitance, R_{ct} is related to the interfacial charge transfer reaction, and CPE_2 and R_2 are associated with the dielectric properties and the resistance of the electrode itself.

Table 5.2. Overpotentials of samples synthesized through electrodeposition with different loading times to reach 10 mA cm⁻².

Deposition time (min)	Overpotential (mV, at 10 mA cm ⁻²)
0	274
5	213
10	207
15	214

The OER performance of Ni(OH)₂/NMO is highly influenced by sample preparation conditions, as detailed in **Figure 5.6a** and **Table 5.2**. The sample synthesized *via* 10-min

Ni(OH)₂ deposition exhibits the lowest resistance (3.04 Ω) at the reaction interface (R_{ct}, **Figure 5.6b**, and **Table 5.3**), whereas both shorter and longer depositions (5 and 15 min) increase the R_{ct} (5.28 and 5.49 Ω , respectively). Long-term chronopotentiometry without *i*R correction demonstrates the exceptional stability of Ni(OH)₂/NMO during OER in 1 M KOH, maintaining current densities of 100 and 500 mA cm⁻² for over 600 h (**Figure 5.7**).

Table 5.3. Parameters of EIS simulation for samples synthesized through electrodeposition with different loading times.

Deposition time (min)	$R_s(\Omega)$	Rct (\O)	$R_2(\Omega)$	CPE ₁ (F)	CPE ₂ (F)
0	2.34	20.52	0.66	0.49	0.13
5	2.33	5.28	0.17	1.65	0.93
10	2.33	3.04	0.15	0.67	2.04
15	2.32	5.49	0.28	0.01	5.29

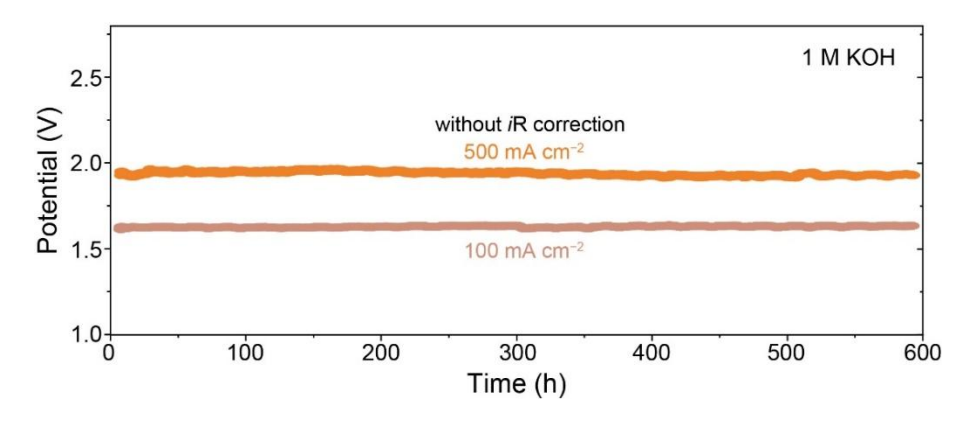


Figure 5.7. Chronopotentiometric curves of Ni(OH)₂/NMO in 1 M KOH.

The OER activity of Ni(OH)₂/NMO was further evaluated in alkaline seawater electrolytes (natural seawater + 1 M KOH) to assess its potential for seawater electrolysis application. As shown in **Figure 5.8a**, Ni(OH)₂/NMO exhibits a similar trend on the LSV curve (with *i*R correction) in seawater, indicating its superior OER performance. Compared to Ni(OH)₂, its overpotentials at 100 and 500 mA cm⁻² slightly increase by only 9 and 2 mV, respectively

(**Figure 5.8b**), suggesting excellent OER selectivity of Ni(OH)₂/NMO. This OER performance of Ni(OH)₂/NMO surpasses or matches other state-of-the-art catalysts designed for seawater oxidation (**Figure 5.8c** and **Table 5.4**). Additionally, Ni(OH)₂/NMO achieves a high average FE of 95.3 % at a high current density of 500 mA cm⁻² in alkaline seawater (**Figure 5.8d**). Iodide titration confirms the high OER selectivity of Ni(OH)₂/NMO against the hypochlorite reaction, as evidenced by the absence of a characteristic absorption peak for hypochlorite ions in the post-FE test electrolyte (**Figure 5.9b**). [34]

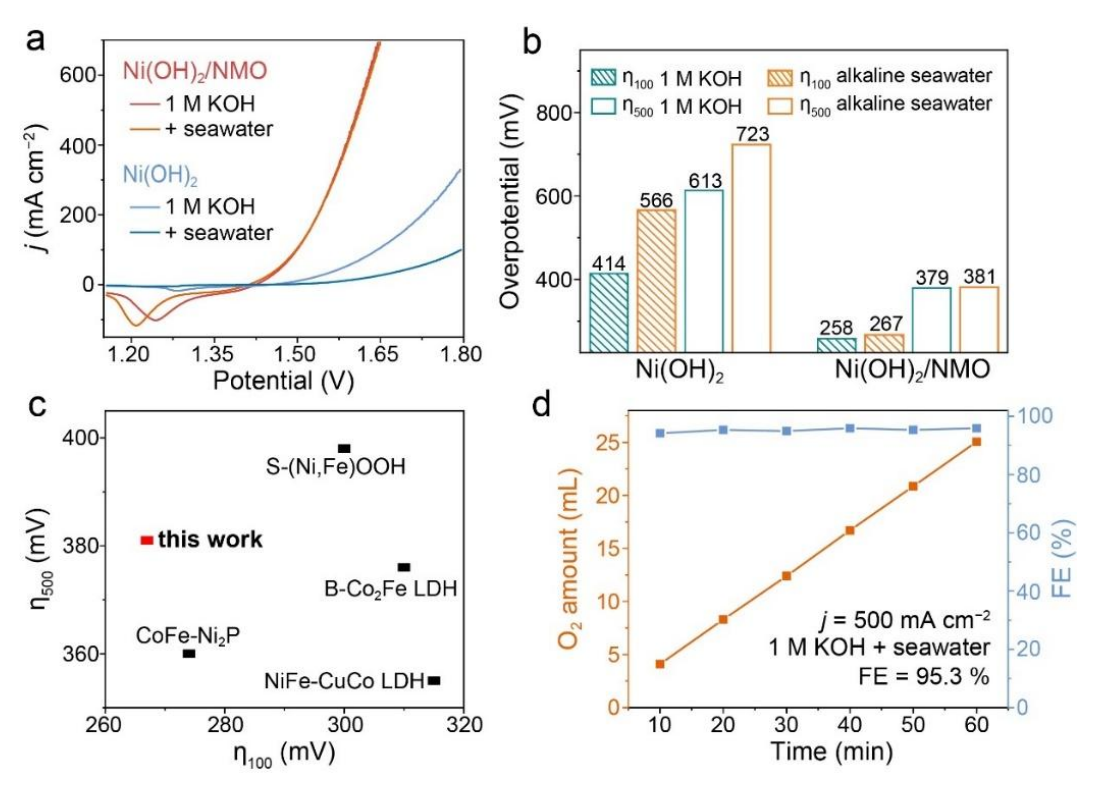


Figure 5.8. (a) LSV curves (with iR correction) of Ni(OH)₂ and Ni(OH)₂/NMO in alkaline freshwater and seawater. (b) Overpotentials of Ni(OH)₂/NMO and Ni(OH)₂ in alkaline seawater oxidation. (c) Comparison of OER overpotentials (at 100 and 500 mA cm⁻²) of Ni(OH)₂/NMO with other electrocatalysts. (d) FE (blue squares) of Ni(OH)₂/NMO measured at 500 mA cm⁻² in seawater + 1 M KOH. Orange squares show the O₂ amount generated during the FE test. FE = 95.3 %.

Table 5.4. Comparison of electrocatalytic performance of Ni(OH)₂/NMO in 1 M KOH + seawater with previously reported materials.

Samples	Overpotential (mV, at 100 mA cm ⁻²)	Overpotential (mV, at 500 mA cm ⁻²)	Ref.
Ni(OH) ₂ /NMO	267	381	this work
B-Co ₂ Fe LDH	310	376	[35]
NiFe-CuCo LDH	315	355	[36]
S-(Ni,Fe)OOH	300	398	[20]
CoFe-Ni ₂ P	274	360	[37]

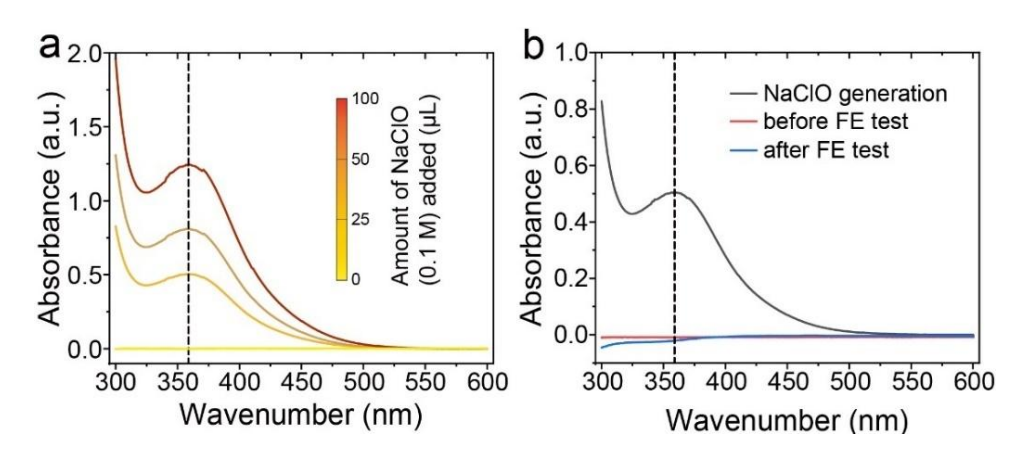


Figure 5.9. UV–vis spectra of (a) iodide titration with various NaClO concentrations and (b) electrolytes before and after the FE test.

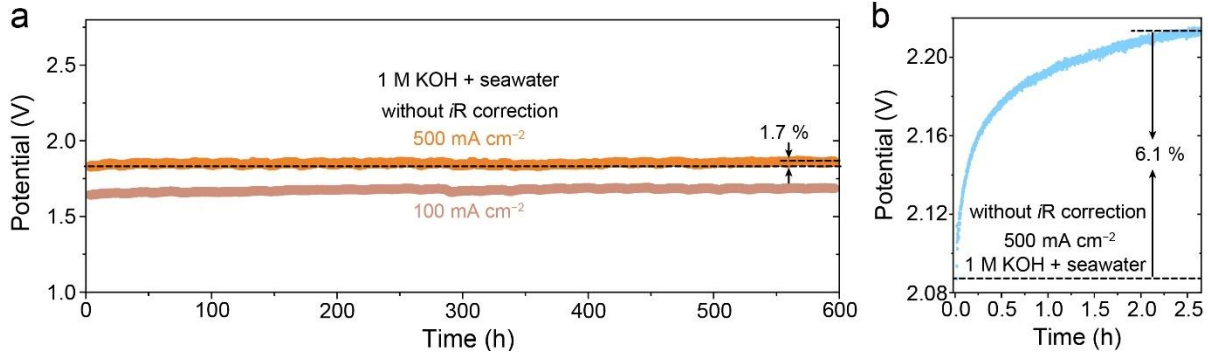


Figure 5.10. (a) Chronopotentiometric curves of Ni(OH)₂/NMO in 1 M KOH + seawater. (b) Chronopotentiometric curves of Ni(OH)₂ in 1 M KOH + seawater.

Chronopotentiometry further reveals the superior long-term electrocatalytic stability of Ni(OH)₂/NMO during seawater OER. Remarkably, Ni(OH)₂/NMO maintains excellent

stability at both 100 and 500 mA cm⁻² in alkaline seawater over 600 h (**Figure 5.10a**). The potential difference at 500 mA cm⁻² in freshwater and seawater electrolytes can be ascribed to lower Ohmic potential drop in seawater because of its rich ions environment that causes lower electrolyte resistance. While a slight increase (1.7 %) is observed in the potential required to sustain 500 mA cm⁻² for seawater OER, this is significantly lower than the 6.1 % increase for Ni(OH)₂ within just 2.5 h (**Figure 5.10b**). This further demonstrates the superior long-term stability of Ni(OH)₂/NMO in seawater oxidation.

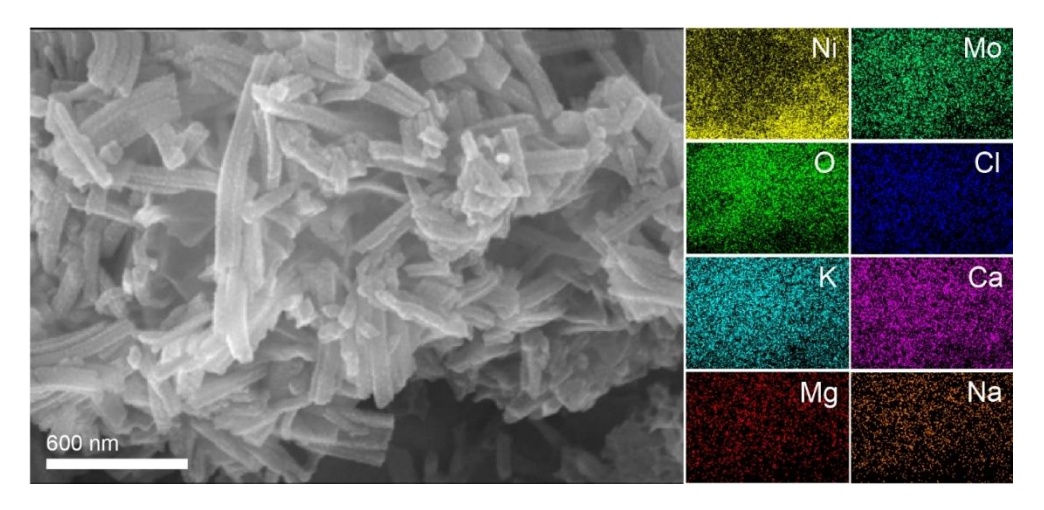


Figure 5.11. SEM image and the corresponding EDS mapping images of Ni(OH)₂/NMO after 600-h stability test in 1 M KOH + seawater.

The post-electrolysis SEM image of Ni(OH)₂/NMO reveals that its hierarchical morphology is well retained after a 600-h stability test (**Figure 5.11**), supporting its high corrosion resistance in seawater. However, EDS mapping images detect the deposition of additional Ca and Mg elements, likely due to the formation of insoluble Ca(OH)₂ and Mg(OH)₂ on the catalyst surface during OER. These deposits may obscure active sites, potentially contributing to the increased potential required for long-term reaction. To demonstrate the practical application for seawater splitting, a 1.5-V commercial battery was used to power a NiMo||Ni(OH)₂/NMO electrolysis system. The NiMo alloy was employed as the cathode because of its Pt-like hydrogen evolution reaction performance (**Figure 5.12a**). NiMo cathode

was coupled with Ni(OH)₂/NMO anode to form a seawater-splitting system. A commercial 1.5-V battery was used to power the device setup. The continuous and vigorous production of bubbles at both the cathode and anode was observed (**Figure 5.12b**), which were assigned to H₂ and O₂, respectively, confirming its feasibility for practical application.

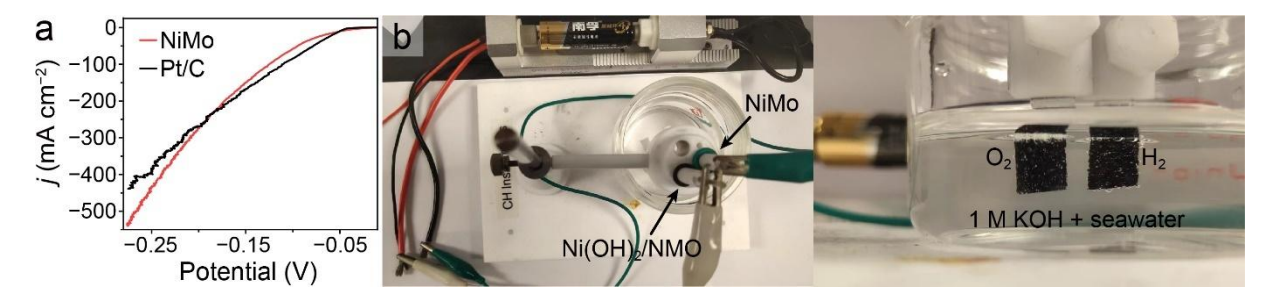


Figure 5.12. (a) LSV curves of NiMo and commercial Pt/C catalysts in 1 M KOH. (b) A photo of NiMo||Ni(OH)₂/NMO two-electrode electrolysis system driven by a commercial 1.5-V battery.

5.4.4. MOR and Methanol-assisted Seawater Electrolysis

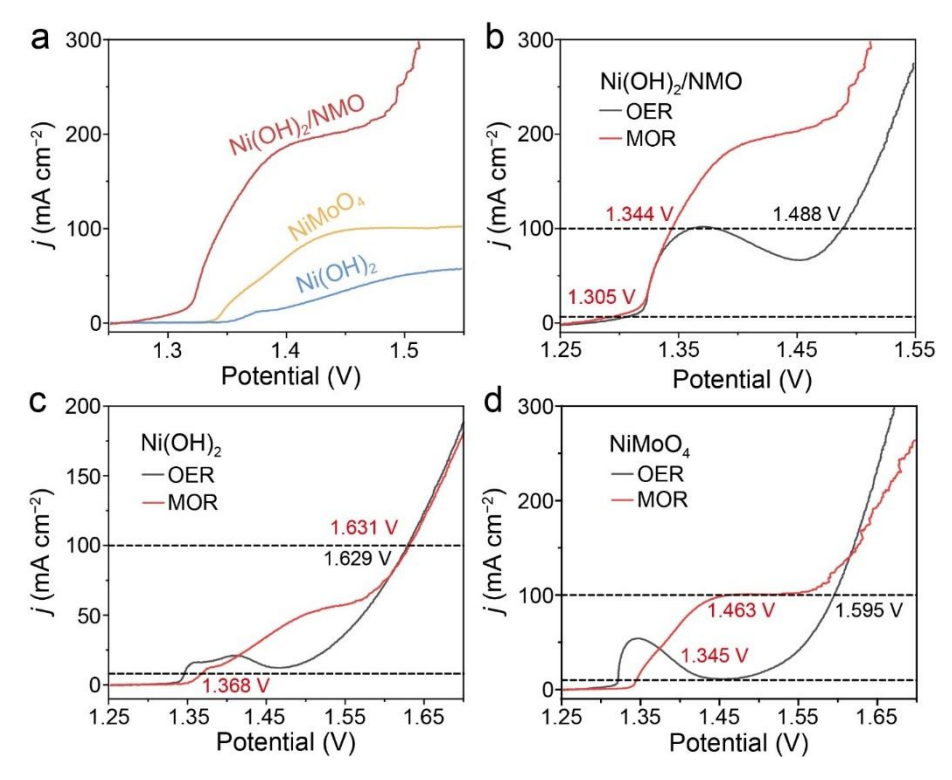


Figure 5.13. (a) LSV curves of NiMoO₄, Ni(OH)₂, and Ni(OH)₂/NMO in 1 M KOH + 0.1 M methanol. LSV curves of (b) Ni(OH)₂/NMO, (c) Ni(OH)₂, and (d) NiMoO₄ during OER and MOR.

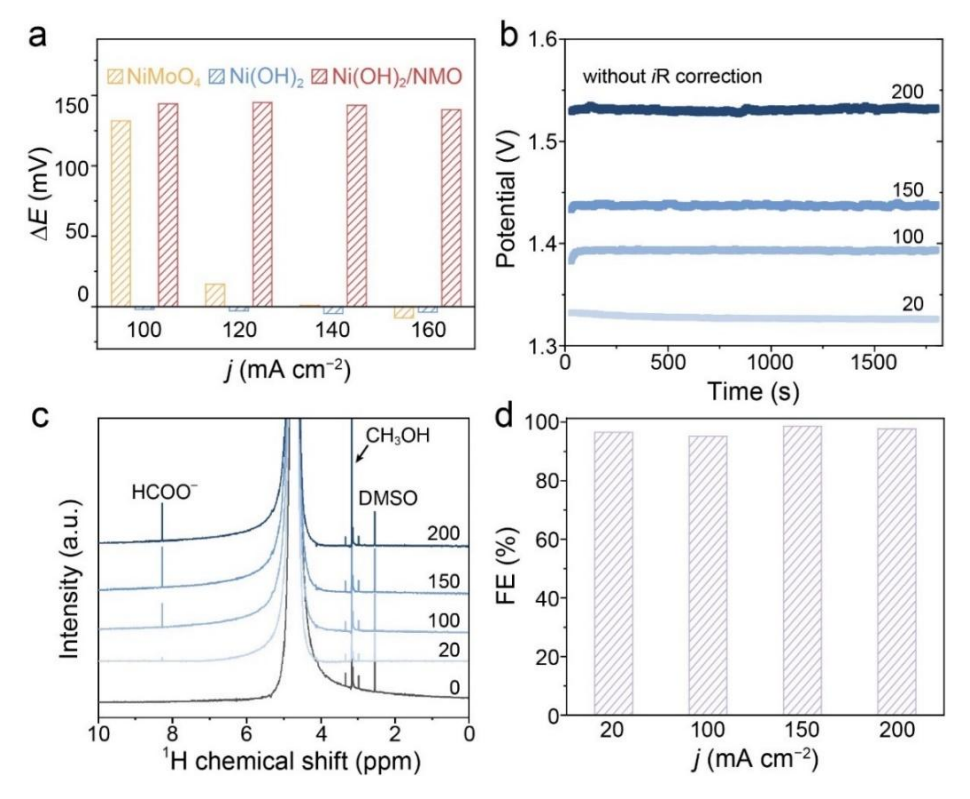


Figure 5.14. (a) Potential differences between OER and MOR at various current densities. (b) Chronopotentiometric curves of 0.5-h MOR at current densities from 20 to 100, 150, and 200 mA cm⁻². (c) NMR spectra of electrolytes after 0.5-h MOR at current densities from 0 to 20, 100, 150, and 200 mA cm⁻². (d) MOR FE at various current densities.

The MOR performances of Ni(OH)₂, NiMoO₄, and Ni(OH)₂/NMO were investigated in an aqueous electrolyte containing 1 M KOH and 0.1 M methanol. As shown in **Figure 5.13a**, Ni(OH)₂/NMO exhibits a significantly lower MOR potential (1.305 V) to reach a current density of 10 mA cm⁻² compared to Ni(OH)₂ (1.372 V) and NiMoO₄ (1.345 V). Furthermore, Ni(OH)₂/NMO demonstrates the greatest reduction in potential between MOR and OER at all current densities tested (100, 120, 140, and 160 mA cm⁻²) compared with Ni(OH)₂ and NiMoO₄, (**Figures 5.13b–d** and **5.14a**), which signifies superior MOR selectivity of Ni(OH)₂/NMO. Chronopotentiometry at various current densities for 0.5 h was employed to determine the FE of the MOR process by Ni(OH)₂/NMO. The stable *U*-t curves indicate steady MOR between 20 and 200 mA cm⁻² (**Figure 5.14b**). ¹H nuclear magnetic resonance (NMR) spectroscopy further identifies and quantifies formate products (**Figure 5.14c**). Ni(OH)₂/NMO

maintains a high FE exceeding 95 % at these current densities in alkaline methanol electrolytes (**Figure 5.14d**).

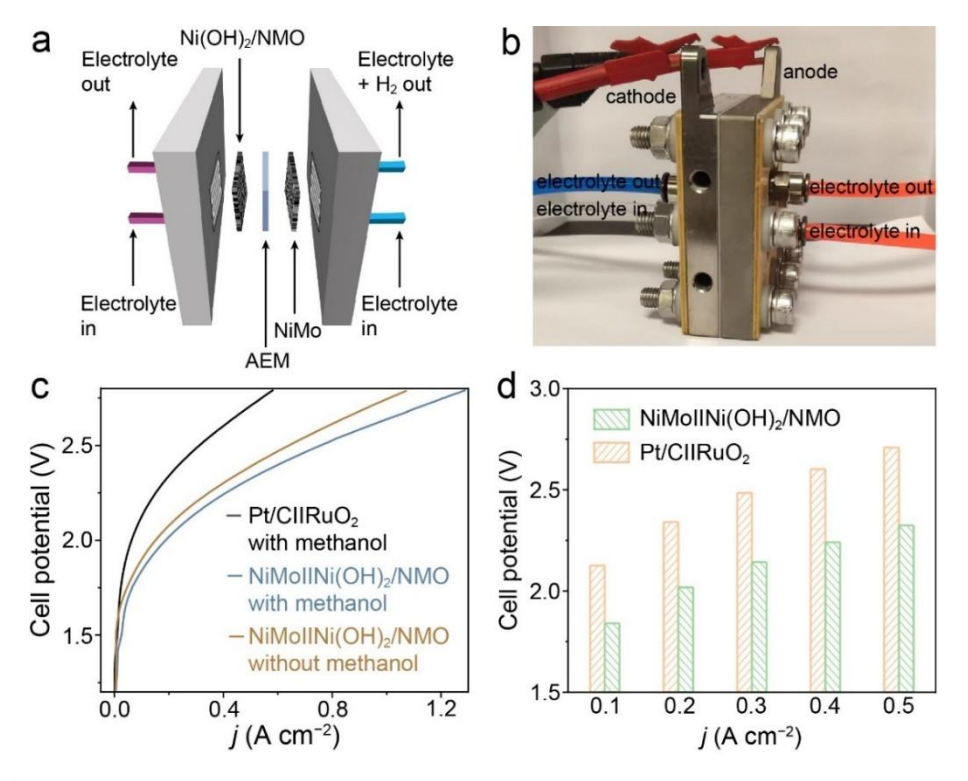


Figure 5.15. (a) A schematic diagram of the MEA, where Ni(OH)₂/NMO and NiMo are used as the anode and cathode, respectively. (b) A photo of the flow cell water-splitting system. (c) MEA polarization curve measured in various electrolytes. (d) Comparison of cell potentials of NiMo||Ni(OH)₂/NMO and Pt/C||RuO₂ required to achieve current densities of 0.1, 0.2, 0.3, 0.4, and 0.5 A cm⁻².

To assess the potential for large-scale applications, a 1-cm² Ni(OH)₂/NMO electrode was paired with a 1-cm² NiMo cathode in an MEA, as depicted in **Figure 5.15a** (with the setup shown in **Figure 5.15b**). In a hybrid seawater electrolyte (1 M KOH + 0.1 M methanol + seawater) at 23 °C, the NiMo||Ni(OH)₂/NMO system achieves current densities of 0.1 and 0.5 A cm⁻² at considerably lower cell voltages (1.840 and 2.324 V, respectively) compared to the alkaline-seawater electrolyte (1.904 and 2.392 V, respectively; **Figures 5.15c** and **5.15d**). The calculated energy consumption for H₂ production using the NiMo||Ni(OH)₂/NMO system are 177.5 and 224.2 kJ mol⁻¹ H₂ at current densities of 0.1 and 0.5 A cm⁻², respectively (**Figure**

5.16 and **Table 5.5**). These values are substantially lower than those for the commercial Pt/C||RuO₂ system (205.1 and 261.4 kJ mol⁻¹ H₂, respectively), representing energy savings of over 13.5 %. This highlights the potential of the NiMo||Ni(OH)₂/NMO system for cost-effective and practical H₂ production from seawater, offering a more energy-efficient alternative to existing technologies. Importantly, the NiMo||Ni(OH)₂/NMO flow cell demonstrates stable and continuous operation for over 130 h at current densities of 0.1, 0.5, and 1.0 A cm⁻² with minimal performance degradation (**Figure 5.17**).

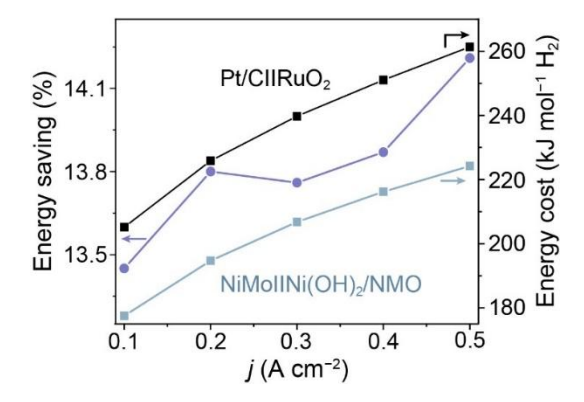


Figure 5.16. Energy costs of NiMo||Ni(OH) $_2$ /NMO and Pt/C||RuO $_2$ at 0.1-0.5 A cm $^{-2}$ and the corresponding energy savings.

Table 5.5. Cell potentials and estimated energy consumption for H_2 production using $Pt/C|RuO_2$ and $NiMo|Ni(OH)_2/NMO$ as electrode materials in methanol-contained alkaline seawater.

Current density (A cm ⁻²)	Pt/C RuO2		NiMo Ni(OH)2/NMO	
	Potential (V)	Energy (kJ mol ⁻¹ H ₂)	Potential (V)	Energy (kJ mol ⁻¹ H ₂)
0.1	2.126	205.13	1.840	177.50
0.2	2.341	225.87	2.018	194.71
0.3	2.485	239.77	2.143	206.77
0.4	2.602	251.05	2.241	216.22
0.5	2.709	261.38	2.324	224.23

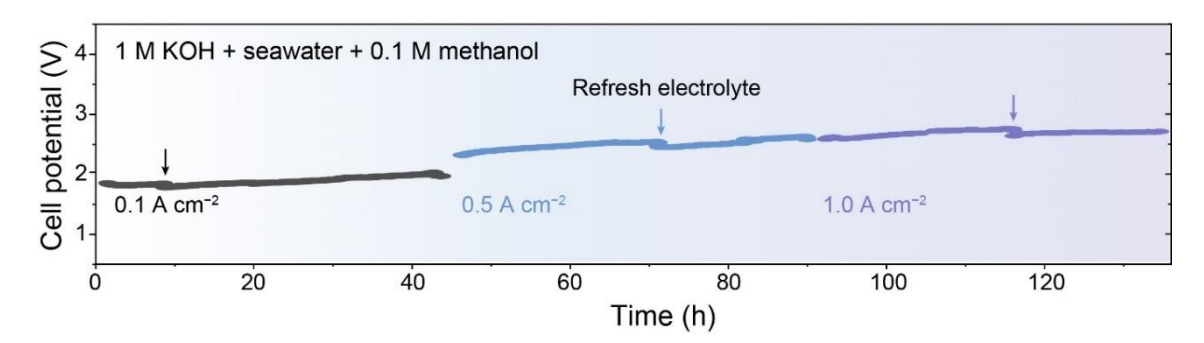


Figure 5.17. Chronopotentiograms of NiMo||Ni(OH)₂/NMO measured at 0.1, 0.5, and 1.0 A cm⁻² in alkaline seawater.

5.4.5. Mechanisms and Anti-corrosion Properties of Ni(OH)2/NMO

EIS was conducted to elucidate the mechanism responsible for the enhanced OER performance. The corresponding Nyquist plots were analyzed to investigate the charge transfer dynamics at the electrode/electrolyte interface (**Figure 5.18**). The resistance at this interface (R_{ct}) is significantly reduced for Ni(OH)₂/NMO (2.9 Ω) compared to Ni(OH)₂ (17.5 Ω) and NiMoO₄ (20.1 Ω). This indicates a lower charge transfer barrier in the composite material.

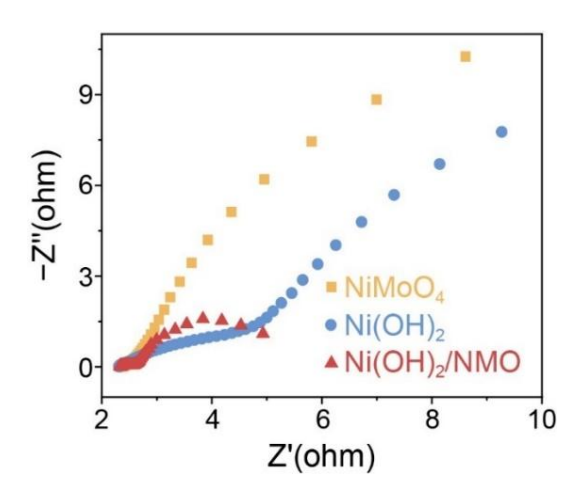


Figure 5.18. Nyquist plots of Ni(OH)₂, NiMoO₄, and Ni(OH)₂/NMO.

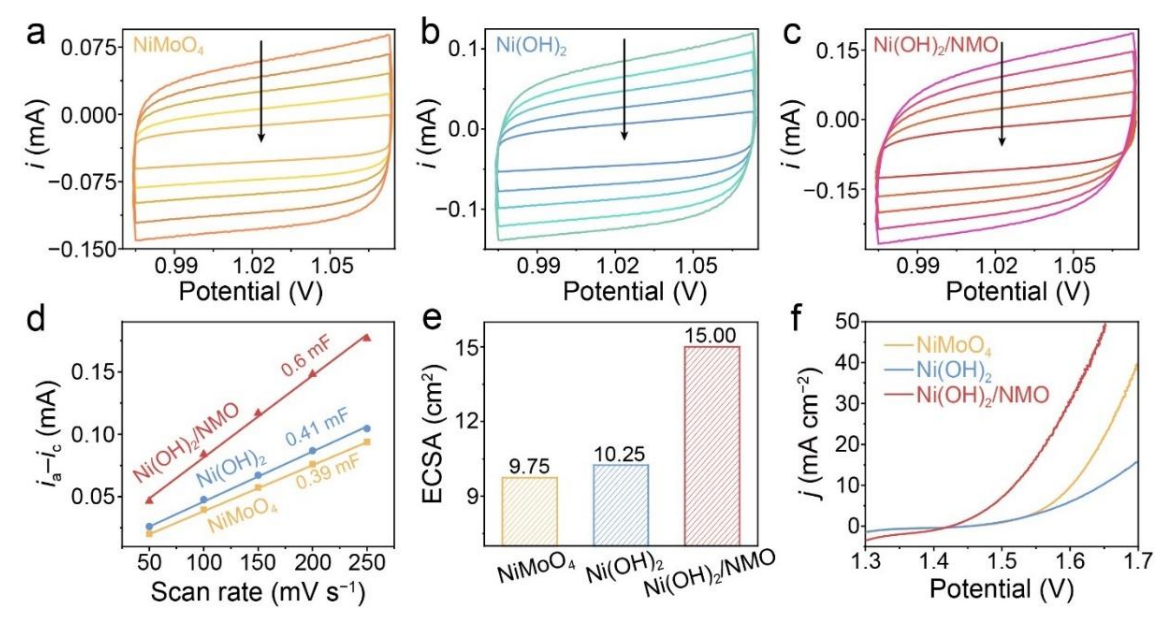


Figure 5.19. Cyclic voltammograms measured in a non-Faradaic region at various scan rates. (a) NiMoO₄, (b) Ni(OH)₂, and (c) Ni(OH)₂/NMO. The scan rate decreased from 250 to 50 mV s⁻¹. (d) Linear fitting of double-layer capacitance (*C*_{dl}) against CV scan rate for the estimation of electrochemically active surface area (ECSA) of Ni(OH)₂, NiMoO₄, and Ni(OH)₂/NMO. I ECSA and (f) ECSA-normalized LSV curves of Ni(OH)₂, NiMoO₄, and Ni(OH)₂/NMO.

We further assessed the ECSA of the as-prepared catalysts by measuring the electrochemical $C_{\rm dl}$ in a non-Faradaic potential region at various scan rates (**Figures 5.19d**). Ni(OH)₂/NMO exhibits the largest ECSA, exceeding that of Ni(OH)₂ and NiMoO₄ by factors of 1.46 and 1.54, respectively (**Figure 5.19e**). This suggests that the hierarchical structure provides a significantly larger surface area with more accessible active sites for the OER. Interestingly, even after normalizing the polarization curves by ECSA, the OER activity of Ni(OH)₂/NMO remains superior to Ni(OH)₂ and NiMoO₄ (**Figure 5.19f**), which implies that its excellent performance is not solely due to the increased ECSA from the hierarchical structure but also a higher intrinsic activity. Furthermore, Arrhenius plots were obtained from LSVs conducted at various temperatures (**Figure 5.20**) and used to determine the E_a from their slopes. Ni(OH)₂/NMO displays the lowest E_a of 23.22 kJ mol⁻¹, followed by NiMoO₄ (32.37 kJ mol⁻¹) and Ni(OH)₂ (50.39 kJ mol⁻¹). This lower activation energy suggests that the OER process on Ni(OH)₂/NMO proceeds more readily compared to the other two materials.

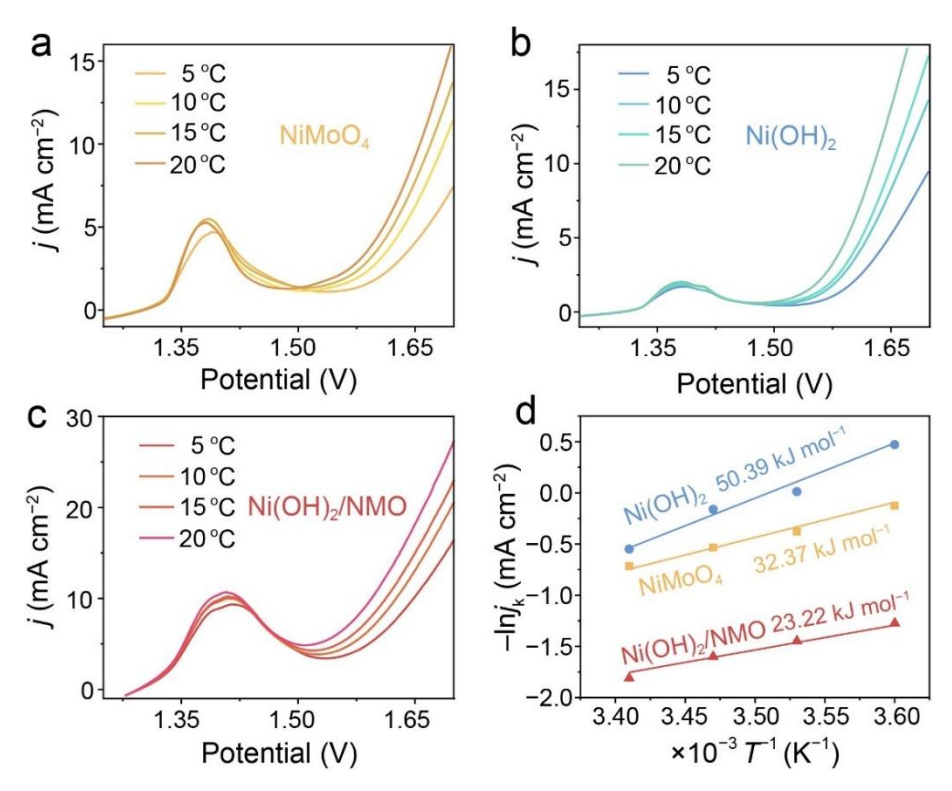


Figure 5.20. LSVs measured at various temperatures: (a) NiMoO₄, (b) Ni(OH)₂, and (c) Ni(OH)₂/NMO. (d) Arrhenius plots of Ni(OH)₂, NiMoO₄, and Ni(OH)₂/NMO.

In situ Raman spectroscopy was employed to track the real-time evolution of surface species during OER. **Figure 5.21a** shows the Raman spectra of Ni(OH)₂, captured from the OCP to an applied potential of 1.499 V (vs. RHE). At 1.399 V, the characteristic peaks for NiOOH species, associated with the Ni³⁺(e_g)—O and Ni³⁺(a_{1g})—O vibration modes, are observed at 476 (peak **i**) and 558 cm⁻¹ (peak **ii**), respectively, [38] signifying a transformation from the starting materials during the OER process. The intensity ratio of these peaks (I₅₅₈/I₄₇₆) increases from 1.44 at 1.399 V to 1.64 at 1.499 V (**Figure 5.21b**). The pronounced increase in the peak **ii** intensity, relative to peak **I**, suggests a phase transition from the initial γ-NiOOH to the more active β-NiOOH phase at higher anodic potentials. [39, 40] Similar trends are observed for Ni(OH)₂/NMO (**Figure 5.21c**), but the transition to the β-NiOOH phase occurs at a lower potential, as reflected by a higher I₅₅₈/I₄₇₆ ratio of 1.97 at 1.424 V. Besides, Mo—O bending (347 cm⁻¹) and symmetric Mo=O stretching (941 cm⁻¹) disappear when the potential increases to 1.399 V, which suggests the partial collapse of NiMoO₄ structure. On the other hand,

NiMoO₄ exhibits sluggish phase transition during the OER activation process, which can be related to its poorer catalytic performance (**Figure 5.21d**).

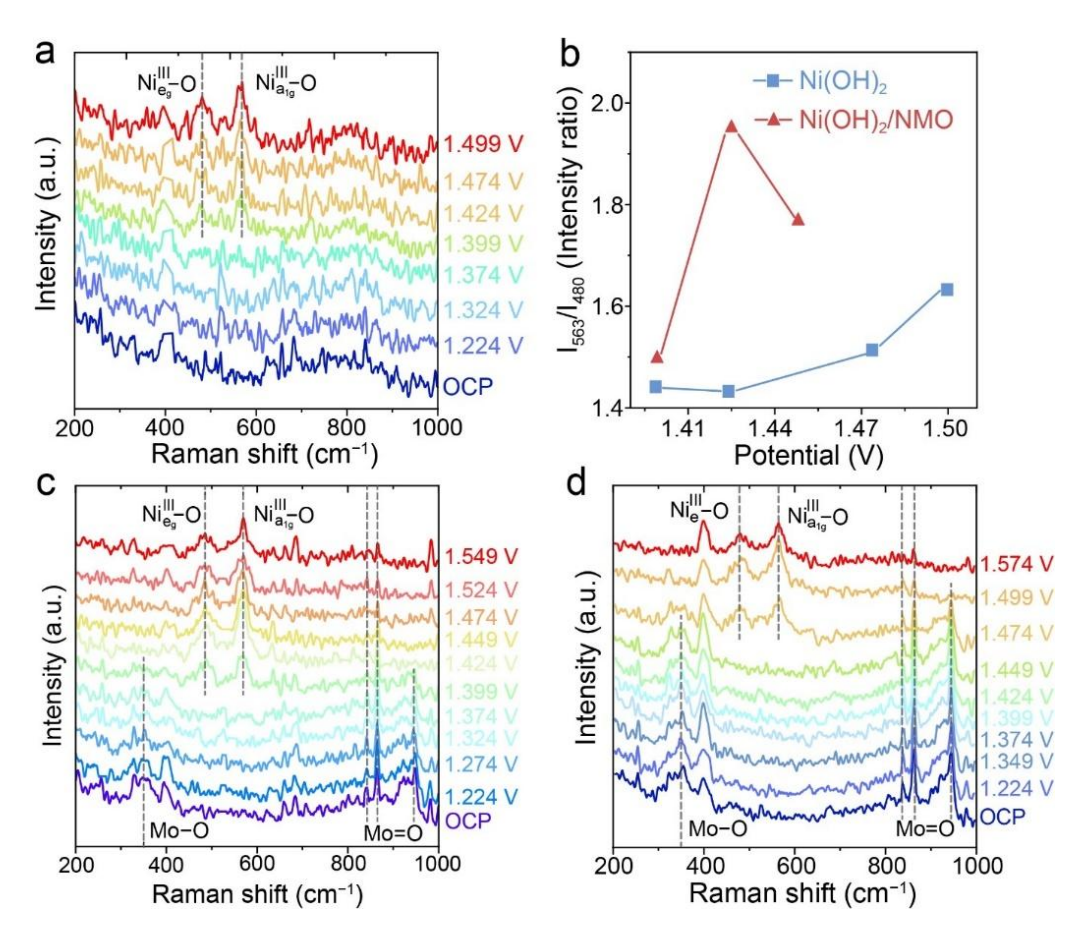


Figure 5.21. *In situ* Raman spectra of (a) Ni(OH)₂, (c) Ni(OH)₂/NMO, and (d) NiMoO₄ in 1 M KOH. (b) Intensity ratio of peak **ii**-to-**I** (I₅₆₃/I₄₈₀) at various applied potentials.

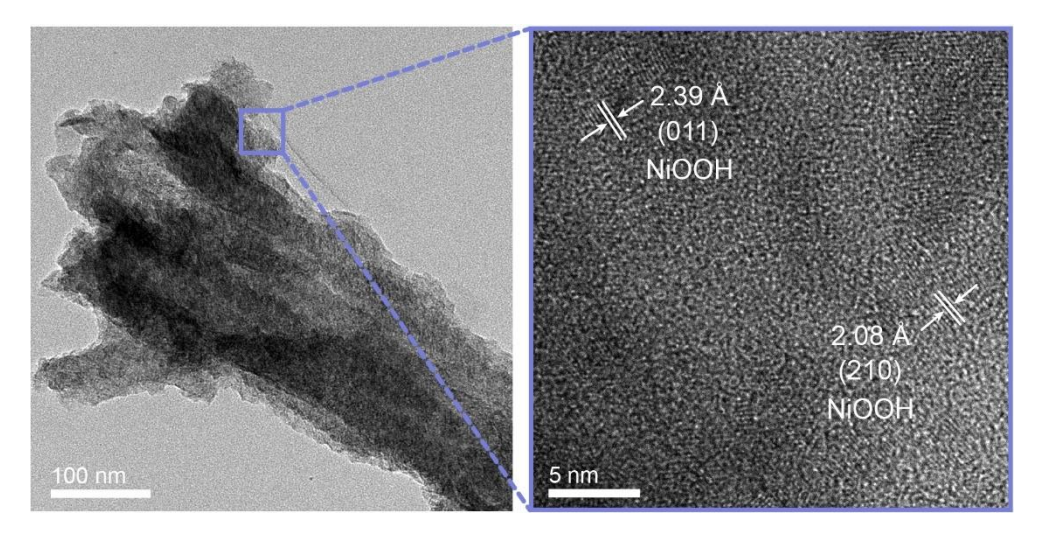


Figure 5.22. TEM and HRTEM images of Ni(OH)₂/NMO after OER activation.

TEM confirms the formation of NiOOH in Ni(OH)₂/NMO after OER activation as evidenced by the lattice spacings of 2.39 and 2.08 Å, corresponding to the (011) and (210) plane of NiOOH, respectively, (**Figure 5.22**). Further analysis using XPS reveals the shifts in Mo 3*d* peaks toward lower binding energies by 0.14 eV, indicating an increase in electron density around Mo and the charge transfer during the OER activation process (**Figure 5.23**).^[41] Notably, the peak intensity of these Mo peaks decreases with higher potentials, suggesting a loss of Mo during OER activation. Quasi-*in-situ* UV–Vis spectroscopy corroborated the release of MoO₄²⁻ anion (**Figure 5.24a**). An absorption peak for MoO₄²⁻ appears at around 209 and 231 nm after applying 2.5 V to Ni(OH)₂/NMO, and its intensity increases with prolonged oxidation processes (**Figure 5.24b**). This observation confirms the release of MoO₄²⁻ from NiMoO₄ during OER. It is worth noting that these released anions can change the local coordination environment of NiOOH, driven by the positive potential of the anode, thereby influencing the adsorption behaviors of other molecules, such as Cl⁻ and methanol, and the reaction kinetics of CER and MOR.^[42]

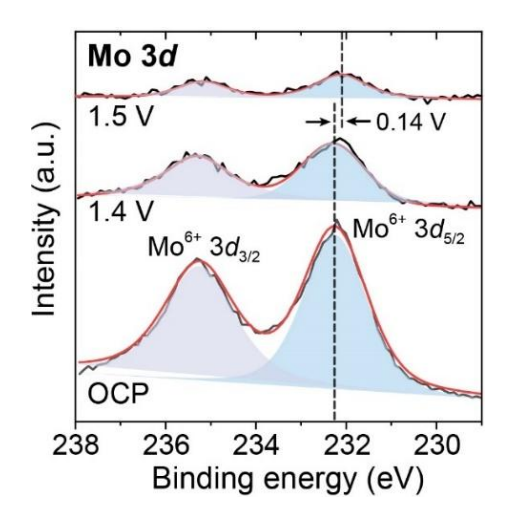


Figure 5.23. Ex situ XPS Mo 3d spectra of Ni(OH)₂/NMO during OER activation.

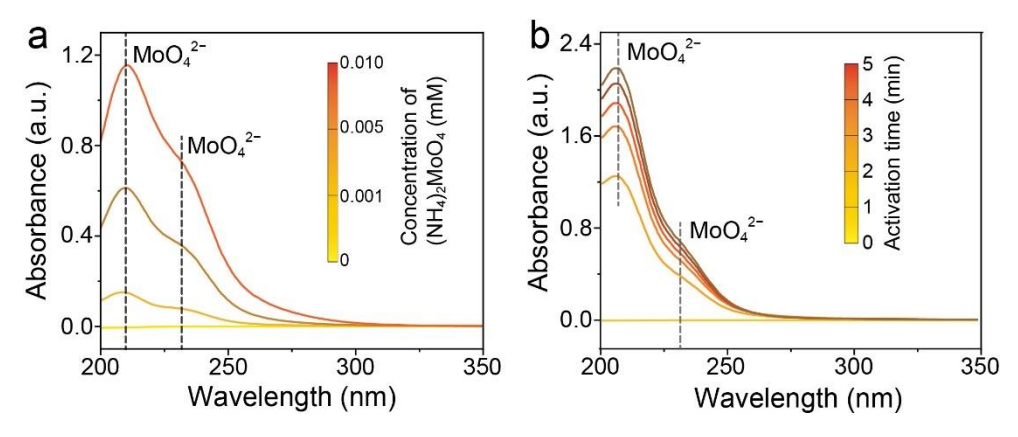


Figure 5.24. (a) UV–Vis spectra of ammonium molybdate spectrophotometry with various (NH₄)₂MoO₄ concentrations. (b) Quasi-*in-situ* UV–vis spectra for MoO₄²⁻ detection.

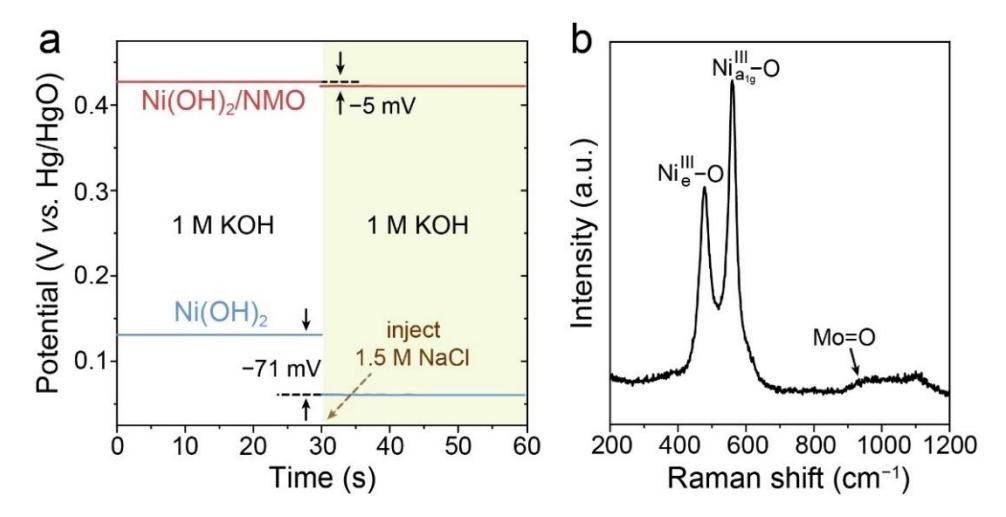


Figure 5.25. (a) OCP measurements of Ni(OH)₂ and Ni(OH)₂/NMO upon NaCl injection. (b) Raman spectra of Ni(OH)₂/NMO after 600-h *U*-t OER at 500 mA cm⁻² in seawater.

The OCP measurement can provide insights into the impact of Cl⁻ adsorption on the Helmholtz layer of catalysts. A larger OCP shift upon introducing Cl⁻ indicates a stronger influence of Cl⁻ on the catalyst surface. [43, 44] Upon the addition of 1.5 M NaCl, the OCP of Ni(OH)₂/NMO slightly decreases by 5 mV, while Ni(OH)₂ exhibits a significant drop of 71 mV (**Figure 5.25a**), suggesting a weaker impact of Cl⁻ on Ni(OH)₂/NMO. Notably, Raman spectroscopy performed after a 600-h stability test in alkaline seawater confirms the persistence of NiOOH and symmetric Mo=O stretching mode (**Figure 5.25b**). [45, 46] This highlights the durability and corrosion resistance of the Ni(OH)₂/NMO catalyst under harsh conditions.

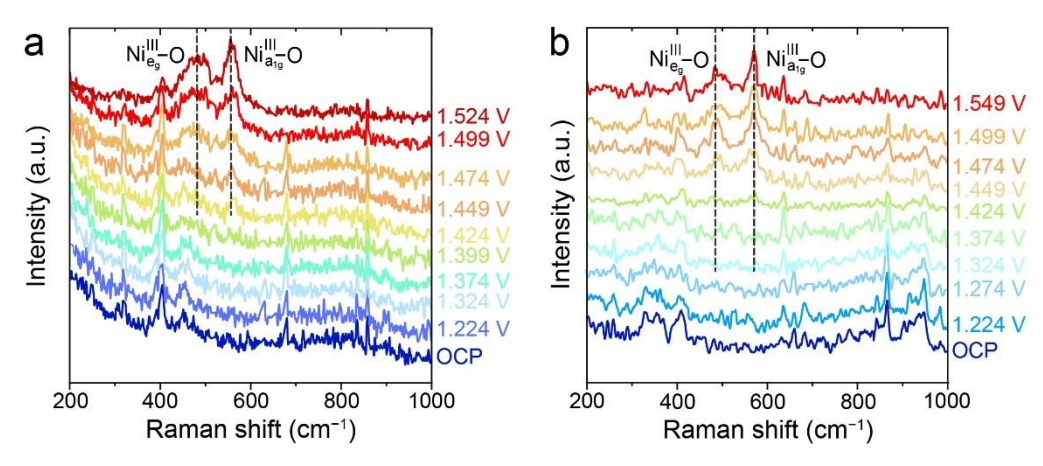


Figure 5.26. *In situ* Raman spectra of (a) Ni(OH)₂ and (b) Ni(OH)₂/NMO in 1 M KOH + 0.1 M methanol.

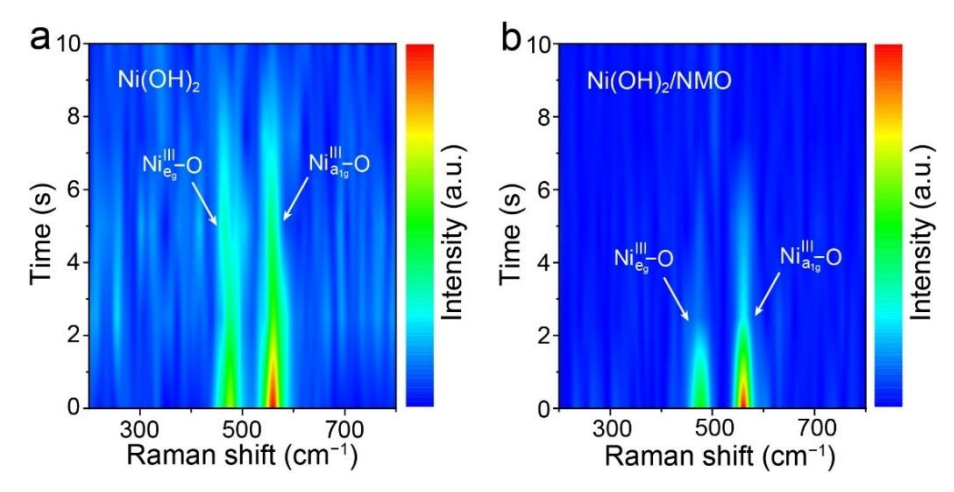


Figure 5.27. Quasi-*in-situ* Raman spectra of oxidized (a) Ni(OH)₂ and (b) Ni(OH)₂/NMO during the reaction with methanol.

In situ Raman spectroscopy was conducted to validate the mechanism of enhanced MOR performance of Ni(OH)₂/NMO. For Ni(OH)₂, the characteristic peak for Ni³⁺–O appears at a higher potential (1.424 V, **Figure 5.26a**) in a KOH–methanol electrolyte than in the blank KOH (**Figure 5.21a**), indicating that the conversion of Ni²⁺ to Ni³⁺ is retarded until 1.424 V. This is due to the MOR process that consumes produced Ni³⁺ species. The accumulation of Ni³⁺ above 1.424 V can be attributed to the accelerated Ni³⁺ generation rate over the methanol dehydrogenation rate. The further delayed appearance of the Ni³⁺–O peak (1.449 V, **Figure 5.26b**) indicates the faster methanol dehydrogenation rate on Ni(OH)₂/NMO.

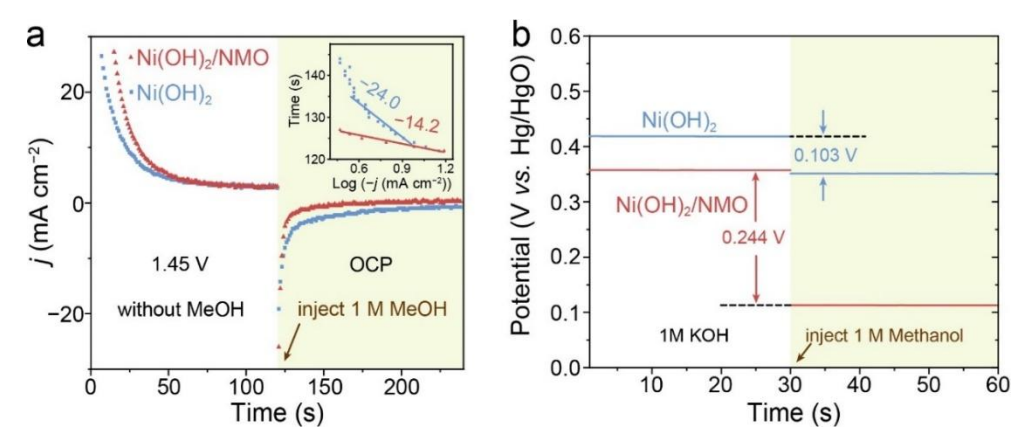


Figure 5.28. (a) Chronoamperometric responses of Ni(OH)₂ and Ni(OH)₂/NMO upon methanol injection. (b) OCP curves of Ni(OH)₂ and Ni(OH)₂/NMO upon 1 M methanol injection.

We further investigated the non-electrochemical step using quasi-operando Raman spectroscopy. The electrodes were first oxidized at a fixed potential of 1.50 V, followed by methanol addition and Raman measurement at different reaction time intervals. The Ni³⁺-O vibration mode on Ni(OH)₂ weakens and disappears after 10 s of reaction with methanol (**Figure 5.27a**). Notably, the Ni³⁺–O peak in Ni(OH)₂/NMO vanishes much faster, completely disappearing within 5 s (Figure 5.27b). This implies a significantly faster hydrogen transfer rate during the non-electrochemical step for Ni(OH)2/NMO. Periodic electrochemical measurements support this observed change in the hydrogen transfer rate (Figure 5.28a). After the initial activation by applying 1.45 V for 120 s, the transient current change was monitored upon methanol injection. The current response of Ni(OH)₂/NMO drops to 0 mA cm⁻² faster than Ni(OH)₂. The calculated Tafel slope for Ni(OH)₂/NMO (-14.2; inset in **Figure 5.28a**) is much lower than that of Ni(OH)₂ (-24.0), confirming faster catalytic kinetics of the PCET process in Ni(OH)₂/NMO. The change in methanol adsorption within the Helmholtz layer was also assessed by OCP measurements. A significantly larger OCP drop (0.244 V) is observed for Ni(OH)₂/NMO compared to Ni(OH)₂ upon adding methanol (**Figure 5.28b**). This indicates a stronger interaction between methanol and Ni(OH)₂/NMO, potentially leading to enhanced MOR activity.

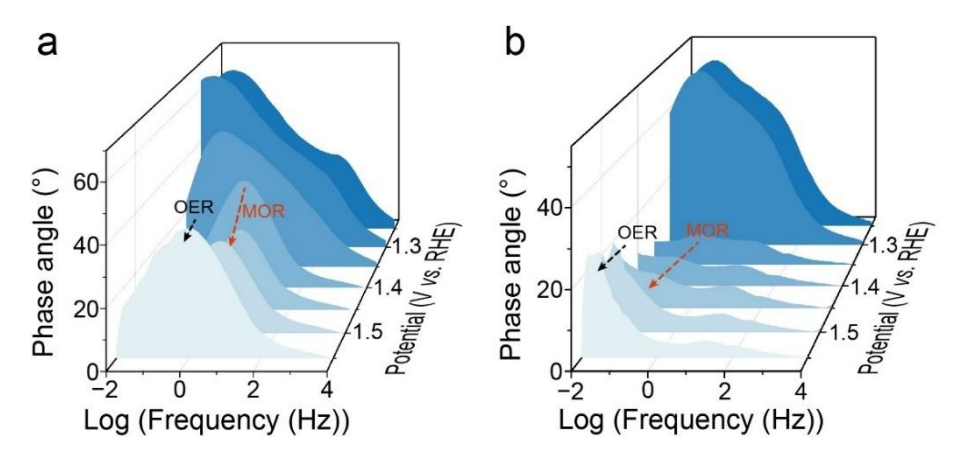


Figure 5.29. Bode phase plots for Ni(OH)₂ and Ni(OH)₂/NMO obtained from *operando* EIS in 1 M KOH + 0.1 M methanol.

Operando EIS provided further insights into the interfacial dynamics and electron transfer mechanisms. The low-frequency domain (0.01 - 10 Hz) in the Bode plots (**Figures 5.29a** and **5.29b**) corresponds to the MOR and OER interfaces, while the high-frequency region $(10 - 10^5 \text{ Hz})$ reflects surface oxidation processes. [47, 48] Compared to Ni(OH)₂, the phase angle of transition peaks attributed to MOR (0.1 - 1 Hz) on Ni(OH)₂/NMO is smaller at the same voltage. This suggests a faster conversion rate of oxide species at the interface.

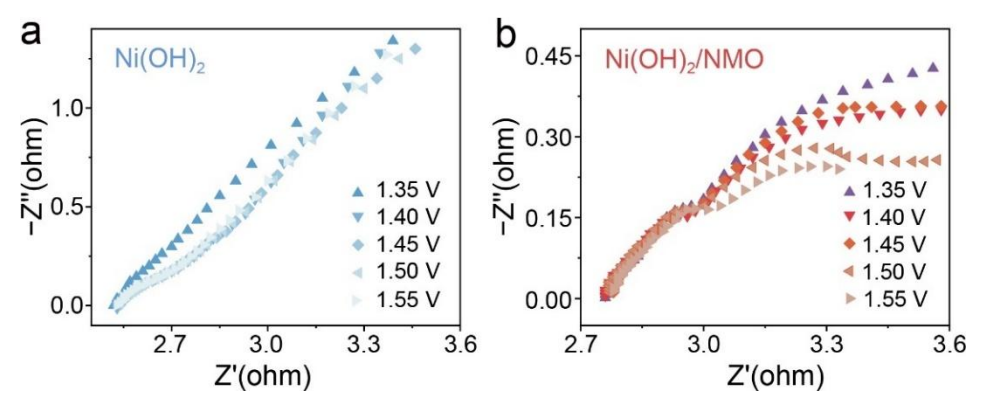


Figure 5.30. Nyquist plots of (a) Ni(OH)₂ and (b) Ni(OH)₂/NMO at various applied potentials.

Nyquist plots offer additional information about the interfacial resistances at various potentials (**Figure 5.30** and **Table 5.6**). Ni(OH)₂/NMO consistently exhibits lower resistance at the electrode/electrolyte interface compared to Ni(OH)₂, indicating enhanced charge transfer

efficiency (**Figure 5.31**). The peak observed at 10 - 100 Hz in Ni(OH)₂/NMO can be attributed to the oxidation of NiMoO₄, consistent with the UV–vis spectra (**Figure 5.24b**).

Table 5.6. Resistances of catalyst/electrolyte interfaces at various applied potentials.

Detential (V)	Resistance (Ω)			
Potential (V)	Ni(OH)2	Ni(OH)2/NMO		
1.35	45.67	1.90		
1.40	18.74	1.04		
1.45	8.17	1.14		
1.50	11.20	1.15		
1.55	15.49	0.98		

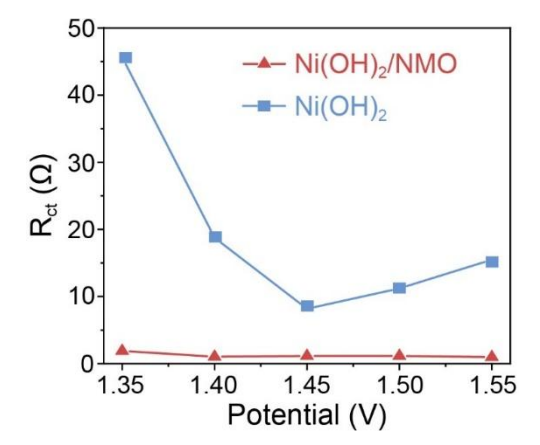


Figure 5.31. Solid—liquid interfacial resistances at various applied potentials.

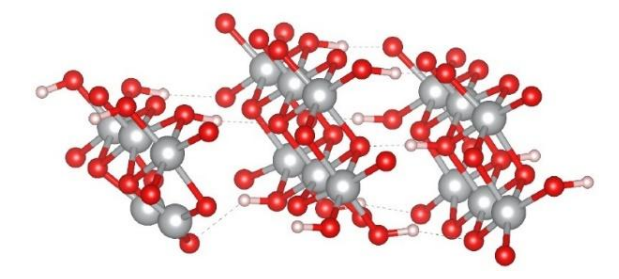


Figure 5.32. Optimized atomic structures of NiOOH. Ni, O, and H atoms are shown in gray, red, and pink, respectively.

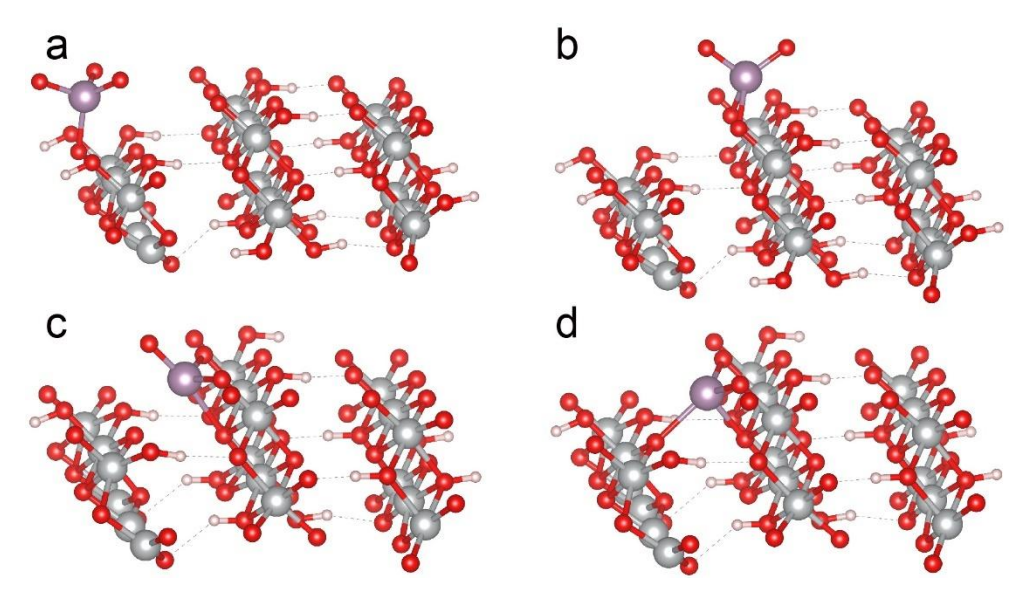


Figure 5.33. Various adsorption configurations of MoO₄²⁻ on the O site in NiOOH. (a) Monooxygen, (b) di-oxygen, (c) tri-oxygen, and (d) tetra-oxygen coordinations. Ni, Mo, O, and H atoms are shown in gray, violet, red, and pink, respectively.

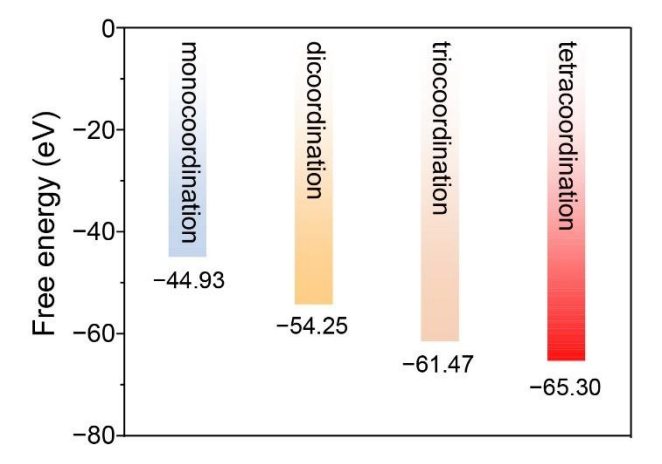


Figure 5.34. Adsorption free energies for MoO₄²⁻ with different adsorption sites on NiOOH.

Density functional theory (DFT) calculations were conducted to gain insights into how MoO₄²⁻ enhances the anti-corrosion property, water oxidation activity, and methanol oxidation selectivity of Ni(OH)₂/NMO. The activated states of Ni(OH)₂ and Ni(OH)₂/NMO were 169odelled using the crystal structures of NiOOH and MoO₄²⁻ adsorbed NiOOH (Mo-NiOOH), respectively. The (010) surface of NiOOH was chosen as the model (**Figure 5.32**) based on its reported low reaction barrier.^[49-51] Among four adsorption sites on the NiOOH surface considered (**Figure 5.33**), the most favorable configuration involves MoO₄²⁻ coordinated with

four O atoms, with an adsorption free energy of -65.3 eV (**Figure 5.34**). This configuration was selected for further calculations. The corresponding charging density difference image (**Figure 5.35**) reveals that the MoO_4^{2-} exhibits strong chemisorption on NiOOH by forming the Ni–O–Mo bond.

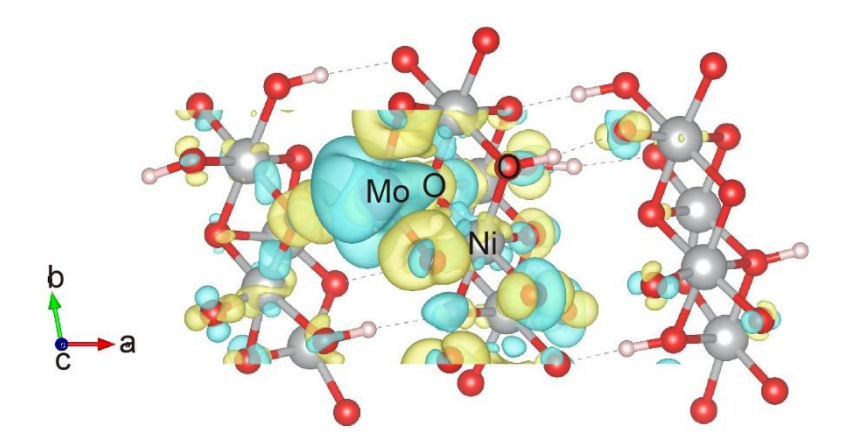


Figure 5.35. Charge density difference of Mo-NiOOH. Yellow and blue regions represent electron accumulation and depletion, respectively.

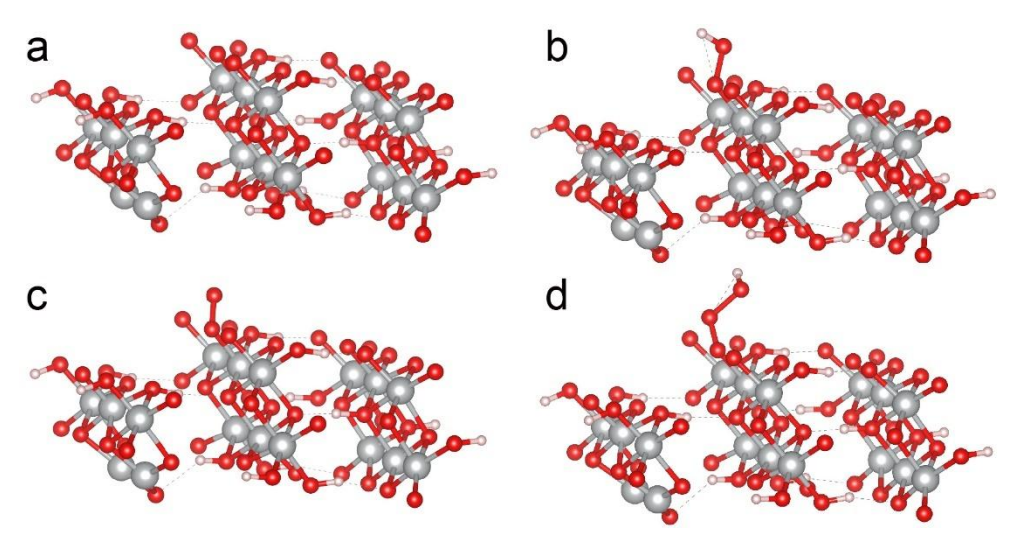


Figure 5.36. Structures of (a) bare NiOOH and (b) *OH, (c) *O, and (d) *OOH adsorbed NiOOH (O site). Ni, O, and H atoms are shown in gray, red, and pink, respectively.

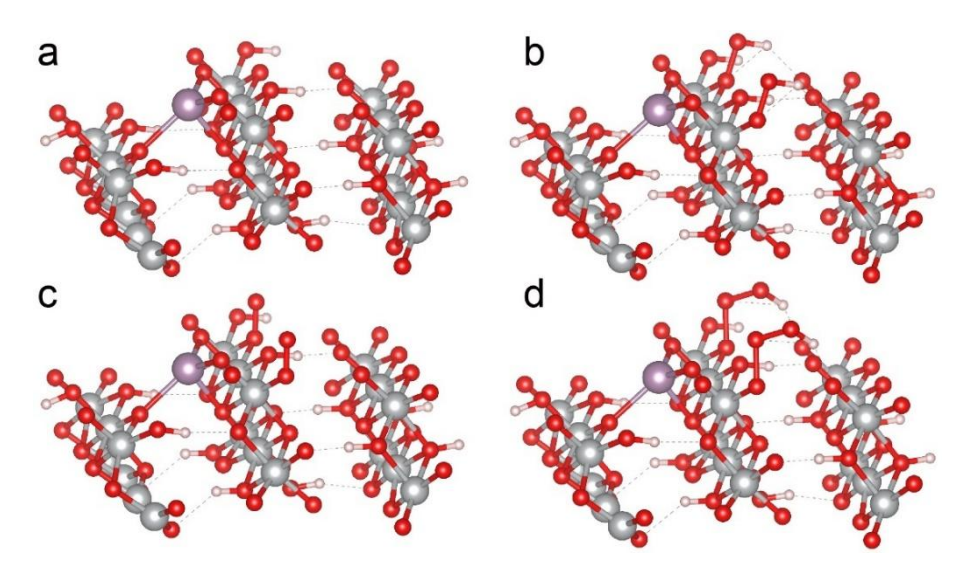


Figure 5.37. Structures of (a) bare Mo-NiOOH and (b) *OH, (c) *O, and (d) *OOH adsorbed Mo-NiOOH (O site). Ni, Mo, O, and H atoms are shown in gray, violet, red, and pink, respectively.

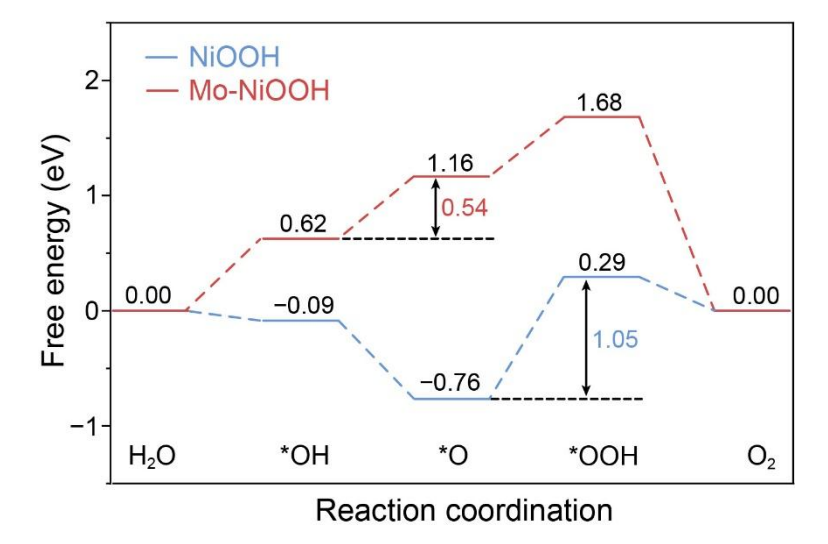


Figure 5.38. The Gibbs free energy diagrams for OER pathway on NiOOH and Mo-NiOOH.

DFT calculations were employed to calculate the free energy diagrams for each step of the OER (**Figures 5.36** and **5.37**). The OER free energy diagram (**Figure 5.38**) reveals that the second step, involving deprotonation and electron transfer from *OH to form *O, is the RDS for NiOOH. Interestingly, in Mo-NiOOH, the RDS shifts to the third step (*OOH formation). Consequently, the overall OER free energy is significantly reduced from 1.05 eV for NiOOH

to 0.54 eV for Mo-NiOOH, highlighting the beneficial effects of MoO₄²⁻ adsorption on OER catalysis.

Meanwhile, Mo-NiOOH shows a lower Cl⁻ adsorption energy of -1.32 eV compared to NiOOH (-2.32 eV, **Figures 5.39**, **5.40**, and **5.41**), which reveals that the leached MoO₄²⁻ could effectively reduce the adsorption of Cl⁻ on the NiOOH surface, thus effectively suppressing CER and enhancing the corrosion resistance of the electrode.

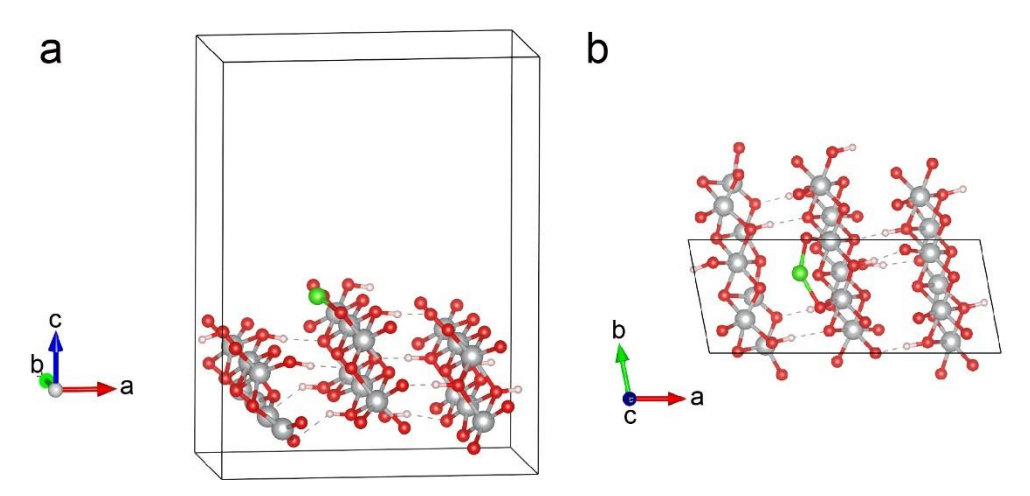


Figure 5.39. The atomic arrangement of *Cl adsorbed NiOOH (O site): (a) side- and (b) top-views. Ni, O, Cl, and H atoms are shown in gray, red, green, and pink, respectively.

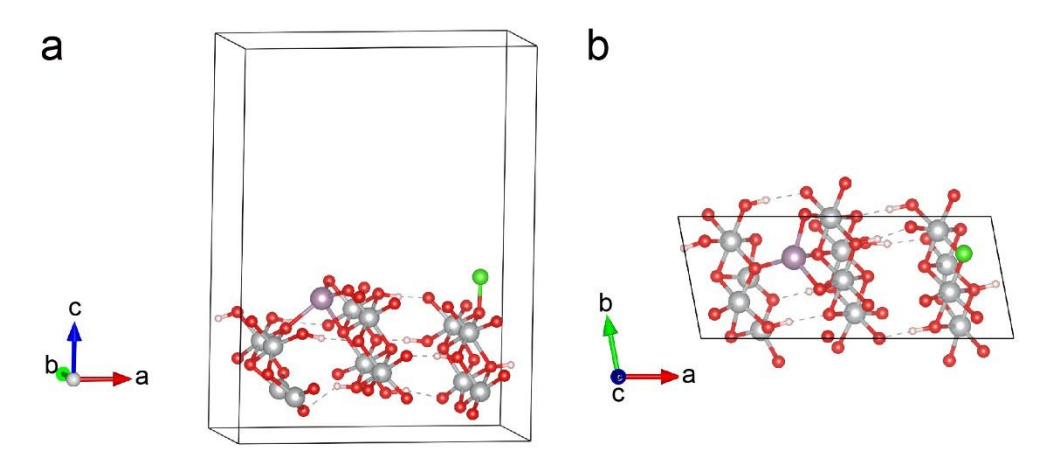


Figure 5.40. Structure of *Cl adsorbed Mo-NiOOH (Mo site): (a) side- and (b) top-views. Ni, Mo, O, Cl, and H atoms are shown in gray, violet, red, green, and pink, respectively.

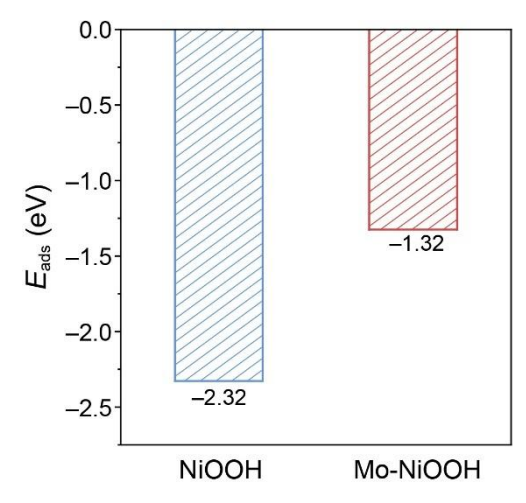


Figure 5.41. Adsorbed free energy of Cl⁻ on NiOOH and Mo-NiOOH.

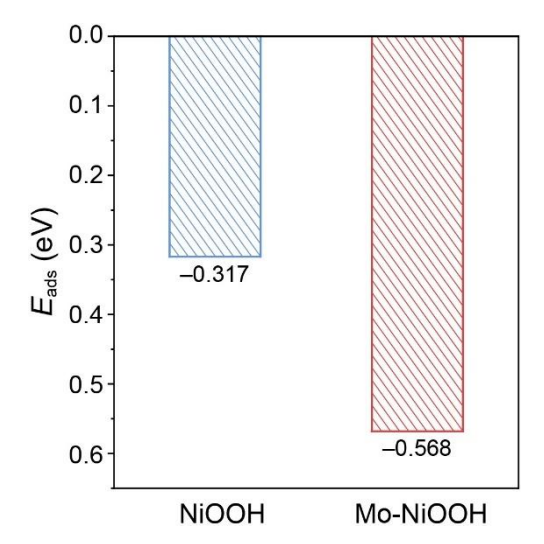


Figure 5.42. Adsorbed free energy of methanol molecules on NiOOH and Mo-NiOOH.

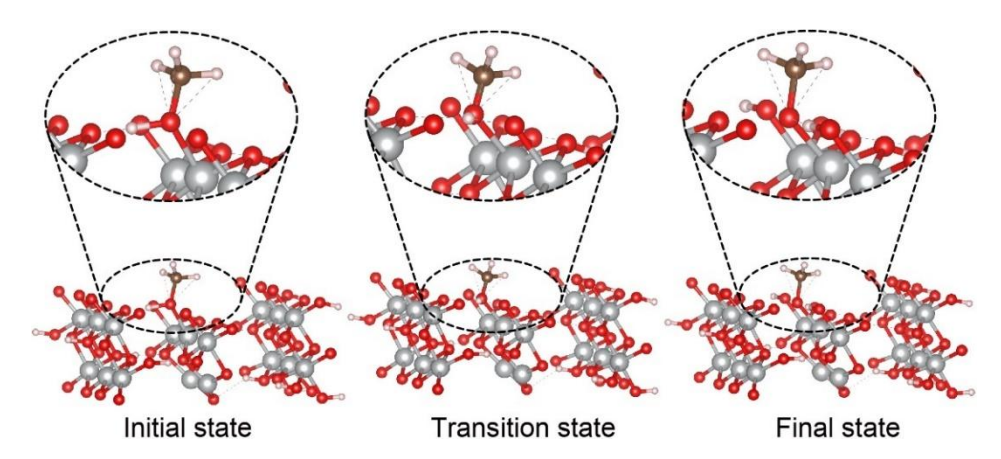


Figure 5.43. Side views of optimized methanol-adsorbed NiOOH (O site) during the hydrogen transfer process.

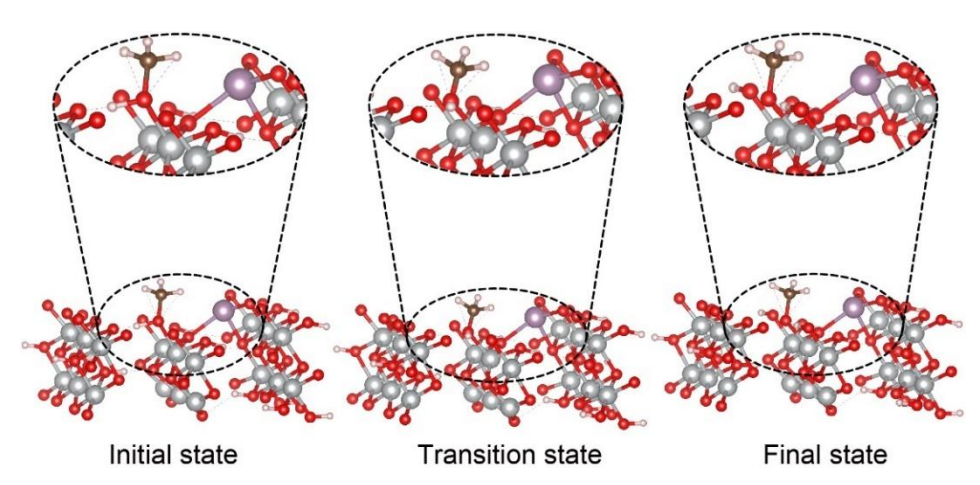


Figure 5.44. Side views of optimized methanol-adsorbed Mo-NiOOH (O site) during the hydrogen transfer process.

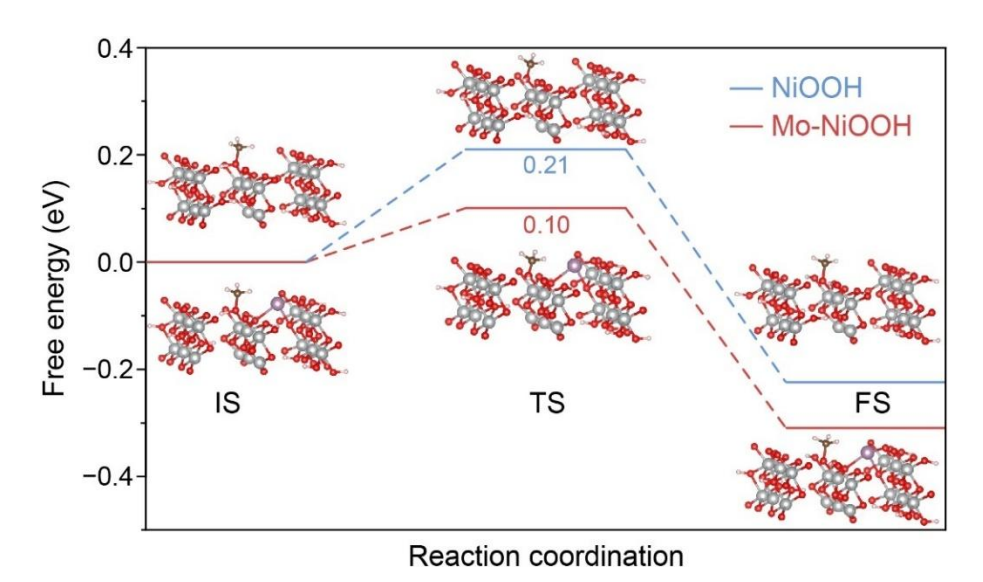


Figure 5.45. free energy changes in the hydrogen transfer process on NiOOH and Mo-NiOOH.

During methanol adsorption on the Mo-NiOOH surface, an energy of 0.568 eV is released (**Figure 5.42**), which exceeds the energy released on the NiOOH surface (0.317 eV). This indicates a more favorable adsorption of methanol on Mo-NiOOH. To gain a theoretical understanding of the influence of MoO₄²⁻ adsorption on the PCET process, DFT calculations were further engaged to analyze the hydrogen transfer energy barrier. As the core mechanism of methanol electrooxidation involves proton transfer from the substrate molecule to NiOOH, the energy barriers of proton transfer from methanol to NiOOH or Mo-NiOOH surface were calculated using optimized models of the initial state (IS), transition state (TS), and final state

(FS, **Figures 5.43–5.45**). The energy barrier for the PCET process on NiOOH is reduced from 0.21 to 0.10 eV after MoO_4^{2-} decoration, indicating a faster rate of the PCET process and an accelerated cycle between Ni³⁺ reduction and methanol dehydrogenation.

5.5. Conclusions

In summary, this Chapter demonstrates that the incorporation of MoO_4^{2-} effectively improves the methanol oxidation activity of NiOOH during seawater electrolysis, simultaneously protecting NiOOH from chlorine-induced corrosion. The 3D hierarchical structure of Ni(OH)₂/NMO pre-catalyst expands the ECSA, providing an abundance of active sites. Additionally, the interfacial interaction between Ni(OH)₂ and NiMoO₄ facilitates the reconstruction process to form MOR- and OER-activated NiOOH. Furthermore, in situ leached MoO₄²⁻ modifies the surface microenvironment of NiOOH. These anions decrease the adsorption strength of Cl⁻, thereby mitigating electrode corrosion. The adsorbed MoO₄²⁻ also facilitates the adsorption of methanol and concurrently reduces the energy barrier for the nonelectrochemical process, promoting the PCET during MOR. Consequently, Ni(OH)₂/NMO catalyst exhibits significantly enhanced OER activity and durability in alkaline seawater, achieving 100 mA cm⁻² at 267 mV and demonstrating remarkable long-term stability, with only a 1.7 % activity loss for 600 h at 500 mA cm⁻². When combined with a NiMo cathode, the NiMo||Ni(OH)₂/NMO cell requires only 1.305 V to reach 10 mA cm⁻² in seawater, assisted by methanol oxidation. Compared with Pt/C||RuO2, the NiMo||Ni(OH)2/NMO cell offers a 13.5 % energy saving for hydrogen production at 0.5 A cm⁻² in hybrid seawater. This cell demonstrates stable operation for over 130 h at 0.1, 0.5, and 1.0 A cm⁻². This study introduces a novel design concept for modulating the catalytic surface microenvironment, paving the way for Ni-based catalysts with high selectivity towards small molecule oxidation reactions and strong anti-corrosion properties in hybrid seawater electrolysis.

5.6. References

- J. Peng, W. Dong, Z. Wang, Y. Meng, W. Liu, P. Song, Z. Liu, *Mater. Today Adv.* 2020, 8, 100081.
- [2] J. F. Chang, G. Z. Wang, Z. Z. Yang, B. Y. Li, Q. Wang, R. Kuliiev, N. Orlovskaya, M. Gu, Y. G. Du, G. F. Wang, Y. Yang, Adv. Mater. 2021, 33, 2101425.
- [3] F. S. Hegner, F. A. Garces-Pineda, J. Gonzalez-Cobos, B. Rodriguez-Garcia, M. Torrens, E. Palomares, N. Lopez, J. R. Galan-Mascaros, *ACS Catal.* **2021**, *11*, 13140.
- [4] X. Luo, P. X. Ji, P. Y. Wang, X. Tan, L. Chen, S. C. Mu, Adv. Sci. 2022, 9, 2104846.
- [5] P. Shen, B. W. Zhou, Z. Chen, W. P. Xiao, Y. L. Fu, J. Wan, Z. X. Wu, L. Wang, *Appl. Catal. B-Environ. Energy* **2023**, *325*, 122305.
- [6] L. S. Zhang, L. P. Wang, H. P. Lin, Y. X. Liu, J. Y. Ye, Y. Z. Wen, A. Chen, L. Wang, F. L. Ni, Z. Y. Zhou, S. G. Sun, Y. Y. Li, B. Zhang, H. S. Peng, *Angew. Chem. Int. Ed.* 2019, 58, 16820.
- [7] C. F. Liu, X. R. Shi, K. H. Yue, P. J. Wang, K. Zhan, X. Y. Wang, B. Y. Xia, Y. Yan, Adv. Mater. 2023, 35, 2211177.
- [8] J. X. Zhu, L. X. Xia, R. H. Yu, R. H. Lu, J. T. Li, R. H. He, Y. C. Wu, W. Zhang, X. F. Hong, W. Chen, Y. Zhao, L. Zhou, L. Q. Mai, Z. Y. Wang, J. Am. Chem. Soc. 2022, 144, 15529.
- [9] Y. Yang, X. X. Wu, M. Ahmad, F. Z. Si, S. J. Chen, C. H. Liu, Y. Zhang, L. Wang, J. J. Zhang, J. L. Luo, X. Z. Fu, *Angew. Chem. Int. Ed.* 2023, 62, e202302950.
- [10] J. S. Li, L. M. Li, J. Wang, A. Cabot, Y. F. Zhu, ACS Energy Lett. 2024, 9, 853.
- [11] J. S. Li, X. Tian, X. Wang, T. Zhang, M. C. Spadaro, J. Arbiol, L. M. Li, Y. Zuo, A. Cabot, *Inorg. Chem.* 2022, 61, 13433.
- [12] B. Zhao, J. W. Liu, X. W. Wang, C. Y. Xu, P. F. Sui, R. F. Feng, L. Wang, J. J. Zhang, J. L. Luo, X. Z. Fu, *Nano Energy* 2021, 80, 105530.
- [13] W. Chen, J. Q. Shi, C. Xie, W. Zhou, L. T. Xu, Y. Y. Li, Y. D. Wu, B. B. Wu, Y. C. Huang, B. Zhou, M. Yang, J. L. Liu, C. L. Dong, T. H. Wang, Y. Q. Zou, S. Y. Wang, *Natl. Sci. Rev.* 2023, 10, nwad099.
- [14] S. L. Li, R. G. Ma, J. C. Hu, Z. C. Li, L. J. Liu, X. L. Wang, Y. Lu, G. E. Sterbinsky, S. H. Liu, L. Zheng, J. Liu, D. M. Liu, J. C. Wang, *Nat. Commun.* 2022, *13*, 2916.
- [15] B. You, N. Jiang, X. Liu, Y. J. Sun, Angew. Chem. Int. Ed. 2016, 55, 9913.
- [16] Y. Huang, X. D. Chong, C. B. Liu, Y. Liang, B. Zhang, Angew. Chem. Int. Ed. 2018, 57, 13163.

- [17] Y. M. Shi, W. Du, W. Zhou, C. H. Wang, S. S. Lu, S. Y. Lu, B. Zhang, Angew. Chem. Int. Ed. 2020, 59, 22470.
- [18] W. M. Tong, M. Forster, F. Dionigi, S. Dresp, R. S. Erami, P. Strasser, A. J. Cowan, P. Farràs, *Nat. Energy* **2020**, *5*, 367.
- [19] P. F. Guo, D. Liu, R. B. Wu, Small Struct. 2023, 4, 2300192.
- [20] L. Yu, L. B. Wu, B. McElhenny, S. W. Song, D. Luo, F. H. Zhang, Y. Yu, S. Chen, Z. F. Ren, *Energy Environ. Sci.* 2020, 13, 3439.
- [21] B. S. Zhang, S. Liu, S. J. Zhang, Y. Cao, H. L. Wang, C. Y. Han, J. Sun, Small 2022, 18, 2203852.
- [22] Z. Li, M. J. Liu, J. Yan, L. Y. S. Lee, *Chem. Eng. J.* **2023**, *473*, 145293.
- [23] L. Yu, Q. Zhu, S. W. Song, B. McElhenny, D. Z. Wang, C. Z. Wu, Z. J. Qin, J. M. Bao, Y. Yu, S. Chen, Z. F. Ren, *Nat. Commun.* 2019, 10, 5106.
- [24] M. Fang, W. Gao, G. F. Dong, Z. M. Xia, S. Yip, Y. B. Qin, Y. Q. Qu, J. C. Ho, *Nano Energy* 2016, 27, 247.
- [25] R. N. Dürr, P. Maltoni, H. N. Tian, B. Jousselme, L. Hammarström, T. Edvinsson, *ACS Nano* **2021**, *15*, 13504.
- [26] S. Q. Niu, Y. C. Sun, G. J. Sun, D. Rakov, Y. Z. Li, Y. Ma, J. Y. Chu, P. Xu, ACS Appl. Energy Mater. 2019, 2, 3927.
- [27] G. Solomon, A. Landström, R. Mazzaro, M. Jugovac, P. Moras, E. Cattaruzza, V. Morandi, I. Concina, A. Vomiero, *Adv. Energy Mater.* **2021**, *11*, 2101324.
- [28] J. R. Ran, W. W. Guo, H. L. Wang, B. C. Zhu, J. G. Yu, S. Z. Qiao, Adv. Mater. 2018, 30, 1800128.
- [29] Y. N. Zhou, W. L. Yu, Y. N. Cao, J. Zhao, B. Dong, Y. Ma, F. L. Wang, R. Y. Fan, Y. L. Zhou, Y. M. Chai, Appl. Catal. B-Environ. Energy 2021, 292, 120150.
- [30] Z. Y. Zhao, Q. Shao, J. Y. Xue, B. L. Huang, Z. Niu, H. W. Gu, X. Q. Huang, J. P. Lang, Nano Res. 2022, 15, 310.
- [31] K. Dastafkan, X. J. Shen, R. K. Hocking, Q. Meyer, C. Zhao, *Nat. Commun.* **2023**, *14*, 547.
- [32] L. N. Sha, K. Ye, J. L. Yin, K. Zhu, K. Cheng, J. Yan, G. L. Wang, D. X. Cao, *Chem. Eng. J.* 2020, 381, 122603.
- [33] L. Liu, Y. C. He, Q. Li, C. S. Cao, M. H. Huang, D. D. Ma, X. T. Wu, Q. L. Zhu, *Exploration* **2024**, *4*, 20230043.
- [34] H. J. Song, H. Yoon, B. Ju, D. Y. Lee, D. W. Kim, ACS Catal. 2020, 10, 702.

- [35] L. B. Wu, L. Yu, Q. C. Zhu, B. McElhenny, F. H. Zhang, C. Z. Wu, X. X. Xing, J. M. Bao, S. Chen, Z. F. Ren, *Nano Energy* 2021, 83, 105838.
- [36] L. Yu, J. Y. Xiao, C. Q. Huang, J. Q. Zhou, M. Qiu, Y. Yu, Z. F. Ren, C. W. Chu, J. C. Yu, Proc. Natl. Acad. Sci. USA 2022, 119, e2202382119.
- [37] C. Q. Huang, Q. C. Zhou, L. Yu, D. S. Duan, T. Y. Cao, S. H. Qiu, Z. Z. Wang, J. Guo, Y. X. Xie, L. P. Li, Y. Yu, Adv. Energy Mater. 2023, 13, 2301475.
- [38] M. X. Chen, Y. Y. Zhang, R. Wang, B. Zhang, B. Song, Y. C. Guan, S. W. Li, P. Xu, *J. Energy Chem.* **2023**, *84*, 173.
- [39] B. J. Trzesniewski, O. Diaz-Morales, D. A. Vermaas, A. Longo, W. Bras, M. T. M. Koper, W. A. Smith, J. Am. Chem. Soc. 2015, 137, 15112.
- [40] M. J. Liu, K. A. Min, B. Han, L. Y. S. Lee, Adv. Energy Mater. 2021, 11, 2101281.
- [41] J. Jiang, F. F. Sun, S. Zhou, W. Hu, H. Zhang, J. C. Dong, Z. Jiang, J. J. Zhao, J. F. Li, W. S. Yan, M. Wang, *Nat. Commun.* 2018, 9, 2885.
- [42] T. F. Ma, W. W. Xu, B. R. Li, X. Chen, J. J. Zhao, S. S. Wan, K. Jiang, S. X. Zhang, Z. F. Wang, Z. Q. Tian, Z. Y. Lu, L. Chen, *Angew. Chem. Int. Ed.* 2021, 60, 22740.
- [43] Z. H. Yang, S. Wang, C. Y. Wei, L. Chen, Z. M. Xue, T. C. Mu, Energy Environ. Sci. 2024, 17, 1603.
- [44] Y. X. Lu, T. Y. Liu, C. L. Dong, Y. C. Huang, Y. F. Li, J. Chen, Y. Q. Zou, S. Y. Wang, *Adv. Mater.* **2021**, *33*, 2007056.
- [45] B. Konkena, J. Masa, A. J. R. Botz, I. Sinev, W. Xia, J. Kossmann, R. Drautz, M. Muhler, W. Schuhmann, ACS Catal. 2017, 7, 229.
- [46] J. Huang, Y. Li, Y. Zhang, G. Rao, C. Wu, Y. Hu, X. Wang, R. Lu, Y. Li, J. Xiong, *Angew. Chem. Int. Ed.* **2019**, *58*, 17458.
- [47] S. Q. Li, S. B. Wang, Y. H. Wang, J. H. He, K. Li, Y. J. Xu, M. X. Wang, S. Y. Zhao, X. N. Li, X. Zhong, J. G. Wang, Adv. Funct. Mater. 2023, 33, 2214488.
- [48] Y. X. Lu, T. Y. Liu, C. L. Dong, C. M. Yang, L. Zhou, Y. C. Huang, Y. F. Li, B. Zhou, Y. Q. Zou, S. Y. Wang, Adv. Mater. 2022, 34, 2107185.
- [49] S. H. Lee, Y. C. Chu, L. C. Bai, H. M. Chen, X. L. Hu, Chem Catal. 2023, 3, 100475.
- [50] Z. Y. Wang, W. A. Goddard, H. Xiao, Nat. Commun. 2023, 14, 4228.
- [51] F. Dionigi, Z. H. Zeng, I. Sinev, T. Merzdorf, S. Deshpande, M. B. Lopez, S. Kunze, I. Zegkinoglou, H. Sarodnik, D. X. Fan, A. Bergmann, J. Drnec, J. F. de Araujo, M. Gliech, D. Teschner, J. Zhu, W. X. Li, J. Greeley, B. Roldan Cuenya, P. Strasser, *Nat. Commun.* 2020, 11, 2522.

Chapter VI Light-Assisted Seawater Electrooxidation by MoO₃/Fe₂O₃/MoS₂

6.1. Objective and Motivation

In **Chapter 5**, the MoO₄²—repelling principle was employed to reduce CI⁻ adsorption, thereby alleviating corrosion. However, this approach may also repel OH⁻ due to electrostatic effects, which can negatively impact mass diffusion at the reaction interface and lead to the decline of OER activity. To date, no effective strategy has been proposed to address this issue. It is well known that the electronic structure of active sites can be optimized through the formation of heterojunctions, which can enhance the adsorption of OH⁻. In this Chapter, a novel ternary heterojunction composed of MoO₃/Fe₂O₃/MoS₂ was designed to attract OH⁻ and counterbalance the repelling effect caused by leached MoO₄²⁻ and SO₄²⁻. A systematic analysis of this ternary heterojunction was conducted, focusing on the impact of the MoO₃/Fe₂O₃/MoS₂ heterointerfaces on both OER and CER, utilizing experimental and theoretical approaches.

Additionally, as discussed in **Chapter 1**, external field assistance can provide extra driving forces to promote catalytic reactions. Light assistance has been integrated into electrocatalytic OER systems to increase the current or lower the potential through photo-excited carriers, thereby reducing electricity consumption. However, the efficiency of carrier utilization in catalytic reactions has often been overlooked in previous studies. In **Chapter 6**, light assistance has been introduced to this catalytic system, as MoO₃, Fe₂O₃, and MoS₂ are all semiconductors. The energy band structures were systematically investigated to understand the photo-generated charge transfer behavior in this ternary heterojunction system. Enhanced charge transfer contributes to improved charge utilization efficiency and, consequently, to the improved electrocatalytic activity for seawater oxidation.

6.2. Introduction

Direct seawater electrolysis still suffers from severe corrosion resulting from competitive CER and high thermodynamic barrier of OER.^[1, 2] Chloride anions in seawater (approximately 0.5 M) can be readily adsorbed on anodes and oxidized to Cl₂ or ClO⁻ in acidic or alkaline

seawaters, respectively, leading to severe corrosion of catalysts and compromised stability. [3, 4] For example, Fe₂O₃, a typical OER electrocatalyst, is prone to chlorine corrosion, thus limiting its applicability in seawater electrolysis. [5] Although alkalizing seawater provides a thermodynamic advantage for OER ($E^{\circ}_{anode} = 1.23 \text{ V}$) over CER ($E^{\circ}_{anode} = 1.72 \text{ V}$), Cl⁻ ions can still attack electron-deficient metal sites, fostering competition between CER and the desired OER, especially at large current densities. [6,7] Recently, local environmental design has been proposed to improve the selectivity towards OER.[8] For example, introducing anion species such as SO_4^{2-} and MoO_4^{2-} during the electrocatalytic process has been shown to create a permselective protective species that repels Cl⁻ through electrostatic repulsion.^[9,10] However, those anion-enriched areas may also impede the diffusion of OH⁻ ions, creating obstacles for OER.^[11] Recent studies have demonstrated that constructing heterojunctions can create robust catalytic interfaces that modulate the electronic structure and OH⁻ adsorption behavior, thereby lowering the reaction energy barrier and improving electrocatalytic OER performance. [12-14] For instance, heterojunctions composed of Fe- and Mo-based materials, such as Fe₂O₃/MoO₃ and Fe₂O₃/P-CoMoO₄, exhibit superior OER activity compared to their single-component counterparts. [15, 16] This enhancement is primarily attributed to the strongly coupled interfaces that facilitate charge redistribution and optimize reactant adsorption energy.

Recently, inspired by electro-assisted photocatalysis strategies, photo-generated carrier-assisted electrocatalysis is considered an innovative and feasible way to improve water-splitting performance. This innovative strategy involves utilizing light energy to excite the photo-active component, generating carriers that promote the electrochemical reaction on the electro-active component by lowering overpotential or increasing catalytic current densities. While most studies on light-assisted water electrolysis have focused on broadening the absorption spectrum or modifying the electro-active component, the transfer of photo-generated carriers between photo-active and electro-active components in

light-assisted electrocatalytic OER systems has been overlooked. Inefficient carrier transfer often results in severe recombination of photo-generated electrons and holes, limiting their utilization in catalytic reactions. [25-27] Previous reports demonstrated that introducing a built-in electric field through heterojunction formation could effectively facilitate the migration of photo-generated carriers to active sites, enabling their participation in catalytic reactions. [28-31] For light-assisted seawater electrolysis, the primary challenge lies in simultaneously mitigating chlorine corrosion and achieving efficient photo-electric coupling.

In this study, we report an efficient and stable seawater oxidation electrocatalyst MoO₃/Fe₂O₃/MoS₂ with excellent OER selectivity and photoelectric coupling effect. Nanosized particles and amorphous-crystalline interfaces induced by laser ablation effectively enlarge the electrochemical surface area for efficient mass diffusion. MoO₄²⁻ and SO₄²⁻ ions, which are leached during the OER activation process, contribute to repelling Cl⁻ ions in seawater. Besides, the MoO₃/Fe₂O₃/MoS₂ heterojunctions are particularly advantageous for ensuring OH⁻ adsorption and enlarging the potential gap between OER and CER, thus mitigating catalyst corrosion. Furthermore, dual built-in electric fields formed at the three-phase heterointerfaces benefit the fast migration of photo-generated carriers and reduce interfacial resistance, thereby enabling more charges to participate in OER.

6.3. Experimental Section

6.3.1. Raw Materials

Iron nitrate nonahydrate (Fe(NO₃)₃·9H₂O, 99.9 %), molybdenum disulfide (MoS₂, 99 %), sodium sulfate (Na₂SO₄, 98 %) and potassium hydroxide (KOH, 99.99 %) were purchased from Sigma–Aldrich. Sulfuric acid (H₂SO₄, 98.0 %), methanol (99.8 %), and acetone (99.8 %) were purchased from Duksan Chemicals. Ammonium molybdate tetrahydrate ((NH₄)₆Mo₇O₂₄·4H₂O, 83.0 %), sodium chloride (NaCl, 99.5 %), and potassium iodide (KI, 99.0 %) were obtained from Shenzhen Dieckmann Tech. The aqueous solution was prepared

Chapter VI Light-Assisted Seawater Electrooxidation by MoO₃/Fe₂O₃/MoS₂

using deionized (DI) water produced by MilliQ Water System. Natural seawater (pH ~8) was collected from Tsim Sha Tsui near the Hong Kong Polytechnic University, Kowloon, Hong Kong SAR, China. All chemicals were used as received.

6.3.2. Catalysts Synthesis

Synthesis of Fe-L-MoS₂

A pre-determined amount of Fe(NO₃)₃·9H₂O was dropped into acetone (5 mL) containing MoS₂ (20 mg) to form a uniform dispersion (Fe(NO₃)₃ concentration = 0.025, 0.05, and 0.1 M) by sonicating for 30 min. A Nd:YAG Q-switched pulsed laser (wavelength = 1,064 nm, Nimma-600 Laser system) with an energy output of 320 mJ (650 V) and energy stability (root mean square) \leq 1 % was purchased from Beamtech Optronics Co. Ltd., China. The beam diameter was approximately 8 mm, and the MoS₂ suspension was laser-ablated under continuous stirring at 20 °C for pre-determined min (5, 15, 25, and 35 min). Finally, the product was collected by centrifugation, washed with DI water and ethanol several times, and dried at 60 °C under vacuum.

Synthesis of Fe₂O₃/MoS₂ composites

For the synthesis of Fe₂O₃, Fe(NO₃)₃·9H₂O (1 mmol) was placed in a crucible and calcined at 200 °C for 0.5 h at a heating rate of 15 °C min⁻¹ in an air atmosphere. Fe₂O₃/MoS₂ composites were synthesized using a conventional adsorption–calcination method. Specifically, MoS₂ (1 mmol) was dispersed in ethanol (20 mL) by sonicating for 30 min. To this suspension, Fe(NO₃)₃·9H₂O (2 mmol) was added and sonicated for 30 min. The mixture was then steam dried at 90 °C with continuing stirring, followed by calcination at 200 °C for 0.5 h at a heating rate of 15 °C min⁻¹ in an air atmosphere.^[32]

Synthesis of Fe₂O₃

1 mmol Fe(NO₃)₃·9H₂O was placed in a crucible to be calcined at 200 °C for 0.5 h with a heating rate of 15 °C min⁻¹ in an air atmosphere.

Fabrication of Pt/C and RuO2 electrodes

Catalyst ink was prepared by dissolving 5 mg of 20 wt.% Pt/C or RuO₂ into a mixture solution of 960 μ L ethanol and 40 μ L 5 wt.% Nafion and sonicated for 60 min. Next, 50 μ L catalyst ink was dropped on the pre-treated nickel foam (0.25 cm²).

6.3.3. Electrochemical Performance Test

Electrochemical tests were carried out in a standard three-electrode configuration in 1.0 M KOH electrolyte using a graphite rod and the Hg/HgO electrode as the counter and reference electrodes, respectively. All data were collected by an electrochemical station (CHI760E). For OER experiments, homogeneous catalyst ink (5 mg mL⁻¹) was first prepared in an ethanolic solvent (960 μ L) with the addition of 40 μ L Nafion and 2 mg carbon conductor (VXC-72). Nickel foam was cleaned by sonication in acetone and washed with 3 M HCl for 10 min to remove the surface oxide layer. Catalyst ink (25 μ L) was then pipetted onto a nickel foam (0.25 cm²) and used as the working electrode after the solvent was dried naturally. All potentials in this work were given against the RHE ($E_{RHE} = E_{Hg/HgO} + 0.059 \times pH + 0.098$). Before testing, the working electrode was stabilized by 100 cyclic 1840ltametric (CV) cycles in the potential range between 1.124 and 1.624 V. LSV was carried out from 1.2 to 1.8 V (vs. RHE) at a scan rate of 5 mV s⁻¹. All polarization curves were corrected by 85 % iR compensation for ohmic losses. All measurements were repeated at least three times. EIS was performed at 1.524 V (vs. RHE) from 100 kHz to 0.1 Hz with an amplitude of 10 mV.

6.3.4. Light-assisted Electrocatalysis Measurements

A Xe lamp (PLS-SXE300, Perfectlight Chia) equipped with a UV-vis filter was used as the light source (350 nm $\leq \lambda \leq$ 780 nm) and placed on one side of the electrolytic cell with a constant distance of 26 cm. A circulating cooling water system was used to maintain the temperature of the electrolyte at 30 °C. The light intensity on the surface of the electrode is about 200 mW cm⁻². The OER tests in seawater were carried out with the same parameters

under light irradiation. For seawater splitting experiments, the Pt/C cathode (0.25 cm^2) was coupled with a Fe-L-MoS₂ anode (0.25 cm^2) to form a full-cell water-splitting system. For comparison, commercial RuO₂ and Pt/C on Ni foam were used as a benchmark for the anode and cathode, respectively.

6.4. Results and Discussion

6.4.1. Structure Characterization

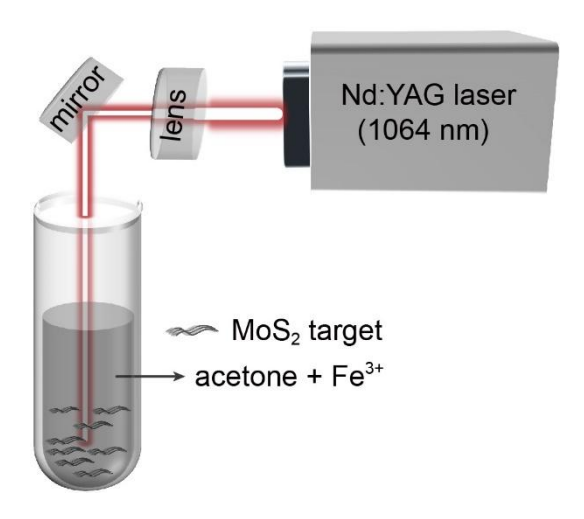


Figure 6.1. A schematic diagram showing the synthetic procedure of Fe-L-MoS₂.

Bulk MoS_2 powder was ablated with a pulsed laser in acetone containing $0.05 \text{ M Fe}(NO_3)_3$ for 25 min to produce MoS_2 microparticles (denoted as Fe-L-MoS₂) decorated with numerous nanoparticles (d = 21.5 nm, **Figures 6.1** and **6.3a**). During the laser ablation, MoS_2 powder evolves into a mixture of microparticles and microplates (**Figures 6.2a–f**). The laser-ablated time significantly influences the morphology, with microparticles gradually dominating as the laser-ablated time is extended (**Figures 6.2b–d**). The BET adsorption–desorption isotherms and specific surface areas of samples are present in **Figure 6.3b** and **Supplementary Table 3.1**, respectively. The BET surface area of Fe-L-MoS₂ (47.35 m² g⁻¹) is 5.7 times higher than that of pristine MoS_2 (8.33 m² g⁻¹). This enlarged surface area provides more active sites to promote the catalytic reaction.

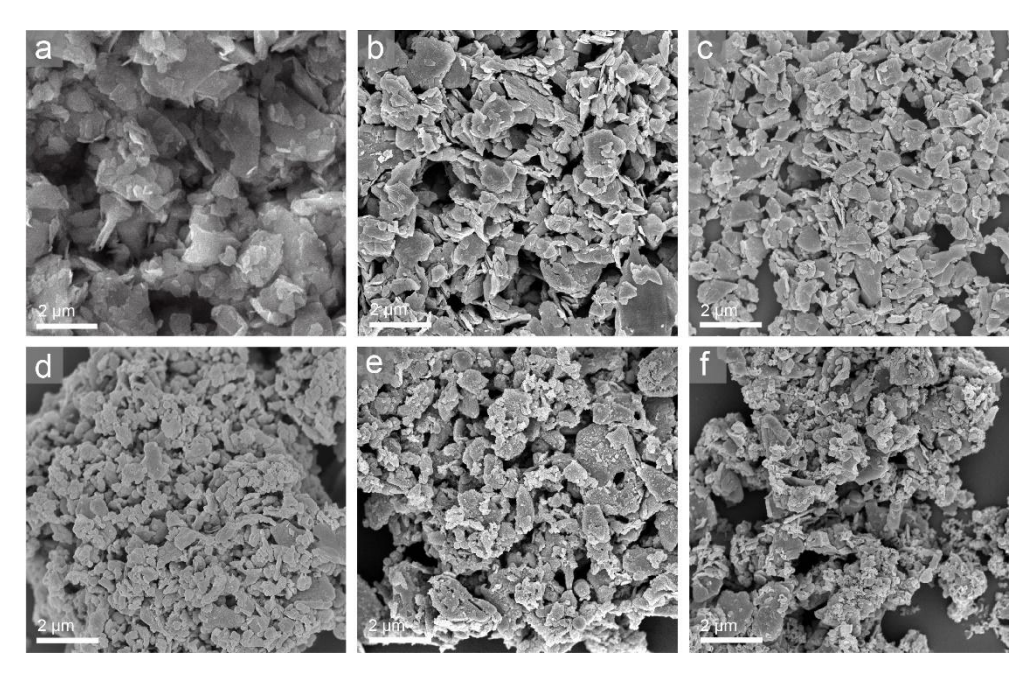


Figure 6.2. SEM images of (a) bulk MoS₂, samples with different laser-ablated times: (b) 5 min, (c) 15 min, (d) 35 min. With different Fe³⁺ concentrations: (e) 0.025 M, and (f) 0.1 M Fe³⁺.

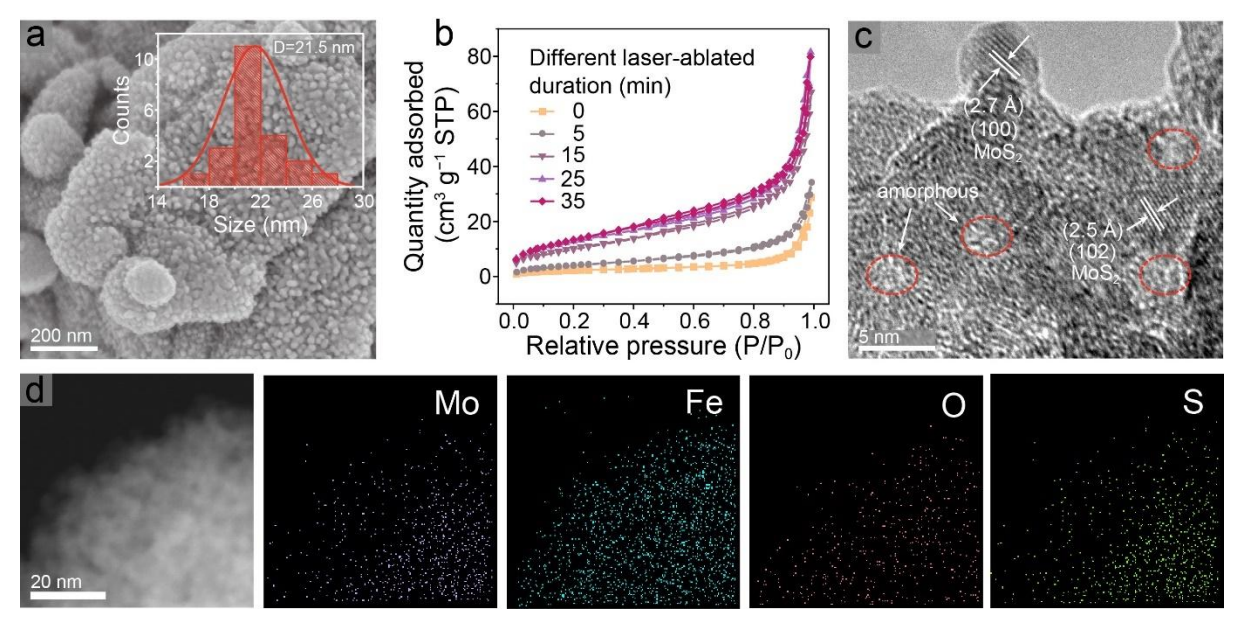


Figure 6.3. (a) The SEM image of Fe-L-MoS₂. (b) Adsorption/desorption isotherms for MoS₂ and products synthesized by different laser-ablated times. (c) High-resolution TEM image of Fe-L-MoS₂. (d) STEM image and corresponding EDS mapping images.

Figure 6.3c displays the high-resolution TEM image of Fe-L-MoS₂, where the observed interplanar spacings of 2.7 and 2.5 Å are assigned to the (100) and (102) planes of MoS₂.

Chapter VI Light-Assisted Seawater Electrooxidation by MoO₃/Fe₂O₃/MoS₂

Amorphous areas (yellow dotted circles) indicate the formation of defects-rich structures. The STEM and the corresponding EDS mapping images (**Figure 6.3d**) reveal the uniform distribution of Mo, Fe, O, and S elements over the entire area of Fe-L-MoS₂. The content of Mo and Fe elements before and after laser ablation was measured by ICP-OES and summarized in **Table 6.2**. The Fe/Mo ratio increases with extended laser-ablation time, exceeding 1.0 for laser ablation longer than 25 min, which indicates the successful Fe incorporation as a second component, rather than a dopant.

Table 6.1. BET surface area of samples after laser ablation.

Samples	$S(m^2/g)$		
MoS_2	8.33		
Fe-L-MoS ₂ -5 min	15.82		
Fe-L-MoS ₂ -15 min	38.63		
Fe-L-MoS ₂ -25 min	47.35		
Fe-L-MoS ₂ -35 min	50.06		

Table 6.2. ICP-OES analysis data of metals in different products prepared by different laser ablation times and Fe(NO₃)₃ concentrations.

g 1	Element co	ntent (ppm)	Ratio (atomic)		
Samples	Мо	Fe	Mo	Fe	
MoS_2	44.79	0	1	/	
Fe ₂ O ₃ /MoS ₂	13.31	15.15	0.34	0.66	
Fe-L-MoS ₂ -5 min	33.71	0.82	0.96	0.04	
Fe-L-MoS ₂ -15 min	26.88	6.03	0.72	0.28	
Fe-L-MoS ₂ -25 min	19.63	11.86	0.49	0.51	
Fe-L-MoS ₂ -35 min	13.63	15.37	0.34	0.66	
0.025 M Fe-L-MoS ₂	29.16	6.93	0.71	0.29	
0.1 M Fe-L-MoS ₂	15.57	14.22	0.39	0.61	

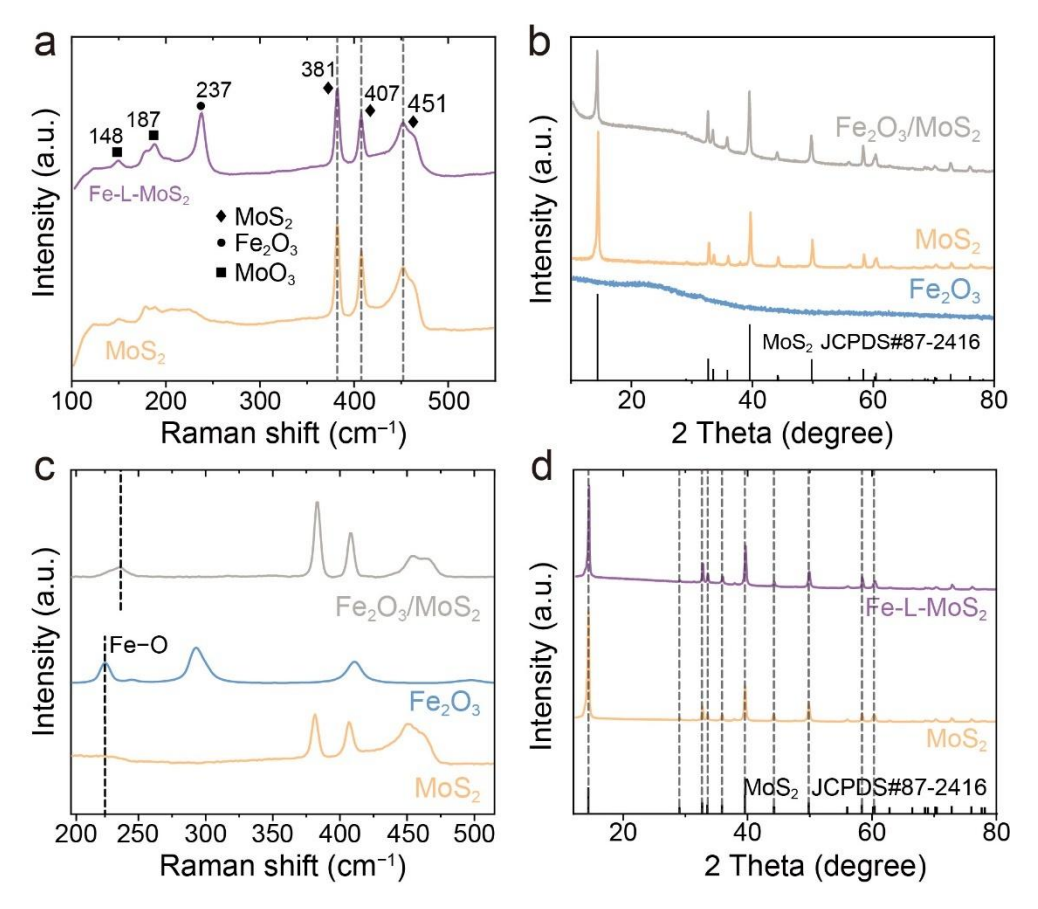


Figure 6.4. (a) Raman spectra of MoS₂ and Fe-L-MoS₂. (b) XRD patterns and (c) Raman spectra of MoS₂, Fe₂O₃, and Fe₂O₃/MoS₂. (d) XRD patterns of MoS₂ and Fe-L-MoS₂.

The Raman peak observed at 237 cm⁻¹ in Fe-L-MoS₂ is attributed to A_{1g} symmetric stretching vibrations of the Fe-O band (**Figure 6.4a**), aligning with the Raman spectrum of Fe₂O₃/MoS₂ (**Figure 6.4c**), which suggests the formation of Fe₂O₃ after laser ablation.^[33] In addition to the characteristic Raman peaks of MoS₂ at 381, 407, and 451 cm⁻¹,^[34] two new peaks attributed to MoO₃ are observed at 148 and 187 cm⁻¹.^[35] These observations indicate the coexistence of MoO₃ and Fe₂O₃ within Fe-L-MoS₂. However, the MoS₂ phase remains dominant in the XRD pattern of Fe-L-MoS₂ (**Figure 6.4d**), suggesting that Fe₂O₃ and MoO₃ likely exist as amorphous structures. A possible formation mechanism involves a high-temperature and high-pressure transient plasmas plume, containing oxygen and hydroxyl radicals, forming on the incident surface of the MoS₂ target upon the irradiation of a powerful pulsed laser.^[36,37] This leads to the rapid oxidation of a portion of MoS₂ to MoO₃. Concurrently,

Fe $^{3+}$ ions adsorbed on negatively charged MoS₂ (**Figure 6.5**) can easily transform into amorphous species due to the rapid-cooling property of laser ablation.

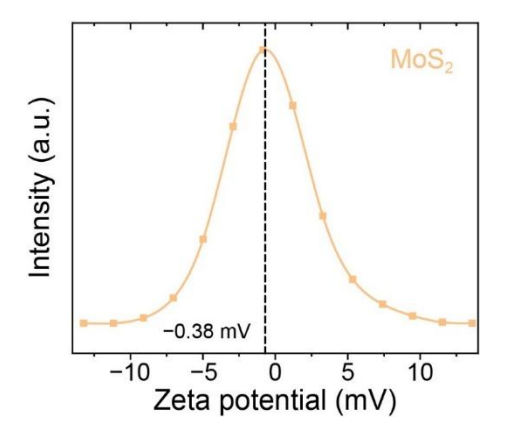


Figure 6.5. Zeta potential of pristine MoS₂.

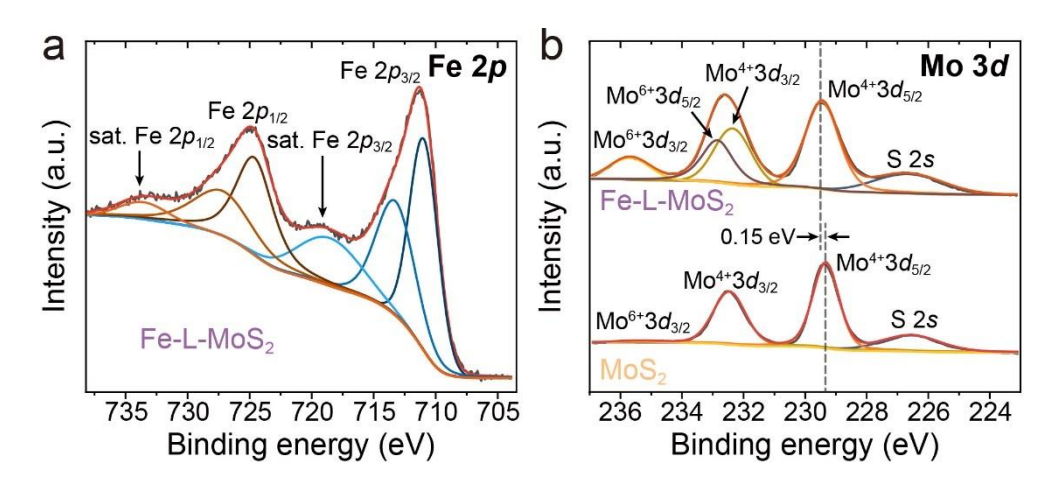


Figure 6.6. XPS (a) Fe 2p and (b) Mo 3d spectra of Fe-L-MoS₂.

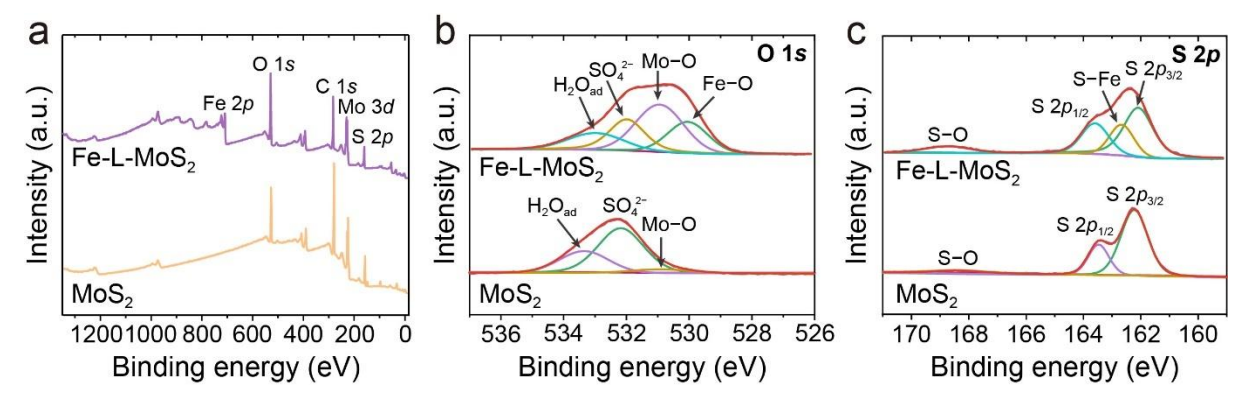


Figure 6.7. (a) XPS survey, (b) O 1s, and (c) S 2p spectra of bulk MoS₂ and Fe-L-MoS₂.

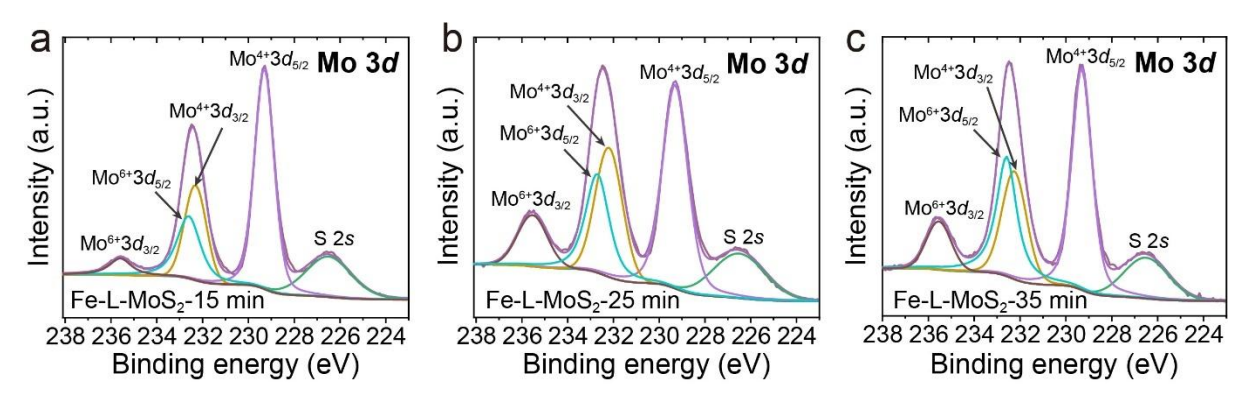


Figure 6.8. XPS Mo 3*d* spectra of Fe-L-MoS₂ synthesized by different laser-ablated times: (a) 15 min, (b) 25 min, and (c) 35 min.

Figure 6.6a shows the XPS Fe 2p spectrum of Fe-L-MoS₂. Two distinct peaks at binding energies of 711.1 (Fe $2p_{3/2}$) and 724.4 eV (Fe $2p_{1/2}$) are observed, along with satellite peaks at 719.1 and 733.8 eV, consistent with reported Fe₂O₃ results. [38] Besides, the binding energy of 713.5 eV could be assigned to the Fe^{III}–SO₄²⁻ bond. [39] Unlike pristine MoS₂, two peaks at 531.0 and 530.1 eV which can be assigned to Mo–O and Fe–O bonds, respectively, dominate in the O 1s spectrum of Fe-L-MoS₂ (**Figure 6.7b**), further confirming the formation of MoO₃ and Fe₂O₃. [40, 41] Similarly, in the Mo 3d spectrum of Fe-L-MoS₂, two new peaks for Mo⁶⁺ 3d_{5/2} and Mo⁶⁺ 3d_{3/2} are observed at 232.9 and 235.7 eV, respectively (**Figure 6.6b**). Notably, the Mo⁴⁺ peak at 229.35 eV shifts by 0.15 eV towards higher binding energy, indicative of reduced electronic density around Mo atoms and suggesting strong interaction among the three components. The Mo⁶⁺/Mo⁴⁺ atomic ratios of Fe-L-MoS₂ samples synthesized using different laser ablation times are estimated (**Figure 6.8**) and summarized in **Table 6.3**. This ratio increases with the laser ablation time, reaching a value of 0.48 at 25 min-ablation. Furthermore, the S–Fe bond is identified at 162.7 eV in the S 2p spectrum (**Figure 6.7c**), [43, 44] consistent with the Fe 2p results and indicating the interaction between Fe₂O₃ and MoS₂.

Table 6.3. The weight ratios of Fe₂O₃ and atomic ratios of Mo⁶⁺/Mo⁴⁺ in samples synthesized by different laser ablation times.

Samples	les Weight ratio of Fe ₂ O ₃ Atomic ratio of Mo ⁶⁺ /		
Fe-L-MoS ₂ -15 min	0.16	0.35	
Fe-L-MoS ₂ -25 min	0.35	0.48	
Fe-L-MoS ₂ -35 min	0.50	0.57	

6.3.2. Electrocatalytic Performance in Alkaline Freshwater and Seawater

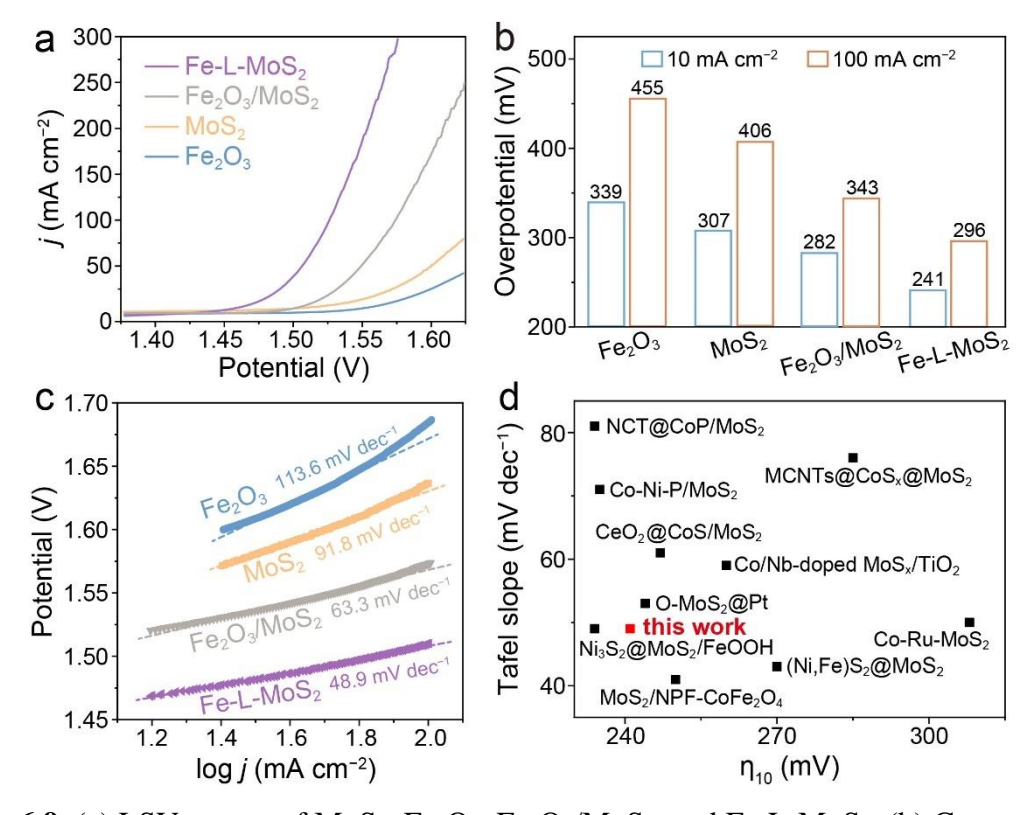


Figure 6.9. (a) LSV curves of MoS₂, Fe₂O₃, Fe₂O₃/MoS₂, and Fe-L-MoS₂. (b) Comparison of the OER overpotentials of those catalysts required to achieve 10 and 100 mA cm⁻². (c) the corresponding Tafel slopes of Fe₂O₃, MoS₂, Fe₂O₃/MoS₂, and Fe-L-MoS₂. (d) Comparison of overpotential and Tafel slope with previously reported MoS₂-based catalysts for oxygen evolution reaction.

Table 6.4. The OER performance of previously reported materials comparison to Fe-L-MoS₂ in 1 M KOH.

Samples	Overpotential η ₁₀ (mV)	Tafel (mV dec ⁻¹)	Ref.
$CeO_2@CoS/MoS_2$	247 mV	64	[45]
$N\text{-}doped\ carbon\ nanotube@CoP@MoS_2$	234 mV	81	[46]
$MCNTs@CoS_x@MoS_2$	285 mV	76	[47]
Co,Nb-doped MoS ₂ /TiO ₂	260 mV	59	[48]
O-MoS ₂ @Pt	244 mV	53	[49]
Co–Ni–P/MoS ₂	235 mV	71	[50]
Co–Ru-MoS ₂	308 mV	50	[51]
(Ni, Fe)S ₂ @MoS ₂	270 mV	43	[52]
$Ni_3S_2@MoS_2/FeOOH$	234 mV	49	[53]
vacancy-rich MoS ₂ /NPF-CoFe ₂ O ₄	250 mV	41	[54]
This work	241 mV	48.9	

The OER activity of the as-prepared samples was accessed in O₂-saturated 1 M KOH using a standard three-electrode cell. **Figure 6.9a** compares LSV collected at a scan rate of 2 mV s⁻¹. Fe-L-MoS₂ requires overpotentials of 241 and 296 mV to reach 10 and 100 mA cm⁻² (**Figure 6.9b**), respectively, which are significantly lower than Fe₂O₃/MoS₂ (282, 343 mV), pristine MoS₂ (307, 406 mV) and Fe₂O₃ (339, 455 mV). The Tafel plots derived from the polarization curves reveal that Fe-L-MoS₂ exhibits the lowest Tafel slope (48.9 mV dec⁻¹) among all samples investigated (**Figure 6.9c**), indicating its fast reaction kinetics. When comparing OER overpotential at 10 mA cm⁻² and Tafel slope, Fe-L-MoS₂ outperforms or matches other benchmark MoS₂-based catalysts (**Figure 6.9d** and **Table 6.4**).

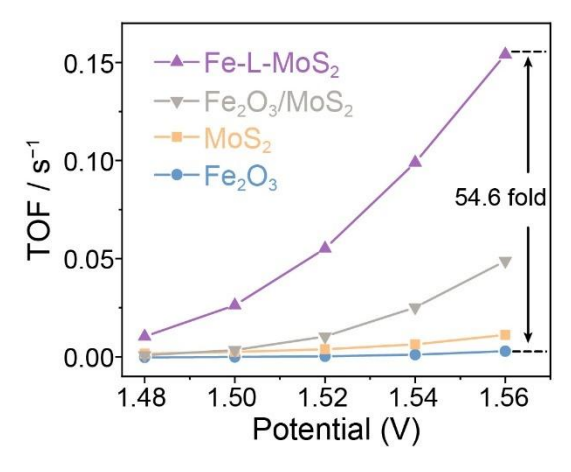


Figure 6.10. TOF of Fe₂O₃, MoS₂, Fe₂O₃/MoS₂ and Fe-L-MoS₂.

Moreover, Fe-L-MoS₂ demonstrates a high TOF value of 0.154 s⁻¹ (**Figure 6.10**), approximately 54.6 times that of Fe₂O₃ (0.003 s⁻¹), highlighting the substantial enhancement of intrinsic catalytic activity achieved through the formation of amorphous/crystalline heterojunctions. The OER performance of Fe-L-MoS₂ could be optimized by adjusting laserablated time and Fe³⁺ concentrations (**Figure 6.11a** and **b**). The lowest OER overpotential is obtained with a sample synthesized using 0.05 M Fe(NO₃)₃ and 25 min of ablation, resulting in a 34.2 % Fe₂O₃ content and a Mo⁶⁺/Mo⁴⁺ ratio of *ca*. 0.48 (**Figure 6.11c**). Excessive laser ablation or Fe³⁺ usage decreases OER performance due to increased charge transfer resistance (**Figure 6.12**) likely caused by the excessive formation of Fe₂O₃ and MoO₃ (**Table 6.3**).

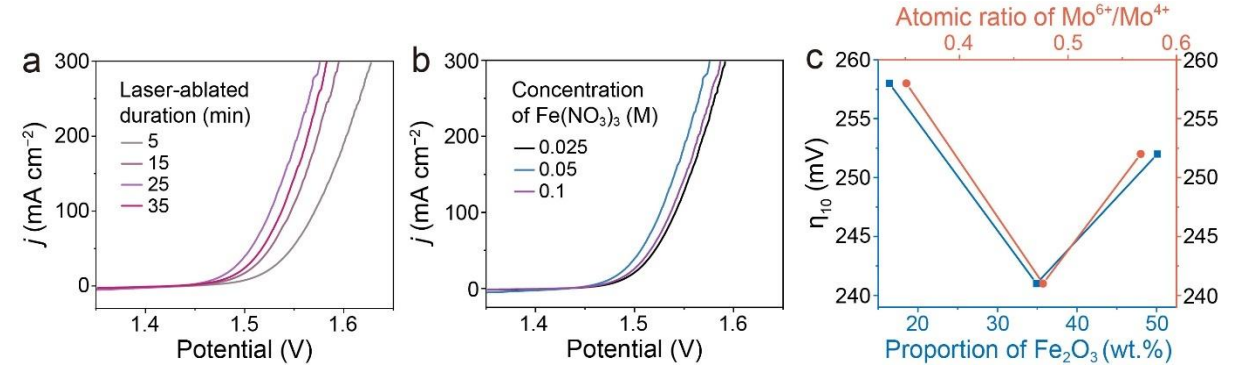


Figure 6.11. LSV curves of samples prepared with various (a) ablating time and (b) $Fe(NO_3)_3$ concentrations. (c) The relations between overpotentials and proportion of Fe_2O_3 (blue squares) and the atomic ratio of Mo^{6+}/Mo^{4+} (red circles).

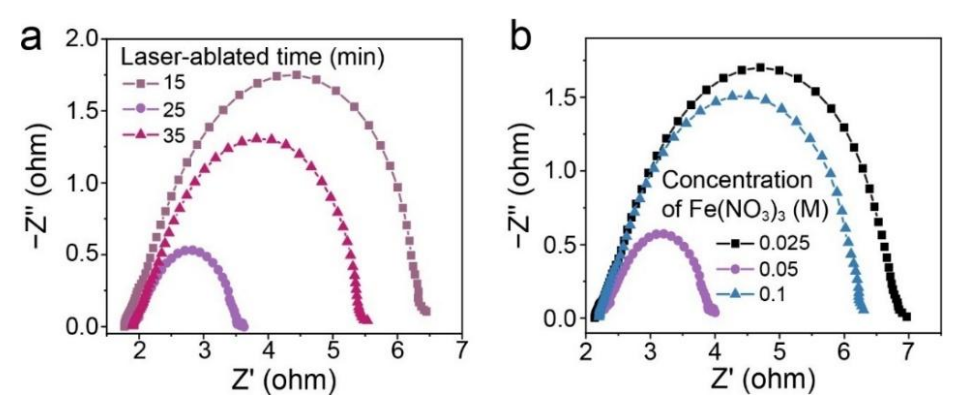


Figure 6.12. Nyquist plots of products synthesized by different (**a**) laser-ablated time and (**b**) Fe(NO₃)₃ concentrations.

The OER activity of Fe-L-MoS₂ was further evaluated in saline (0.5 M NaCl + 1 M KOH) and alkaline natural-seawater electrolytes to investigate their potential in seawater electrolysis application. As shown in **Figure 6.13a**, Fe-L-MoS₂ exhibits superior OER performance with minimal activity decline in saline water electrolytes, indicating that the impact of highly concentrated Cl⁻ ions on its catalytic activity is not significant. However, a noticeable deterioration in OER performance is observed in the alkaline seawater, which can be attributed to the presence of bacteria, microbes, and insoluble precipitates formed during the seawater OER process.^[55] In alkaline seawater, the Fe-L-MoS₂ electrode requires only 267 and 333 mV to reach 10 and 100 mA cm⁻², respectively (**Figure 6.13b**), which are considerably lower than those of Fe₂O₃ (398 and 638 mV) under the same conditions. Notably, the electrode achieves a high average FE of 96.7 % at a large current density of 100 mA cm⁻² in alkaline seawater (**Figure 6.14a**). Iodide titration was engaged to detect the generation of reactive chlorine species.^[56] No typical absorption peak of hypochlorite ions is observed in the electrolyte after the FE test (**Figure 6.14c**), indicating the catalyst's high selectivity for OER over the hypochlorite formation reaction.

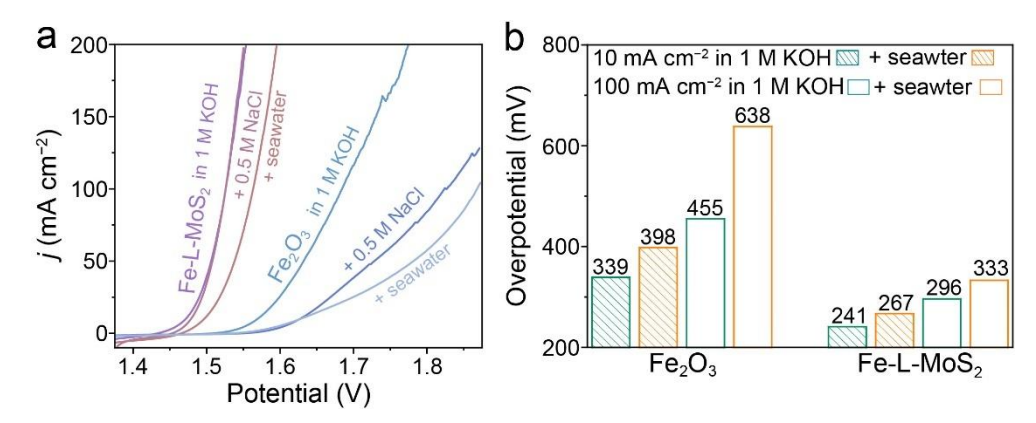


Figure 6.13. (a) LSV curves of Fe-L-MoS₂ and Fe₂O₃ in saline water of various NaCl concentrations and alkaline seawater. (b) Comparison of overpotentials of Fe-L-MoS₂ and Fe₂O₃ at 10 and 100 mA cm⁻² in various electrolytes.

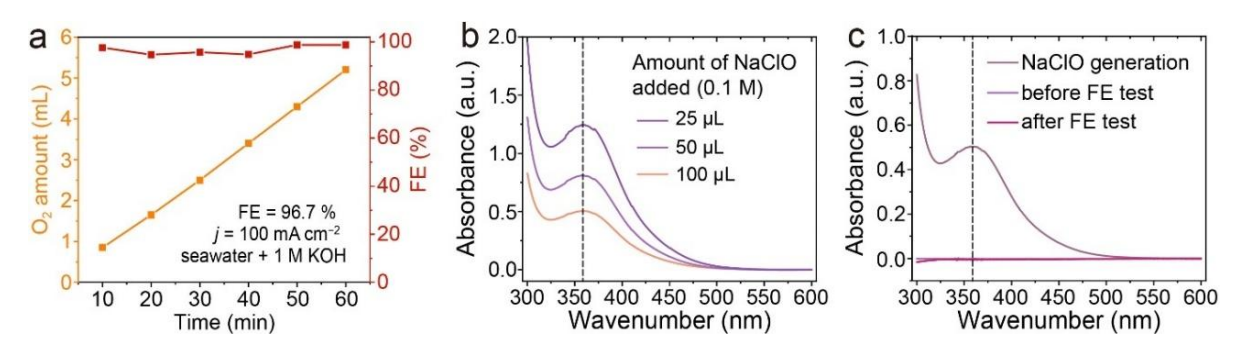


Figure 6.14. (a) FE (red squares) of Fe-L-MoS₂ measured at 100 mA cm⁻² in seawater + 1 M KOH. Yellow squares show the amount of O₂ generated during the FE test. UV–vis spectra of (b) iodide titration with various NaClO concentrations and (c) electrolytes before and after the FE test.

The operational stability is another crucial parameter for the electrocatalyst. The long-term chronopotentiometry was performed to evaluate the electrocatalytic durability of Fe-L-MoS₂ during OER in alkaline freshwater and seawater. Impressively, Fe-L-MoS₂ shows excellent stability at a current density of 100 mA cm⁻² in alkaline freshwater and natural seawater + 1 M KOH over 100 h (**Figure 6.15**), although there is a slight increase (1.89 %) in the applied potential for seawater OER.

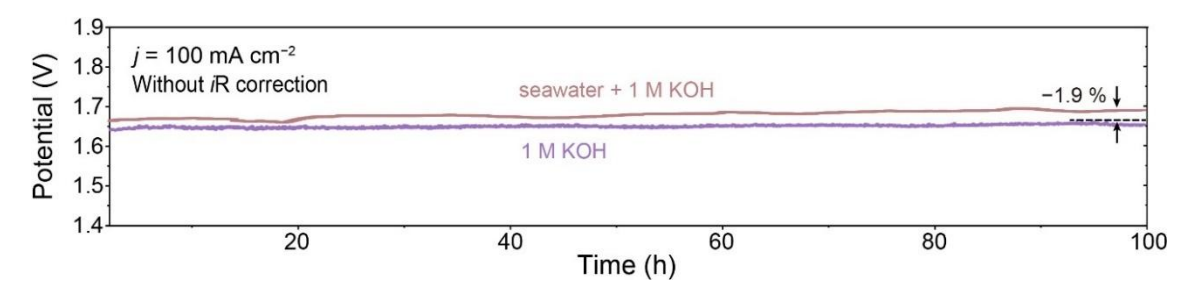


Figure 6.15. Chronopotentiometric curves of Fe-L-MoS₂ in alkaline freshwater and seawater + 1 M KOH.

6.4.3. Exploration of OER and Anti-corrosion Mechanisms

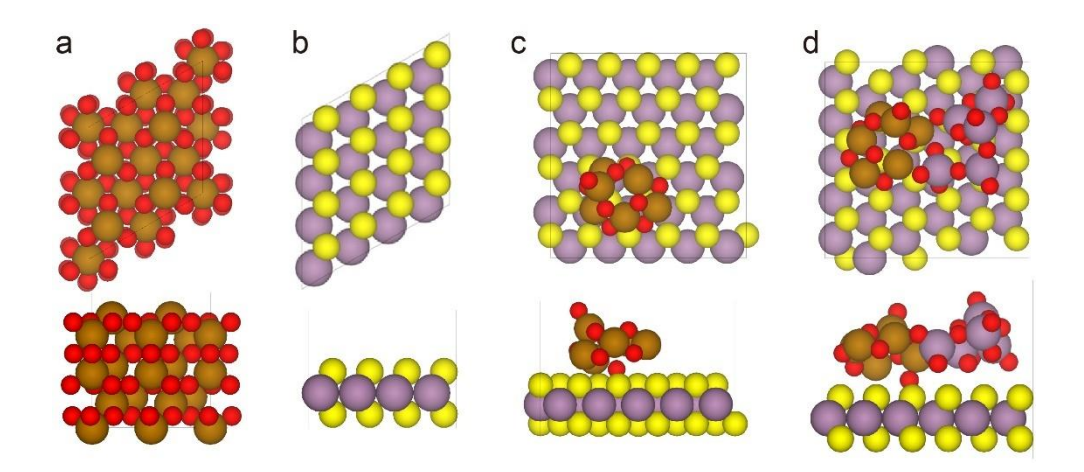


Figure 6.16. Optimized atomic structures of (a) Fe₂O₃, (b) MoS₂, (c) Fe₂O₃/MoS₂, and (d) MoO₃/Fe₂O₃/MoS₂. Mo, Fe, O, and S atoms are shown in violet, brown, red, and yellow, respectively.

DFT calculations were conducted to gain insights into how heterojunction enhances the water oxidation activity and anti-corrosion properties. Models of the amorphous Fe_2O_3 , amorphous/crystalline Fe_2O_3/MoS_2 , and $MoO_3/Fe_2O_3/MoS_2$ heterojunction are built via ab initio molecular dynamics (AIMD) simulations, and their crystal structures are provided in **Figure 6.16**. The charge redistribution across the three-phase heterojunction in Fe-L-MoS₂ was quantitatively analyzed by using planar-averaged differential charge density $\Delta \rho$. Positive and negative values denote the charge accumulation/depletion. **Figure 6.17** shows the $\Delta \rho$ profile along the z-direction (perpendicular to the interface), with charge accumulation and depletion

depicted in yellow and cyan regions. Along the *z*-axis, charge depletion is observed at the interface between the MoS₂ and the two amorphous oxides, while charge accumulation occurs where the two amorphous oxides are located. This result suggests charge transfer from the MoS₂ to the amorphous oxides upon heterointerface formation. Furthermore, the Bader charge distributions in the binary and ternary heterointerfaces are shown in **Figure 6.18**. The net charge of the Mo site in the MoS₂ phase of the Fe₂O₃/MoS₂ heterointerface is higher than that in the pristine MoS₂ phase (**Figure 6.19a**), while the charge of the Fe site in the Fe₂O₃ phase of the heterostructure is lower than that observed in the single Fe₂O₃, suggesting charge transfer from MoS₂ to Fe₂O₃. Upon incorporating a third phase, MoO₃, to form the MoO₃/Fe₂O₃/MoS₂ ternary heterointerface, the Mo site in MoO₃ exhibits a higher Bader charge compared to single-phase MoS₂ (**Figure 6.19b**), while the Fe site has a lower Bader charge compared to single-phase Fe₂O₃. This confirms charge transfers from MoO₃ to Fe₂O₃ in ternary heterojunction, suggesting Fe as the reactive site. Notably, the change of Baser charge at Fe and Mo sites in MoO₃/Fe₂O₃/MoS₂ compared to the binary hybrid can be ascribed to the strong interaction in the ternary heterointerface.

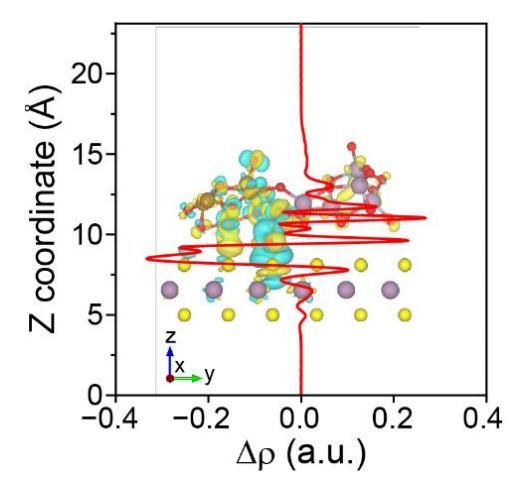


Figure 6.17. Charge density difference of MoO₃/Fe₂O₃/MoS₂ heterojunction in Fe-L-MoS₂ and planar average charge density difference (red line) along z-direction for MoO₃/Fe₂O₃/MoS₂ heterojunction.

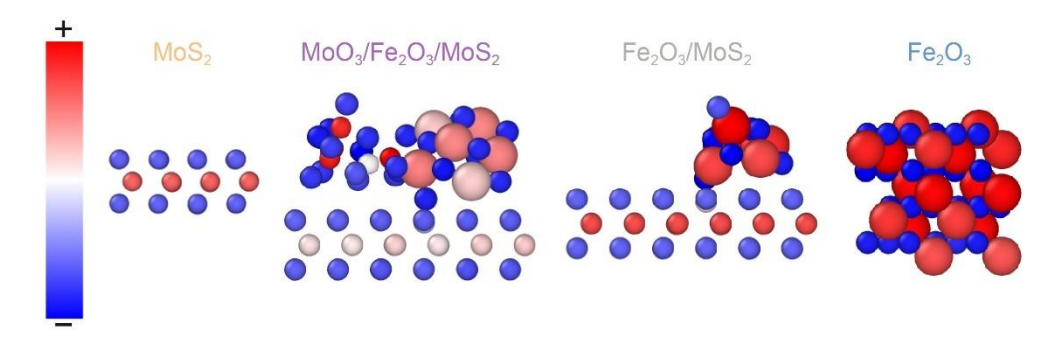


Figure 6.18. Bader charge distribution in Fe₂O₃, MoS₂, Fe₂O₃/MoS₂ and MoO₃/Fe₂O₃/MoS₂ heterointerface.

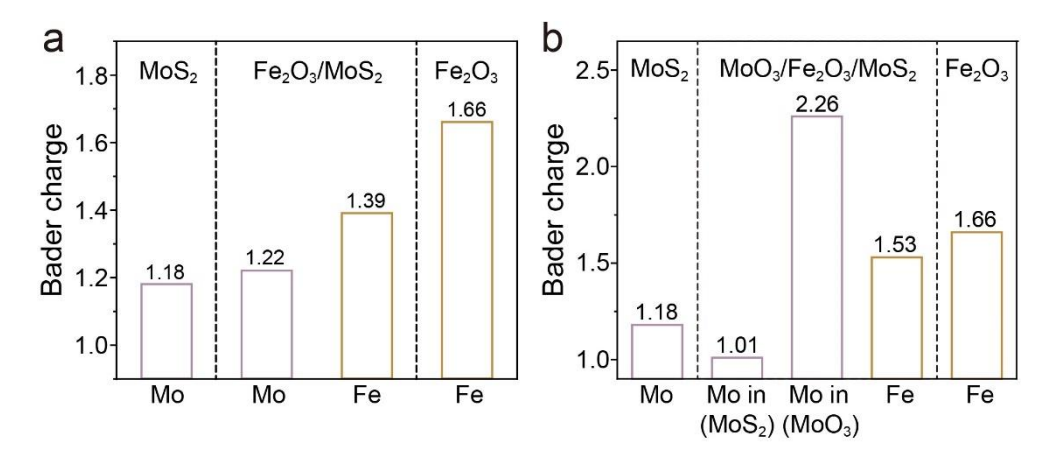


Figure 6.19. (a) Bader charges at Mo and Fe sites in Fe₂O₃, MoS₂, and Fe₂O₃/MoS₂ heterointerface. (b) Bader charges at Mo and Fe sites in Fe₂O₃, MoS₂, and MoO₃/Fe₂O₃/MoS₂ heterointerface.

EIS was carried out to understand the charge transfer process, and the corresponding Nyquist plots are given in **Figure 6.20** and **Table 6.5**. The catalyst resistance (R_2) for MoS₂ (0.61 Ω), Fe₂O₃ (3.30 Ω), and Fe₂O₃/MoS₂ (1.26 Ω) is considerably reduced to 0.24 Ω in Fe-L-MoS₂, demonstrating the effective synergistic effects of three-phase heterointerfaces in lowing the charge transfer barrier in electrocatalysts. The solid-liquid interface resistance (R_{ct}) also decreases from 114.50 Ω (Fe₂O₃) and 74.67 Ω (MoS₂) to 2.0 Ω in Fe-L-MoS₂, indicating facilitated charge exchange between the electrode and the electrolyte, as well as improved OER kinetics. ^[57] The formation of heterointerfaces promotes charge redistribution within the space charge layer at the electrode–solution interface. Mott–Schottky analysis was performed to

assess the charge concentration, which involved measuring the capacitance across a range of applied potentials. The Mott–Schottky plot for the Fe-L-MoS₂ shows a carrier density (5.39 \times 10²¹ cm⁻³) *ca.* 14.9, 18.7 and 54.2 times greater than that of Fe₂O₃/MoS₂ hybrid (3.61 \times 10²⁰ cm⁻³), pristine MoS₂ (2.88 \times 10²⁰ cm⁻³) and Fe₂O₃ (9.95 \times 10¹⁹ cm⁻³), respectively, as shown in **Figure 6.21**. This enhanced charrier density indicates that the Fe-L-MoS₂ interface provides more mobile charges available for catalytic reactions, potentially contributing to improved catalytic performance.

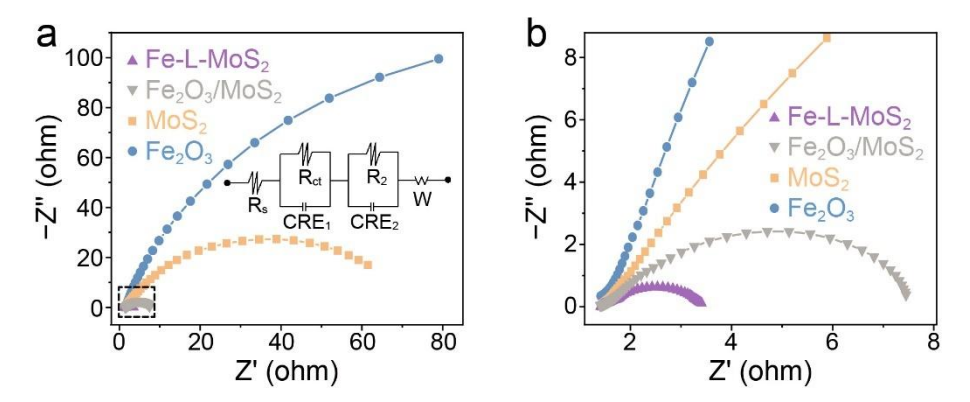


Figure 6.20. (a) Nyquist plots of MoS_2 , Fe_2O_3 , Fe_2O_3/MoS_2 , and $Fe-L-MoS_2$ and (b) corresponding enlarged part in dotted box. The inserted image is an equivalent circuit, in which R_s stands for the electrolyte resistance, CPE_1 represents double-layer capacitance, R_{ct} is related to the interfacial charge transfer reaction, W is Warburg, and CPE_2 and R_2 are associated with the dielectric properties and the resistance of the electrode itself.

Table 6.5. Parameters of EIS simulation for catalysts of MoS_2 , Fe_2O_3 , Fe_2O_3 / MoS_2 , and $MoO_3/Fe_2O_3/MoS_2$.

Deposition time (min)	$R_s(\Omega)$	R _{ct} (Ω)	$R_2(\Omega)$	CPE ₁ (F)	CPE ₂ (F)	W (S sec ⁵)
MoS_2	1.45	74.67	0.61	0.011	0.007	0.054
Fe ₂ O ₃	1.43	114.50	3.30	0.005	0.001	0.035
Fe ₂ O ₃ /MoS ₂	1.45	3.47	1.26	0.002	0.001	0.836
Fe-L-MoS ₂	1.41	2.00	0.24	0.005	0.221	0.161

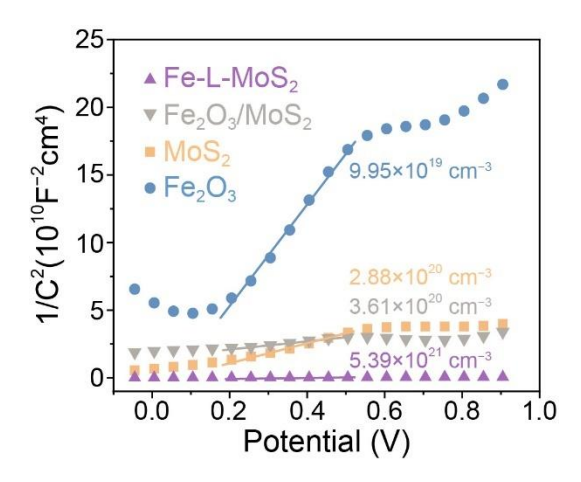


Figure 6.21. Mott–Schottky plots of MoS₂, Fe₂O₃, Fe₂O₃/MoS₂, and Fe-L-MoS₂.

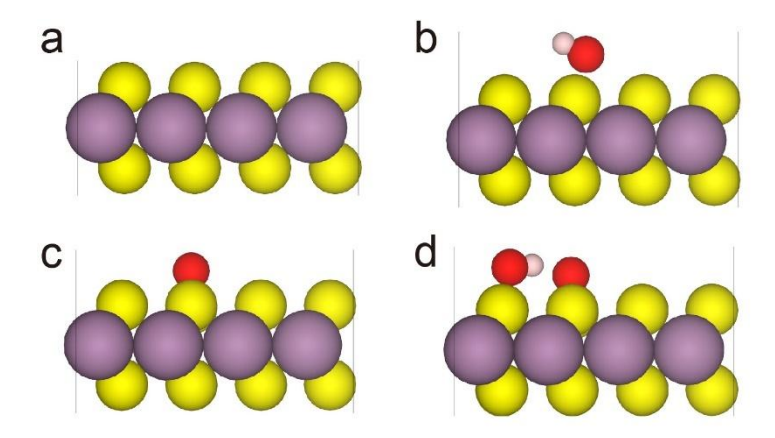


Figure 6.22. Structures of (a) MoS₂, and (b) *OH, (c) *O, and (d) *OOH adsorbed MoS₂ (S site). Mo, O, S, and H atoms are shown in violet, red, yellow, and pink, respectively.

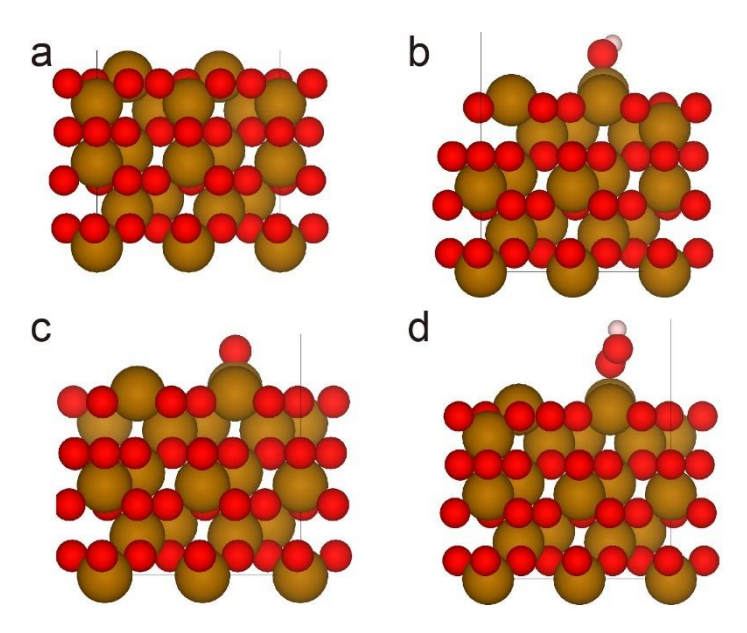


Figure 6.23. Structures of (a) Fe₂O₃, and (b) *OH, (c) *O, and (d) *OOH adsorbed MoS₂ (S site). Fe, O, and H atoms are shown in brown, red, and pink, respectively.

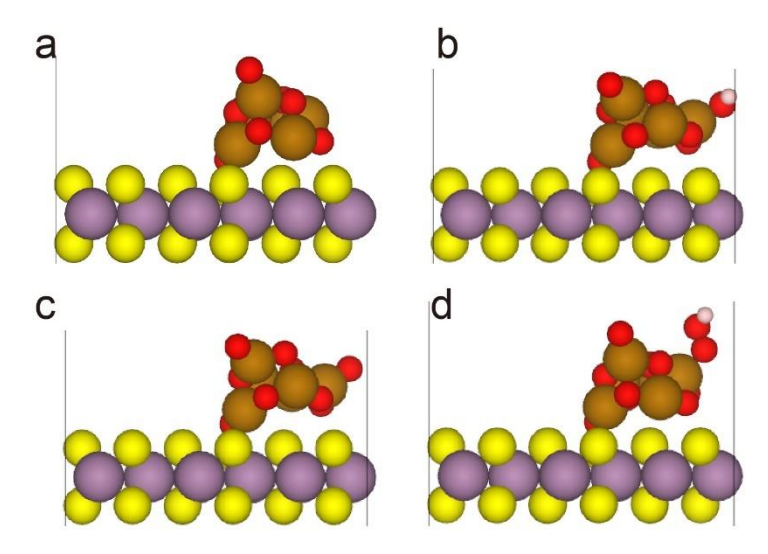


Figure 6.24. Structures of (a) Fe₂O₃/MoS₂ heterojunction, and (b) *OH, (c) *O, and (d) *OOH adsorbed Fe₂O₃/MoS₂ (Fe site). Mo, Fe, O, S, and H atoms are shown in violet, brown, red, yellow, and pink, respectively.

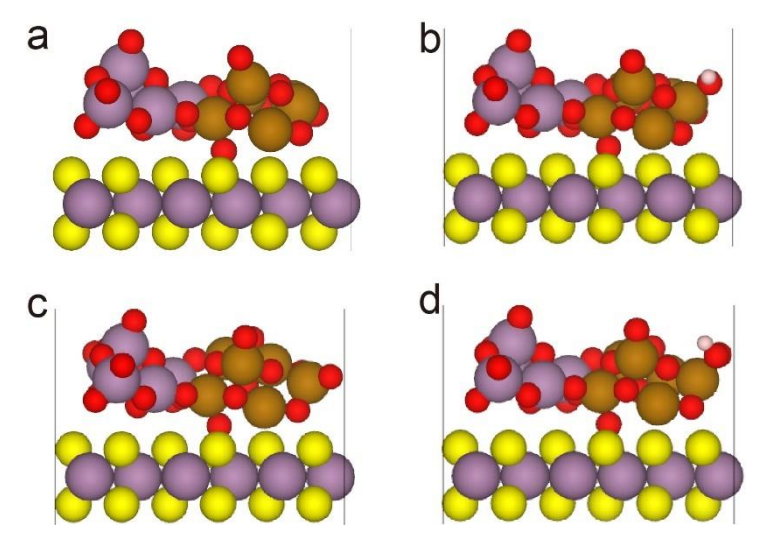


Figure 6.25. Structures of (a) MoO₃/Fe₂O₃/MoS₂ heterojunction, and (b) *OH, (c) *O, and (d) *OOH adsorbed MoO₃/Fe₂O₃/MoS₂ (Fe site). Mo, Fe, O, S, and H atoms are shown in violet, brown, red, yellow, and pink, respectively.

DFT calculations were employed to calculate the free energy diagrams for each step of the OER (**Figure 6.22–25**). The OER free energy diagram in **Figure 6.26** reveals that for Fe₂O₃, the RDS is the deprotonation and electron transfer from *OH to form *O (the second step). In contrast, for both Fe₂O₃/MoS₂ and Fe-L-MoS₂, the RDS shifts to the *OH adsorption (the first step). At the same time, the overall OER free energy decreases significantly from 0.81, 0.89,

and 0.58 eV for Fe₂O₃, MoS₂, and Fe₂O₃/MoS₂, respectively, to 0.40 eV for Fe-L-MoS₂, highlighting the beneficial effects of heterointerfaces on OER catalysis.

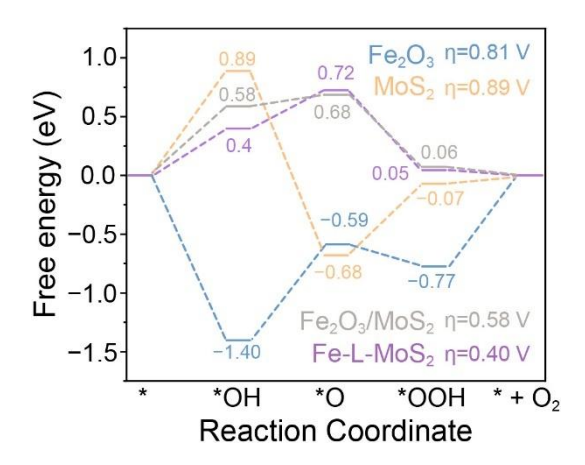


Figure 6.26. The Gibbs free energy diagrams for OER.

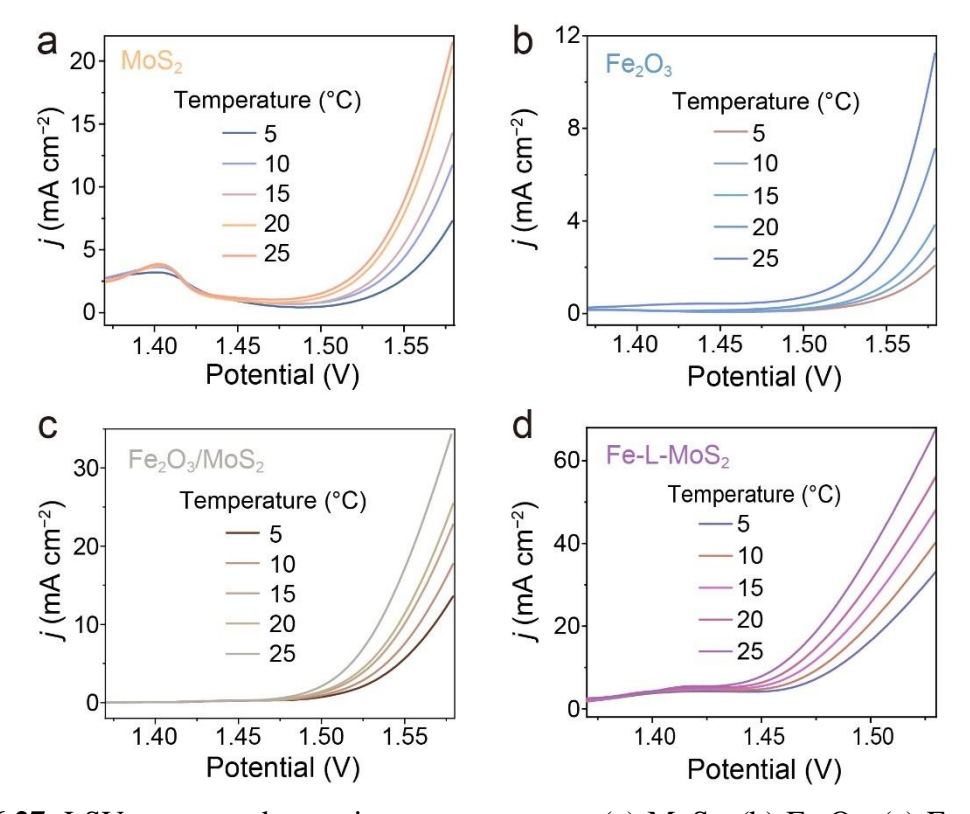


Figure 6.27. LSVs measured at various temperatures: (a) MoS_2 , (b) Fe_2O_3 , (c) Fe_2O_3/MoS_2 , and (d) Fe-L- MoS_2 .

To further investigate the impact of interfaces on the OER thermodynamics, **Figure 6.27** compares the Arrhenius plots of Fe₂O₃, MoS₂, and Fe-L-MoS₂, which were obtained by

measuring LSVs at various temperatures (**Figure 6.28**). The E_a , extracted from the slope of the Arrhenius plot, is the lowest for Fe-L-MoS₂ (23.5 kJ mol⁻¹), followed by Fe₂O₃/MoS₂ (37.4 kJ mol⁻¹), MoS₂ (41.3 kJ mol⁻¹) and Fe₂O₃ (53.5 kJ mol⁻¹). This reduction in E_a indicates a significant decrease in the kinetic barrier for electrocatalytic water oxidation at the heterojunctions.

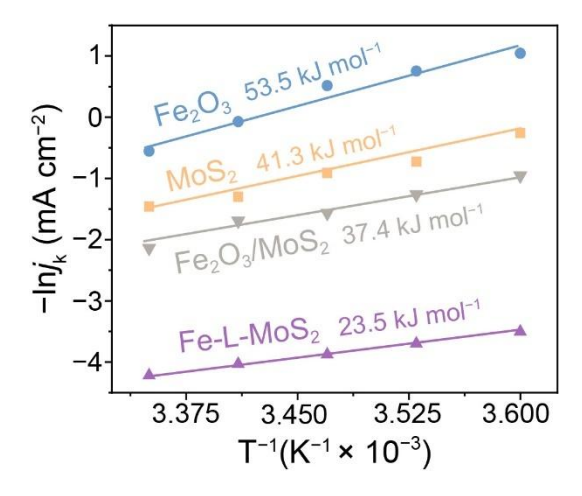


Figure 6.28. Arrhenius plots of MoS₂, Fe₂O₃, Fe₂O₃/MoS₂, and Fe-L-MoS₂.

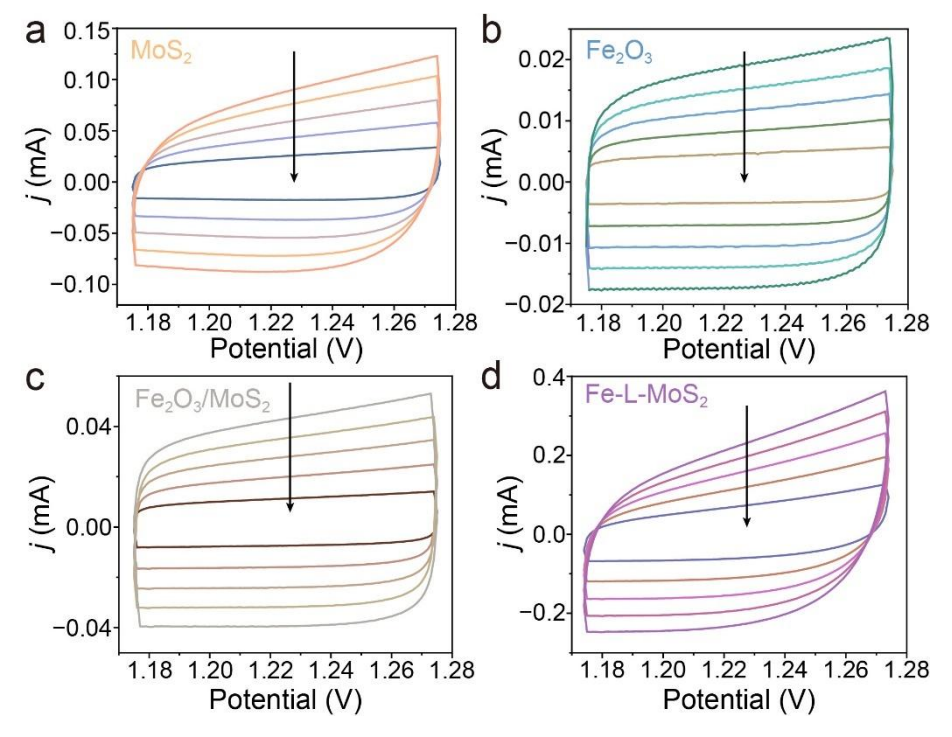


Figure 6.29. CV measured in a non-Faradaic region at various scan rates. (a) MoS₂, (b) Fe₂O₃, (c) Fe₂O₃/MoS₂, and (d) Fe-L-MoS₂. The scan rate is from 100 to 20 mV s⁻¹.

ECSAs of the as-prepared catalysts were also determined using electrochemical $C_{\rm dl}$ from cyclic voltammograms (**Figures 6.29** and **6.30**). Notably, Fe-L-MoS₂ exhibits the largest ECSA, 2.25 times greater than that of MoS₂ (**Figure 6.31a**), suggesting that the heterointerfaces and nanoparticle structure provide more active sites for OER. Even after normalizing the polarization curves by ECSA (**Figure 6.31b**), Fe-L-MoS₂ maintains superior OER activity compared to its counterparts. This suggests that its outstanding performance is not solely due to the enlarged ECSA but also stems from enhanced intrinsic catalytic activity facilitated by the three-phase interfaces.

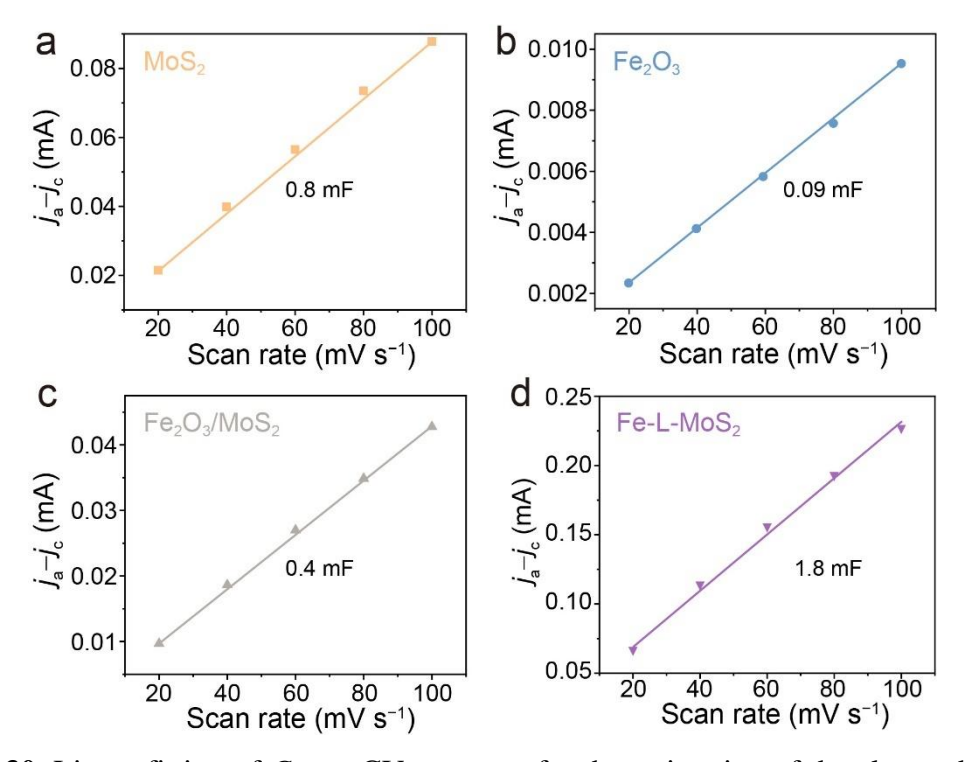


Figure 6.30. Linear fitting of $C_{\rm dl}$ vs. CV scan rate for the estimation of the electrochemically active surface area of different catalysts: (a) MoS₂, (b) Fe₂O₃, (c) Fe₂O₃/MoS₂, and (d) Fe-L-MoS₂.

Furthermore, *in situ* Raman spectroscopy was employed to monitor the surface species as the applied potential varies in real time. **Figure 6.32** shows the *in situ* Raman spectra of Fe-L-MoS₂ collected between the OCP and an applied potential of 1.524 V. Characteristic peaks

corresponding to MoO_3 , Fe_2O_3 , and MoS_2 can observed clearly at the open-circuit potential and maintain at same positions except the decreasing intensity. Notably, a new peak at 975 cm⁻¹ corresponding to SO_4^{2-} appears at 1.474 V,^[59] indicating the oxidation of MoS_2 during the OER process.

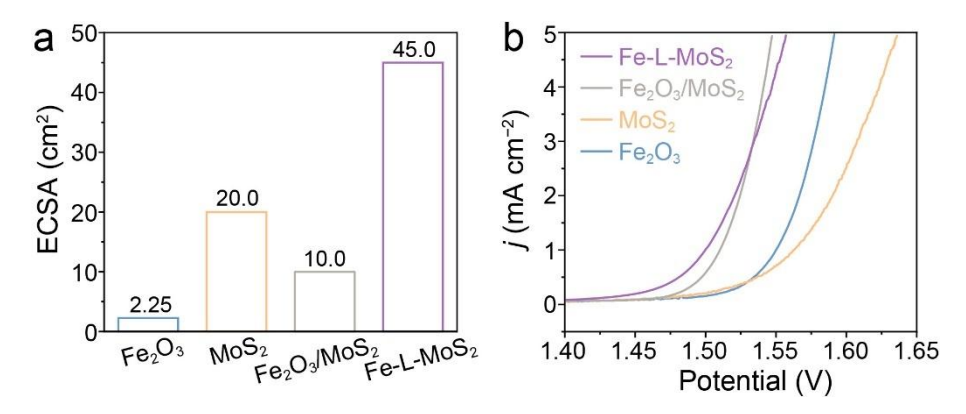


Figure 6.31. (a) ECSA and (b) ECSA-normalized LSV curves of Fe_2O_3 , MoS_2 , Fe_2O_3/MoS_2 and $Fe-L-MoS_2$.

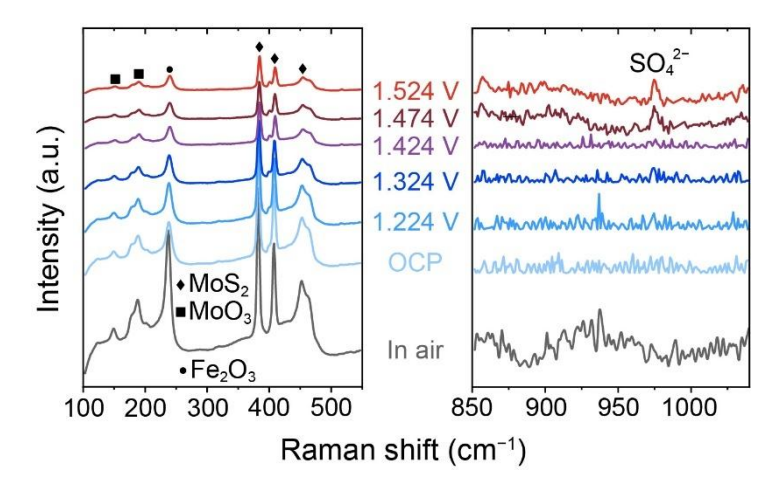


Figure 6.32. *In situ* Raman of Fe-L-MoS₂.

Quasi-*in-situ* UV–Vis spectroscopy was employed to further verify the release of MoO_4^{2-} and SO_4^{2-} anions (**Figure 6.33a** and **b**). When a potential of 2.5 V is applied to Fe-L-MoS₂ in a two-electrode system, absorption peaks for MoO_4^{2-} (211 and 232 nm) and SO_4^{2-} (216 nm) after 1 min (**Figure 6.33c**). This peak gradually intensifies with prolonged oxidation time, further substantiating the release of MoO_4^{2-} and SO_4^{2-} from MoS_2 in Fe-L-MoS₂ during the

OER process. Notably, the protector of MoO₄²⁻ and SO₄²⁻ anions, which form around Fe-L-MoS₂ under the influence of the positive potential of anodic electrode, can repel and obstruct Cl⁻ through electrostatic repulsion, thereby mitigating corrosion during seawater oxidation.^[60]

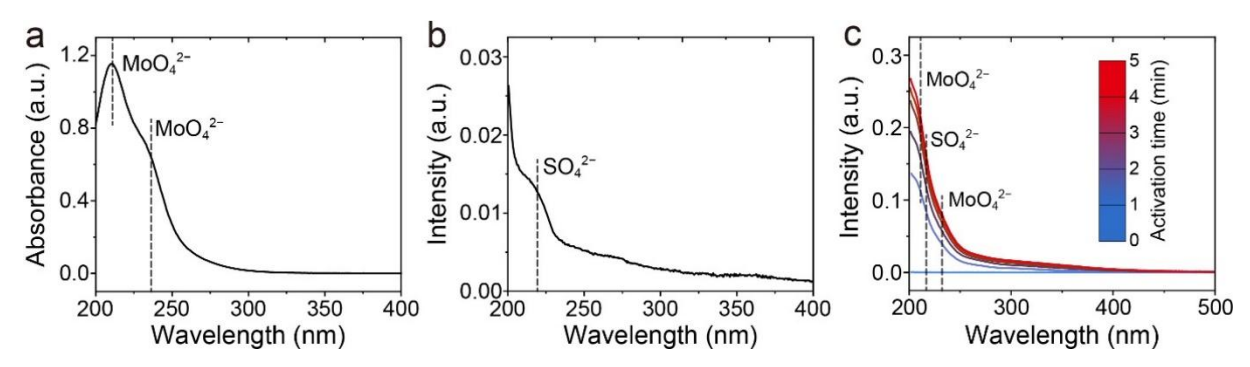


Figure 6.33. UV–Vis absorption spectra of (a) 0.1 mM NH₄MoO₄ and (b) 0.01 mM Na₂SO₄. (c) Quasi-*in-situ* UV–Vis spectra for MoO₄²⁻ and SO₄²⁻ detection.

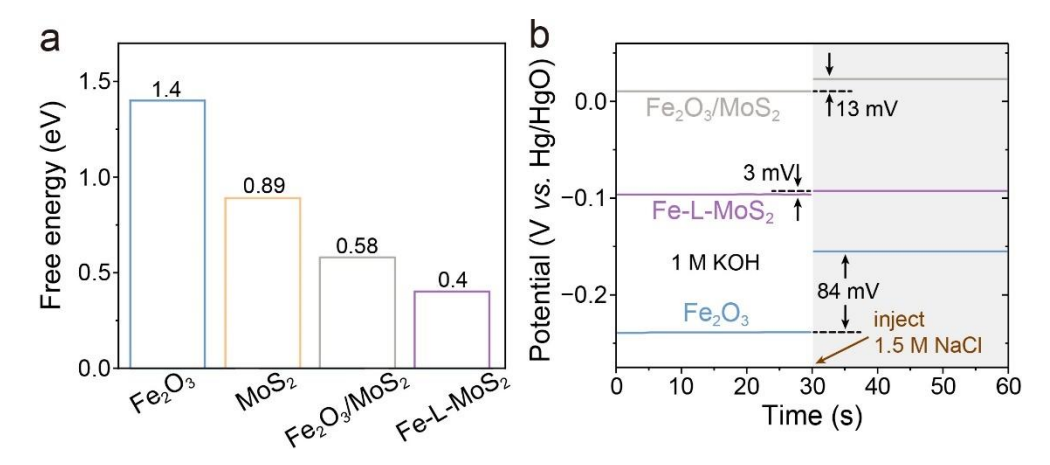


Figure 6.34. (a) Free energy change of on $E_{*OH}-E_{slab}$ in Fe₂O₃, MoS₂, Fe₂O₃/MoS₂ and Fe-L-MoS₂. (b) OCP curves of Fe₂O₃, Fe₂O₃/MoS₂, and Fe-L-MoS₂.

Moreover, Fe-L-MoS₂ exhibits the smallest energy gap between E_{*OH} and E_{slab} (**Figure 6.34a**), which indicates the heterojunction benefits the OH⁻ adsorption, thereby counteracting the electrostatic repelling effect of anion ions on OH⁻. The strong hydrogen bonding between OH⁻ and MoS₂ further prevents electrostatic repulsion during OH⁻ diffusion, ensuring rapid OER kinetics.^[61] This is supported by the OCP measurements, which reflect the extent of Cl⁻ adsorption on the Helmholtz layer; the greater the influence of the catalyst surface on Cl⁻, the more profound the

shift in OCP upon introducing an equivalent concentration of Cl⁻.^[62, 63] A significant increase in OCP of 84 mV is observed for Fe₂O₃ compared to Fe₂O₃/MoS₂ (13 mV) upon adding 1.5 M NaCl to the electrolyte (**Figure 6.34b**), which decreases to 3 mV for Fe-L-MoS₂, proving the reduced impact of Cl⁻ due to the three-phase heterointerface.

The CER process in Fe-L-MoS₂ was investigated using a two-step Volmer–Heyrovsky mechanism, encompassing Cl⁻ adsorption and subsequent molecular Cl₂ release (**Figures 6.35** – **38**). The Gibbs free energy changes for each elementary step of the CER are presented in **Figure 6.39a**. The free energy diagram indicates that Fe-L-MoS₂ requires substantially higher energy (1.36 eV) for CER compared to Fe₂O₃ (0.32 eV), signifying that the heterojunction effectively suppresses CER, thereby enhancing the corrosion resistance of the electrode. MoS₂ exhibits the greatest free energy for CER due to the unfavorable Cl⁻ adsorption on S sites. Additionally, the thermodynamic OER selectivity can be described by the overpotential gap between OER and CER ($\eta_{CER} - \eta_{OER}$). A large gap indicates a higher selectivity of OER. The overpotential gap for Fe₂O₃ is determined to be -0.49 V (**Figure 6.39b**), indicating that CER is more favorable for Fe₂O₃ than OER. In contrast, positive overpotential gap values for MoS₂, Fe₂O₃/MoS₂, and Fe-L-MoS₂ indicate that OER dominates the anodic reaction, with Fe-L-MoS₂ exhibiting the largest gap of 0.96 V for enhanced OER selectivity.

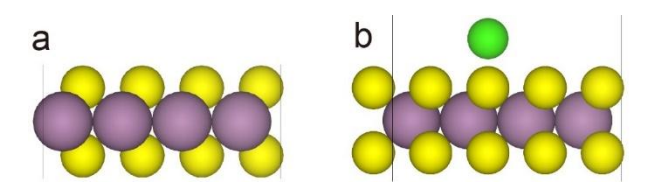


Figure 6.35. Structures of (a) MoS₂ and (b) *Cl adsorbed MoS₂ (S site). Mo, O, S, and Cl atoms are shown in violet, red, yellow, and green, respectively.

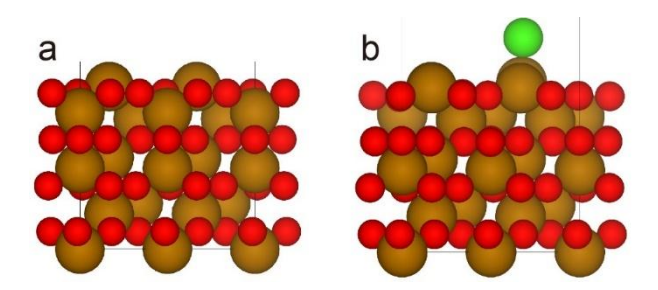


Figure 6.36. Structures of (a) Fe₂O₃ and (b) *Cl adsorbed Fe₂O₃ (Fe site). Fe, O, and Cl atoms are shown in brown, red, and green, respectively.

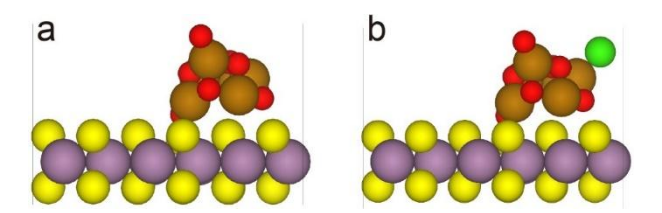


Figure 6.37. Structures of (a) Fe₂O₃/MoS₂ heterojunction, and (b) *Cl adsorbed Fe₂O₃/MoS₂ (Fe site). Mo, Fe, O, S, Cl, and H atoms are shown in violet, brown, red, yellow, green, and pink, respectively.

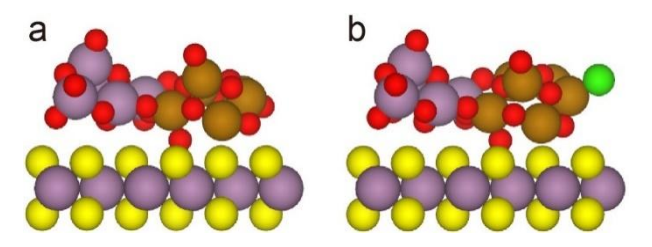


Figure 6.38. Structures of (a) MoO₃/Fe₂O₃/MoS₂ heterojunction, and (b) *Cl adsorbed MoO₃/Fe₂O₃/MoS₂ (Fe site). Mo, Fe, O, S, Cl, and H atoms are shown in violet, brown, red, yellow, green, and pink, respectively.

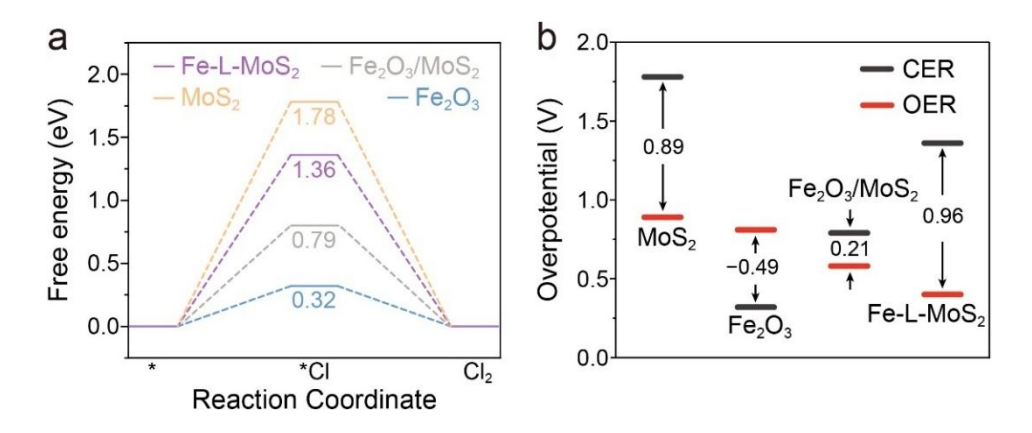


Figure 6.39. (a) The Gibbs free energy diagrams for CER. (b) The overpotential difference between OER and CER for Fe_2O_3 , MoS_2 , Fe_2O_3/MoS_2 , and $Fe-L-MoS_2$.

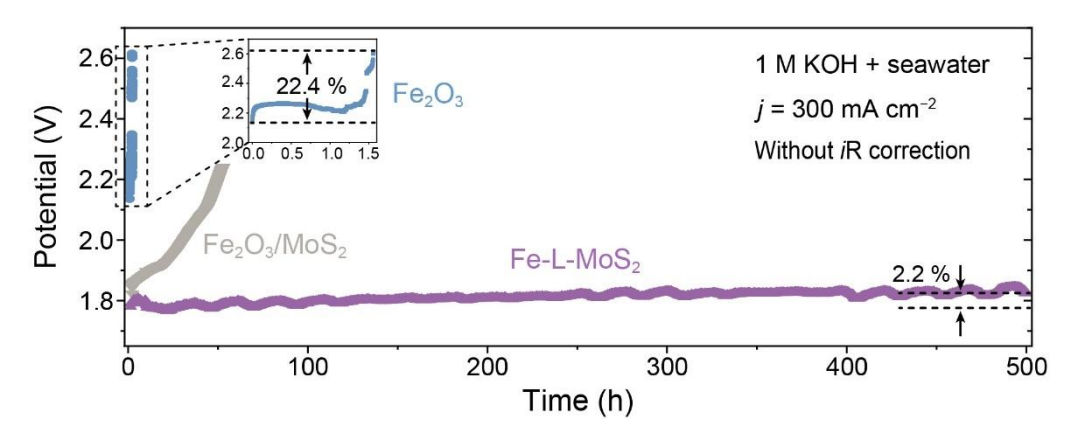


Figure 6.40. Chronopotentiometric curves of Fe₂O₃, Fe₂O₃/MoS₂ and Fe-L-MoS₂. in seawater + 1 M KOH.

Moreover, Long-term seawater electrolysis at a high current density of 300 mA cm⁻² was conducted on Fe₂O₃, Fe₂O₃/MoS₂, and Fe-L-MoS₂ (Figure 6.40). Fe-L-MoS₂ maintains relatively stable activity over 500 h, while Fe₂O₃ and Fe₂O₃/MoS₂ rapidly lose activity within 1.5 and 53 h. Although a slight increase (2.2 %) in the potential required to sustain 300 mA cm⁻² for seawater OER is significantly less than the 22.4 % increase observed for Fe₂O₃ within just 1.5 h, further confirming the excellent corrosion resistance of Fe-L-MoS₂. Corrosion polarization curves obtained in natural seawater show that Fe-L-MoS₂ has a lower corrosion current density (0.101 mA cm⁻²) and a higher corrosion potential (-0.28 V) compared to Fe₂O₃ (1.101 mA cm⁻² and -0.37 V), indicating stronger corrosion resistance in seawater (**Figure 6.41a-c**). [64] Notably, Mo-O, Fe-O, and Mo-S peaks can still be well maintained after the OER activation and 100-h stability test in alkaline seawater^[65, 66] (**Figure 6.41d**), suggesting the integrity of the three-phase structure. However, the intensity of the Mo-S mode has diminished relative to the Fe-O mode after OER activation, likely due to the oxidation of MoS₂. Besides, the nanoparticles on Fe-L-MoS₂ are preserved during seawater electrolysis (Figure **6.42a**), verifying a high corrosion resistance to seawater. Moreover, the Ca element was detected due to the formation of insoluble Ca(OH)₂ on the catalyst's surface during the OER

process (**Figure 6.42b**), which can explain the decayed performance in the alkaline seawater electrolyte.

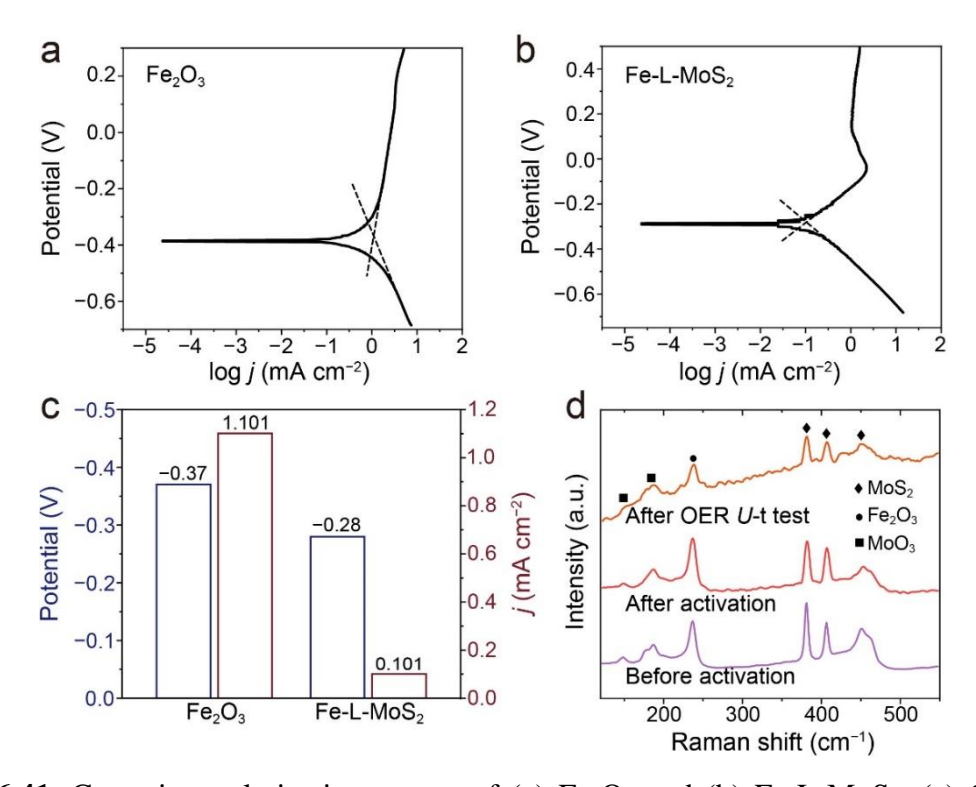


Figure 6.41. Corrosion polarization curves of (a) Fe₂O₃ and (b) Fe-L-MoS₂. (c) Corrosion current densities and potentials of pristine Fe₂O₃ and Fe-L-MoS₂ in natural seawater. (d) Raman spectra of Fe-L-MoS₂ before and after OER activation and after long-term *U*-t test in alkaline seawater.

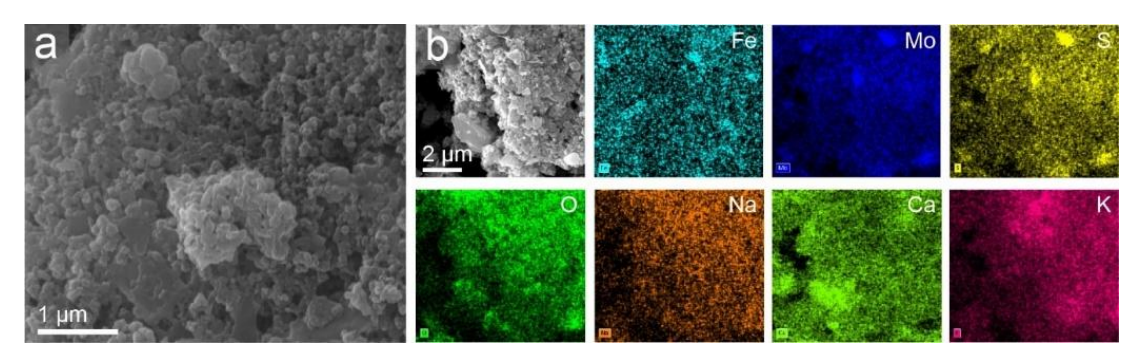


Figure 6.42. (a) SEM image and (b) Energy-dispersive spectrometer mapping images of Fe-L-MoS₂ after OER stability in seawater.

6.3.4. Light-assisted OER Performance and Mechanism

The light-assistance electrochemical OER performance of Fe-L-MoS₂ was further evaluated. Under UV-vis light irradiation (**Figure 6.42a**), a 20.4 % increase in the current density at the applied potential of 1.550 V (*vs.* RHE) can be obtained in the alkaline seawater electrolyte. Moreover, The Tafel slope decreases from 48.9 to 41.9 mV dec⁻¹ under light irradiation (**Figure 6.42b**), indicating accelerated OER kinetics under irradiation. Encouraged by these promising results, a two-electrode electrolyzer was assembled using Fe-L-MoS₂ and 20 % Pt/C as the anode and cathode, respectively, to evaluate light-assisted seawater splitting performance at large current densities. The Fe-L-MoS₂||Pt/C seawater electrolyzer delivers a current density of 0.5 A cm⁻² at a cell voltage of 2.476 V (**Figure 6.42c**), significantly lower than the benchmark RuO₂||Pt/C system (2.718 V). Furthermore, during the 170-h chronopotentiometry test at 0.2 A cm⁻² (**Figure 6.43**), the decrease of the cell potential can be observed when the light was on and the cell kept running at lower potentials until the light was off, which indicates the stable light-assisted OER catalysis of Fe-L-MoS₂ in seawater.

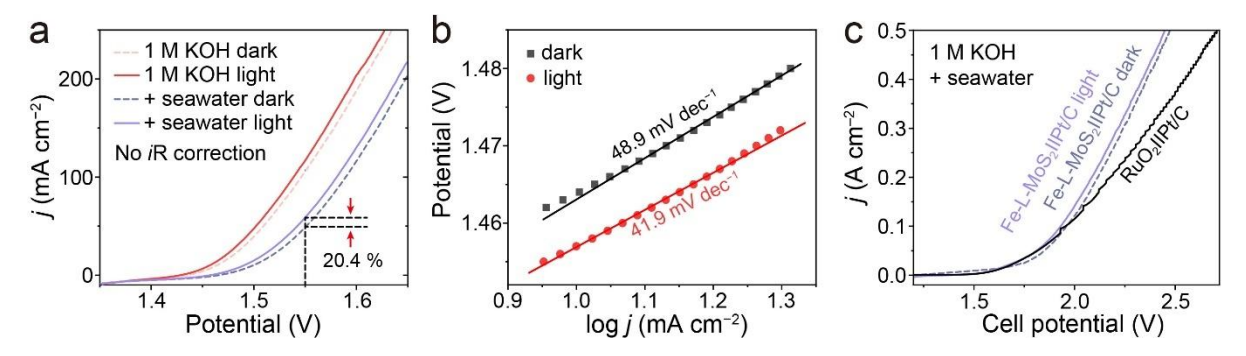


Figure 6.42. (a) LSV curves of Fe-L-MoS₂ in the dark and under light irradiation in different electrolytes. (b) Tafel slopes of Fe-L-MoS₂ in the dark and light. (c) LSV curves of two-electrode systems.

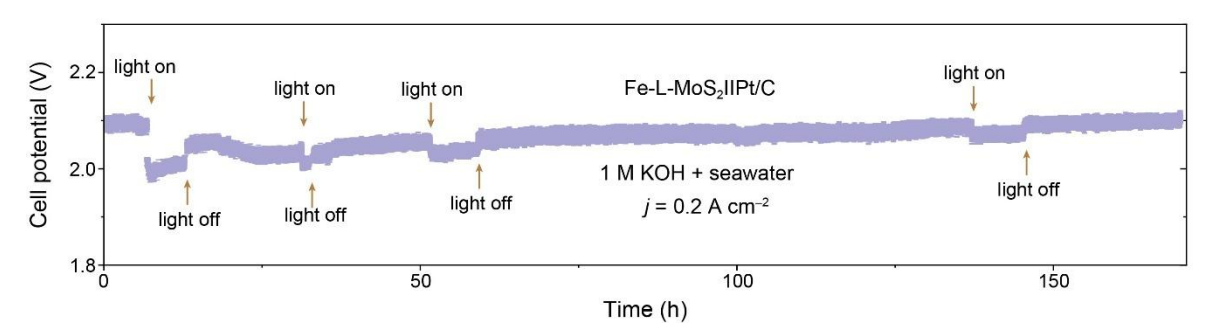


Figure 6.43. Chronopotentiometric curve of Fe-L-MoS₂ $\|$ Pt/C alkaline seawater electrolyzer operated at 1 A cm⁻².

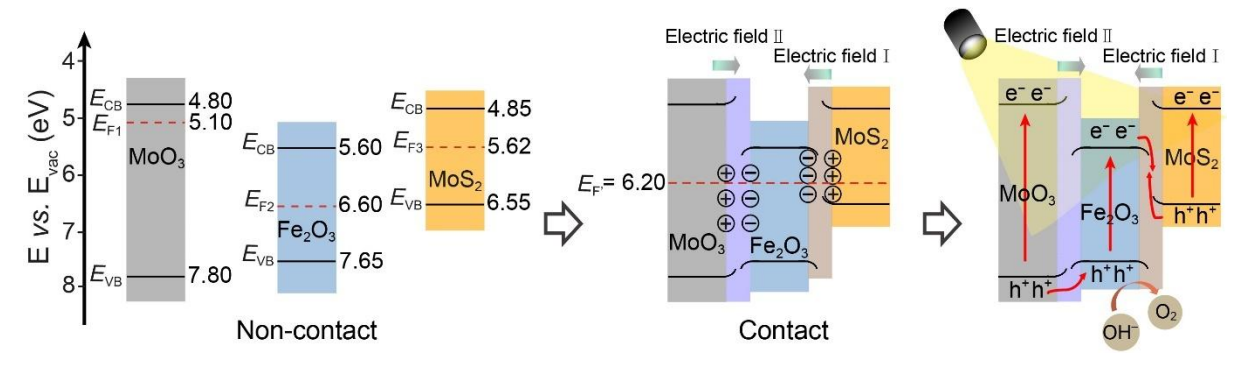


Figure 6.44. The formation of built-in electric fields and migration routes of photo-generated carriers at the interfaces. E_{CB} and E_{VB} are conduction and valence band energies, respectively.

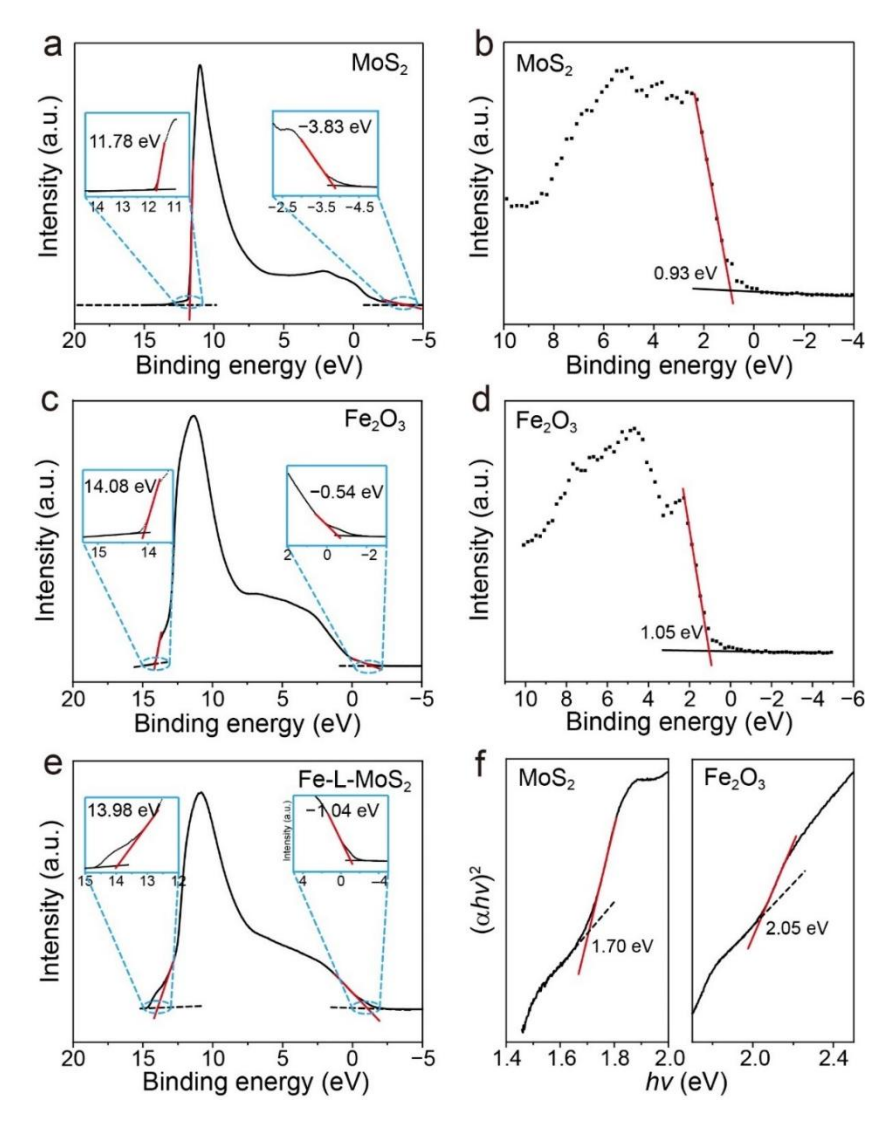


Figure 6.45. UPS spectra of (a) MoS_2 , (c) Fe_2O_3 , and (e) $Fe-L-MoS_2$. VB-XPS spectra of (b) MoS_2 and (d) Fe_2O_3 . (f) Tauc plots of MoS_2 and Fe_2O_3 .

To better understand the light-assisted mechanism, the band structures of MoS_2 , Fe_2O_3 , and MoO_3 before and after contact are illustrated in **Figure 6.44**. The work functions (Φ) of MoS_2 , Fe_2O_3 , and Fe-L- MoS_2 were determined by UPS (**Figures 6.45a**, **6.45c**, and **6.45e**). The work function of MoS_2 (5.62 eV) is smaller than that of Fe_2O_3 (6.60 eV), which suggests that electrons spontaneously migrate from MoS_2 to Fe_2O_3 when the interface is formed, narrowing the gap of their Fermi levels (E_F). This electron transfer establishes a built-in electric field I directed from MoS_2 to Fe_2O_3 , resulting in charge redistribution at the interface. Consequently, Fe_2O_3 becomes negatively charged while the surface of MoS_2 becomes electrophilic. The

positively charged MoS₂ can attract electron-rich OH⁻, which is expected to enhance catalytic kinetics, while the negatively charged Fe₂O₃ improves corrosion resistance by repelling Cl⁻. A second built-in electric field II, directed from MoO₃ to Fe₂O₃, forms at the Fe₂O₃/MoO₃ interface.

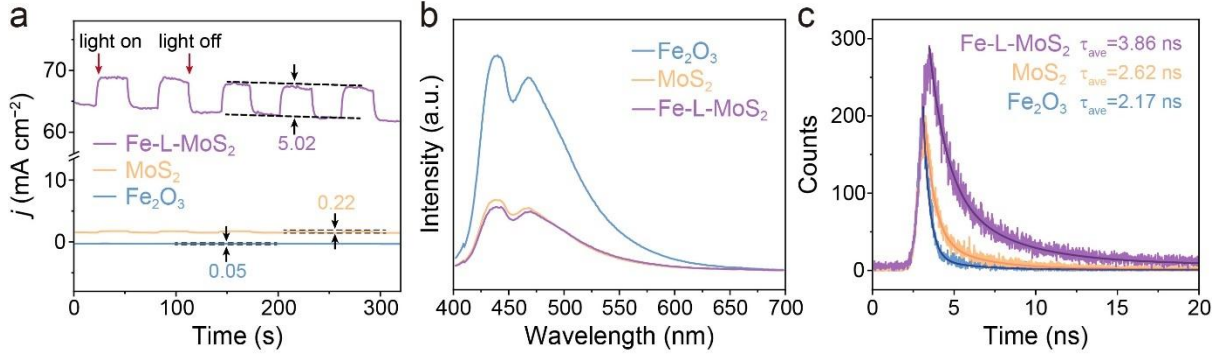


Figure 6.46. (a)Transient photocurrent, (b) PL spectra, and (c) time-resolved PL spectra of Fe₂O₃, MoS₂, and Fe-L-MoS₂.

Under light irradiation, electrons are excited from VBM to CBM while photo-generated holes are left on VBM in those three components. The built-in electric fields drive the migration of these charge carriers across the interface. Specifically, electrons transfer from the CBM of Fe₂O₃ to MoS₂, recombining with photo-generated holes in the VBM of MoS₂ due to the influence of electric field I,^[68] which generates holes with strong oxidation properties in the VBM of Fe₂O₃. Similarly, photo-generated holes in the VBM of MoO₃ migrate to Fe₂O₃, while electrons in the CBM of Fe₂O₃ move to MoO₃ under the influence of electric field II. This results in the accumulation of photo-generated holes on Fe₂O₃, thereby promoting the water oxidation reaction.

Table 6.6. Lifetimes of carriers in Fe₂O₃, MoS₂, and Fe-L-MoS₂.

Sample	τ1			τ2			
	Value (ns)	\mathbf{A}_1	Rel.%	Value (ns)	\mathbf{A}_2	Rel.%	
Fe ₂ O ₃	0.40	200.57	66.08	2.69	15.38	33.92	
MoS_2	0.60	151.54	43.40	2.94	40.54	56.60	

Chapter VI Light-Assisted Seawater Electrooxidation by MoO₃/Fe₂O₃/MoS₂

Fe-L-MoS ₂	1.07	181.94	31.56	4.18	101.02	68.44	-
-----------------------	------	--------	-------	------	--------	-------	---

The transient photocurrent was carried out at a constant potential of 1.524 V to investigate the photo response behavior. The current density of Fe-L-MoS₂ increases immediately upon light exposure and returns to its initial level when the light is turned off, indicating a rapid photoresponse (Figure 6.46a). Although MoS₂ and Fe₂O₃ exhibit photo-response behavior, their photocurrents (0.22 and 0.05 mA cm⁻², respectively) are much lower than that of Fe-L-MoS₂ (5.02 mA cm⁻²), further suggesting the enhanced utilization efficiency of photo-generated carriers in the hybrid. Besides, the photoluminescence (PL) emission spectrum was utilized to verify the recombination of photogenerated electron/hole pairs. Usually, the higher the intensity of the PL spectrum, the greater the recombination rate of photo-generated carriers. [69] As shown in **Figure 6.46b**, all catalysts exhibit a broad band in the range of 480 – 600 nm, suggesting the multiple radiation processes of the excited carriers. Notably, Fe-L-MoS₂ displays lower emission intensity compared to MoS₂ and Fe₂O₃, which means that the threephase heterointerfaces effectively alleviate the carrier recombination. Time-resolved PL spectrum was further employed to investigate the charge dynamics. The carrier lifetime of Fe-L-MoS₂ is determined to be 3.86 ns (**Figure 6.46c** and **Table 6.6**) which is 1.77 and 1.47 times higher than that of Fe₂O₃ (2.17 ns) and MoS₂ (2.62 ns), respectively. The longer carrier lifetime of Fe-L-MoS₂ can be ascribed to the efficient carrier separation and suppression of carrier recombination.

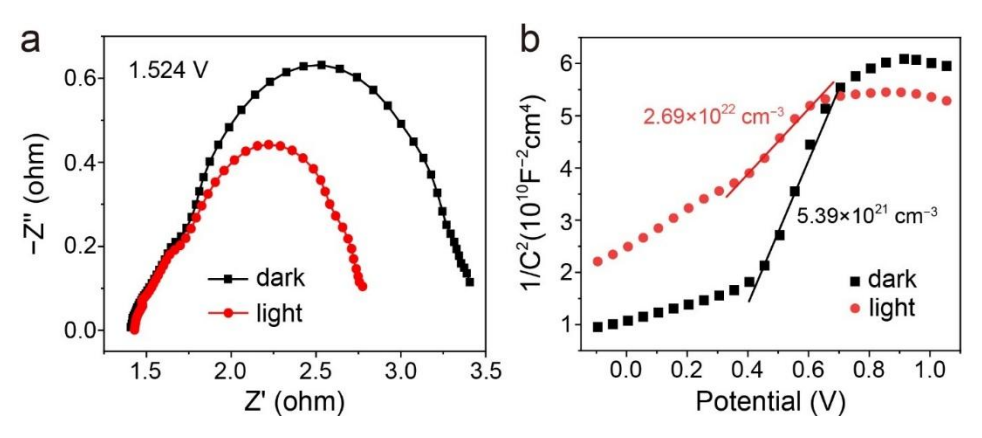


Figure 6.47. (a) Nyquist plots (1.524 V vs. RHE) of Fe-L-MoS₂ in dark and under light irradiation. (b) Mott–Schottky plots of Fe-L-MoS₂ in dark and under light irradiation.

Moreover, charge-transfer resistance between catalyst and electrolyte is decreased from 2.0 to 1.43 Ω under light irradiation (**Figure 6.47a**), thereby reducing charge loss. This reduction is likely due to photogenerated holes acting as electron traps, attracting OH⁻ reactants.^[23] As a result, the charge concentration of Fe-L-MoS₂ increases nearly fivefold under light irradiation (**Figure 6.47b**), which is consistent with EIS and transient photocurrent results, further confirming that light irradiation can generate more carriers to participate in catalytic reactions.

6.5. Conclusion

This Chapter demonstrates that the construction of photoand electric-active MoO₃/Fe₂O₃/MoS₂ heterojunctions significantly enhances light-assisted seawater oxidation from while simultaneously protecting Fe_2O_3 chlorine-induced corrosion. The amorphous/crystalline interfaces in the Fe-L-MoS₂, characterized by a nanoparticle-decorated structure, expand the ECSA and provide abundant active sites. These heterointerfaces facilitate the OER process and, along with in situ leached MoO₄²⁻ and SO₄²⁻, mitigate Cl⁻ adsorption, thereby suppressing electrode corrosion. Additionally, built-in electric fields promote charge migration and decrease the recombination of photogenerated carriers, leading to increased participation of photocarriers in the OER process. Consequently, the Fe-L-MoS₂ exhibits significantly enhanced OER activity and durability in alkaline seawater, achieving 10 mA cm⁻²

Chapter VI Light-Assisted Seawater Electrooxidation by MoO₃/Fe₂O₃/MoS₂

at 267 mV with remarkable long-term stability, showing only a 2.2 % activity loss over 500 h at 300 mA cm⁻². Light irradiation excites Fe-L-MoS₂, generating carriers and reducing interfacial resistance, resulting in a 20.4 % increase in seawater oxidation current density. When combined with a Pt/C cathode, the Fe-L-MoS₂||Pt/C cell, assisted by light irradiation, requires only 2.476 V to reach 0.5 A cm⁻² in seawater, demonstrating stable operation for over 170 h at 0.2 A cm⁻². This study introduces a novel design concept for OER electrocatalysts that integrate excellent photoelectric synergistic effects with strong anti-corrosion properties for scalable seawater electrolysis.

6.6. References

- [1] S. Li, B. B. Chen, Y. Wang, M. Y. Ye, P. A. van Aken, C. Cheng, A. Thomas, *Nat. Mater.* **2021**, *20*, 1240.
- [2] Z. P. Wu, H. B. Zhang, S. W. Zuo, Y. Wang, S. L. Zhang, J. Zhang, S. Q. Zang, X. W. Lou, Adv. Mater. 2021, 33, 2103004.
- [3] N. Wang, P. F. Ou, S. F. Hung, J. E. Huang, A. Ozden, J. Abed, I. Grigioni, C. R. Chen, R. K. Miao, Y. Yan, J. Q. Zhang, Z. Y. Wang, R. Dorakhan, A. Badreldin, A. Abdel-Wahab, D. Sinton, Y. C. Liu, H. Y. Liang, E. H. Sargent, *Adv. Mater.* 2023, 35, 2210057.
- [4] L. Z. Zhuang, J. K. Li, K. Y. Wang, Z. H. Li, M. H. Zhu, Z. Xu, *Adv. Funct. Mater.* **2022**, 32, 2201127.
- [5] C. H. Liu, N. S. Zhang, Y. Li, R. L. Fan, W. J. Wang, J. Y. Feng, C. Liu, J. U. Wang, W. C. Hao, Z. S. Li, Z. G. Zou, *Nat. Commun.* 2023, *14*, 4266.
- [6] F. S. Hegner, F. A. Garces-Pineda, J. Gonzalez-Cobos, B. Rodriguez-Garcia, M. Torrens, E. Palomares, N. Lopez, J. R. Galan-Mascaros, ACS Catal. 2021, 11, 13140.
- [7] X. Luo, P. X. Ji, P. Y. Wang, X. Tan, L. Chen, S. C. Mu, Adv. Sci. 2022, 9, 2104846.
- [8] J. F. Chang, G. Z. Wang, Z. Z. Yang, B. Y. Li, Q. Wang, R. Kuliiev, N. Orlovskaya, M. Gu, Y. G. Du, G. F. Wang, Y. Yang, Adv. Mater. 2021, 33, 2101425.
- [9] L. Yu, L. B. Wu, B. McElhenny, S. W. Song, D. Luo, F. H. Zhang, Y. Yu, S. Chen, Z. F. Ren, *Energy Environ. Sci.* 2020, 13, 3439.
- [10] H. Zhang, X. He, K. Dong, Y. C. Yao, S. J. Sun, M. Zhang, M. Yue, C. X. Yang, D. D. Zheng, Q. Liu, Y. L. Luo, B. W. Ying, S. Alfaifi, X. Q. Ji, B. Tang, X. P. Sun, *Mater. Today Phys.* 2023, 38, 101249.
- [11] T. ul Haq, M. Arooj, A. Tahir, Y. Haik, Small 2023, 20, 2305694.
- [12] D. Li, Y. Y. Qin, J. Liu, H. Y. Zhao, Z. J. Sun, G. B. Chen, D. Y. Wu, Y. Q. Su, S. J. Ding, C. H. Xiao, Adv. Funct. Mater. 2022, 32, 2107056.
- [13] X. Y. Zhang, Y. X. Li, Z. J. Wu, H. B. Sheng, Y. B. Hu, C. Li, H. Y. Li, L. X. Cao, B. H. Dong, *Mater. Today Energy* 2022, 26, 100987.
- [14] Y. P. Zhang, F. Gao, D. Q. Wang, Z. L. Li, X. M. Wang, C. Q. Wang, K. W. Zhang, Y. K. Du, *Coord. Chem. Rev.* 2023, 475, 214916.
- [15] K. Maiti, N. H. Kim, J. H. Lee, Chem. Eng. J. 2021, 410, 128358.
- [16] B. W. Wang, X. X. Chen, Y. J. He, Q. Liu, X. X. Zhang, Z. Y. Luo, J. V. Kennedy, J. H. Li, D. Qian, J. L. Liu, G. I. N. Waterhouse, *Appl. Catal. B-Environ. Energy* 2024, 346, 123741.

- [17] X. Z. Ma, M. Y. Zhang, F. H. Aza, Q. Gao, Z. K. Xu, L. Li, L. L. Wu, X. T. Zhang, Y. J. Chen, J. Mater. Chem. A 2022, 10, 8258.
- [18] X. L. Han, Y. F. Yu, Y. Huang, D. L. Liu, B. Zhang, ACS Catal. 2017, 7, 6464.
- [19] H. Xu, H. Y. Shang, L. J. Jin, C. Y. Chen, C. Wang, Y. K. Du, J. Mater. Chem. A 2019, 7, 26905.
- [20] Y. M. Yang, Y. J. Ji, G. Y. Li, Y. Y. Li, B. H. Jia, J. Q. Yan, T. Y. Ma, S. Z. Liu, *Angew. Chem. Int. Ed.* **2021**, *60*, 26790.
- [21] L. H. Ai, N. Li, M. Chen, H. L. Jiang, J. Jiang, J. Mater. Chem. A 2021, 9, 16479.
- [22] D. X. Zhang, Y. H. Liu, L. H. Li, D. Li, T. Y. Jiang, H. Huang, D. L. Jiang, Z. H. Kang,B. D. Mao, J. Mater. Chem. A 2023, 11, 1927.
- [23] H. Y. Meng, W. Xi, Z. Y. Ren, S. C. Du, J. Wu, L. Zhao, B. W. Liu, H. G. Fu, Appl. Catal. B-Environ. Energy 2021, 284, 119707.
- [24] Q. W. Dong, M. L. Li, M. S. Sun, F. Y. Si, Q. Z. Gao, X. Cai, Y. H. Xu, T. Yuan, S. S. Zhang, F. Peng, Y. P. Fang, S. Y. Yang, Small Methods 2021, 5, 2100878.
- [25] H. Li, S. Y. Wang, M. T. Wang, Y. Y. Gao, J. B. Tang, S. L. Zhao, H. B. Chi, P. F. Zhang, J. S. Qu, F. T. Fan, C. Li, *Angew. Chem. Int. Ed.* 2022, 61, e202204272.
- [26] P. P. Wang, C. M. Ding, Y. T. Deng, H. B. Chi, H. B. Zheng, L. Liu, H. Li, Y. K. Wu, X. Liu, J. Y. Shi, C. Li, ACS Catal. 2023, 13, 2647.
- [27] Q. Y. Niu, X. T. Gu, L. Li, Y. N. Zhang, G. H. Zhao, Appl. Catal. B-Environ. Energy 2020, 261, 118229.
- [28] Q. J. Shi, J. Li, Y. B. Liu, K. J. Kong, A. Z. Li, H. H. Duan, ACS Catal. 2024, 14, 10728.
- [29] T. H. Lee, S. A. J. Hillman, S. Gonzalez-Carrero, A. Difilippo, J. R. Durrant, *Adv. Energy Mater.* **2023**, *13*, 2300400.
- [30] H. J. Li, L. H. Jian, Y. Chen, G. W. Wang, J. H. Lyu, X. L. Dong, X. H. Liu, H. C. Ma, Chem. Eng. J. 2022, 427, 131716.
- [31] J. C. Wang, T. S. Zhou, Y. Zhang, L. Li, C. H. Zhou, J. Bai, J. H. Li, H. Zhu, B. X. Zhou, *ACS Appl. Mater. Inter.* **2022**, *14*, 45392.
- [32] L. Shi, Y. Li, F. L. Zeng, S. J. Ran, C. Y. Dong, S. Y. Leu, S. T. Boles, K. H. Lam, *Chem. Eng. J.* 2019, 356, 107.
- [33] N. G. Divya, M. J. Bushiri, Crystengcomm 2019, 21, 1378.
- [34] B. R. Carvalho, Y. X. Wang, S. Mignuzzi, D. Roy, M. Terrones, C. Fantini, V. H. Crespi, L. M. Malard, M. A. Pimenta, *Nat. Commun.* 2017, 8, 14670.
- [35] L. Sharma, T. Botari, C. S. Tiwary, A. Halder, ACS Appl. Energy Mater. 2020, 3, 5333.

- [36] M. R. Kalus, N. Barsch, R. Streubel, E. Gokce, S. Barcikowski, B. Gokce, *Phys. Chem. Chem. Phys.* **2017**, *19*, 7112.
- [37] M. S. Shakeri, O. Polit, B. Grabowska-Polanowska, A. Pyatenko, K. Suchanek, M. Dulski, J. Gurgul, Z. Swiatkowska-Warkocka, *Scientific Reports* 2022, 12, 11950.
- [38] J. C. Wang, J. Ren, H. C. Yao, L. Zhang, J. S. Wang, S. Q. Zang, L. F. Han, Z. J. Li, *J. Hazard. Mater.* **2016**, *311*, 11.
- [39] J. Deng, C. Ye, A. H. Cai, L. Y. Huai, S. Q. Zhou, F. L. Dong, X. Y. Li, X. Y. Ma, Chem. Eng. J. 2021, 420, 129863.
- [40] A. Alrasheed, J. M. Gorham, B. C. T. Khac, F. Alsaffar, F. W. DelRio, K. H. Chung, M. R. Amer, ACS Appl. Mater. Inter. 2018, 10, 18104.
- [41] L. Q. Guo, F. Chen, X. Q. Fan, W. D. Cai, J. L. Zhang, *Appl. Catal. B-Environ. Energy* **2010**, *96*, 162.
- [42] J. R. Ran, W. W. Guo, H. L. Wang, B. C. Zhu, J. G. Yu, S. Z. Qiao, Adv. Mater. 2018, 30, 1800128.
- [43] X. L. Chen, T. Shi, K. L. Zhong, G. L. Wu, Y. Lu, Chem. Eng. J. 2020, 379, 122240.
- [44] J. Ye, Y. P. Zang, Q. Y. Wang, Y. D. Zhang, D. Sun, L. J. Zhang, G. M. Wang, X. S. Zheng, J. F. Zhu, J. Energy Chem. 2021, 56, 283.
- [45] W. H. Huang, X. M. Li, X. F. Yang, H. Y. Zhang, P. B. Liu, Y. M. Ma, X. Lu, Chem. Eng. J. 2021, 420, 127595.
- [46] C. A. L. Zhang, Y. Xie, J. T. Liu, F. H. Cao, H. P. Cong, H. Li, Chem. Eng. J. 2021, 419, 129977.
- [47] C. Wang, L. Zhang, G. C. Xu, L. F. Yang, J. H. Yang, Chem. Eng. J. 2021, 417, 129270.
- [48] D. C. Nguyen, T. L. L. Doan, S. Prabhakaran, D. T. Tran, D. Kim, J. H. Lee, N. H. Kim, Nano Energy 2021, 82, 105750.
- [49] F. L. Gong, S. Ye, M. M. Liu, J. W. Zhang, L. H. Gong, G. Zeng, E. C. Meng, P. P. Su, K. F. Xie, Y. H. Zhang, J. Liu, *Nano Energy* 2020, 78, 105284.
- [50] J. H. Bao, Y. M. Zhou, Y. W. Zhang, X. L. Sheng, Y. Y. Wang, S. Liang, C. Guo, W. Yang, T. Zhuang, Y. J. Hu, J. Mater. Chem. A 2020, 8, 22181.
- [51] I. S. Kwon, T. T. Debela, I. H. Kwak, Y. C. Park, J. Seo, J. Y. Shim, S. J. Yoo, J. G. Kim, J. Park, H. S. Kang, *Small* 2020, 16, 2000081.
- [52] Y. K. Liu, S. Jiang, S. J. Li, L. Zhou, Z. H. Li, J. M. Li, M. F. Shao, Appl. Catal. B-Environ. Energy 2019, 247, 107.
- [53] M. Y. Zheng, K. L. Guo, W. J. Jiang, T. Tang, X. Y. Wang, P. P. Zhou, J. Du, Y. Q. Zhao, C. L. Xu, J. S. Hu, Appl. Catal. B-Environ. Energy 2019, 244, 1004.

- [54] J. Sun, N. K. Guo, Z. Y. Shao, K. K. Huang, Y. W. Li, F. He, Q. Wang, Adv. Energy Mater. 2018, 8, 1800980.
- [55] J. Y. Liu, X. Liu, H. Shi, J. H. Luo, L. Wang, J. S. Liang, S. Z. Li, L. M. Yang, T. Y. Wang, Y. H. Huang, Q. Li, Appl. Catal. B-Environ. Energy 2022, 302, 120862.
- [56] H. J. Song, H. Yoon, B. Ju, D. Y. Lee, D. W. Kim, ACS Catal. 2020, 10, 702.
- [57] P. C. Ye, K. Q. Fang, H. Y. Wang, Y. H. Wang, H. Huang, C. B. Mo, J. Q. Ning, Y. Hu, Nat. Commun. 2024, 15, 1012.
- [58] M. Q. Guan, C. Wang, S. Li, H. W. Du, Y. P. Yuan, ACS Sustainable Chem. Eng. 2020, 8, 10313.
- [59] M. X. Chen, Y. Y. Zhang, R. Wang, B. Zhang, B. Song, Y. C. Guan, S. W. Li, P. Xu, J. Energy Chem. 2023, 84, 173.
- [60] T. F. Ma, W. W. Xu, B. R. Li, X. Chen, J. J. Zhao, S. S. Wan, K. Jiang, S. X. Zhang, Z.
 F. Wang, Z. Q. Tian, Z. Y. Lu, L. Chen, *Angew. Chem. Int. Ed.* 2021, 60, 22740.
- [61] N. A. Ran, E. H. Song, Y. W. Wang, Y. Zhou, J. J. Liu, Energy Environ. Sci. 2022, 15, 2071.
- [62] Z. H. Yang, S. Wang, C. Y. Wei, L. Chen, Z. M. Xue, T. C. Mu, Energy Environ. Sci. 2024, 17, 1603.
- [63] Y. X. Lu, T. Y. Liu, C. L. Dong, Y. C. Huang, Y. F. Li, J. Chen, Y. Q. Zou, S. Y. Wang, *Adv. Mater.* **2021**, *33*, 2007056.
- [64] F. H. Zhang, Y. F. Liu, L. B. Wu, M. H. Ning, S. W. Song, X. Xiao, V. G. Hadjiev, D. E. Fan, D. Z. Wang, L. Yu, S. Chen, Z. F. Ren, *Mater. Today Phys.* 2022, 27, 100841.
- [65] B. Konkena, J. Masa, A. J. R. Botz, I. Sinev, W. Xia, J. Kossmann, R. Drautz, M. Muhler, W. Schuhmann, ACS Catal. 2017, 7, 229.
- [66] J. Huang, Y. Li, Y. Zhang, G. Rao, C. Wu, Y. Hu, X. Wang, R. Lu, Y. Li, J. Xiong, Angew. Chem. Int. Ed. 2019, 58, 17458.
- [67] Z. Li, F. Huang, Y. F. Xu, A. H. Yan, H. M. Dong, X. Xiong, X. H. Zhao, Chem. Eng. J. 2022, 429, 132476.
- [68] Z. F. Jiang, W. M. Wan, H. M. Li, S. Q. Yuan, H. J. Zhao, P. K. Wong, Adv. Mater. 2018, 30, 1706108.
- [69] F. Huang, Z. Li, Y. F. Xu, A. H. Yan, T. Y. Zhang, Q. D. Wang, S. H. Li, S. J. Lu, W. X. Zhao, Y. Gao, J. X. Zhang, *Chem. Eng. J.* 2023, 473, 145430.

Chapter VII Conclusions and Perspectives

7.1. Conclusions

Direct seawater electrolysis has emerged as a sustainable pathway for industrial hydrogen production, addressing pressing energy challenges and conversion to a non-fossil-based energy society. Despite significant efforts to develop effective electrocatalysts, the practical application of seawater electrolysis is often hampered by non-ideal electrocatalysts that exhibit high energy consumption and severe chlorine corrosion on anodic electrodes. The primary challenge lies in optimizing the properties of these electrocatalysts to reduce the energy barrier for the OER while maintaining catalytic activity over long-term operation in seawater.

The research work presented in this Thesis aims to enhance the electrocatalytic performance of transition-metal-based materials for seawater oxidation. Various strategies, including heteroatom doping, binary and ternary heterojunction formation, and anion adsorption, were employed to modulate the catalytic properties of NiFe-LDH, NiOOH, and Fe₂O₃. To lower the energy consumption on the anode, MOR was engaged to replace OER. Additionally, a photo-assisted system was constructed to provide an extra driving force for OER catalysis. The key findings in these works are summarized as follows:

- 1) Heteroatom Doping and Heterojunction Formation: Heteroatom doping increased the number of OER-active sites in NiFe-LDH, while heterojunction adjusted interfacial charge distribution and facilitated electron transfer. The built-in electric field, combined with the presence of harder Lewis acidic sites, Ni³⁺, enhanced the adsorption of OH⁻, thus improving OER selectivity.
- **2) Hydrogen Bond Utilization:** Effective utilization of hydrogen bonding ensured the diffusion of OH⁻ at the reaction interface while PO₄³⁻ ions successfully repelled Cl⁻. The heterojunction reduced the energy barrier for OER while increasing that for CER.

- **3) Anion Modulation:** The investigation into anion-induced microenvironment modulation demonstrated its ability to simultaneously promote the PCET process in MOR and alter the adsorption behaviors of Cl⁻ ions and methanol molecules.
- **4) Ternary Heterojunction Formation:** The formation of a ternary heterojunction equilibrated the electrostatic effects from anions, maintaining undisrupted OH⁻ diffusion to the electrode surface. This heterojunction also facilitated channels for photo-excited charge transfer within the composite.

The detailed findings of each work are listed below:

In **Chapter 3**, the hybrid catalyst, Li-NFL/CN was synthesized through chemical coprecipitation and self-assembly methods. It delivered a current density of 100 mA cm⁻² at a low overpotential of 319 mV in alkaline seawater and maintained stable operation seawater oxidation at 200 mA cm⁻² for 100 h. Li-ion doping increased the population of Ni³⁺ sites, while Li-NFL/CN heterointerface redistributed interfacial charge and established a built-in electric field, enhancing the selectivity towards OH⁻, thus the OER activity and stability of NiFe-LDH in seawater. Theoretical calculations demonstrated that the synergistic effect of Li doping and CN/NiFe-LDH decreased the free energy of each elementary step in the OER process, while increasing the energy barrier of CER, thereby promoting the OER performance and durability of NiFe-LDH in seawater.

In **Chapter 4**, Ni(OH)₂/L-LFP was synthesized *via* laser ablation and electrodeposition methods using recycled LFP cathode materials. The Ni(OH)₂/L-LFP demonstrated exceptional electrocatalytic OER performance, achieving a current density of 10 mA cm⁻² at a low overpotential of 237 mV in alkaline seawater, with excellent stability at 100 mA cm⁻² for 600 h. The formation of Ni(OH)₂/L-LFP heterojunctions significantly increased electrochemical surface area, enhancing mass transfer capabilities and promoting effective adsorption of OH⁻ while repelling Cl⁻. Theoretical calculations revealed that the NiOOH/FP heterointerface

formed after reconstruction had an abundant DOS at adsorption sites near the Fermi level, implying enhanced electronic conductivity. The NiOOH/FP heterojunction was particularly advantageous for enlarging the overpotential range between OER and CER, ensuring OH⁻ adsorption through the hydrogen bond, while concurrently suppressing Cl⁻ adsorption. Additionally, PO₄³⁻ ions, which were leached during the reconstruction process, contributed to repelling Cl⁻ ions in seawater, thus mitigating catalyst corrosion.

In Chapter 5, a hierarchical Ni(OH)₂/NiMoO₄ heterostructured electrocatalyst was synthesized *via* hydrothermal and electrodeposition techniques. During the reconstruction process, *in situ* leached MoO₄²⁻ optimized the coordination environment on the surface of active species of NiOOH, promoting the non-electrochemical reaction during the MOR process. Meanwhile, the adsorbed MoO₄²⁻ weakened the adsorption strength of Cl⁻ ions on NiOOH, thus mitigating catalyst corrosion. As a result, the Ni(OH)₂/NiMoO₄ delivered excellent electrocatalytic MOR performance, achieving a current density of 10 mA cm⁻² at a low potential of 1.305 V in alkaline methanol. Ni(OH)₂/NiMoO₄ required low overpotentials of 267 and 381 mV to reach 100 and 500 mA cm⁻², respectively, in alkaline seawater. The full cell consisting of NiMo||Ni(OH)₂/NMO required merely 1.305 V to reach 10 mA cm⁻² in seawater splitting assisted by methanol oxidation. Compared with commercial Pt/C||RuO₂, the NiMo||Ni(OH)₂/NMO cell offered a 13.5 % energy saving for hydrogen production at 0.5 A cm⁻² in hybrid seawater.

In **Chapter 6**, amorphous Fe₂O₃ and MoO₃ were integrated into crystalline MoS₂ *via* laser ablation. The resulting structure exhibited an enlarged surface area and abundant active sites. Theoretical calculations indicated that the three-phase heterointerfaces extended the overpotential gap between OER and CER while promoting OH⁻ adsorption to counteract the electrostatic repealing effect. *In situ* generated SO₄²⁻ and MoO₄²⁻ served as the protective species to repel Cl⁻ to further enhance OER stability in seawater. Double built-in electric fields

formed at the heterointerfaces redistributed charges and facilitated the transfer of photogenerated charges to promote the OER process. Fe-L-MoS₂ catalyst exhibited significantly enhanced OER activity and durability in alkaline seawater, achieving 10 mA cm⁻² at 267 mV and demonstrating remarkable long-term stability, with only a 1.9 % activity loss for 100 h at 100 mA cm⁻². Light irradiation excited Fe-L-MoS₂ to generate carriers and reduced reaction interfacial resistance, thereby contributing to a 20.4 % increase in the seawater oxidation current density.

Materials cost and H₂ generation activity are two important parameters for evaluating the potential of catalyst application. All catalysts in this Thesis are based on transition metals, Ni (17.7 \$ kg⁻¹), Mo (64.2 \$ kg⁻¹), and Fe (5.9 \$ kg⁻¹), which are much cheaper than those of Pt (33,444 \$ kg⁻¹), Ru (19,164 \$ kg⁻¹), and Ir (153,998 \$ kg⁻¹). Those catalysts developed in this work exhibit superior OER activity than commercial RuO₂. Those catalysts also exhibit excellent long-term OER stability (>100 h) in alkaline seawater. The Faradic efficiencies of those catalysts are higher than 94 % at a current density of 100 mA cm⁻². Nonetheless, those catalysts have not been tested at 2 A cm⁻² (the United States Department of Energy target parameter for the AEM-water-electrolysis system). In a word, those catalysts have potential for industrial application but still need more evaluation under strict conditions.

7.2. Perspectives

While this Thesis has successfully developed high-performance transition-metal-based electrocatalysts for seawater oxidation, several important areas and unresolved issues warrant further exploration:

1) Anion-repelling mechanism: The current understanding of the anion-repelling mechanism primarily explains the enhanced anti-corrosion properties during seawater oxidation. However, the generation of bubbles can influence anion adsorption, raising questions about the stability of anion on the catalyst surface. Additionally, experimental observations of OH⁻ diffusion at

Chapter VII Conclusions and Perspectives

the reaction interface in the presence of anions are lacking. *In situ* techniques that allow real-time monitoring of reactions are necessary to elucidate the dynamic adsorption behavior of anions and their influence on OH⁻ diffusion. For instance, *in situ* UV–Vis spectroscopy combined with an electrochemical station could directly verify anion adsorption or desorption. Similarly, *in situ* sum frequency generation vibrational spectroscopy could be employed to study OH⁻ diffusion at the electrode–electrolyte interface during the OER process.

- 2) Role of chloride ions: While repelling Cl⁻ to reduce its negative influence is a primary focus in the design of seawater oxidation catalysts, recent studies suggest that Cl⁻ may also play a positive role in improving OER activity and durability.^[1,2] Therefore, the true impact of Cl⁻ on anodes during the seawater oxidation process requires further investigation. This includes understanding how Cl⁻ influences the catalyst reconstruction process, the behavior of catalytic sites, and the diffusion of OH⁻ and other cations, as well as the stability of anodes. Such insights could provide new directions for designing efficient seawater OER catalysts.
- 3) Utilization of CER: The CER, a competing reaction of OER in seawater splitting, is an important reaction for the chlor-alkali industry. As discussed in Chapter 1, the thermodynamic potential for CER is close to that of OER in an acidic environment (pH \leq 3.0), and the reaction kinetics for CER, which involves two-electron transfer, is faster than that for OER. This implies that CER can easily occur in acidic electrolytes, potentially leading to the production of high-value Cl₂ instead of O₂ during anodic oxidation reaction. While coupling CER with HER presents an effective strategy for advancing acidic seawater electrolysis, the development of cost-effective and durable anode catalysts for CER remains a significant challenge.
- 4) Microenvironment modulation: In this Thesis, $MoO_4^{2^-}$ was utilized to facilitate the PCET during the MOR process on NiOOH. However, other oxygen-containing anions, such as $PO_4^{3^-}$, $SO_4^{2^-}$, $SeO_4^{2^-}$, $WO_4^{2^-}$, and $VO_4^{3^-}$, could serve as alternatives for microenvironment modulation to adjust the kinetics of non-electrochemical processes in MOR. Furthermore, non-

Chapter VII Conclusions and Perspectives

electrochemical processes are also relevant in other small molecule reactions such as 5-hydroxymethylfurfural oxidation reaction (HMFOR). Therefore, it is advisable to extend the concept of microenvironment modulation through anion adsorption to other catalytic reactions, potentially enhancing their efficiency and selectivity.

7.3. References

- [1] H. Liu, W. Shen, H. Y. Jin, J. Xu, P. X. Xi, J. C. Dong, Y. Zheng, S. Z. Qiao, *Angew. Chem. Int. Ed.* **2023**, *62*, e202311674.
- [2] X. X. Duan, Q. H. Sha, P. S. Li, T. S. Li, G. T. Yang, W. Liu, E. D. Yu, D. J. Zhou, J. J. Fang, W. X. Chen, Y. Z. Chen, L. R. Zheng, J. W. Liao, Z. Y. Wang, Y. P. Li, H. B. Yang, G. X. Zhang, Z. B. Zhuang, S. F. Hung, C. F. Jing, J. Luo, L. Bai, J. C. Dong, H. Xiao, W. Liu, Y. Kuang, B. Liu, X. M. Sun, *Nat. Commun.* 2024, 15, 1973.